Spectral analyses of solar-like stars

Amanda Doyle

Doctor of Philosophy

Keele University

March 2015

Abstract

Accurate stellar parameters are important not just to understand the stars themselves, but also for understanding the planets that orbit them. Despite the availability of high quality spectra, there are still many uncertainties in stellar spectroscopy. In this thesis, the finer details of spectroscopic analyses are discussed and critically evaluated, with a focus on improving the stellar parameters.

Using high resolution, high signal-to-noise HARPS spectra, accurate parameters were determined for 22 WASP stars. It is shown that there is a limit to the accuracy of stellar parameters that can be achieved, despite using high S/N spectra. It is also found that the selection of spectral lines used and the accuracy of atomic data is crucial, and different line lists can result in different values of parameters.

Different spectral analysis methods often give vastly different results even for the same spectrum of the same star. Here it is shown that many of these discrepancies can be explained by the choice of lines used and by the various assumptions made. This will enable a more reliable homogeneous study of solar-like stars in the future.

The Rossiter-McLaughlin effect observed for transiting exoplanets often requires prior knowledge of the projected rotational velocity ($v \sin i$). This is usually provided via spectroscopy, however this method has uncertainties as spectral lines are also broadened by photospheric velocity fields known as "macroturbulence" ($v_{\rm mac}$). Using rotational splitting frequencies for 28 *Kepler* stars that were provided via asteroseismology, accurate $v \sin i$ values have been determined.

By inferring the $v_{\rm mac}$ for 28 *Kepler* stars, it was possible to obtain a new calibration between $v_{\rm mac}$, effective temperature and surface gravity. Therefore macroturbulence, and thus $v \sin i$, can now be determined with confidence for stars that do not have asteroseismic data available. New spectroscopic vsini values were then determined for the WASP planet host stars.

Acknowledgements

I would like to thank my supervisor, Barry Smalley, for always encouraging me to believe in myself and have confidence in my work. It has been a pleasure to work with someone who shares the same passion for science that I do. I consider myself extremely lucky that his door was always open and that he always made time to discuss my work even when I brought an infamously long list of things I wanted to talk about. I am also grateful that he gave me room to express my own ideas and to take my research in the direction I wanted it to go in.

I would like to thank Guy Davies and Bill Chaplin for providing the asteroseismic rotational velocity data used in this thesis, and for greatly improving my understanding of asteroseismology. In particular I want to thank Guy for putting in a lot of work to make sure I had all the data I needed well in advance of my thesis deadline.

There are many others with whom I've had enlightening conversations, or who have made my life so much easier by taking the time to answer my burning questions via email; Pierre Maxted, John Southworth, Yvonne Elsworth, Sarbani Basu, Andrea Miglio, Amaury Triaud, Yilen Gomez, David Brown, Luan Ghezzi, and Richard Gray. I am particularly grateful to Patrick Francois for helping me appreciate the work that goes into obtaining spectra at the telescope, and for his patience and enthusiasm in teaching me skills that have been invaluable. I would like to thank Davide Gandolfi who helped to improve both my paper and my thesis with his insightful comments. I'm also extremely grateful to Deepak Mahtani, Ben Clark, and Oli Turner for helping me out when I really needed it.

I would never have been able to do my PhD without my wonderful, selfless husband Dwane Doyle. He took a huge risk in giving up his job and moving to another country with me just so that I could follow my dream. He has always been there to support me, and never lost faith in my ability to do this. He has offered words of encouragement on the days when everything seemed to go wrong and it felt like I would never finish, and then celebrated with me when I found solutions to those problems. He is my best friend and my soul mate and I am so glad that he has been there to share this adventure with me.

I also never would have gotten this far without my parents, Maria and John Ryan. They always encouraged my interest in science and have made my journey so much easier. They get as excited about my various achievements as I do, even if they

don't quite understand what I'm talking about half of the time!

I would like to thank Niamh Lalor for being an absolutely incredible friend. For always making an effort to meet for coffee, for never failing to make me smile when I really needed it, and for lots of wonderful conversations over the years.

I am extremely grateful to Mandy Bailey, who is always on hand to offer me advice whenever I need it. She has opened up a new world of opportunities for me, including kick-starting my science writing career which has ultimately been a big help when writing my thesis.

Finally, I would like to dedicate to this thesis to my late granduncle Joe Holland. He sparked my interest in science and nature when I was very young, and then continued to fan that flame into a desire to study astronomy. He gave me so many books, which opened my eyes to the world of science. He was an incredible man who knew so much about so many different topics, and had so many wonderful stories to tell. He always showed such interest in my progress at school and university, and I know he would be proud of me for getting this far.

Contents

List of Figures

List of Tables

1 Understanding stellar spectra

Many of the lines, especially the stronger ones, have been identified with respect to the substance producing them, but this must be a labour of years.

- Henry Augustus Rowland, 1895

1.1 Motivation

The overall aim of this work was to analyse spectra of solar-like stars in detail, with a focus on improving stellar parameters. This in turn feeds into exoplanet studies, as a planet cannot be understood without first gaining an appreciation of the star which it orbits. In particular this work is relevant to transiting exoplanets, both from the analysis of the Wide Angle Search for Planets (WASP) host stars and from improving knowledge of spectral line broadening, which needs to be known in order to study transiting planet obliquities.

A planet seen transiting its parent star can be coaxed into unveiling much about itself. Transiting planets were first suggested as a possible cause of stellar variability by Lardner (1858), and Struve (1952) proposed that it should be possible to detect the periodic dip in magnitude by a Jupiter-mass planet passing in front of its host star. The first detection of a transiting exoplanet had to wait nearly half a century (Charbonneau et al. 2000; Henry et al. 2000), which paved the way for hundreds more being discovered in the subsequent years. However, one does not get very far in planetary research without first knowing something about the parent stars.

Transiting planets, yield information such as the orbital period of the planet from the light curve, however measuring the planet's mass and radius require knowledge of the mass and radius of the host star. The transit of an exoplanet across its host star will only yield the ratio of the planet to star radius. Similarly, the mass of a planet, acquired from combining transiting and radial velocity data, cannot be determined independently from the mass of the star (Winn 2011).

It is thus imperative that the mass and radius of the host star are known precisely, but obtaining direct measurements of these parameters is only possible for a limited number of stars. For instance, a fundamental value of mass cannot be obtained unless the star is in a suitable binary system (Andersen 1991; Torres, Winn & Holman 2008), and determining the radius of a star often requires knowledge of the angular diameter,

which in turn needs a known distance (North et al. 2007). Most current distance measurements were acquired using the parallax technique with ESA's *Hipparcos* satellite (Perryman & ESA 1997; van Leeuwen 2007), but these will soon be complemented by data from ESA's *Gaia* mission (Perryman et al. 2001).

For stars without direct mass and radius measurements, spectroscopy can be used to provide an estimate of these parameters. If the effective temperature ($T_{\rm eff}$), surface gravity ($\log g$) and chemical composition are known, then a calibration or grid of stellar evolutionary models can be used to find the stellar mass and radius, and thus the planetary mass and radius. Accurate values for the planetary radii can be used to study unusual properties of some systems, such as "bloated" planetary radii (Fortney et al. 2008; Spiegel & Burrows 2013).

Discerning the chemical composition of host stars has additional value. It is well established that higher metallicity stars are more likely to have planets (Gonzalez 1998; Santos, Israelian & Mayor 2004; Fischer & Valenti 2005; Ghezzi et al. 2010; Mortier et al. 2013a), and it is possible that other planetary parameters, such as planet core size and planet radius, are related to the stellar metallicity (Guillot et al. 2006; Dodson-Robinson 2012; Enoch, Collier Cameron & Horne 2012). It is not just the overall composition that is important as individual elements have a role to play in the formation of planets. The stellar Fe abundance is often the only elemental abundance used, as it is easiest to obtain, but O and C are the first and second most important contributor to the mass of giant planets respectively, along with oxides of Si, Mg, Ca and Al (Brugamyer et al. 2011).

It has also been suggested that stars with planets can have different chemical compositions to stars without known planets (Meléndez et al. 2010; Meléndez et al. 2009; Ramírez, Meléndez & Asplund 2009; Gonzalez, Carlson & Tobin 2010; Ramírez et al. 2010). In particular, Si may be enriched in planet host stars (Robinson et al. 2006; Brugamyer et al. 2011). There is still some dispute regarding these supposed trends (González Hernández et al. 2010) and it is complicated by the Galactic chemical evolution (Schuler et al. 2011b). Therefore these relationships need to be thoroughly verified by ensuring that the trend isn't simply arising from systematics of the adopted method. Can we truly understand these correlations, and thus planetary formation, without being confident in the value of the metallicity? It is imperative that the spectroscopic parameters are obtained in the best way possible.

While the exoplanets might steal the limelight, stellar parameters are important

whether or not the star comes equipped with a planetary system. For example, the mass is important for stellar evolution studies. The $T_{\rm eff}$ and metallicity are also required as prior information before other stellar parameters can be extracted via asteroseismology.

The initial goal for this thesis was to determine stellar parameters using high signal-to-noise ratio (S/N) spectra from the High Accuracy Radial velocity Planet Searcher (HARPS) spectrograph, which is installed on the 3.6 m telescope at La Silla. The spectra are those of planet host stars, namely a subset of the WASP stars. These stars already had spectra with lower resolution and lower S/N available, but such spectra are not necessarily appropriate for revealing the stellar parameters with the accuracy and precision desired for planetary studies.

My intention was to analyse each HARPS spectrum in detail by measuring a selection of the spectral lines, rather than using an automated method to extract the parameters. Using this "hands on" approach has enabled me to critically evaluate spectral analysis techniques and come to a better understanding of the problems that can arise with such analyses. For instance, there will always be errors in low S/N spectra due to the noise that pollutes them, however significant errors can still be present in the parameters derived from high S/N spectra and there are limits as to how much we can extract even from these ideal spectra. It was my goal to identify any systematics, so that ultimately numerous spectra can be analysed with confidence via automated methods.

The motivation for the second part of this thesis was spawned from the first, as it came to light that the ambiguity between two different sources of line broadening could be solved. The macroturbulence[1] ($v_{\rm mac}$) and projected rotational velocity ($v \sin i$) are intertwined in spectral line profiles. These two broadening parameters can be disentangled via Fourier methods, however this method is limited to stars with exceptionally high S/N and high resolution spectra, and it is also a difficult method to utilise. By using asteroseismic results from *Kepler* to pinpoint the $v \sin i$ with good accuracy, $v_{\rm mac}$ can be disentangled from the $v \sin i$ relatively simply. This in turn leads to a calibration between macroturbulence and $T_{\rm eff}$ and $\log g$, allowing the macroturbulence to be estimated and the $v \sin i$ to be measured.

It is desirable to know each of these parameters individually for a number of reasons. Macroturbulence is not even accurately known for the solar spectrum, with

[1] Also given as $\zeta_{\rm RT}$, where RT stands for radial-tangential.

values ranging from 1.9 $\mathrm{km\,s^{-1}}$ (Bean et al. 2006) to 3.8 $\mathrm{km\,s^{-1}}$ (Gray 1984a), and this can make a significant difference in the shape of spectral line profiles. Previous calibrations exist (Gray 1984a; Saar & Osten 1997; Gonzalez 1998; Valenti & Fischer 2005; Bruntt et al. 2010a), however none of these use an independent measurement of $v \sin i$.

The $v \sin i$ is important for estimating the age of stars, which in turn is vital for stellar evolution studies. A prior knowledge of $v \sin i$ is also needed to obtain the spin-orbit misalignment of planetary systems (Triaud et al. 2010). Depending on the geometry of the system, there can be a degeneracy between $v \sin i$ and the inclination angle. In these cases, the only way to measure the spin-orbit angle is to have a measurement of $v \sin i$ from an external source, such as spectroscopy, however current spectroscopic values are plagued with uncertainty from the macroturbulence.

1.2 A brief history of stellar spectroscopy

The stars have fascinated mankind for millennia. Monitoring the skies was important for making predictions on when to sow or harvest crops, and knowledge of the stars was imperative for navigation. Attempts at measuring stellar parameters began with the invention of the telescope, but their meaning was not truly understood for some time later (Tassoul & Tassoul 2004).

In 1666, Isaac Newton first used a prism to disperse the white light of the Sun into a rainbow of colours; a spectrum. The gradual change in colour from red to blue was noted to be interspersed with seven vertical dark bands by Hyde Wollaston (1802), who incorrectly assumed that these bands signified the boundaries of the different colours. With the advent of the first spectroscope by Joseph von Fraunhofer, it was revealed that the solar spectrum was littered with hundreds of these dark lines, and Fraunhofer named the most prominent lines with letters of the alphabet (Fraunhofer 1817). This notation is still in use today, for example the sodium doublet at 5889 Å is the "D" line, while the two calcium lines at 3933 and 3968 Å are the K and H lines respectively.

Over 40 years after Fraunhofer's lines were discovered, the connection between spectral lines and chemical elements was made (Kirchhoff 1859; Kirchhoff & Bunson 1860). Huggins & Miller (1864) observed numerous elements in several bright stars, and confirmed that the same elements are present in the stars as on Earth. In 1868, Anders Jonas Ångström published a dataset of the wavelengths of lines in the solar

spectrum, to which further lines were added by Rowland (1895). By 1891, 36 elements had been identified in the solar spectrum (Hoskin 1999; Tassoul & Tassoul 2004).

Spectral lines can be used to decipher the composition of the photosphere of a star, as well as provide estimates on the effective temperature and surface gravity. Different types of stars exhibit vastly different spectra, and it is the temperature that is the main factor in dictating which elements are present in the spectra and their subsequent pattern of lines. In order to understand what this pattern is telling us, we first need to classify the stars. Henry Draper first photographed a stellar spectrum in 1872, which eventually led to a catalogue being compiled by Edward Pickering (Pickering & Fleming 1897), who along with Willamina Fleming and Antonia Maury arranged the spectra in a continuous series. The modern classification system was introduced by Annie Jump Cannon, and is based on the strength of the hydrogen Balmer lines. Cannon arranged the order of spectral classes into the familiar OBAFGKM sequence, with O being the hottest and M being the coolest (Cannon & Pickering 1912). The OBAFGKM spectral sequence is used for both main sequence (MS) and evolved stars, with the hotter stars being referred to as "early-type", while the cool stars are called "late-type". Each spectral class is further divided with ten subclasses per group, however some classes are not commonly used. For example, the main subclasses for G stars are G0, G2, G5, and G8 (Gray 2008).

In this system, the Balmer lines peak in A-type stars, and other spectral line features change smoothly between different classes. Successful investigations into the theory behind this were implemented by Megh Nad Saha, who realised how temperature and pressure play a role in stellar spectra (Saha 1921). Ralph Howard Fowler and Edward Arthur Milne then combined Saha's work with the Boltzmann equation, which led to Cecilia Payne-Gaposchkin refining the spectral classification system with a temperature scale based on chemical composition (Payne 1929; Payne 1930). This work paved the way for modern stellar spectroscopy and the investigation of stellar parameters.

1.3 The continuous spectrum

Fraunhofer also noted that the intensity of the light of the Sun peaked in the yellow-green region of the spectrum. It is now known that the intensities of stars at different temperatures peak at different wavelengths, with the radiation emanating from hot

stars peaking at short wavelengths, while cool stars peak at long wavelengths. The relationship between the temperature and peak wavelength is given by Wien's Law, $\lambda_{max} = 2.9 \times 10^{-3}/T_{\rm eff}$, and the spectrum produced at a particular temperature is assumed to be that of a perfect blackbody.

If one were able to send a spectroscope deep enough into the interior of a star, then the resulting spectrum would almost mimic a blackbody spectrum that is free of the "taint" of spectral lines. However, there are various processes that can remove photons from a beam of light as it travels through the outer layers of the star, and this can in turn change the overall shape of the spectrum in a number of different ways. The change in the intensity (I_v) of light is given by

$$\mathrm{d}I_v = -I_v \, \mathrm{d}\tau_v, \tag{1.1}$$

where τ_v is the optical depth which is given by

$$\tau_v = \int_0^L \kappa_v \rho \, \mathrm{dx}, \tag{1.2}$$

and x is the geometrical depth, L is the path length, and ρ is the density of the star. The opacity, κ_v, also known as the absorption coefficient, is a measure of a material's ability to absorb or scatter radiation at a given frequency. The continuous opacity is typically dominated by bound-free and free-free processes which cause chunks of the spectrum to be removed via absorption. The continuous opacity varies gradually with wavelength, thus determining the shape of the star's continuous spectrum, called the continuum.

Bound-free transitions (also called photoionisation) of neutral hydrogen is a strong source of opacity from early A-type to mid F-type stars. The Balmer lines are created when a hydrogen atom with an electron in the $n = 2$ energy level (where n is the principal quantum number) receives enough energy to be excited to a higher energy level. However, if a photon with a wavelength of 3647 Å or shorter hits the hydrogen atom, it will become ionised. The continuum will rise gradually towards the blue end of the spectrum, but when it reaches this wavelength, it will drop suddenly as the photons become absorbed by the H atoms. This drop is known as the Balmer jump, or discontinuity. Similarly, the Paschen jump occurs at 8212 Å, and the optical spectrum in between the two is known as the Paschen continuum. This behaviour results in the "saw-tooth" appearance of the continuous spectrum as seen in Figure 1.1.

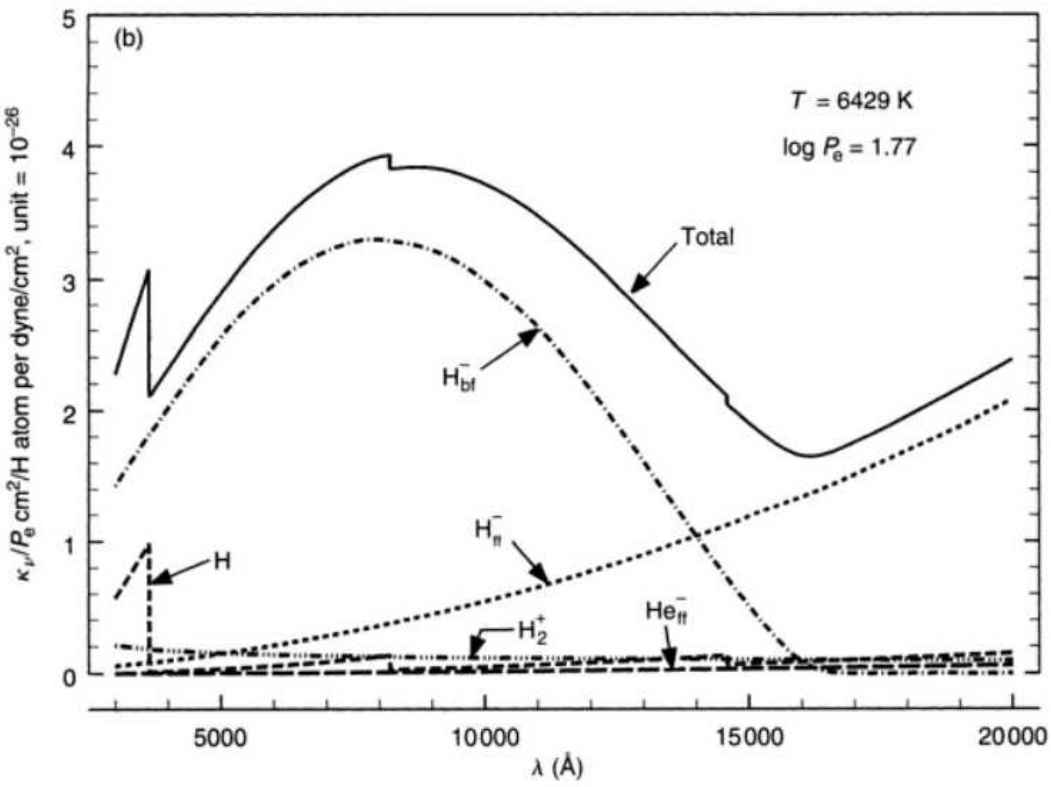

Figure 1.1: The solid line shows the continuous spectrum for a star of $T_{\rm eff} = 6429$ K, which is the combination of different sources of opacity at different wavelengths. Credit: Gray (2008). Reproduced with permission.

The negative hydrogen ion, H^-, is the dominant opacity source for late-A to mid-F, and it also contributes significantly in G-type stars. The negative hydrogen ion is a hydrogen atom that has captured a second electron. This second electron is very weakly bound and its ionisation energy is only 0.754 eV, meaning that a photon with a wavelength of 16450 Å or shorter will remove the electron and cause dissociation of the atom. The origin of the extra electron is in the ionisation of metals. Photodissociation of H^- peaks at a wavelength of around 8500 Å before gradually decreasing again, taking a bell-shaped chunk out of the continuum. There is also a contribution to the opacity by free-free transitions in the H^- ion, which rises into the infrared and rivals the bound-free opacity at around 14500 Å. The free-free transition takes place as the second electron absorbs a photon that changes the type of orbit of the electron. For K and M-type stars, the opacity is dominated by that from molecular absorption bands, although there is also some continuous opacity present from the Rayleigh scattering of H_2 molecules.

While a particular process will dominate the continuous opacity, the final shape of the continuum will be dictated by a combination of different types, as is shown in the

example of a 6429 K star in Figure 1.1 (Collins 1989; Carroll & Ostlie 2006; Robinson 2007; Gray 2008; Gray & Corbally 2009).

1.4 Spectral lines

While hydrogen, and to a lesser extent, helium cause the continuous opacity in stars, it is the metallic elements that give rise to line opacity, i.e. spectral lines. The continuum is formed deep within the photosphere, the wings of the lines are formed higher up, and the cores of the lines are formed in the upper layers of the photosphere. If the continuous opacity is high then there is only a limited range in the photosphere in which a spectral line can form. This means that line will be weaker than if the continuous opacity was low. Thus the line strength for weak lines is proportional to the line opacity and inversely proportional to the continuous opacity. This correlation is only valid for weak lines, as strong lines are more likely to be affected by collisional broadening (discussed in Section 1.8.4) and microturbulence[2] ($v_{\rm mic}$; discussed in Section 1.8.3.1) than weak lines (Gray & Corbally 2009). Line opacity can also behave like continuous opacity in the upper photosphere if many lines are present, which is known as "line blanketing".

An absorption line is formed via a bound-bound transition, as an electron in an atom moves up an energy level when a photon is absorbed. Similarly, an emission line is formed when a photon is released and the electron drops to a lower level. The amount of energy needed for an electron to be excited to a higher energy level is called the lower-level excitation potential[3], (EP) with units of eV. The difference in energy between two levels will determine the wavelength of the spectral line based on Planck's equation $E = hc/\lambda$. If the atom receives more energy than the excitation potential, then the incoming photon will either be scattered or the atom will become ionised. The energy needed to liberate an electron completely from an atom is known as the ionisation potential, and this is the energy difference between the ground state and the continuum, which in this case is the area beyond the atom's influence (Gray 2008; Robinson 2007).

Spectral lines can be measured by means of the equivalent width[4] (EW). The EW is given as

[2]Also given as ξ.
[3]Also given as χ
[4]Also given as W_λ.

$$\mathrm{EW} = \int \frac{F_c - F_\lambda}{F_c} d\lambda, \tag{1.3}$$

where F_c is the flux at the continuum and F_λ is the radiant flux as a function of wavelength. It is so called because the area of the spectral line on the plot of wavelength versus intensity is equivalent to the width of a rectangular box where the height of the box is equal to that of the continuum. Dividing the area within the spectral line by F_c is done in order to have the flux measurements in units of the continuum. For spectral lines, the full width at half maximum (FWHM) is used to describe the broadening of the line, rather than the strength of the line (Carroll & Ostlie 2006). EW has wavelength units, so that it is usually given in Å or nm.

The most prominent elements evident in a stellar spectrum are dependent on the T_{eff} of the star. This is because there is a preferred temperature range for each possible electron transition in an atom, as given by the Saha and Boltzmann equations.

The Saha equation denotes how the spectral line strength depends on the ionisation state of the atoms present:

$$\frac{N_{(i+1)}}{N_i} = \frac{2Z_{i+1}}{n_{\mathrm{e}} Z_i} \left(\frac{2\pi m_{\mathrm{e}} kT}{h^2} \right)^{3/2} e^{-\chi_i / kT}, \tag{1.4}$$

where N_{i} is the number of atoms, χ_{i} is the ionisation energy and i is the ionisation stage, n_{e} is the number density of free electrons, m_{e} is electron mass, h is Planck's constant, and Z_{i} is the partition function. The partition function is the weighted sum of different possible electron configurations depending on the ionisation state and is given as

$$Z = \sum_{j=1}^{\infty} g_j e^{-(E_j - E_1)/kT}, \tag{1.5}$$

where E_j in the energy of the jth energy level, and g_j is the degeneracy of that level.

The Boltzmann equation denotes the distribution of electrons in different levels of the atoms;

$$\frac{N_{\mathrm{b}}}{N_{\mathrm{a}}} = \frac{g_{\mathrm{b}} e^{-E_{\mathrm{b}}/kT}}{g_{\mathrm{a}} e^{-E_{\mathrm{a}}/kT}} = \frac{g_{\mathrm{b}}}{g_{\mathrm{a}}} e^{-(E_{\mathrm{b}} - E_{\mathrm{a}})/kT}, \tag{1.6}$$

where g_{a} and g_{b} are the number of degenerate states with energy of E_{a} and E_{b} respectively, and N_{a} and N_{b} are the number of atoms with energy E_{a} and E_{b} respectively.

Combining the two yields information as to what elements will peak at what temperatures. For example, the Boltzmann equation indicates that the strength of the Balmer lines will increase with temperature because there will be more electrons in

the first excited state. However the Saha equation shows that at temperatures above ∼12,000 K almost all of the hydrogen is ionised, resulting in the Balmer lines peaking at around 10,000 K. Most elements do not peak at a certain temperature in the way that H does. This is because the resonance line, that which emanates from the ground state, increases in strength with decreasing temperature. Another example lies in the fact that even though the Sun has much more H than Ca, at a temperature of 5777 K very few H atoms will be able to produce Balmer lines, whereas almost all of the Ca atoms will be able to produce lines. This means that the strongest lines in the Sun are the Ca II H and K lines (Carroll & Ostlie 2006; Gray & Corbally 2009).

The Fe I abundance is sensitive to changes in $T_{\rm eff}$, but relatively insensitive to changes in $\log g$, meaning that Fe I can be used as a temperature indicator. This temperature sensitivity is greater for low EP lines, and is almost negligible for high EP lines. Thus requiring that there is no trend between EP and abundance should yield the $T_{\rm eff}$ of the star. The same principle can be applied to Fe II lines, where in this case it is the high EP lines that are sensitive to $T_{\rm eff}$ changes, however there are not usually a sufficient number of Fe II lines present.

Similarly, the Fe II abundance is sensitive to changes in $\log g$. Thus, requiring that the Fe I and Fe II abundances agree should result in a value for $\log g$. These methods for determining the $T_{\rm eff}$ and $\log g$ from Fe lines are known as excitation and ionisation balance respectively (Takeda, Ohkubo & Sadakane 2002).

1.5 Non-local thermodynamic equilibrium (NLTE)

The majority of spectral analysis techniques (e.g. Santos, Israelian & Mayor 2004; Valenti & Fischer 2005; Sozzetti et al. 2006; Gonzalez & Laws 2007; Sousa et al. 2008; Bruntt et al. 2010a; Ghezzi et al. 2010; Fossati et al. 2011; Schuler et al. 2011b; Torres et al. 2012) still assume that thermodynamic equilibrium is possible for small volumes within the star, i.e. local thermodynamic equilibrium (LTE). This assumption is usually made due to the computational difficulties inherent with non-LTE calculations.

In LTE assumptions, the Saha-Boltzmann equations are used to determine the atomic level populations from the local gas temperature. However, the atomic level population is also coupled with the radiation field, which is non-local due to photons being scattered into other parts of the star. This means that the actual level populations are different from those calculated using the Saha-Boltzmann equations.

The atomic level populations in NLTE are calculated by means of a statistical equilibrium (SE) equation, which occurs when there is a balance between radiative and collisional population and de-population processes, i.e.

$$n_{\rm i} \sum_{j \neq i} (R_{\rm ij} + C_{\rm ij}) = n_{\rm j} \sum_{j \neq i} (R_{\rm ji} + C_{\rm ji}), \tag{1.7}$$

where R and C represent the radiative and collisional rates respectively and i and j are energy levels. Each ion, along with all of its energy levels, needs to be taken into account as well as the rate of interactions between particles and photons, such as excitation and ionisation of atoms. As Asplund (2005) phrases it: "*In non-LTE, in principle everything depends on everything else, everywhere else.*" Rates of collision are influenced by temperature and the number density of particles, whereas radiative rates are influenced by the radiative field (Asplund 2005; Bergemann 2011; Mashonkina 2010a).

The departure coefficient, b_i, is used to quantify the effects of the departure from LTE on the line strength;

$$b_{\rm i} = \frac{n_{\rm i}}{n_{\rm i}^*}, \tag{1.8}$$

where n_i is the number density computed from SE and n_i^* is the number density computed from the Saha-Boltzmann equations. The departure coefficient varies depending on the layer of formation, which means that NLTE may induce opposite effects in the wings and core of one line. When b_i is greater than 1, the line is stronger because of extra absorbing atoms in the lower level of the transition. When b_i is less than 1, the line is weaker than in LTE because there are fewer absorbing atoms (Asplund 2005; Mashonkina 2010c).

The abundance obtained from Fe I lines can be different depending on whether LTE or NLTE is assumed. In particular, using LTE for metal-poor stars leads to a large discrepancy between abundances of Fe I and Fe II lines. This is because of both decreasing collision rates as there are fewer electrons from metals, as well as increasing photoionisation rates. In addition, Fe I lines with low excitation potential deviate more from LTE than lines with high excitation potential (Mashonkina 2010b; Mashonkina et al. 2011). NLTE effects are more prominent for Fe I than Fe II lines, and there can be a difference of up to 0.1 dex in abundance between the two ionisation states (Asplund 2005; Caffau et al. 2011). Fe II can thus be used as a more reliable indicator

for abundance, however this is not easy due to the paucity of lines (Meléndez & Barbuy 2009).

1.6 Model atmospheres

In order to compute a synthetic spectrum, a model atmosphere of the star is needed. The most commonly used models are the 1D models of ATLAS (Kurucz 1993) and MARCS (Gustafsson et al. 1975). 1D models are time independent and assume hydrostatic equilibrium. Energy is mainly transported by convection in late-type stars, and this is approximated by the mixing length theory (MLT) (Bonifacio et al. 2012).

The MLT (Böhm-Vitense 1958) assumes that convective energy is transported by eddies that move in the atmosphere. An eddy will move up in the atmosphere until it reaches the same temperature as the surrounding material, at which point it will dissolve. The height that an eddy moves up or down is known as the mixing length parameter, α. This is a free parameter that is usually between 0.5 and 2.0 (Castelli, Gratton & Kurucz 1997).

MARCS and ATLAS models agree very well and the abundances determined from the two models will only differ by $\sim$0.04 dex (Bonifacio et al. 2009; Magic 2014). However, for large optical depths, MARCS and ATLAS will produce slightly different results due to a different treatment of MLT (Bonifacio et al. 2012).

The ATLAS models also have the option of including overshooting. Overshooting is the assumption that the eddy stops moving upward when its centre is at the top of the convection zone. Therefore part of the eddy is actually above the boundary of the convection zone (Castelli, Gratton & Kurucz 1997). However, the inclusion of overshooting produces an unrealistic temperature structure in the atmosphere, which results in the abundances being overestimated by $\sim$0.1 dex, and this option should not be used (Castelli, Gratton & Kurucz 1997; Bonifacio et al. 2009; Bonifacio et al. 2012).

Another variation of the MLT was proposed by Canuto & Mazzitelli (1991, 1992). The CM theory assumes that the mixing length is equal to the distance of the nearest stable layer, and thus has no need for the free parameter α.

Despite the simplifications and crude assumptions of 1D models, they have still proven to be remarkably good at reproducing the stellar spectra. This has improved with the acquisition of more precise laboratory data and improvements in opacity sampling or opacity distribution functions (Magic et al. 2013).

However, hydrodynamic, time-dependant 3D models will produce a more accurate representation of stellar atmospheres as they can model the convection directly. The difference between 3D and 1D models can have an appreciable effect on the strength of synthetic line profiles. This can lead to systematic effects in abundance determination, especially if the star is of low metallicity (Collet, Asplund & Trampedach 2007).

This is because the 1D models assume radiative equilibrium. The thermal balance comes from the radiative heating from spectral line re-absorption of continuum radiation and the adiabatic cooling from the expansion of upflowing gas. For solar metallicity, there are enough spectral lines to generate sufficient radiative heating in the optically thin layers so that the mean temperature is then close enough to that expected from radiative equilibrium. This means that the difference between 1D and 3D is small at solar metallicity.

However, metal-poor stars do not have enough lines and therefore the cooling from the expansion of upflowing material dominates over the radiative heating from the spectral lines. The 1D models do not take this into account, so that they can overestimate the temperature by $\sim$1000 K in the optically thin layers (Asplund 2005; Magic et al. 2013).

In 3D models, there is no need to change the $T_{\rm eff}$ to get an agreement between the abundances of low and high EP lines (Asplund et al. 2000). However, as the low EP lines are more sensitive to changes in $T_{\rm eff}$, they are also more sensitive to departures from LTE. NLTE effects are thus more prominent in 3D models compared to 1D models, particularly for low metallicities. This is because the outer layers of the star are cooler in 3D models so that there is larger decoupling between radiation and local temperature. The low EP lines then become stronger and more sensitive to the conditions in the outer photosphere (Bergemann et al. 2012).

1.7 Oscillator strength

The oscillator strength, f, is a vital piece of atomic data that is needed in order to obtain elemental abundances. It is the strength of the electron transition taking place and it is typically written as $\log gf$, where g is the statistical weight of the energy level that the transition initiated from. A high value of $\log gf$ does not necessarily mean that the spectral line will appear strong, as other factors such as temperature, pressure and chemical composition will also influence the line strength (Wahlgren 2010).

The *f*-value can be obtained once the mean lifetime of the excited level and intensity of the emission line are measured. In an ideal world, the laboratory oscillator strengths should be the most reliable, however according to Wahlgren (2010), many lines in data sets still include oscillator strengths based on work by Corliss & Bozman (1962). It has been shown that these values are often too high by an order of magnitude and include scale errors that vary depending on the element. These *f*-values are also partially correlated with the EP of the different transitions (Sneden & Lawler 2005; Wahlgren 2010).

Due to the paucity of laboratory data available, an "astrophysical" $\log gf$ is often used instead. This is done by adjusting the oscillator strengths by the value equal to the amount needed to change the individual abundance of that line to a fixed solar value. For example, if the abundance of a line in the Sun[5] is found to be 7.55 and the $\log gf$ is -1.50, then the $\log gf$ will be changed to -1.45 if the solar abundance is fixed to 7.50. The result is that scatter is completely reduced for the Sun as all lines now yield the same abundance. Alternatively, a line-by-line differential analysis can be performed with respect to the Sun, which will also eliminate the problems caused by inaccurate oscillator strengths and reduce the scatter in the abundances (Bruntt, De Cat & Aerts 2008; Brugamyer et al. 2011).

However, this method is not without its problems. For instance, if the star being analysed is not the same spectral type as the one where the oscillator strength was determined from, then there will be different excitation and line blending conditions which will create errors in the astrophysical $\log gf$. The lines in the different stars to be compared must be equally sensitive to abundance and broadening and this requirement is only satisfied for a limited range of stellar values. Differential analysis should also use the same line list between stars in order to minimise errors (Takeda, Ohkubo & Sadakane 2002; Takeda et al. 2005b; Gonzalez 2006; Meléndez et al. 2010; Bergemann 2011; Wahlgren 2010).

Theoretical and laboratory obtained $\log gf$ values tend to disagree more with decreasing line strengths, and this can introduce a scale error such that the deviation between the measured and true values of $\log gf$ increases for lower values of $\log gf$ (Blackwell & Shallis 1979; Meléndez & Barbuy 2009). This is most likely because experimental *gf* values of weak lines can have errors of around 20 per cent or more, as

[5] Abundances and their notation will be discussed in Section 2.3.

it is difficult to measure gf values for weak transitions (Bergemann 2011).

Uncertainties in oscillator strengths can be larger than the difference between LTE and NLTE abundances, thus an error in the $\log gf$ could be misinterpreted as an NLTE effect. Errors are also introduced if the meteoritic abundances are used for gf calculation, as these have additional uncertainties (Wahlgren 2010). For instance, problems with sample sizes and preparation between different authors can be a cause of uncertainty in the meteoritic abundances and there is a spread in the values obtained (Lodders, Palme & Gail 2009). Also, volatile depletion in the CI-meteorites, whose composition closely resembles that of the Sun, makes measurements of the initial abundance of these difficult. As such, elements need to be compared to Si rather than H, and this assumes knowledge of the photospheric Si abundance (Asplund et al. 2009).

1.8 Line broadening

In the initial output of a spectrograph, the spectral lines do appear as narrow lines such as the ones the Fraunhofer described. However, when spectra are plotted as flux against wavelength, it is clear that they are not actually "lines", but appear more rounded as they have been broadened by many different processes. Knowledge of these processes is essential to correctly fit the lines and to understand the underlying physics.

1.8.1 Doppler broadening

Doppler broadening occurs when atoms move at high velocities due to high temperatures. As such, the emitted photon will be redshifted or blueshifted to a slightly lower or higher wavelength, causing broadening of the line profile. This broadening will be greater for hotter temperatures. If the velocity distribution is Maxwellian, then the line profile is a Gaussian (Collins 1989; Gray 2008).

1.8.2 Rotation

Stellar rotation was first observed by Johann Fabricius in 1610, who noticed that spots on the surface of the Sun were a part of the Sun, and thus that their motion is due to the rotation of the Sun (Tassoul & Tassoul 2004). Nowadays, rotation periods ($P_{\rm rot}$) from spots have been determined from the light curves of many stars and space-based photometry, such as the *Kepler* mission, have been used to measure $P_{\rm rot}$ for thousands of active stars (Nielsen et al. 2013; Reinhold, Reiners & Basri 2013).

The light reaching us from a rotating star will exhibit a Doppler shift, as the approaching limb causes the spectral lines to be blueshifted and the receding limb causes the spectral lines to be redshifted. As we cannot resolve the stellar discs, we see the combined light from the star and the Doppler effect is averaged across the line profile. This has the effect of broadening the line profile by causing the line to become more rounded without changing the EW of the line. The amount of rotational broadening also depends on the inclination of the stellar rotation axis relative to the line of sight (i). For instance, a star viewed equator-on will have the maximum amount of rotational broadening possible in the spectral lines, but a pole-on star will have no visible rotational broadening. Therefore the rotation inferred from spectroscopy is the sky-projected rotational velocity, $v \sin i$, and is thus a lower limit on the rotational velocity at the equator (Gray 2008).

The notion that stellar rotation could broaden spectral lines was first suggested by Abney (1877), and Struve (1930) used this knowledge to show that early-type stars rotate much faster than late-type stars. The explanation for this was not suggested until Schatzman (1962) realised that late-type stars lose angular momentum due to magnetised winds. This is because late-type stars have convective envelopes and thus exhibit stellar activity.

Stellar rotation will be discussed in more detail in Chapter 5.

1.8.3 Velocity fields

The convective motion of the outer layers of cool stars can have a substantial effect on the shape of spectral line profiles. Rosseland (1928) was the first to suggest that "eddy motion" should be taken into account in stellar models. He attributed this motion to turbulence in the photosphere, a term which has unfortunately persisted. The velocity fields that reshape spectral lines have little to do with turbulence, and in the context of stellar spectroscopy turbulence is taken to mean non-thermal velocity fields (Gray 1978).

It is difficult to adequately model these velocity fields in 1D spectra, which led to the introduction of "microturbulence" and "macroturbulence" as a way to broaden the spectral lines in a way that simulates velocity fields. The size of the microturbulent "cell" is defined as being less than the mean free path of a photon. This means that a photon will be absorbed by other microturbulent cells before eventually leaving the star. Macroturbulence represents velocities that occur where the cell is larger than the unit

optical depth, i.e. the photons remain within the cell from the time they are created until the time that they are emitted from the star. This division between micro and macroturbulence is crude, as in reality the motion would occur over a range of scales (Mucciarelli 2011; Asplund et al. 2000; Nordlund, Stein & Asplund 2009).

1.8.3.1 Microturbulence

The velocity distribution of $v_{\rm mic}$ is assumed to be Gaussian, since the small values of less than $\sim$2 km s^{-1} means that it is impossible to measure the shape of this distribution as it is smaller than the other components of line broadening. Microturbulence is included in the synthetic spectrum by means of adding it in quadrature to the thermal Doppler broadening, which still results in a Gaussian. Microturbulence is unlikely to actually be caused by a small scale velocity field, and is more likely to be caused by differential velocities along the line of sight (Landstreet 2007; Gray 2008).

Struve & Elvey (1934) found that the abundance derived from strong lines differed from that calculated using weak lines. In order to bring the abundances into agreement, they introduced $v_{\rm mic}$ so that the strong lines would be spread over a larger wavelength interval and the saturation reduced. This has the effect of increasing the total absorption and changing the EW so that the strong lines should now give the same abundance as the weak lines. Therefore, by assuming that all lines have the same abundance, it is possible to determine the $v_{\rm mic}$ for a star. This is done by plotting abundance against EW, and changing the $v_{\rm mic}$ until the correlation coefficient is negligible (Magain 1984; Mucciarelli 2011).

According to Magain (1984), this can result in systematic errors of the $v_{\rm mic}$ due to random errors in the EWs. The errors between EW and abundance are correlated so that a positive error on the EW will result in an overestimate of the abundance and vice versa. This means that a point that moves to the right in the plot will also move upwards, and one that moves to the left of the plot also moves downwards, which in turn leads to a positive trend in the slope of the line. Thus the $v_{\rm mic}$ has to be increased in order to remove the slope. Magain also noted that numerous lines aren't necessary for the $v_{\rm mic}$ calculation, as long as the ones that are selected are of good quality.

Alternatively, $v_{\rm mic}$ can be determined by using a Blackwell Diagram (Blackwell & Shallis 1979; Blackwell, Shallis & Simmons 1982). The abundance of a line required to produce the measured EW is computed for different values of microturbulence and this

is plotted as a curve for each spectral line. The slope is different for each spectral line, and the point of intersection of the lines should give the abundance and microturbulence of the star in question. Saffe & Levato (2004) showed that the abundances for several elements agree with the abundances derived from classical methods for a number of stars. Only weak and medium lines should be used, as strong lines will not work with the Blackwell diagram. Both the oscillator strengths and the EWs should be of the highest accuracy possible in order for a clear solution to be achieved.

Spectral analysis often assumes that we understand the Sun, and if a method produces the known solar parameters, then it is valid. However, not all solar parameters are known with great precision and $v_{\rm mic}$ is one of them. Various values of solar $v_{\rm mic}$ exist throughout the literature, as shown in Table 1.1, and this is partially due to the type of spectrum used. Solar spectra can be taken of the disc centre, or over the integrated disc. The $v_{\rm mic}$ obtained from the integrated flux spectra will be greater than that from disc centre spectra, as there are horizontal velocities near the solar limb (Gadun 1994). As flux spectra contain disc averaged rotation and velocity fields, as well as centre-to-limb variations, they are more appropriate when comparing the Sun with other stars (Wallace et al. 2011).

Table 1.1: Solar $v_{\rm mic}$ values

$v_{\rm mic}$ (km s^{-1})	Type	Ionisation state	Reference
0.81 ± 0.20	Disc centre	Fe I	Gadun (1994)
0.86 ± 0.04	Disc centre	Fe II	Gadun (1994)
0.85	Disc centre		Blackwell, Booth & Petford (1984)
1.11 ± 0.14	Disc integrated	Fe I	Gadun (1994)
1.20 ± 0.10	Disc integrated	Fe II	Gadun (1994)
1.18 ± 0.03	Disc integrated		Blackwell et al. (1976)
1.24	Disc integrated		Bean et al. (2006)

1.8.3.2 Macroturbulence

Unlike microturbulence, macroturbulence does not alter the EW of the lines. If individual spectra from each macro "cell" could be obtained, they would be Doppler shifted by the velocity of that particular cell. However, as multiple cells are viewed simultaneously because the stellar disc is unresolved, they become blurred and the overall effect is to broaden the line profile (Gray 2008). Macroturbulence mostly represents the velocity dispersion of granulation. Some of the macroturbulent velocity is from acoustic

oscillations, although these velocities are an order of magnitude lower than those from granulation (Asplund et al. 2000; Gray 2009).

The radial-tangential (RT) macroturbulence model was developed by Gray (1975, 1977b, 2008). In this model, it is assumed that the velocity distribution is Gaussian and the velocity vectors are either along the stellar radius or tangential to the surface. The need for both a radial and tangential component is necessary as we know that a convective cell will move vertically as it rises and falls, and that horizontal motion occurs between the rising and falling material. The RT macroturbulence is calculated by integrating across the stellar disc and the flux is given by

$$F_v = \pi I_v * \left[\frac{2A_R \Delta\lambda}{\pi^{1/2}\zeta_R^2} \int_0^{\zeta_R/\Delta\lambda} e^{-1/u^2} du + \frac{2A_T \Delta\lambda}{\pi^{1/2}\zeta_T^2} \int_0^{\zeta_T/\Delta\lambda} e^{-1/u^2} du \right], \tag{1.9}$$

where I_v is the intensity, * represents a convolution, A is the fraction of the surface area of the stellar disc that has radial (R) or tangential (T) motion, ζ is the macroturbulence dispersion, $u = \zeta_R \cos\theta/\Delta\lambda$ in the first integral, $u = \zeta_T \sin\theta/\Delta\lambda$ in the second integral and θ is the angle between our line of sight and the normal to the stellar surface.

From this, it can be seen that the radial and tangential components behave in the same manner. This treatment of macroturbulence assumes that the lines in the disc integrated spectrum are symmetric, as it doesn't account for the temperature and velocity differences that give rise to the asymmetric profiles seen in observed spectra.

Including rotation and linear limb darkening in the line profile gives

$$F_v = H(\lambda) * \oint I_c^0 (1 - \epsilon + \epsilon \cos\theta) \Theta(\Delta\lambda - \Delta\lambda_R) \cos\theta d\omega, \tag{1.10}$$

where $H(\lambda)$ is the thermal profile (including microturbulence), ϵ is the limb darkening coefficient, Θ is the macroturbulence velocity distribution, and $\Delta\lambda_R$ is the rotational Doppler shift.

The disc integrated profile of macroturbulence is not a Gaussian, and has broader wings and a "cusp" shape to the core. This shape is evident in spectral lines, assuming the $v \sin i$ is low enough to preserve the shape. This can be seen in Figure 1.2, where a synthetic line of Fe I 5538 Å in the Sun is shown for three different broadening scenarios. When $v \sin i$ is set to zero, the "cusp" shaped core and broad wings are evident for $v_{\rm mac}$ = 8 km s^{-1}. For $v_{\rm mac}$ of zero and $v \sin i$ = 8 km s^{-1}, it is obvious that $v \sin i$ has the effect of broadening the line with a rounded core, and there is no additional broadening in

the wings. The combination of both profiles, with $v_{\rm mac}$ and $v \sin i$ both having 8 km s^{-1} is also shown. For higher $v \sin i$ values, the $v_{\rm mac}$ signal becomes washed out.

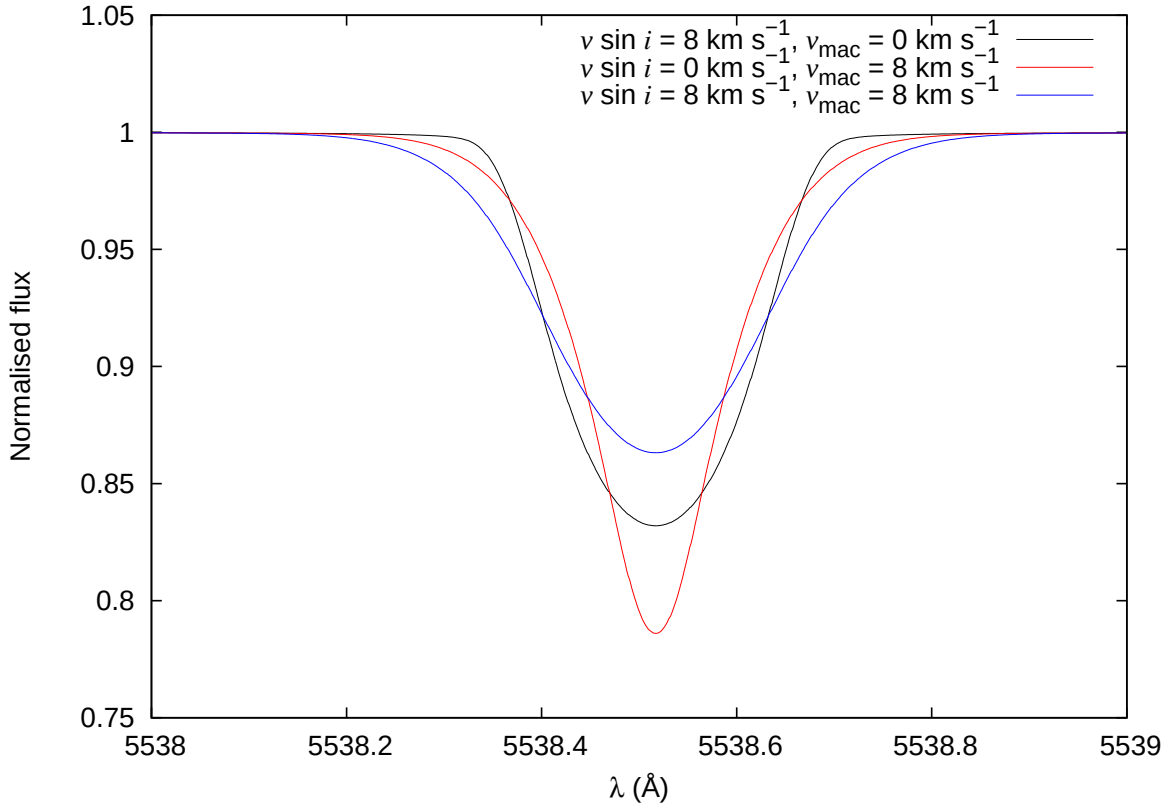

Figure 1.2: Line profile shapes of $v_{\rm mac}$ and $v \sin i$. The "cusp" shaped core and broadened wings of the pure macroturbulent broadening is obvious.

As with $v_{\rm mic}$, there are many different solar $v_{\rm mac}$ in the literature, some of which are shown in Table 1.2. Some of this can be explained by the choice of lines used. The Takeda (1995) value is for strong lines, whereas the Gray (1977b) value is for weak lines. Weak lines are formed deeper in the photosphere and thus have higher macroturbulence.

Table 1.2: Solar $v_{\rm mac}$ values

$v_{\rm mac}$ (km s^{-1})	Reference
1.9	Bean et al. (2006)
2.3 ± 0.4	Takeda (1995)
2.6 ± 0.3	Sheminova & Gadun (1998)
2.7	Saar & Osten (1997)
3.5 ± 0.2	Gonzalez (1998)
3.8	Gray (1977b)

1.8.3.3 3D models

While 1D models require microturbulence and macroturbulence to emulate velocity fields, 3D models have no need for these adjustable parameters as convective energy transport can be included directly in the models. 3D models can fit the depths, shifts, and asymmetries of the synthetic lines well with the observed spectrum (Asplund et al. 2000; Asplund 2007; Bigot & Thévenin 2006).

Even though 3D models don't require $v_{\rm mic}$ and $v_{\rm mac}$ they can still be used to extract these parameters, as a test of the reliability of the models (Steffen, Ludwig & Caffau 2009). Steffen, Caffau & Ludwig (2013) found that the theoretical $v_{\rm mic}$ values determined from the 3D models are less than the actual values for the Sun and Procyon. Higher resolution models increase the $v_{\rm mic}$, but it still falls short of the actual value. This suggests that the 3D models still can't model the velocity fields sufficiently, and that a resolution-dependent 3D $v_{\rm mic}$ might be needed in addition to the large-scale hydrodynamical velocity fields. This is in disagreement with Asplund et al. (2000), but in agreement with Allende Prieto et al. (2002), who found that the iron abundance increases with lines strength in Procyon, which can also be explained by $v_{\rm mic}$ being underestimated.

1.8.4 Line damping

Line "damping" occurs from interactions at the atomic level. This type of broadening can have a subtle, but important, effect on the line profile shape and damping parameters are more enhanced in strong lines (Ryan 1998).

1.8.4.1 Natural broadening

Natural line broadening, also known as radiative damping, occurs due to uncertainties in the lifetimes of energy levels. Electron transitions between different levels do not result in the photon being absorbed or emitted at an exact wavelength. Instead, the wavelength is dependent on how long the electron spends in a particular level. Electrons that spend a short amount of time in an energy level have a very uncertain energy, whereas electrons that spend a long time in an energy level have a better defined energy. The natural damping can be expressed as combination of the widths of the separate energy levels $\delta\nu_{\rm i}$ and $\delta\nu_{\rm j}$ so that the overall FWHM of natural broadening is given by

$$\delta\nu_{\mathrm{ij}} = (2\pi\tau_{\mathrm{i}})^{-1} + (2\pi\tau_{\mathrm{j}})^{-1}, \tag{1.11}$$

where τ is the mean lifetime of the level. If the lower level is the ground state, then the broadening from $\delta\nu_{\mathrm{i}}$ will be negligible as the lifetime of the ground state is infinitely long. The upper level will have a finite lifetime, and will thus have a spread in frequency which causes broadening. Broadening is stronger for lines with a high excitation potential, as there is a high level of uncertainty in the wavelength of the emitted photon (Thorne 1988; Gray 2008; Wahlgren 2010). At stellar temperatures, the broadening caused by Doppler motion is much larger than that due to natural line broadening (Collins 1989; Gray 2008).

1.8.5 Pressure broadening

Pressure broadening, also known as collisional broadening, is caused by a change in energy due to a collisional interaction at the atomic level. This change in energy is proportional to R^n, where R is the distance between the absorber and the perturber and the integer n depends on the type of interaction. The change in energy can be converted into a change in the spectrum frequency $\Delta\nu = C_{\mathrm{n}}/R^n$, where C_n is the interaction constant. C_n needs to be measured in the laboratory or calculated for each transition, as well as for each type of interaction, and it isn't always well known (Collins 1989; Gray 2008).

1.8.5.1 Stark effect

Stark broadening is one type of collisional broadening, where neighbouring charged particles create an external electric field, thus perturbing energy levels of an atom. This will cause the atom to temporarily be in an electric field. The linear Stark effect has $n = 2$, and as such the distance between the atom and the perturbers will have the longest range compared to other types of collisional broadening. The perturbers are protons and electrons and it is usually hydrogen lines that are most affected by the linear Stark effect. The quadratic Stark effect has $n = 4$, and it affects most lines, particularly in hot stars. The perturbers in this case are ions and electrons (Gray 2008).

1.8.5.2 Resonance broadening

Resonance broadening occurs when an interaction occurs between two neutral atoms; one an excited atom and the other in the ground state, where the excited atom has a strong transition to the ground state and the perturber is in the ground state. It is also known as self-broadening since the atom and the perturber must be of the same species. Resonance broadening has $n = 3$, and it is an important broadening factor in late-type stars. It influences the H lines, and affects the Hα line more than Hβ (Collins 1989; Molisch & Oehry 1998; Allard et al. 2008; Mashonkina 2010d).

1.8.5.3 Van der Waals broadening

Van der Waals (VDW) broadening occurs regardless of the type of atom or its ionisation state (Molisch & Oehry 1998) and it is one of the most prominent broadening processes of metallic lines in cool stars, after thermal broadening and microturbulence are accounted for (Ryan 1998). The perturber is neutral hydrogen, the atoms of which are four times more common than electrons in stars with a $T_{\rm eff} < 10{,}000$ K. The perturber becomes polarised, i.e. becomes an induced dipole, and it is this induced electric field that changes the energy levels of the atom. The broadening of strong lines is dominated by this process (O'Mara & Barklem 2003; Gray 2008; Mashonkina 2010d).

The ABO theory (Anstee & O'Mara 1991; Anstee & O'Mara 1995a; Anstee & O'Mara 1995b; Barklem & O'Mara 1997; Barklem, Anstee & O'Mara 1998; Barklem & Aspelund-Johansson 2005), uses calculated cross sections to determine the width of the lines. These are given as a function of the principal quantum number of both the upper and lower levels of the transition (Ryan 1998; O'Mara & Barklem 2003; Mashonkina 2010d). ABO theory allows strong lines to be used for abundance calculations, assuming accurate $\log gf$ values exist for those lines (Doyle et al. 2005). Abundance analyses typically rely on weak lines as they aren't affected by microturbulence, whereas the broad wings of strong lines require knowledge of collisional broadening. However, VDW broadening can still affect weak lines (Ryan 1998).

1.8.6 Additional broadening factors

1.8.6.1 Zeeman broadening

There are other atomic mechanisms that can result in line broadening. If a magnetic field is present, electron transitions become complicated as the magnetic quantum number is no longer degenerate. Instead of one line being produced, the line is split into multiple components as numerous transitions now take place. This is known as the Zeeman effect. The width that the lines are split by is related to the strength of the magnetic field and the number of lines visible depends on the direction the atom is viewed in (Robinson 2007). Zeeman broadening mainly effects stars that are cooler than spectral type G6 (Gray 1984b), however the splitting is usually small compared to other line broadening factors, meaning that it cannot usually be resolved in solar-like stars (Robinson 1980). On the Sun, the inhomogeneous magnetic fields average across the disc, which makes them rather elusive. Cool stars that are noticeably active with prominent spots are also likely to be fast rotators, and the rotational broadening then washes out the Zeeman effect. Zeeman broadening can still be detected as the Zeeman effect introduces a line shift that depends on the Landé g-factor, the line wavelength, and the strength of the magnetic field (Hartmann 1987). The dimensionless Landé g-factor describes the magnetic sensitivity of the line and can be measured in laboratory experiments, with reasonable reliability, and can also be computed where necessary (Romanyuk 1997).

1.8.6.2 Hyperfine splitting and isotope shift

Hyperfine splitting (HFS) is also unresolved and causes some lines to be broadened. The lines become desaturated so that the core appears to be flattened. HFS occurs when energy levels are perturbed by the interaction between the nuclear magnetic moment, caused by the intrinsic spin of the protons and neutrons in the nucleus, and the magnetic field at the nucleus produced by the angular momentum of the electrons (Thorne 1988; Wahlgren 2005). HFS is more prominent in elements with an odd atomic number, such as Mn and Co, which have a large atomic mass and large nuclear spin respectively (Bergemann 2011).

The mass and/or volume of the nucleus influences the energy levels, so that comparable transitions in different isotopes will result in a small difference in energy, known as isotope shift. Lines of different isotopes will be displaced as each energy level is shifted by a different amount (Thorne 1988).

2 Obtaining stellar parameters

While we can conceive of the possibility of determining their shapes, their sizes, and their motions, we shall never be able by any means to study their chemical composition...I regard any notion concerning the true mean temperature of the various stars as forever denied to us.

- French philosopher Auguste Comte, 1835

While spectroscopy can be used to extract some stellar parameters, other techniques are also needed in order to explore the full range of data than can be obtained from the stars. This chapter will outline the parameters that we can obtain from stars, and the methods in which they are determined.

2.1 Effective temperature

The effective temperature is the surface temperature of a star assuming that it is a blackbody radiating at its measured luminosity. The $T_{\rm eff}$ can be calculated from the Stefan-Boltzmann relationship if stellar luminosity (L) and radius (R) are known;

$$T_{\rm eff} = \left(\frac{L}{4\pi R^2 \sigma}\right)^{\frac{1}{4}}, \tag{2.1}$$

where σ is the Stefan-Boltzmann constant.

However, luminosity and radius are not known for many stars, and it is usually the flux and angular diameter that can be measured from Earth (Boyajian et al. 2012). The $T_{\rm eff}$ can thus be calculated from the angular diameter and bolometric flux via

$$F_{\rm bol(Earth)} = \frac{\theta^2}{4}\sigma {T_{\rm eff}}^4. \tag{2.2}$$

As $T_{\rm eff}$ is twice as sensitive to angular diameter as to the flux received at Earth, it is important to get accurate angular diameter measurements (Smalley et al. 2002). However, this can be difficult for dwarfs given their small radii, and so only a small number of stars have angular diameters measured to a level of precision high enough to obtain a fundamental $T_{\rm eff}$ for the star (Casagrande et al. 2010).

An accurate $T_{\rm eff}$ is important for many reasons. It is essential in order to have accurate abundance determinations, as abundance estimates are sensitive to the value of $T_{\rm eff}$ used (Gonzalez 2006; Kovtyukh et al. 2003). Stellar activity can alter the measured temperatures of stars, due to the presence of spots and faculae (Biazzo et al.

2007), therefore high precision temperature measurements can help rule out any false detections of low mass planet candidates which may have been caused by starspots (Kovtyukh et al. 2003). Thus it is important that an accurate value of $T_{\rm eff}$ be known in order to decipher other stellar parameters (Fischer & Valenti 2003).

As direct determinations of $T_{\rm eff}$ are difficult to obtain, a wide variety of indirect methods based on spectroscopy and photometry exist in order to estimate values for $T_{\rm eff}$.

2.1.1 Multicolour photometry

The shape of the continuous spectrum of a star is different depending on its spectral type, and as such it can be used to determine $T_{\rm eff}$. Multicolour photometry uses filters that measures the light within a certain wavelength range, making it possible to create colour indices where the difference is taken between the magnitudes at different wavelengths. There are many different photometric systems, for example Johnson-Cousins *UBVRI* (Johnson & Morgan 1953) and Strömgren *ubvy* (Strömgren 1966).

The difference in a star's magnitude between the blue (B) and visual (V) wavelengths will give the $(B-V)$ index. As a hot star is brighter at short wavelengths, the B magnitude will have a smaller value than the V magnitude, making the index negative or neutral for hot stars, and positive for cool stars. The $(B-V)$ index is sensitive to temperature as it measures the slope of the Paschen continuum. However the temperature determined from the $(B-V)$ index depends on whether the star is a giant or dwarf and whether it is metal-rich or metal-poor (Gray & Corbally 2009).

2.1.2 Infrared flux method

One method of determining $T_{\rm eff}$ which relies very little on model atmospheres is the InfraRed Flux Method (IRFM; Blackwell & Shallis 1977; Blackwell, Shallis & Selby 1979; Blackwell, Petford & Shallis 1980). The bolometric flux at the surface of a star, $F_{\rm bol} = \sigma {T_{\rm eff}}^4$, is not directly measurable, and instead we have to use the bolometric flux as is seen on Earth which relies on the angular diameter, i.e. using Equation 2.2. If the photometry doesn't cover the entire range of flux, then model atmospheres can be used to compute this part of the flux which can account for between 15 to 30 per cent of the total flux (Casagrande, Portinari & Flynn 2006).

The IRFM breaks the degeneracy between angular diameter and temperature by using the fact that the flux received on Earth in the infrared, $F_{\rm IR(Earth)}$, is relatively

insensitive to temperature,

$$F_{\mathrm{IR(Earth)}} = \frac{\theta^2}{4}\phi(T_{\mathrm{eff}}, \log g, [\mathrm{Fe/H}]), \tag{2.3}$$

where ϕ (T_{eff}, $\log g$, [Fe/H]) is the flux at the surface of the star. The ratio of $F_{\mathrm{bol}}/F_{\mathrm{bol(Earth)}}$ eliminates the angular diameter term, and yields the observational ratio (R_{obs}). The theoretical ratio, $R_{\mathrm{theo}} = \frac{\sigma {T_{\mathrm{eff}}}^4}{\phi}$ is calculated at a given wavelength using a grid in T_{eff}, $\log g$ and [Fe/H] space, where the T_{eff} is an initial estimate. Interpolating over the grid of model atmospheres generates a synthetic spectrum, which is then used to obtain the bolometric correction by estimating the flux beyond the range of the photometry.

By equating both ratios as in Equation 2.4, it is possible to rearrange for T_{eff} and there is no longer a dependence on angular diameter. The angular diameter can then be determined separately (Blackwell, Petford & Shallis 1980; Ramírez & Meléndez 2005; Casagrande, Portinari & Flynn 2006).

$$\frac{F_{\mathrm{bol(Earth)}}}{F_{\mathrm{IR(Earth)}}} = \frac{\sigma {T_{\mathrm{eff}}}^4}{\phi(T_{\mathrm{eff}}, \log g, [\mathrm{Fe/H}])} \tag{2.4}$$

The T_{eff} derived from the IRFM can be verified by comparing the resulting angular diameter with direct measurements, such as those obtained via interferometry. Ramírez & Meléndez (2005) found a good agreement between their IRFM diameters and the fundamental values for giant stars, although this agreement broke down at temperatures below 3800 K. This comparison is more difficult to perform with dwarf stars, however there does still seem to be an agreement with the angular diameters using solar metallicity stars.

Disadvantages of the IRFM include sensitivity to cool companions, which has the effect of lowering T_{eff} for the primary star. This is because the cool companion has more flux in the infrared region, which lowers the flux ratio (Smalley 2005). Other sources of error come from the method's dependence on photometry and metallicity values, differences in the absolute flux calibrations, and on which types of model atmospheres are used (Casagrande, Portinari & Flynn 2006). The IRFM can also fall victim to interstellar reddening, which can increase the T_{eff} by 50 K for an extinction of 0.01 mag. However stars within 70 parsecs should have negligible reddening (Casagrande et al. 2010).

2.1.3 Balmer lines

The Balmer lines can serve as an important $T_{\rm eff}$ indicator for stars below 8000 K, as the core to wing transition of the lines are sensitive to temperature changes, but not to changes in other parameters (Mashonkina 2010d). Above this temperature, the Balmer lines become dually dependent on gravity and are no longer reliable as temperature indicators. However, if $T_{\rm eff}$ is obtained via an independent method, the lines can still play a role in $\log g$ determinations (Smalley 2005; Gray 2008). Using NLTE calculations for the Balmer lines results in the core being strengthened by a significant amount, as well as a slight weakening of the core to wing transition. Differences in derived temperatures between LTE and NLTE are around 100 K for Hα and around 10 K for Hβ (Mashonkina 2010d).

The Balmer lines are very broad in A, F and G-type stars and this can make continuum determination and fitting difficult as metal lines are prominent. Continuum determination is made more tedious when using echelle spectra, as the overlapping orders are merged. This affects Hα more than Hβ (Bruntt et al. 2010a). A single order spectrograph would produce more appropriate spectra for Balmer line measurements.

As the Hα line is formed above the convection zone in stars later than mid A-type, and the Hβ line is formed just within the CZ, the $T_{\rm eff}$ from the Balmer lines is influenced by convection. This causes a difference in temperature for the two lines. Hα temperatures are typically between 100 and 200 K hotter than Hβ temperatures at around 6000 K. However this discrepancy decreases for hotter temperatures (Gardiner, Kupka & Smalley 1999).

2.2 Surface gravity

The surface gravity of a star is the measure of acceleration due to gravity on the surface of a star, and it is related to the radius (R) and mass (M) of the star by $g = GM/R^2$, where G is the gravitational constant. Surface gravity is usually expressed in logarithmic form $\log g = \log M$ - 2 $\log R + 4.437$, where M and R are in solar units and $\log g$ is expressed in cgs units.

Stars swell as they evolve off the main sequence, and this increase in radius will decrease the pressure and lower the surface gravity. Main sequence stars have a much greater pressure due to their smaller radii, which results in more frequent atomic collisions than their evolved counterparts. The multitude of collisions results

in electrons having less well defined energies, and this will broaden the wings of strong spectral lines. Such broadening is absent in giant stars, making it possible to tell the difference between a dwarf and giant of the same temperature and spectral class. The pressure broadened lines are also much stronger in late-type dwarf stars than early-type, once again due to the smaller radius.

2.2.1 Pressure broadened lines

The pressure-sensitive wings of the Na I D lines at 5889 and 5893 Å can be used for $\log g$ determination, as they persist over a large temperature range. It is best to fit the profiles of the lines rather than measure the EWs, as it is difficult to measure the EW accurately for strong, blended lines (Gray 2008). The surface gravity can be determined from Mg I b lines at 5167, 5173 and 5184 Å, but these lines can be blanketed with MgH and C2 lines (Fischer & Valenti 2005). It is also difficult to normalise the continuum of the Mg I b lines because the lines are wide and two of them are too close together to define the continuum. The red wing (at around 5160 Å) has no discernible continuum, particularly for stars earlier than K0, meaning that only the 5184 Å line can be used with any confidence. Bruntt et al. (2010a) use the Ca I lines at 6122, 6162, and 6439 Å, as the continuum can be obtained easier than with Mg I b lines. The Ca I lines are also narrower and there are more weak lines present compared to Na or Mg, which allows the abundance to be determined with greater confidence.

2.2.2 $\log g$ from planet transits

The $\log g$ can be indirectly obtained from the transit photometry, and this can have greater precision than its spectroscopic counterpart. This method relies on determining the stellar density, which can be calculated once the normalised separation between the star and the planet, $a/R_{\rm s}$, and the period, P, are known from the transit data;

$$\frac{M_{\rm s}}{R_{\rm s}^3} = \frac{4\pi^2}{GP^2}\left(\frac{a}{R_{\rm s}}\right)^3 - \frac{M_{\rm p}}{R_{\rm s}^3}, \tag{2.5}$$

where a is the semi-major axis. The left hand side of the equation corresponds to the stellar density and the first term on the right hand side includes only measurable properties. The second term involves two unknown parameters, but this term is neglected as it is two to three orders of magnitude smaller than the first term for the majority of transiting exoplanets. This then leads to the stellar density being determined directly from observable parameters. Density (ρ), like surface gravity, is also a measure

of stellar evolution. Sozzetti et al. (2007) use the parameters that are directly observed to compute the isochrones (see Section 2.5.1 for a further discussion on isochrones). That is, they use $a/R_{\rm s}$ rather than using the density. The theoretical values of $a/R_{\rm s}$ for the isochrones were calculated by rearranging the above equation and this was then compared with the actual value from the transit. Once mass and radius are determined from the isochrones, the $\log g$ can be calculated.

As using $a/R_{\rm s}$ is more precise than using the spectroscopic $\log g$, determining the ages of stars via isochrones also has increased precision for this method (Sozzetti et al. 2007). Measuring $\rho_{\rm s}$ directly from the transit light curve also has the advantage of revealing whether the host star is a dwarf or a giant, without the need for spectroscopy (Seager & Mallén-Ornelas 2003).

2.3 Chemical composition

Spectroscopy is the tool for determining the abundances of elements that are present in stellar photospheres. The abundance can be measured via synthesis by adjusting the abundance and other parameters until the synthetic spectrum agrees with the observed one. The abundance can also be determined from the EWs via the curve of growth. This is the rate at which the abundance increases with increasing EW. The abundance increases linearly with EW for weak lines, and as the line core saturates, the curve of growth will flatten out. The curve will then start to rise again for strong lines as the line wings are broadened by damping parameters (Gray 2008).

While it is theoretically possible to gain an accurate elemental abundance from a single spectral line, it is important to measure several good lines for each element. This is because the unreliability of atomic data creates an inevitable scatter in the abundance values for each element, so taking the result of only one line could easily give an incorrect abundance. The iron lines that adorn spectra of cool stars are more numerous than any other element, making it easier to select numerous non-blended lines. This is why the stellar metallicity is often quoted using just the iron abundance. There are many other elements present, although most only have a sparse availability of suitable lines.

Stellar abundances (A) are given as the total abundance as a fraction of hydrogen. They are more typically written as $\log(A) + 12$, where $\log(A)$ is the number ratio of the element with respect to hydrogen, $\log(N_{el}/N_H)$. There are several other ways of

denoting the abundance, for example iron can be written as (Fe/H), $\log A(\mathrm{Fe})$, $\log A_{\mathrm{Fe}}$ or $\log \epsilon_{\mathrm{Fe}}$.

Abundances can also be written relative to the Sun, and in this case square brackets are used, i.e. [Fe/H]. The overall metallicity of a star can be written as [M/H], which is typically in agreement with [Fe/H] though it can differ by up to 0.1 dex. For instance, Holmberg, Nordström & Andersen (2007) found that [Fe/H] was higher than [M/H] by an average of 0.10, 0.09 and 0.03 dex for F, G and K stars respectively.

Metallicity can also be determined via Strömgren photometry, by using the metallicity index index $m_1 = (v-b)-(b-y)$. This measures line blanketing in the spectrum caused by a cluster of metal lines around 4100 Å, and is sensitive to the overall metallicity of the star (Bessell 2005; Árnadóttir, Feltzing & Lundström 2010).

2.4 Mass and radius

The mass of a star is one of its most important fundamental parameters. The initial mass of a star determines what type of star it will be, how long it will live, and how it will die. The mass of a star can only be determined directly if it is in a suitable binary system, due to the gravitational interplay between the two stars, and this is known as the dynamical mass.

Studies of binaries can also yield the stellar radius, as can other methods. Knowledge of the radius can be put to good use by differentiating between dwarfs and subgiants. For example, Baines et al. (2008) used accurate radius measurements to conclude that some stars that has previously been classified as dwarfs have larger radii than initially thought, and thus are actually beginning to evolve off the main sequence.

2.4.1 Masses and radii from binaries

There are three situations in which the dynamical mass can be extracted: in a visual binary with a known parallax, a visual binary with radial velocity (RV) observed over a complete orbit, or in a double lined eclipsing binary. Visual binaries are more common than double-lined eclipsing binaries, with several thousand pairs being catalogued (Malkov et al. 2012).

Eclipsing binaries (EBs) serve another function as the fractional radii, which are the radii divided by the semi major axis, can be extracted from the light curve. The linear radius can be determined from EBs without knowing the distance, however the

distance is still needed to convert this to angular radius in order to find the $T_{\rm eff}$ (Gray 2008; Southworth 2012a).

Currently only a few hundred stars have a mass and radius determined directly from eclipsing binaries that is known to less than three per cent error. If the errors are larger, then the range of different stellar models that will fit the data is quite extensive, making small errors in mass vital for delving into stellar evolution. Torres, Andersen & Giménez (2010) obtained accurate masses and radii of 190 stars which are in binary systems and then derived calibrations for both M and R based on the $T_{\rm eff}$, $\log g$ and [Fe/H]. The values obtained from the calibration are in agreement with the observed values with an accuracy of a few per cent. Enoch et al. (2010) have substituted $\log g$ in the Torres relation with $\log \rho$, determined from the transit light curve, in order to find the stellar masses and radii. Gillon et al. (2011) and Southworth (2011) also computed similar calibrations with $\log \rho$.

2.5 Age

Stars can be as deceptive as people when it comes to revealing their age. Stellar ages are impossible to determine directly, and the resulting model dependence makes some of the results questionable. The only stellar age that we know with a great deal of certainty is that of the Sun. The age of the Sun is derived from the rate of decay of elements in meteorites, and is not determined from observable properties. Thus this method of age determination cannot be applied to other stars (Soderblom 2010).

Knowing the age of the star is of vital importance to understand its evolution and put other stellar parameters in perspective. For instance, putting age constraints on groups of stars can build a picture of Galactic evolution. A knowledge of the age of the star can offer perspective on the dynamics and migration of planets (Soderblom 2010). For example, the age of a star can be important for the search for life on other planets, as an old star could indicate a dying biosphere (O'Malley-James et al. 2013).

2.5.1 Evolutionary models

The location of a star in the Hertzsprung-Russell (HR) diagram can signify its age, as its luminosity increases with time, and the change in luminosity is related to a change in temperature. As mass is also related to luminosity, the HR diagram can also be used extract information on the stellar mass.

Theoretical isochrones can be used to determine stellar ages if the $T_{\rm eff}$ is plotted against a measure of stellar evolution, such as luminosity or absolute magnitude. However, these parameters require a known distance, so sometimes it is preferable to use $\log g$ or $\log \rho$ instead. It is also essential to know the metallicity, as two stars of the same age and mass with differing metallicities could either be on the MS or headed towards the giant branch (Lachaume et al. 1999; Nordström et al. 2004). There are numerous grids of evolutionary models available for calculating isochrones, for example some of the most widely used include the Padova (Girardi et al. 2000) or Y^2 (Yi et al. 2001; Demarque et al. 2004) models.

Determining ages via isochrones is more suited towards early-type stars, which have a rapid evolution, or late-type stars that are at least $\sim$1/3 of their MS lifetimes. Late-type dwarfs evolve along the ZAMS for the first part of their lives, and not only do the isochrones converge at this part of the HR diagram, but they are also unevenly spaced, making it very difficult to place a star correctly (Lachaume et al. 1999; Nordström et al. 2004; Soderblom 2009; Soderblom 2010).

Observational errors propagate through to age errors, with errors in $T_{\rm eff}$ and metallicity creating uncertainties (Holmberg, Nordström & Andersen 2007). Even if a distance measurement is available to calculate absolute magnitude or L, this measurement can still be plagued with errors (Barnes 2007; Chanamé & Ramírez 2012). Observational errors have a tendency to push MS stars onto the subgiant region, which can lead to a general overestimation of ages (Nordström et al. 2004).

2.5.2 Gyrochronology

Skumanich (1972) noticed that the rotation period spindown of stars is related to their age t by $P_{\rm rot} \propto t^b$, where b is -0.5. The loss of angular momentum is due to the mass lost from stellar winds (Mamajek & Hillenbrand 2008). This relationship is sensitive to mass (Cardini & Cassatella 2007), however most calibrations tend to be performed using colour instead of mass for convenience. This technique was dubbed gyrochronology by Barnes (2007). Gyrochronology could be more accurate than isochrone ages for stars of a given mass on the MS, and it has the advantage that it does not require a distance measurement.

Barnes (2007) identified the mass dependency of a number of open clusters and then determined the rotation rate to be $P(B-V,t) = f(B-V)g(t)$, where $f(B-V)$ is the mass dependence and $g(t)$ is the age dependence. Mamajek & Hillenbrand (2008)

fitted the Barnes relation to the Pleiades and Hyades clusters and noted that the Hyades periods are overestimated by up to 50 per cent. As such, they recalibrated the Barnes relation using rotation data from different sources, and updated the fitting coefficients to get a better agreement with the clusters. Soderblom (2010) recommends the Mamajek & Hillenbrand (2008) calibration over the Barnes (2007) one. However, Soderblom (2010) also cautions that both calibrations will result in an asymmetric age distribution that implies that the rapid rotators are younger than they actually are.

There are some other problems inherent with gyrochronology. The use of rotation periods is biased towards young stars that are active enough to show variability due to spots. It is also difficult to test gyrochronology for older stars, as open clusters with ages greater than ∼500 Myr are uncommon and distant (Cardini & Cassatella 2007; Soderblom 2010).

2.5.3 Chromospheric activity

Rotation is not just correlated with age, it is also connected to the chromospheric activity (Noyes et al. 1984), meaning that activity can also be used to calibrate the age of stars. As the rotation rate of a star slows down with time, the activity will also diminish. One of the most commonly used activity indicators is the emission in the cores of the Ca II H and K lines. They are used to calculate the activity index, $\log R'_{\rm HK}$, by measuring the Ca II H and K emission relative to the overall stellar flux. This age indicator is only suitable for late-type stars, and the ages determined from the Ca II lines agree with the rotation ages, which is not surprising as rotation is the main cause of activity in dwarfs (Lachaume et al. 1999; Nordström et al. 2004).

A single, low resolution spectrum can be used to determine the mean activity from the Ca II H and K lines, which is advantageous over trying to determine $P_{\rm rot}$. The Ca II reversal can also still be observed in stars which are too old to have $P_{\rm rot}$ measured from the surface modulation. However, Ca II emission cannot be used for very young stars, because the scatter in rotation is also large (Soderblom 2010). Also, the activity varies over cycles of days, weeks or years so that ages determined from a single measurement of $\log R'_{\rm HK}$ are not as accurate as mean values determined from many measurements collected over time (Lachaume et al. 1999; Nordström et al. 2004).

Another source of error lies in the fact that the chemical composition can have an adverse effect on the $\log R'_{\rm HK}$ because a metal-poor star will have shallow Ca II lines, thus making the emission appear more prominent and the star more active than

it actually is. The metallicity error can outweigh that caused by variability in activity (Rocha-Pinto & Maciel 1998; Rocha-Pinto et al. 2000).

2.5.4 Lithium

The amount of lithium present in the stellar photosphere can be used to estimate the age of young stars, as lithium will deplete over time. However, this depletion is not linear and is not described simply by a t^b law, as found by Sestito & Randich (2005). They determined the ages of open clusters via isochrone fitting and compared these to their Li abundances to determine the Li ages. These Li ages are only effective up to 1 or 2 Gyr, as beyond this there is a Li plateau. In addition, after 1 Gyr a bimodal distribution in the Li depletion becomes evident. Some stars, including the Sun, deplete Li at a faster rate but the reason for this is unclear. Randich (2009) cautions that it is difficult to be more precise than saying that beyond 1 Gyr, a low Li abundance means the star is probably old and/or had a peculiar evolution and that a high Li abundance will only give a lower limit for the age. They cite the example that $\log A(\mathrm{Li})$ of $\sim$2.24 does not help to narrow down the age between 1 Gyr and 8 Gyr. Soderblom (2010) also points out that there is a large scatter in the Li abundances of the Sestito & Randich (2005) work, which is not due to measurement errors. This scatter is greater than any age trend for late F and G-dwarfs, and Li will only provide some estimation of age if the abundance scatter is averaged out in a group of stars.

Of course, this type of calibration assumes that the Li abundance can be measured with ease and without dispute, which is obviously not the case as is seen with the abundance scatter. The Li line at 6708 Å is prone to NLTE effects, especially in Li-rich stars, which can lead to abundance errors if it is not accounted for (Carlsson et al. 1994; Takeda & Kawanomoto 2005; Lind, Asplund & Barklem 2009).

2.6 Asteroseismology

Asteroseismology is the study of pulsations within stars, and it can be used to extract parameters such as mean density, surface gravity, age, mass and radius. Oscillations in a star cause the surface to expand and contract, and thus the star varies in brightness. The first pulsating star to be discovered was o Ceti by David Fabricius in 1595, however at the time the brightness variations were attributed to dark spots on the surface of the star (Carroll & Ostlie 2006). An important milestone in the study of pulsating

stars was the discovery by Henrietta Swan Leavitt of the period-luminosity relationship of Cepheid variables (Leavitt & Pickering 1912), which is used to estimate cosmic distances. Shapley (1914) correctly suggested that the variations seen in the Cepheids could be due to radial pulsation of a single star; arguing against theories of double stars. Leighton, Noyes & Simon (1962) first detected pulsations in the Sun, signifying the birth of helioseismology. Solar-like oscillations in another star were not detected for nearly 30 years, when Brown et al. (1991) measured excess power in the Fourier spectrum of Procyon, although this was disputed at the time and it took a while before the presence of oscillations was confirmed. The floodgates of asteroseismic data opened when the space-based *MOST* (Walker et al. 2003), CoRoT (Baglin et al. 2009) and *Kepler* (Borucki et al. 2010) missions provided exquisite photometry for numerous pulsating stars.

The use of stellar parameters extracted from asteroseismology can prove useful for the study of planet host stars (Christensen-Dalsgaard et al. 2010; Huber et al. 2013). For instance, as asteroseismology can determine the stellar radius, it can then be used to find the planetary radius for transiting planets. Similarly, the asteroseismic mass can help to constrain the planetary mass. Asteroseismology can also provide stellar ages, which can be used to set limits on the ages of planets (Chaplin & Miglio 2013). Using $\log g$ from asteroseismology as a prior for spectroscopic analyses can help to eliminate some of the problems caused by the uncertainties in the spectroscopic $\log g$ (Carter et al. 2012).

2.6.1 Solar-like oscillations

The pulsations discovered in the Cepheid variables are dubbed "classical" pulsations, and their origin differs from those in the Sun. The oscillations in the Cepheids are powered by the κ-mechanism, which is dependant on opacity. Layers of partially ionised H and He have a large opacity which inhibits radiation being transmitted, causing the layers to heat up. This leads to an accumulation of pressure, which pushes the layers outwards. The opacity of the layers then decreases as ions recombine with free electrons, the heat decreases, and the layers once again fall inwards to begin a new cycle (Aerts, Christensen-Dalsgaard & Kurtz 2010; Leblanc 2010).

Solar-like oscillations are standing waves that are excited by turbulent convection near the surface of the star. This excitation makes their amplitudes detectable, and they are seen as an excess of power in a Fourier spectrum, which takes a bell shape

comprised of a comb-like structure of different frequencies (Barban et al. 2009; Chaplin et al. 2010; Mathur et al. 2012). Solar-like oscillations are not restricted to solar-like stars, rather any cool star ($\lesssim$ 7000 K) with an outer convection zone. This includes subgiants and red giants as well as MS stars (Bedding 2011). The detection of solar-like oscillations depends on the brightness and evolutionary state of a star, as the luminosity determines the amplitude of the oscillations (Huber et al. 2013).

Detecting oscillations in a star can be done either using RV measurements or by using photometry. The Doppler shift measures the changes in surface velocity, whereas photometry measures intensity variations from the intrinsic stellar pulsations (Cunha et al. 2007). Selecting an appropriate spectral line for measuring the RV variations due to oscillations depends on the depth of formation of the line as the amplitude of the oscillation increases with height in the atmosphere (Harvey 1985). The background signal of granulation increases with decreasing frequency, which can make it difficult to spot low frequency modes. However these granulation signatures are somewhat diminished in Doppler observations as opposed to the intensity measurements of photometry, which can be advantageous for low frequency measurements. Low frequency modes are particularly narrow in MS stars, which emphasises any rotational frequency splitting present (Chaplin & Miglio 2013). The use of photometry has the advantage of being able to study hundreds of stars simultaneously, which gives rise to the ensemble asteroseismology performed with CoRoT and *Kepler* (Bedding 2011).

2.6.2 Modes

There are two different restoring forces for the standing waves that cause solar-like oscillations. Pressure gradients act as a restoring force for the acoustic waves, and these are called p-modes. The second restoring force is buoyancy, and the resulting modes are called gravity modes, or g-modes (Aerts, Christensen-Dalsgaard & Kurtz 2010; Chaplin & Miglio 2013). G-modes probe to great depths beneath the convection zone, but they are not detectable in MS stars due to the lengthy periods (Harvey 1985).

Each mode in the star is described by a characteristic frequency for particular values of n, l and m. The overtone of the mode, n, is the number of radial nodes, or nodal shells. The degree of the mode, l, is the number of nodal lines at the surface and the azimuthal order of the mode, m, is the number of surface nodes that cross the equator. It is only possible to detect m modes if a star is rotating, which will be discussed further in Section 5.3. A mode is described by the central frequency,

line width, and line height and a particular mode will give the radial displacement of material within the star as a function of latitude, longitude and radius (Harvey 1985; Benomar et al. 2009; Aerts, Christensen-Dalsgaard & Kurtz 2010).

Measuring the frequencies of as many modes as possible that exist in different cavities is the best way to obtain high resolution in asteroseismic measurements. Stars that have higher degree l modes will have more zones on the surface that are moving in antiphase with each other, and some of these damp the oscillations in a process known as partial cancellation (Harvey 1985; Aerts, Christensen-Dalsgaard & Kurtz 2010; Chaplin & Miglio 2013). This means that only modes of low degree, typically with $l \leq 3$, can be resolved (Bedding 2011). Detection of $l = 3$ modes is more likely in Doppler measurements than with photometry, although it is still possible to detect these modes via photometry, for example, in the *Kepler* data of 16 Cyg A (Metcalfe et al. 2012).

In young solar-type stars, the p-mode and g-modes clearly have different frequency ranges. Once a star evolves and hydrogen is depleted, the increased core density causes the g-mode frequencies from the stellar interior to increase to the point that they are comparable to p-mode frequencies. If a p-mode meets a g-mode of the same degree, the modes won't cross each other and instead an "avoided crossing" occurs. This is due to the coupling between the p-mode and g-mode cavities, and it causes the modes to exchange nature. Therefore, both g-modes and p-modes behave as p-modes in the envelope, and both g-modes and p-modes behave as g-modes in the interior. Mixed modes, unlike pure g-modes, can be detected. As a star ages, it is possible to observe multiple $l = 1$ modes in a single order, as the g-modes become detectable. In red giants, there can be a lot of $l = 1$ mixed modes per order. It is also possible for mode bumping to occur, where a mode is bumped upwards by one below so that the regular frequency spacing is disrupted (Bedding et al. 2011; Bedding 2011; Chaplin et al. 2010; Deheuvels et al. 2012; Chaplin & Miglio 2013).

2.6.3 Parameters from pulsations

The oscillation frequencies measured via asteroseismology can be used to determine stellar parameters, however a prior knowledge of the $T_{\rm eff}$ and metallicity is usually needed. Of particular importance is the large frequency separation, $\Delta\nu$, the frequency of maximum amplitude, $\nu_{\rm max}$, and the small frequency separation, $\delta\nu_{\rm nl}$ (Chaplin & Miglio 2013).

The large frequency separation is the frequency spacing between consecutive radial overtones as is illustrated in Figure 2.1, i.e. the n modes differ by 1, but have the same value of l. It is the inverse of the time it takes the sound wave to travel from the surface to the core and back to the surface again. The small frequency separation, also depicted in the figure, is where n differs by 1, and l differs by 2 such that $\delta\nu_{02} = \nu_{\mathrm{n},0} - \nu_{\mathrm{n}-1,2}$ for a given value of n (Bedding 2011). The maximum frequency is the frequency with the largest amplitude, which is the central frequency in the power excess (Chaplin et al. 2011).

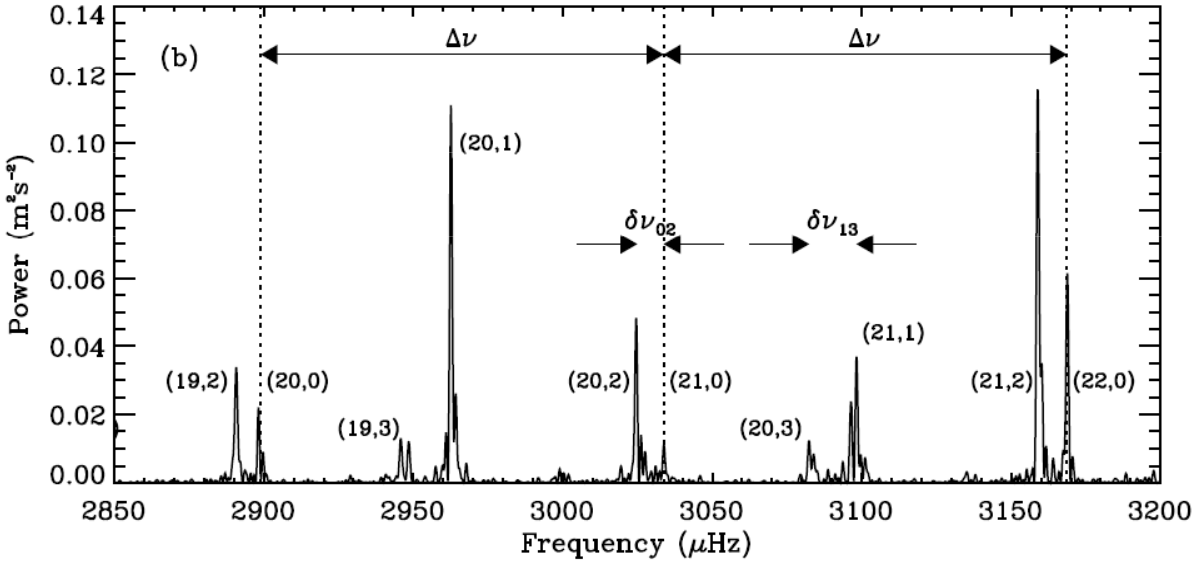

Figure 2.1: The large and small separations are indicated, with each mode being labelled as (n,l). The dotted lines indicate the radial modes. Credit: Bedding (2011). Reproduced with permission.

The small frequency separation can be used to determine the age of a star. The sound speed increases with increasing radius, and this corresponds to a decrease in $\delta\nu_{\mathrm{nl}}$. The amount of helium within the core will increase as a star evolves, which will then cause the sound speed to decrease near the core of the star. Overall this has the effect of decreasing $\delta\nu_{\mathrm{nl}}$ as the star ages. This relationship does not hold for more evolved stars such as red giants (Soderblom 2009; Doğan 2010; Christensen-Dalsgaard 2011).

Even when individual oscillation frequencies can't be determined due to low S/N, $\Delta\nu$ can usually be extracted, which can be used to determine the stellar density from

$$\left(\frac{\Delta\nu}{\Delta\nu_{\odot}}\right) \approx \sqrt{\frac{\bar{\rho}}{\bar{\rho}_{\odot}}} \approx \left(\frac{M}{M_{\odot}}\right)^{0.5} \left(\frac{R}{R_{\odot}}\right)^{-1.5}. \tag{2.6}$$

If ν_{max} can also be determined, then this can be used to ultimately find the

mass and radius. The maximum frequency is scaled approximately with the acoustic cut-off frequency, $\nu_{\rm c}$, although the physical meaning of this relationship is still poorly understood;

$$\left(\frac{\nu_{\rm max}}{\nu_{\rm max,\odot}}\right) \approx \left(\frac{\nu_{\rm c}}{\nu_{\rm c,\odot}}\right) \approx \left(\frac{M}{M_{\odot}}\right)\left(\frac{R}{R_{\odot}}\right)^{-2}\left(\frac{T_{\rm eff}}{T_{\rm eff,\odot}}\right)^{-0.5}. \tag{2.7}$$

The acoustic cut-off frequency rises sharply close to the stellar surface and acts as a boundary below which a wave will be reflected back into the envelope if it has a frequency less than $\nu_{\rm c}$ (Doğan 2010; Chaplin et al. 2011; Chaplin & Miglio 2013).

If $\Delta\nu$, $\nu_{\rm max}$ and $T_{\rm eff}$ are known, then Equation 2.6 and Equation 2.7 can be rearranged to extract the mass and radius individually in what is known as the "direct" method (Aerts, Christensen-Dalsgaard & Kurtz 2010; Basu, Chaplin & Elsworth 2010; Belkacem et al. 2011; Belkacem 2012; Chaplin et al. 2011; Mathur et al. 2012);

$$\left(\frac{R}{R_{\odot}}\right) = \left(\frac{\nu_{\rm max}}{\nu_{\rm max,\odot}}\right)\left(\frac{\Delta\nu}{\Delta\nu_{\odot}}\right)^{-2}\left(\frac{T_{\rm eff}}{T_{\rm eff,\odot}}\right)^{-0.5} \tag{2.8}$$

and

$$\left(\frac{M}{M_{\odot}}\right) = \left(\frac{\nu_{\rm max}}{\nu_{\rm max,\odot}}\right)^{3}\left(\frac{\Delta\nu}{\Delta\nu_{\odot}}\right)^{-4}\left(\frac{T_{\rm eff}}{T_{\rm eff,\odot}}\right)^{1.5}. \tag{2.9}$$

Using the conventional methods to determine stellar radii outlined in Section 2.4 typically results in errors that can be greater than 50 per cent. Using $\Delta\nu$ from asteroseismology diminishes this error to less than 5 per cent, with the addition of $\nu_{\rm max}$ reducing this a small bit more (Basu, Chaplin & Elsworth 2010). Silva Aguirre et al. (2013) used the asteroseismic radius, along with the limb-darkened angular diameter determined from the IRFM, to calculate an asteroseismic distance and found an excellent agreement with the *Hipparcos* parallax measurements. They then used this technique on all of 565 short-cadence *Kepler* stars to find the distance distribution of the sample.

It should be cautioned that as the oscillations are a stochastic process, $\nu_{\rm max}$ will vary depending on the time of the observations (Belkacem 2012). However, the scaling relations based on $\Delta\nu$ and $\nu_{\rm max}$ still only result in uncertainties that are minuscule in comparison to traditional methods for determining stellar mass and radius (Huber et al. 2013).

The maximum frequency decreases as the star ages, i.e. as $\log g$ decreases, meaning that the relationship between $\nu_{\rm max}$ and $\nu_{\rm c}$ can be used to determine $\log g$ from asteroseismology (Belkacem 2012; Chaplin & Miglio 2013);

$$\log g = \log g_{\odot} + log\left(\frac{\nu_{\rm max}}{\nu_{\rm max,\odot}}\right) + \frac{1}{2} log\left(\frac{T_{\rm eff}}{T_{\rm eff,\odot}}\right). \quad (2.10)$$

Using $\nu_{\rm max}$ to constrain $\log g$ can lead to a precision that is similar to eclipsing binaries, and the seismic gravities typically agree well with other methods of gravity determination. However, Bruntt et al. (2012) found the spectroscopic $\log g$ was systematically higher than the asteroseismic $\log g$ by around 0.08 dex, but could not offer an explanation as to why this is so. The main source of error in seismic gravity values stems from the uncertainty in $\nu_{\rm max}$, which ranges from one to ten per cent. However, a typical uncertainty of five per cent still only equates to an error of around 0.03 dex in $\log g$. The asteroseismic $\log g$ determination is reliant on a prior knowledge of $T_{\rm eff}$, but is not overly sensitive to it. A change in $T_{\rm eff}$ of 100 K will only result in a change in $\log g$ of around 0.004 dex for solar-like stars (Morel & Miglio 2012).

It is also possible to determine parameters from asteroseismology via grid-based methods. For grid based methods, $\Delta\nu$, $\nu_{\rm max}$, $T_{\rm eff}$ and [Fe/H] are used as input parameters in stellar evolutionary models and these models are used to estimate mass and radius. The grids can also be used to determine the $\log g$ when $\nu_{\rm max}$ isn't used as an input value. Grid based methods have smaller uncertainties than scaling relations, but can depend on uncertainties in metallicity (Chaplin et al. 2011).

3 Spectral analysis method

In the stars...there is a multitude of experiments all ready performed for us with a variety of conditions of just the kind we need. It remains for us to observe and interpret these results.

- Henry Draper, 1879

Unfortunately, there is no single, exact method for extracting information from stellar spectra. There are different programmes, different methods for measuring the lines, different assumptions used and so on. In this chapter I describe the spectral analysis method that I have used to determine the parameters of a selection of the stars from the Wide Angle Search for Planets (WASP) programme. Some of the results here have been published in Doyle et al. (2013).

3.1 Software

UCLSYN (University College London SYNthesis) is the software I use for spectral analysis (Smith 1992; Smalley, Smith & Dworetsky 2001). ATLAS 9 models without convective overshooting are used (Castelli, Gratton & Kurucz 1997) and local thermodynamic equilibrium is assumed. Spectral lines can be measured directly by using equivalent widths, or alternatively the lines can be synthesised by using least squares fitting. The atomic data used to generate the synthetic spectra is obtained from Kurucz & Bell (1995), although lines can also be input manually using atomic data from other sources. The broadening parameters that can be input are microturbulence, macroturbulence, rotational velocity and instrumental broadening. The radiative damping constant, Van der Waals damping constant and the Stark broadening factor are input via the line list. The adopted solar abundances previously used in UCLSYN were taken mainly from Anders & Grevesse (1989), the C, N, and O abundances are taken from Grevesse (1991) and the Fe abundance from Biemont et al. (1991). The current version now uses the abundances from Asplund et al. (2009).

3.2 Methods

3.2.1 Input of initial parameters

Before determining the spectroscopic parameters of a star, prior values need to be input to create the model spectrum. An initial guess for $T_{\rm eff}$ can be determined from the Balmer lines or from photometry. The $\log g$ is input as 4.5 under the assumption that the star is a dwarf, and $v_{\rm mic}$ is input as 1 $\rm km\,s^{-1}$. In order to fit the lines, broadening also needs to be accounted for in the synthetic spectrum. An initial estimate of $v_{\rm mac}$ can be determined from the input $T_{\rm eff}$ using a calibration. The $v \sin i$ is input as a low value ($\sim$3 $\rm km\,s^{-1}$), but this can be adjusted if it is obvious that the observed spectrum has a higher rotational velocity.

The instrumental broadening also needs to be input. I determined this from the telluric lines at $\sim$6300 and 6800 Å. This was done by fitting a synthetic spectrum to the telluric lines. The height of the observatory, and the airmass at the time the spectrum was obtained were input. The instrumental broadening was then varied until a good match was achieved between the synthetic and observed spectrum. Coadded spectra cannot be used for this, as the velocity shift incurred by the motion of the Earth will create additional broadening when the spectra are added together. An example is seen in Figure 3.1 for a single HARPS spectrum of WASP-7. For the HARPS spectra, a resolution of 112,000 was used for all spectra and the Kitt Peak Solar Atlas has negligible instrumental broadening (Valenti & Piskunov 1996).

3.2.2 Determining parameters

The first step of analysing a spectrum is to measure the EWs of the lines. Details of the selection of the line list will be discussed in Section 3.4. I interactively measured the EWs of as many absorption lines as possible for each element. In order to directly measure the EWs, a point on each side of the line is selected where the wing of the line reaches the continuum. The continuum was normalised by eye over a small wavelength range around each line.

A curve-of-growth analysis was then used to determine the abundance from the measured EW. A synthetic line profile was generated using that abundance and compared to the observed profile shape, and if the synthetic line profile reproduced the observed line, then this EW was used. In some instances, the synthetic profile failed to produce an acceptable fit to the observed spectrum, possibly due to incorrect broad-

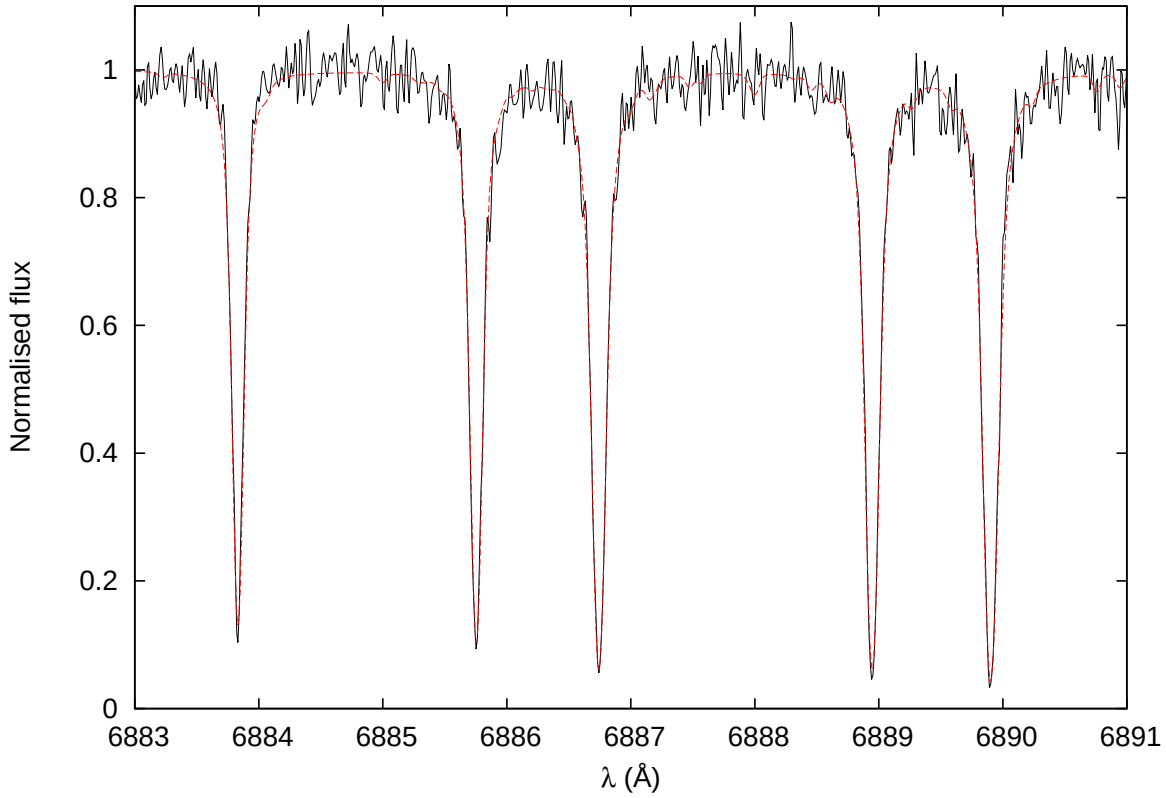

Figure 3.1: Determining the instrumental broadening from the telluric lines for the HARPS spectrum of WASP-7. The solid black line is a single observed spectrum and the red dashed line is the fit. This is for a resolution of 112,000 and also taking into account the observatory height and the airmass at the time the spectrum was taken.

ening parameters. When this occurred, I used a least squares fitting method to fit the line by adjusting the $v_{\rm mic}$, $v_{\rm mac}$, $v \sin i$ and $\log A$ (Fe). This abundance was then used to calculate the EW of the synthetic line. Fitting the lines, as opposed to just measuring the EWs, is required for strong lines, as discussed in Section 3.6.4.

Once all of the EWs are measured, this will give a first guess for the abundances of the Fe lines, which can then be used to determine $T_{\rm eff}$, $\log g$, and $v_{\rm mic}$. This is an iterative procedure, as the final abundance cannot be determined until the $T_{\rm eff}$, $\log g$, and $v_{\rm mic}$ are known.

The first estimate for $T_{\rm eff}$ is determined from the excitation balance of Fe I, as discussed in Section 1.4. I estimated the microturbulence by using the Magain (1984) method to reduce the trend in EW with abundance, as described in Section 1.8.3.1.

The ionisation balance $\log g$ is determined by varying $\log g$ until the Fe I and Fe II abundances agree. Any obvious outliers in the plot of Fe abundance against EW or EP were removed, with a requirement that the abundance of the individual lines should be

within 0.25 dex of the average abundance. This restriction allowed discrepant lines to be removed while still retaining a sufficient number of lines needed to determine the stellar parameters. In general I found that the same lines had abundances that were too high or too low across all stars, indicating that these lines had incorrect atomic data.

I also estimated the $\log g$ from the Na D lines and the Ca line at 6439 Å. The abundance is first determined from several weak lines, and then the $\log g$ is adjusted until the synthetic lines match the observed spectrum. The average $\log g$ is then determined from the ionisation balance, Na D lines, and the Ca line. The $\log g$ from the ionisation balance agrees with the $\log g$ from the pressure broadened lines to within 0.3 dex. This difference is possibly due to the errors in abundance, $T_{\rm eff}$ errors influencing the ionisation balance, or other issues inherent in determining the $\log g$ from pressure broadened lines. The final $\log g$ value is then used to redetermine the $v_{\rm mic}$, and this $v_{\rm mic}$ is used to get a final value for the excitation balance $T_{\rm eff}$.

Once the final parameters have been determined, the final abundances can also be calculated. Now that the $T_{\rm eff}$ is known, the $v_{\rm mac}$ can be calculated from a calibration. I originally calculated the macroturbulence based on the Bruntt et al. (2010a) calibration for stars with $T_{\rm eff}$ below 6500 K, and this was extrapolated for stars greater than 6500 K. However in Chapter 5, I determine my own $v_{\rm mac}$ calibration. Once there is a value of $v_{\rm mac}$, the rotational velocity is fit for a selection of unblended lines and the average value is used as the final $v \sin i$ value.

3.3 Spectrographs

The initial analyses for the WASP planet host stars for the discovery papers are usually performed using coadded spectra from the CORALIE spectrograph, which has a resolution between 55,000 and 60,000 (Queloz et al. 2001; Wilson et al. 2008) and is installed on the Swiss 1.2 m Leonard Euler telescope at La Silla. These spectra have S/N varying from ∼40 to ∼100. I analysed some of these CORALIE spectra for the discovery papers in order to test the spectral analysis methods I was developing and also to understand the limitations inherent with low S/N. These analyses are ongoing in order to contribute to the WASP collaboration, and now include the line list that I constructed as part of this work.

The next step was to analyse these stars using the spectra obtained with the

HARPS spectrograph which has a resolution of ∼115,000 (Mayor et al. 2003). HARPS spectra typically have much higher S/N than their CORALIE equivalents, and the S/N and magnitude of each WASP star used is given in Table 3.1. The raw spectra had already been reduced using the standard HARPS data reduction software and the observation details for these spectra are discussed in Triaud et al. (2010), Queloz et al. (2010) and Gillon et al. (2009).

Table 3.1: Details of the HARPS spectra used in the present work

Star	V mag	No. of spectra	S/N
WASP-2	11.98	32	100
WASP-4	12.50	32	100
WASP-5	12.30	34	125
WASP-6	11.90	44	125
WASP-7	9.50	20	235
WASP-8	9.79	80	430
WASP-15	11.00	51	240
WASP-16	11.30	77	175
WASP-17	11.60	60	230
WASP-18	9.30	21	270
WASP-19	12.59	36	125
WASP-20	10.68	62	305
WASP-21	11.58	62	145
WASP-22	12.00	34	190
WASP-23	12.68	35	105
WASP-24	11.31	63	195
WASP-29	11.30	39	185
WASP-30	11.90	37	200
WASP-31	11.70	25	135
WASP-53		30	100
WASP-69	9.88	21	210
WASP-77A	10.30	8	110
WASP-77B	12.05	4	40
WASP-80	11.90	24	75

Both CORALIE and HARPS are cross-dispersed, fibre fed, echelle spectrographs that use a thorium argon spectrum as a reference. Using the ThAr reference spectrum enables the calibration of wavelength with the detector pixels, as well as tracking and removing instrumental drifts from the radial velocity measurements. A ThAr reference is used on HARPS because it utilises the whole visible range of the spectrum (3800 to 6900 Å), whereas an iodine cell as a reference is limited to the 5000 to 6000 Å range.

HARPS has a larger echelle grating and fibre diameter than CORALIE, which is what enables it to reach a superior resolution. The HARPS spectrograph is contained within a vacuum to eliminate problems with atmospheric pressure variations and the vacuum vessel has an air-conditioning system around it to minimise temperature variations. This gives the spectrograph enhanced stability (Queloz et al. 2001; Rupprecht et al. 2004).

3.4 Line list

While some methods rely on fitting the entire observed spectrum (or sections of it) with a synthetic spectrum, a more detailed analysis requires studying the individual lines. It is impractical to individually measure every line in a spectrum, and so an appropriate selection of lines must be chosen from a high S/N spectrum.

3.4.1 Atomic data

The line list used for the original discovery paper analyses of the WASP stars was constructed mainly from the data of Kurucz & Bell (1995), but also supplemented with other data from Barklem, Piskunov & O'Mara (2000), Gonzalez & Laws (2000), Gonzalez et al. (2001) and Santos, Israelian & Mayor (2004) and hereafter will be referred to as the KB line list. The KB line list included $\log gf$ values that were known to have been obtained from differential solar analyses, which can create problems such as that discussed in Section 4.1.3. A new line list was needed to fully exploit the high quality spectra of HARPS by ensuring the $\log gf$ values used were the most up to date and accurate values available. I obtained a significant proportion of atomic data from the Vienna Atomic Line Database (VALD; Kupka et al. 1999), however the exact source of the data in VALD is not always clear as a group of papers are cited instead of individual work. This means that there could still be $\log gf$ values in the new line list that were determined from the Sun, although I did not intentionally include any. Overall I found that there weren't major abundance differences between the KB and the new line list, as both have a wide range of scatter due to uncertainties in atomic data.

When damping parameters were unavailable in VALD, I obtained them from Kurucz & Bell (1995). In addition, the VALD $\log gf$ value was not always used for certain elements (e.g. Cr II, Ti II), as the value given resulted in abundances that were

inconsistent with the assumed solar abundances. In these cases a different source of $\log gf$ from within VALD was used, so that a more suitable solar abundance could be obtained. For instance, using the default VALD values yields a $\log A$(Cr II) of 5.80 $\pm$ 0.09 for the Sun, which is 0.16 dex higher than the Asplund et al. (2009) abundance. However, using alternative $\log gf$ values from VALD results in a $\log A$(Cr II) of 5.66 $\pm$ 0.01. Of course, this still introduces some bias towards the Sun, but I prioritised values that I knew were obtained in the laboratory if they existed. The $\log gf$ values were also supplemented from other sources (Fuhr & Wiese 2006; Meléndez & Barbuy 2009).

The choice of $\log gf$ can greatly influence the abundance obtained, resulting in a wide range of values for a particular element, even in the Sun. For example, the solar Mn ranges between 5.23 and 5.46 (Bergemann & Gehren 2007). Bigot & Thévenin (2006) computed $\log gf$ values using 3D models for a number of near-IR Fe and Si lines, and found that their values differ from the VALD values by up to 0.5 dex. When comparing their values to laboratory ones, this difference was reduced to 0.1 dex, further emphasising the fact that VALD values are not necessarily the best available.

In some cases it was not possible to find suitable $\log gf$ values. For instance, Si was found to exhibit a strong trend in EW against abundance when using the VALD data, and there currently isn't enough suitable atomic data elsewhere to correct this. Shi et al. (2008) also mention the large scatter in the solar Si abundance due to uncertainties in the some of the laboratory $\log gf$ values. Many of the Si lines are also difficult to fit correctly due to asymmetries and unusually broad wings, which will be discussed further in Section 5.10.

All lines were cross-referenced with the NIST database to check the reliability of $\log gf$ values. Any lines with an "E" rating, i.e. with an uncertainty of greater than $\pm$ 50 per cent (Fuhr & Wiese 2006), were rejected. However, it should be noted that not all lines in the list were present in the NIST database, so some lines that were included in my line list could still have large uncertainties in the $\log gf$ values. The line list is given in Appendix A, showing the NIST rating where available.

3.4.2 Line selection

I selected lines from the Kitt Peak Solar Atlas (Kurucz et al. 1984; S/N $\sim$3000) and prioritised unblended lines where possible, which comprise around one third of the list. Some lines had blending components that could be compensated for via spectral synthesis, and these were included to increase the number of lines. Unresolved blends

were included when there was a paucity of lines for a particular element. In this case, a restriction was imposed to ensure that the blending component comprised no more than five per cent of the overall EW, otherwise the line was deemed to be too severely blended to be of use. Lines which were blended with the same element in a different ionisation state were rejected, even if the weaker component was less than five per cent, as lines blended with other ionisation states could bias the estimate of the $T_{\rm eff}$. Unresolved blends were rejected for Fe, as there are still a sufficient number of Fe lines remaining after these blends are excluded.

A multitude of lines will not necessarily decrease the abundance error, especially if the additional lines are of poor quality. According to Kurucz (2002), abundance errors are likely to increase if there is a wide range of line strengths in a line list. An accurate abundance can theoretically be determined from a single weak line, as weak lines (EW $<$ 30 mÅ) are less affected by damping parameters and microturbulence. As such, including strong lines can increase the abundance errors. However, it is not possible to use only weak lines as there are not a sufficient number of them, and thus strong lines were also included in the list. The EWs for the Fe I lines in the HARPS solar spectrum (Dall et al. 2006; S/N ∼1000) range from 5.6 to 133.1 mÅ and the EP ranges from 0.052 to 5.033 eV. The strongest lines were often removed at a later stage as there can be large uncertainties in damping parameters and microturbulence for these lines (Takeda et al. 2005a; Jenkins et al. 2008).

3.4.3 Line lists for cool and hot stars

The strength of neutral metal lines increases vastly with decreasing temperature, and lines that are weak in the Sun become much stronger in cooler stars. In addition, ionised species will become weaker (Allende Prieto et al. 2004). Therefore a line list optimised for the Sun will not necessarily yield the best results with mid to late K-dwarfs. When I used the line list selected from the Sun on cool star WASP-69 ($T_{\rm eff}$ = 4945 K), there were only 32 measurable iron lines making it very difficult to get a reasonable result for $T_{\rm eff}$, the ionisation balance $\log g$ and $v_{\rm mic}$. The low $T_{\rm eff}$ means that the blue end of the spectrum is littered with spectral lines and it is most likely that molecular lines are present, which are not synthesised with UCLSYN. The multitude of lines in the blue end also makes it almost impossible to discern the position of the continuum. It is thus difficult to measure any lines below ∼5200 Å. In addition, this particular star is also very metal-rich, which makes some of the lines too strong to be useful and also

increases the amount of blending that is present. Adding in additional Fe and Ca lines from the KB line list was required in order to obtain a satisfying result, however it was clear that a new line list needed to be created for such stars. The lines for the cool stars line list were then selected from WASP-29.

Tables 3.2, 3.3 and 3.4 show the comparison between the low $T_{\rm eff}$ line list and the solar line list for the cool stars WASP-23, WASP-53 and WASP-69 respectively. The $T_{\rm eff}$ (unconstrained), $\log g$, and $v_{\rm mic}$ used to determine these abundances for these stars are listed in Table 3.7. The Fe abundance agrees well between both line lists, showing that the use of different line lists does not affect the Fe abundance determination itself. In general, there is a good agreement with the abundances of other elements, although the cool star line list obviously has more Ti and Cr lines. The most discrepant element is Co, and in the solar line list $\log A$ (Co) is 0.22 dex higher for WASP-53, and 0.40 dex higher for WASP-69. It is not immediately obvious what the cause of this discrepancy is, however it is possible that certain lines are more prone to HFS in one line list.

Table 3.2: Abundance comparison between line lists for WASP-23.

Element	Solar line list	No. of lines	Low $T_{\rm eff}$ line list	No. of lines
Ca	6.43 ± 0.09	7	6.35 ± 0.19	6
Sc	3.17 ± 0.04	5	3.10 ± 0.08	7
Ti	5.07 ± 0.08	27	5.02 ± 0.11	32
V	4.10 ± 0.09	11	4.09 ± 0.12	15
Cr	5.67 ± 0.07	11	5.70 ± 0.13	27
Mn	5.49 ± 0.11	8	5.46 ± 0.16	5
Fe	7.56 ± 0.07	34	7.56 ± 0.09	59
Co	5.04 ± 0.13	7	4.98 ± 0.13	7
Ni	6.20 ± 0.08	17	6.21 ± 0.09	14

Table 3.3: Abundance comparison between line lists for WASP-53.

Element	Solar line list	No. of lines	Low $T_{\rm eff}$ line list	No. of lines
Ca	6.55 ± 0.09	7	6.50 ± 0.15	6
Sc	3.42 ± 0.12	5	3.34 ± 0.11	8
Ti	5.23 ± 0.11	27	5.21 ± 0.15	39
V	4.49 ± 0.17	13	4.37 ± 0.20	19
Cr	5.84 ± 0.10	11	5.86 ± 0.11	21
Mn	5.69 ± 0.13	8	5.72 ± 0.20	6
Fe	7.69 ± 0.13	37	7.72 ± 0.11	63
Co	5.45 ± 0.20	9	5.23 ± 0.11	6
Ni	6.41 ± 0.16	22	6.42 ± 0.12	20

Table 3.4: Abundance comparison between line lists for WASP-69.

Element	Solar line list	No. of lines	Low $T_{\rm eff}$ line list	No. of lines
Ca	6.67 ± 0.16	5	6.61 ± 0.16	7
Sc	3.47 ± 0.19	7	3.40 ± 0.12	11
Ti	5.29 ± 0.14	26	5.32 ± 0.16	44
V	4.61 ± 0.14	13	4.62 ± 0.17	18
Cr	6.05 ± 0.17	11	6.10 ± 0.20	35
Mn	5.93 ± 0.34	10	5.85 ± 0.18	8
Fe	7.79 ± 0.12	32	7.82 ± 0.11	71
Co	5.66 ± 0.31	8	5.26 ± 0.16	10
Ni	6.57 ± 0.19	21	6.51 ± 0.10	19

At the other end of the $T_{\rm eff}$ scale, the HARPS spectrum of Procyon (S/N ∼300) was used to select lines that could be used in addition to the solar line list when analysing hotter stars. Using the solar line list for Procyon resulted in only 44 measurable Fe lines, as metallic lines become less prominent in hotter stars. Including the additional lines brought the Fe line count up to 67 for this star, which caused a subtle change in parameters. The final values used were thus based on the hotter line list, and this analysis is discussed in Section 3.5 and the results given in Table 3.5.

3.5 Comparison to standard stars

Before applying the method outlined above to the HARPS spectra of the WASP stars, it was important to verify that the method achieved acceptable results on well known stars such as the Sun and Procyon. Procyon was chosen as a hotter comparison star than the Sun, as many WASP stars are hotter than the Sun. The parameters were derived from the Kitt Peak Solar Atlas and the HARPS sky spectrum for the Sun, and from a HARPS spectrum of Procyon. These parameters, along with literature values, are displayed in Table 3.5. The parameters of the Sun are well known, however the parameters of Procyon are less accurate. The mass, and thus the $\log g$, can be determined with a good deal of accuracy due to the binary nature of Procyon. However, there is still some disagreement as to the $T_{\rm eff}$, mainly due to different values of bolometric flux and angular diameter. The $T_{\rm eff}$ values are given as 6516 ± 87 K (Aufdenberg, Ludwig & Kervella 2005), 6530 ± 49 K (Allende Prieto et al. 2002) and 6591 ± 43 K (Chiavassa et al. 2012). Casagrande et al. (2010) also obtained a value of 6626 ± 80 K using the IRFM. An averaged $T_{\rm eff}$ value is adopted for Table 3.5.

Table 3.5: Parameters obtained for the Sun and Procyon.

Parameter	Sun (Solar Atlas)	Sun (HARPS)	Sun (literature)	Procyon (HARPS)	Procyon (literature)
$T_{\rm eff}$(K)	5760 ± 50	5775 ± 45	5777[a]	6660 ± 95	6566 ± 65[b]
$\log g$	4.42 ± 0.02	4.43 ± 0.02	4.44[a]	4.05 ± 0.06	4.01 ± 0.03[c]
$\log A$(Fe)	7.49 ± 0.06	7.52 ± 0.08	7.50 ± 0.04[d]	7.48 ± 0.09	7.36 ± 0.03[e]
$v_{\rm mic}$ (km s^{-1})	0.85 ± 0.08	0.75 ± 0.15	0.85[f]	1.70 ± 0.08	2.2[e]

[a] Gray (2008), [b] See text, [c] Chiavassa et al. (2012), [d] Asplund et al. (2009), [e] Allende Prieto et al. (2002), [f] Magain (1984)

It is possible that the higher $T_{\rm eff}$ that I determined for Procyon could also be due to NLTE effects. Performing a full NLTE correction is beyond the scope of this work, however I thought it would be interesting to perform a quick test to get an idea of how much NLTE affects the Fe I lines at higher temperatures. Using the INSPECT database[1] (Bergemann et al. 2012; Lind, Bergemann & Asplund 2012), I was able to input the $T_{\rm eff}$, $\log g$, $v_{\rm mic}$ and $\log A$ (Fe) for Procyon and the NLTE corrections for a number of Fe I lines were displayed with an average correction of +0.04 dex. If there was no value available for any of my lines, I used the average value as the correction. I found that the $T_{\rm eff}$ of Procyon derived from the excitation balance was now 60 K lower, bringing it to 6600 K which is in better agreement with the literature.

For the HARPS solar spectrum, I found $\log A$(Fe) to be 7.52 ± 0.08. This is in good agreement with the values of 7.50 ± 0.04 and 7.52 ± 0.06 found by Asplund et al. (2009) and Caffau et al. (2011) respectively, but higher than the value of 7.45 ± 0.02 determined by Meléndez & Barbuy (2009).

3.6 Results and discussion

The $T_{\rm eff}$, $\log g$ and $\log A$(Fe) from the discovery papers are given in Table 3.6, along with the IRFM $T_{\rm eff}$ (Maxted, Koen & Smalley 2011) and the $\log g$ derived from the transits (Southworth 2012b; Southworth et al. 2012; Southworth et al. 2013; Mortier et al. 2013b). Table 3.7 gives the $T_{\rm eff}$ (constrained and unconstrained), $\log g$, $v_{\rm mic}$, $v_{\rm mac}$ and $v \sin i$ determined for each star, as well as the number of Fe lines used in each analysis. The $v_{\rm mac}$ was determined using the Bruntt et al. (2010a) calibration, and was then redetermined in Chapter 5.

[1] www.inspect-stars.net

Table 3.6: Parameters from the literature

Star	IRFM $T_{\rm eff}$ (K)	Transit $\log g$ Southworth	Transit $\log g$ Mortier	Initial $T_{\rm eff}$ (K)	Initial $\log g$	Initial $\log A$(Fe)	Ref.
WASP-2	5110 ± 60	4.537 ± 0.016	4.54 ± 0.01	5200 ± 200	4.30 ± 0.30	∼7.54	Collier Cameron et al. (2007)
WASP-4	5540 ± 55	4.487 ± 0.009	4.49 ± 0.01	5500 ± 150	4.30 ± 0.20	7.54 ± 0.20	Wilson et al. (2008)
WASP-5	5770 ± 65	4.379 ± 0.030	4.39 ± 0.03	5700 ± 150	4.30 ± 0.20	7.54 ± 0.20	Anderson et al. (2008)
WASP-6			4.52 ± 0.01	5450 ± 100	4.60 ± 0.20	7.34 ± 0.10	Gillon et al. (2009)
WASP-7	6520 ± 70	4.218 ± 0.048	4.22 ± 0.01	6400 ± 100	4.30 ± 0.20	7.54 ± 0.10	Hellier et al. (2009b)
WASP-8	5570 ± 85		4.48 ± 0.01	5600 ± 80	4.50 ± 0.10	7.71 ± 0.07	Queloz et al. (2010)
WASP-13		4.086 ± 0.033	3.90 ± 0.03	5826 ± 100	4.04 ± 0.20	7.45 ± 0.20*	Skillen et al. (2009)
WASP-15	6210 ± 60	4.189 ± 0.021	4.22 ± 0.02	6300 ± 100	4.35 ± 0.15	7.37 ± 0.11	West et al. (2009)
WASP-16	5550 ± 60	4.357 ± 0.022	4.49 ± 0.02	5700 ± 150	4.50 ± 0.20	7.55 ± 0.10	Lister et al. (2009)
WASP-17	6500 ± 75	4.149 ± 0.014	4.16 ± 0.01	6550 ± 100	4.20 ± 0.20	7.29 ± 0.09	Anderson et al. (2010)
WASP-18	6455 ± 70	4.365 ± 0.027	4.32 ± 0.03	6400 ± 100	4.40 ± 0.15	7.54 ± 0.09	Hellier et al. (2009a)
WASP-19	5440 ± 60		4.44 ± 0.01	5500 ± 100	4.50 ± 0.20	7.56 ± 0.09	Hebb et al. (2010)
WASP-20				6000 ± 100	4.40 ± 0.15	7.53 ± 0.06	Anderson et al. (2014b)
WASP-21		4.281 ± 0.031	4.28 ± 0.03	5800 ± 100	4.20 ± 0.10	7.08 ± 0.11	Bouchy et al. (2010)
WASP-22	6020 ± 50		4.32 ± 0.02	6000 ± 100	4.50 ± 0.20	7.59 ± 0.09	Maxted et al. (2010b)
WASP-23			4.59 ± 0.01	5150 ± 100	4.40 ± 0.20	7.49 ± 0.13	Triaud et al. (2011)
WASP-24			4.25 ± 0.01	6075 ± 100	4.15 ± 0.10	7.52 ± 0.10*	Street et al. (2010)
WASP-29	4875 ± 65		4.55 ± 0.02	4800 ± 150	4.50 ± 0.20	7.65 ± 0.14	Hellier et al. (2010)
WASP-30				6100 ± 100	4.30 ± 0.15	7.46 ± 0.10	Anderson et al. (2011d)
WASP-31	6175 ± 70		4.31 ± 0.02	6250 ± 150	4.50 ± 0.20	7.25 ± 0.11	Anderson et al. (2011c)
WASP-69				4700 ± 50	4.50 ± 0.15	7.69 ± 0.08	Anderson et al. (2014a)
WASP-80				4150 ± 150	4.60 ± 0.20	7.24 ± 0.17	Triaud et al. (2013a)

*Given as [M/H] = 0.07 and assuming solar $\log A$ (Fe) of 7.45.

The initial values refer to the parameters in the discovery papers, which were usually determined from CORALIE/SOPHIE spectra.

Table 3.7: Results from HARPS spectra.

Star	$T_{\rm eff}$ (K) unconstrained	$T_{\rm eff}$ (K) fixing $\log g$	$\log g$	$v_{\rm mic}$ ($\rm km\,s^{-1}$)	$v_{\rm mac}$* ($\rm km\,s^{-1}$)	$v \sin i$ ($\rm km\,s^{-1}$)	No. of Fe lines
WASP-2	5175 ± 95	5225 ± 95	4.46 ± 0.12	0.70 ± 0.15	0.9 ± 0.3	1.9 ± 0.7	40
WASP-4	5400 ± 90	5420 ± 90	4.47 ± 0.11	0.85 ± 0.10	1.4 ± 0.3	3.4 ± 0.3	50
WASP-5	5690 ± 80	5750 ± 80	4.28 ± 0.09	0.75 ± 0.10	2.2 ± 0.3	3.9 ± 0.2	57
WASP-6	5375 ± 65	5305 ± 60	4.61 ± 0.07	0.70 ± 0.20	1.4 ± 0.3	2.4 ± 0.5	50
WASP-7	6550 ± 70	6480 ± 70	4.32 ± 0.06	1.40 ± 0.08	5.2 ± 0.3	18.1 ± 0.2	29
WASP-8	5560 ± 90	5620 ± 90	4.40 ± 0.09	0.95 ± 0.15	1.9 ± 0.3	2.7 ± 0.5	57
WASP-15	6405 ± 80	6260 ± 80	4.40 ± 0.11	1.15 ± 0.08	4.6 ± 0.3	4.9 ± 0.4	64
WASP-16	5630 ± 70	5750 ± 70	4.21 ± 0.11	0.85 ± 0.10	2.1 ± 0.3	2.5 ± 0.4	59
WASP-17	6700 ± 105	6670 ± 105	4.34 ± 0.23	1.40 ± 0.10	5.8 ± 0.3	9.8 ± 1.1	45
WASP-18	6400 ± 75	6440 ± 75	4.32 ± 0.09	1.15 ± 0.08	4.6 ± 0.3	10.9 ± 0.7	48
WASP-19	5460 ± 90	5520 ± 85	4.37 ± 0.14	1.00 ± 0.15	1.6 ± 0.3	5.1 ± 0.3	52
WASP-20	6030 ± 80		4.54 ± 0.13	0.90 ± 0.15	3.3 ± 0.3	4.3 ± 0.4	57
WASP-21	5835 ± 55	5800 ± 55	4.33 ± 0.09	0.75 ± 0.15	2.7 ± 0.3	2.4 ± 0.2	51
WASP-22	6020 ± 65	6060 ± 70	4.25 ± 0.09	1.00 ± 0.08	3.2 ± 0.3	4.4 ± 0.2	61
WASP-23	5020 ± 50	5040 ± 40	4.31 ± 0.12	0.60 ± 0.10	0.0	2.4 ± 0.3	76
WASP-24	6080 ± 60	6090 ± 60	4.20 ± 0.11	0.85 ± 0.10	3.4 ± 0.3	6.4 ± 0.2	61
WASP-29	4730 ± 70	4730 ± 70	4.48 ± 0.16	0.50 ± 0.20	0.0	2.4 ± 0.5	70
WASP-30	6190 ± 50		4.18 ± 0.08	1.10 ± 0.10	3.7 ± 0.3	12.1 ± 0.5	50
WASP-31	6320 ± 75	6300 ± 75	4.36 ± 0.10	1.05 ± 0.08	4.3 ± 0.4	7.9 ± 0.3	55
WASP-53	4950 ± 60		4.40 ± 0.20	0.60 ± 0.25	0.0	2.7 ± 0.3	63
WASP-69	4750 ± 55		4.36 ± 0.19	0.50 ± 0.20	0.0	2.9 ± 0.3	66
WASP-77A	5500 ± 80		4.33 ± 0.08	0.80 ± 0.10	1.7 ± 0.3	4.0 ± 0.2	54
WASP-77B	4700 ± 100		4.60 ± 0.15		0.0	2.8 ± 0.5	27
WASP-80	4145 ± 100		∼4.6	0.3 ± 0.3	0.0	3.5 ± 0.3	33

* These values are determined from the Bruntt et al. (2010a) calibration. Macroturbulence was redetermined in Chapter 5.

3.6.1 Determination of $\log g$

It is important to include as many Fe II lines as possible in order to get an accurate $\log g$ from the ionisation balance. When using the KB line list on the Kitt Peak Solar Atlas, I found that the $\log g$ from the ionisation balance was too high at 4.62 ± 0.08. Only six out of ten Fe II lines were usable, and these had lower than average abundances (which was only obvious as the solar parameters are already known with good confidence). It is also possible that the ionisation balance $\log g$ could be underestimated using other line lists, depending on the particular Fe II lines used. This shows the importance of not using ionisation balance alone to determine $\log g$; the pressure broadened lines should also be used to compliment this method. Figure 3.2 depicts the ionisation balance of the KB line list when using the correct solar $\log g$ of 4.44, showing the inadequate selection of Fe II lines.

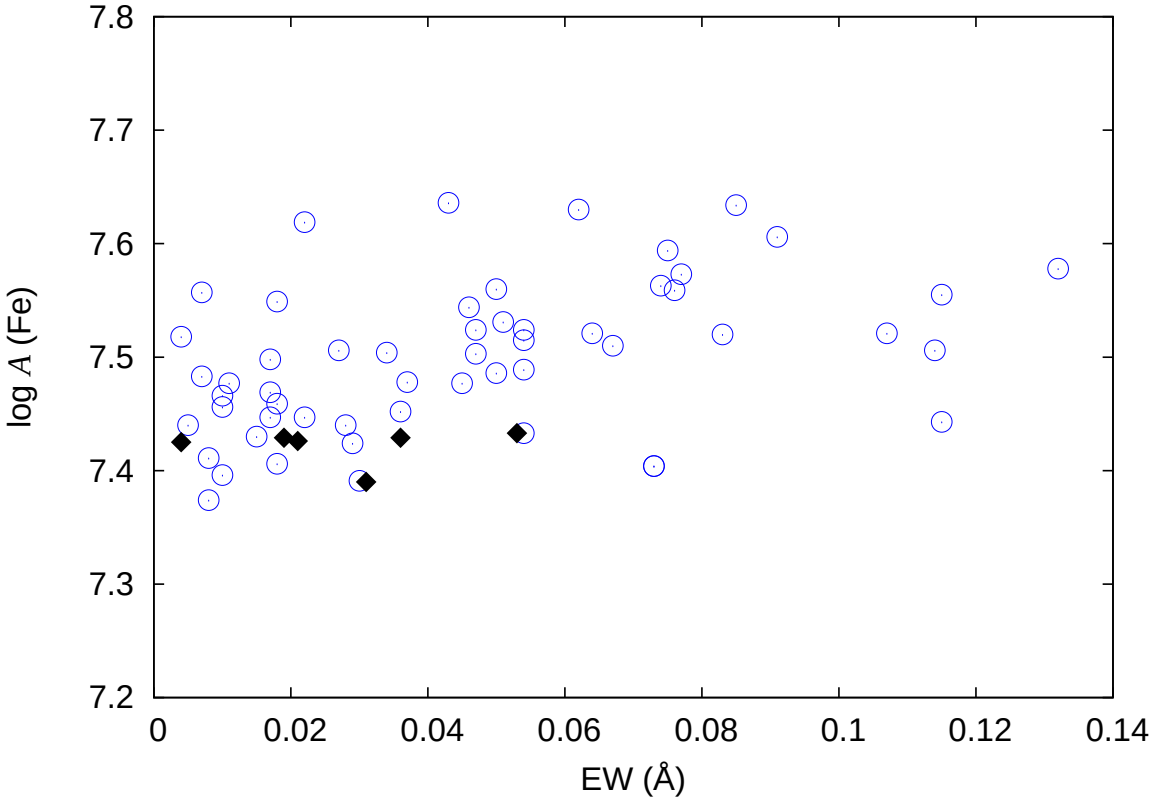

Figure 3.2: The ionisation balance is wrong for the Kitt Peak Solar Atlas when using the KB line list due to a paucity of Fe II lines. The $\log g$ shown here is for the correct value of 4.44. If this was not known, then the $\log g$ would be overesimtated. The Fe I lines are shown as blue circles and the Fe II lines are represented by the black diamonds.

3.6.1.1 The Na I D lines

Using the Na I D lines for $\log g$ determination can be difficult if interstellar Na is present. In addition, the Na I D lines can also be plagued with telluric emission lines.

It is important that an accurate Na abundance is determined prior to any attempt to fit the Na I D lines to obtain $\log g$. Figure 3.3 shows the HARPS solar spectrum along with synthetic spectra computed with [Na/H] abundances of -0.1, 0.1 and 0.3 dex. Even a change of 0.1 dex can make a noticeable difference, and a change of 0.3 dex can have a detrimental effect on the $\log g$ if it is not taken into account. If there is a high abundance of Na, then the $\log g$ can be underestimated.

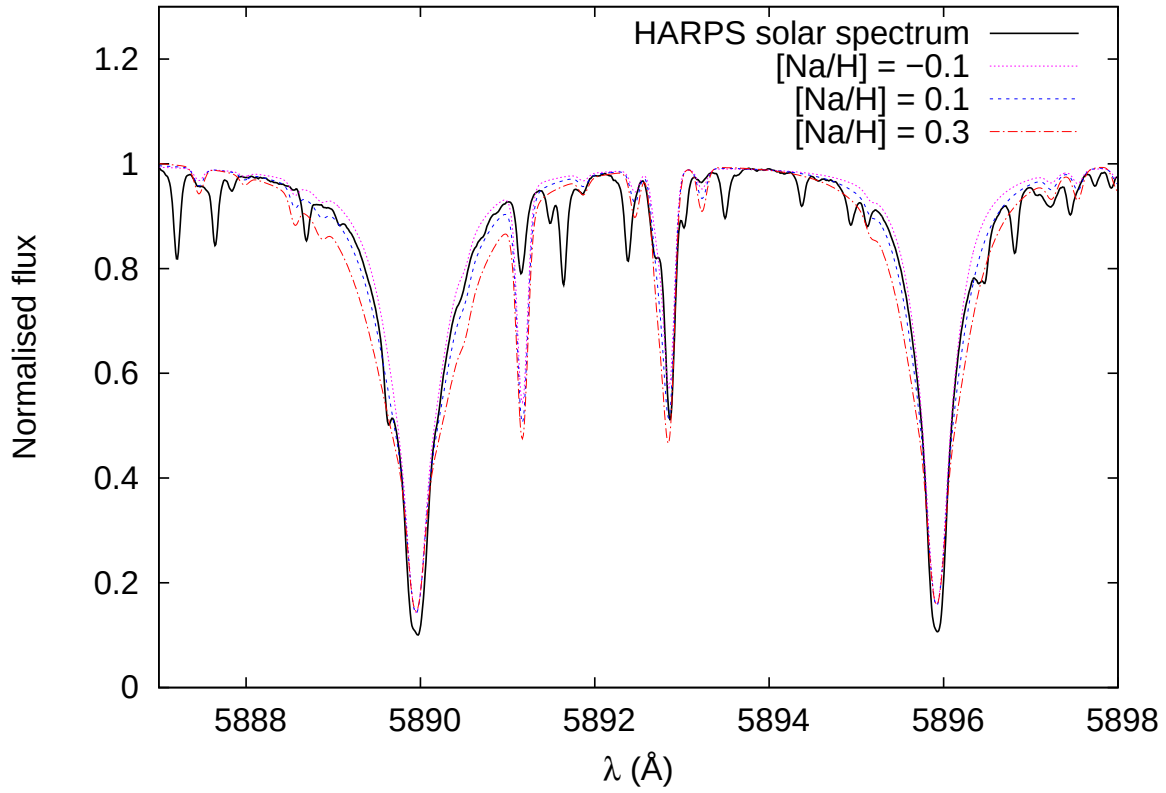

Figure 3.3: The effect that differing values of [Na/H] has on the synthetic spectra is shown. This can in turn affect the $\log g$ determination from the Na I D lines if the abundance is not taken into account.

I noticed that it was particularly difficult to obtain a reasonable value for $\log g$ for stars below ∼5000 K. The $\log g$ was unusually low and suggested that these stars were actually giants. This low $\log g$ was inconsistent with other results, and as the [Na/Fe] abundance seemed abnormally high for these stars, I assumed that the abundance was incorrect. Plotting [Na/Fe] against $T_{\rm eff}$ revealed a trend, shown in Figure 3.4, with

[Na/Fe] increasing for cooler stars and a significant upturn evident at 5000 K. The solid line shown in the figure is a linear regression to the data, where f(x) = m(x) + c and the slope (m) is $-1.73 \times 10^{-4} \pm 3.09 \times 10^{-5}$ and intercept (c) is 1.01 ± 0.17.

A measure of how well the data fits to the line is the coefficient of determination, r^2, which is the square of the correlation coefficient. It has values between 0 and 1. If there was no trend between [Na/Fe] and $T_{\rm eff}$, then r^2 would be expected to be 0. In this case, r^2 is 0.60 indicating that there is a trend with this data, although it is not a perfect linear relationship. The Fischer statistical test (F-test) can be used to test if this linear relationship is significant. If the F-statistic (which is calculated from the ratio of the regression sum of squares and residual sum of squares) is greater than the F-critical value, then the null hypothesis can be rejected. The null hypothesis is that the data is actually a random scatter of points with a slope of zero. The F-statistic is 31.26 for 21 degrees of freedom, so when comparing this to the F-critical value it is found that the probability (p) that the null hypothesis is true is 0.00001507. This means that the null hypothesis can safely be rejected, and that there is indeed a trend between [Na/Fe] and $T_{\rm eff}$.

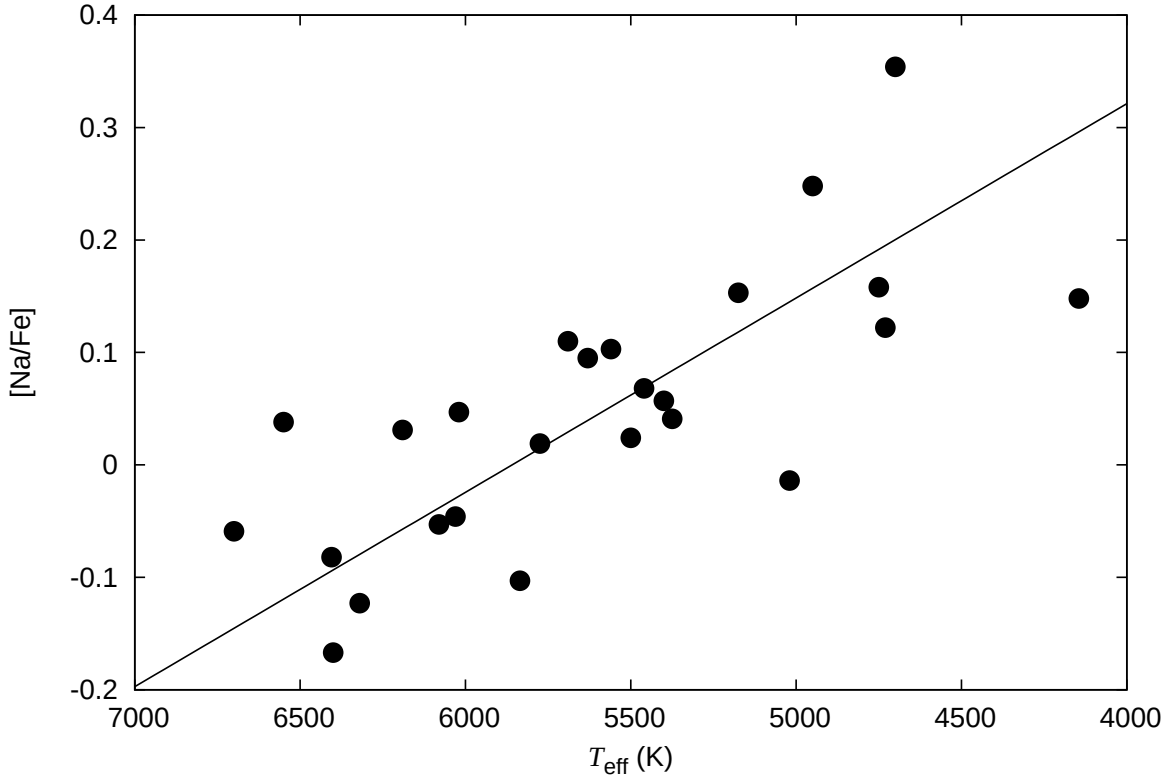

Figure 3.4: A trend was observed between [Na/Fe] and $T_{\rm eff}$, suggesting that the Na abundance is incorrect in stars below 5000 K. The solid line is the linear regression.

The four Na lines I used to measure abundance were at 4751, 5148, 6154 and 6160 Å. There are other Na lines, but I deemed them too strongly blended to be of use. For instance, the Na I 5682 line is in a blend with Cr, and while this can sometimes be measured via synthesis, it produces an abundance that is abnormally low compared to the other lines and so this line is not used in any analysis. The Na I 5688 line is always blended with another Na line, and so is not used at all. The abundance usually agrees between the four lines for solar-like stars and hotter, but the 6154 + 6160 doublet yields significantly higher abundances than the 4751 and 5148 Å lines in cooler stars. No obvious trend with temperature is evident in the data of Shi, Gehren & Zhao (2004) or Thorén & Feltzing (2000), however Shi, Gehren & Zhao (2004) do not have any stars in their sample below 5000 K. They measured the 5682/5688, 5889/5895 and 6154/6160 Å Na I lines via line synthesis, however the first two doublets are prone to blending and NLTE effects respectively. The stellar sample of Thorén & Feltzing (2000) does extend to 4500 K, but there is too much scatter in their data to notice any trend. Beirão et al. (2005) note that [Na/H] is higher in planet host stars than comparison "single" stars, however an overall increase in [Na/H] wouldn't explain the trend with $T_{\rm eff}$.

The Na abundance can be greatly overestimated in LTE calculations. NLTE corrections are always negative and the magnitude of these corrections increases with decreasing metallicity. NLTE Na corrections also increase with increasing $T_{\rm eff}$, until a maximum $T_{\rm eff}$ is reached, then the corrections decrease again. However, the NLTE sensitivity is most prominent for the Na I D lines, which I do not use for abundance determinations as they are too strong. The doublet at 6154 Å is much less sensitive to NLTE corrections, and only needs small NLTE corrections of between -0.05 and -0.10 dex over a wide range of stellar parameters, and this doublet yields good abundances for stars with solar-like metallicity (Mashonkina, Shimanskiĭ & Sakhibullin 2000; Shi, Gehren & Zhao 2004; Asplund 2005; Lind et al. 2011). No NLTE corrections are given for the 4751 and 5148 Å lines, but it is assumed that they behave similarly to the 6154 Å doublet so I ruled out NLTE effects as the cause of the abundance discrepancy.

The [Na/Fe] will increase with [Fe/H] in late-type thin disc stars. Therefore metal-rich thin disc stars would be expected to have higher Na, regardless of $T_{\rm eff}$ (Feltzing & Gustafsson 1998; Thorén & Feltzing 2000; Lind et al. 2011). As thin disc stars are expected to be younger than ∼9 Gyr (Shi, Gehren & Zhao 2004), I checked that all the cooler stars were of the correct age to be classified as thin disc stars. I also plotted my data alongside that from Shi, Gehren & Zhao (2004), depicted in Figure 3.5, which

shows that my data exhibits this trend and is thus unlikely to be composed of thick disc stars, which are confined to the left hand side of the plot. However the stars with the highest overall metallicity, and thus most rich in sodium, don't show a trend with $T_{\rm eff}$, so different populations of stars in the Galaxy can't be used to explain the trend in [Na/Fe] with $T_{\rm eff}$.

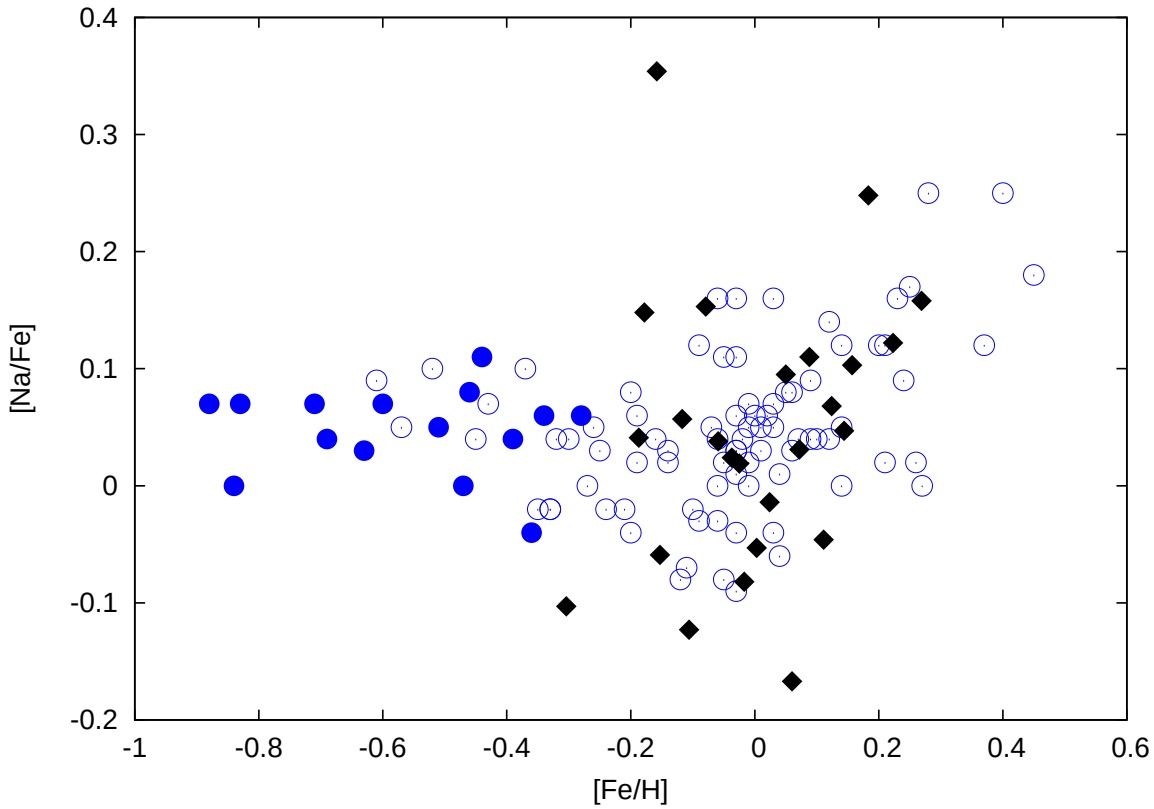

Figure 3.5: The filled and empty blue circles represent the thick disc and thin disc stars data of Shi, Gehren & Zhao (2004) respectively, and the black diamonds are the values from this work. There is no trend observed for the thick disc stars. The thin disc stars exhibit a trend with [Na/Fe] and [Fe/H], which is seen in both data sets.

Incorrect values for VDW broadening can yield large dispersions in Na abundances, as Na is highly sensitive to this broadening factor. Mashonkina, Shimanskiĭ & Sakhibullin (2000) calculated corrections to the Unsöld values, however no values are present for the Na lines used in my analysis. I attempted to calculate these corrections using the CROSS programme for ABO theory (Barklem, Anstee & O'Mara 1998), however this was impossible as the principal quantum number is too high in all lines to result in a reliable broadening value (Barklem & Aspelund-Johansson 2005). Thus, there could still be significant errors in the abundance of sodium at lower temperatures and this could contribute to the high [Na/Fe] values.

Adibekyan et al. (2012a; 2012b) also observed a trend of [Na/Fe] with $T_{\rm eff}$ for low $T_{\rm eff}$ stars in a sample of 1111 FGK stars. They suggest that this trend could be due to the fact that Na is sensitive to $T_{\rm eff}$ at low temperatures, that increased blends at low temperature cause inaccurate abundances, and that there could be deviations from excitation and ionisation balances.

The increased blending at lower temperatures is indeed a likely cause of the trend. The Na I 4751 Å line is a resolved blend in most stars, but for cooler stars it also becomes blended with Zr I, which can make it difficult to measure. The Na I 5148 Å is also in a resolved blend with Ni I, which becomes more difficult to synthesise at lower temperatures. Thus a combination of increased blending and uncertainties in VDW broadening make the Na abundance, and thus the $\log g$, unreliable for stars below 5000 K.

3.6.1.2 Ca lines

There are more Ca lines available compared to Na which can be used to determine abundance, which led to the Ca I line at 6439 Å also being used as a gravity diagnostic. However this line is not as useful in hotter stars, as the sensitivity to changes in $\log g$ is reduced. Bruntt et al. (2010b) also recommend the use of the Ca I 6122 and Ca I 6162 Å lines, however it was found on a number of occasions that these lines gave a $\log g$ value that was inconsistent with the other pressure-broadened lines and the ionisation balance. Therefore these two Ca lines were not included in the overall $\log g$ estimation.

3.6.1.3 The Mg I b triplet

Fuhrmann et al. (1997) advocate that the $\log g$ from the pressure broadened lines, in particular the Mg I b triplet, should be used over the ionisation balance $\log g$. Their reason for this is that they find the ionisation balance much lower (3.58) for Procyon compared to the fundamental value of 4.05 ± 0.06 known from its binary nature. They find the ionisation balance $\log g$ consistently lower than the Mg I b value, with the discrepancy increasing towards hotter stars. However, in my own analysis of Procyon, not only do I find the ionisation balance to give an appropriate $\log g$, but I cannot recreate their results with the lower $\log g$. It is possible that part of the problem lies in the fact that Fuhrmann et al. (1997) created a line list with $\log gf$ adjusted to the Sun (see Section 4.1.3 for more on this). It is also possible that there are not enough Fe II

lines in their list and thus the ionisation balance $\log g$ is artificially low. However, this is difficult to verify without knowing what lines they used.

That said, Fuhrmann et al. (1997) also make the valid point that the $\log g$ derived from the Mg I b lines is relatively insensitive to changes in $T_{\rm eff}$, which makes it a preferable method of determining $\log g$ considering the degeneracies in $T_{\rm eff}$, $\log g$ and $v_{\rm mic}$ when determining parameters with the Fe lines.

I initially didn't use the Mg b triplet for $\log g$ determinations as the 5164 Å line is badly blended and the synthetic lines for 5172 and 5183 Å were much stronger than the observed spectrum using the known $\log g$ in the Sun. This meant that when these lines were fit to the spectrum, the $\log g$ was too low. However, when these lines are updated with the Van der Waals values from ABO theory, as well as recent laboratory $\log gf$ values (Aldenius et al. 2007), the fit is vastly improved. As with sodium, the abundance of magnesium should be calculated from weak lines prior to obtaining the $\log g$ from the triplet.

Herein lies another problem, as not only are Mg lines scarce, but the atomic data is also dubious. After modifying my line list to include the best Mg lines and updating the atomic data, I still found that [Mg/Fe] is consistently high in stars of all $T_{\rm eff}$. I ruled out NLTE effects as the cause, as the deviations are small for Mg in dwarfs of solar metallicity (Zhao, Butler & Gehren 1998) and would not explain the discrepancy. As Mg is quite sensitive to VDW broadening, I thought that updating these values might result in better abundances. However, as with Na, it was not possible to get ABO values for all of the lines used. Fuhrmann et al. (1997) used VDW values that had been adjusted to the solar value. Mashonkina (2013) applied corrections to the VDW for two Mg lines to obtain consistent abundances for all the Mg lines used, however these are not lines that I used as they were unsuitable.

[Mg/Fe] can be used as a tracer for Galactic evolution and Mg can be genuinely higher than the Fe abundance in some stars, particularly in those of low overall metallicity, however it is unlikely that there will be a substantial overabundance of Mg compared to Fe in thin disc stars of solar metallicity (Fuhrmann 1998; Arnone et al. 2005). Beirão et al. (2005) found that [Mg/Fe] is slightly above solar for high metallicity stars, however this is still lower than my values. I found that the high Mg abundance has the effect of lowering the $\log g$ to unrealistic values, such as 4.25 in the Sun, and these $\log g$ values also disagree with those determined from the ionisation balance, Na and Ca lines. As such, I chose not to use Mg as a $\log g$ diagnostic, however it could probably

be used by assuming that the Mg abundance scaled with Fe.

Table 3.8 lists the individual $\log g$ values determined from each Na, Ca, and Mg line.

3.6.1.4 Spectroscopic $\log g$ for cool stars

Not only is the $\log g$ from the Na I D lines unreliable for cool stars, but the ionisation balance is also dubious as the number of Fe II lines is vastly depleted at these temperatures. As seen in Section 3.6.1, the $\log g$ can be overestimated when there aren't enough Fe II lines. In addition, discrepancies in $\log g$ exist as the Fe II abundance can be vastly different from the Fe I abundance. For temperatures above 5500 K, the abundances of Fe I and Fe II are consistent with each other, however for cooler stars the Fe II abundance has a tendency to creep upwards. In the Hyades cluster, Allende Prieto et al. (2004) found that this results in the Fe II abundance being higher by an order of magnitude for metal-rich stars with a $T_{\rm eff}$ of around 4000 K. For the abundances to agree, the $T_{\rm eff}$ needs to be increased by ∼350 K or the $\log g$ needs to be lowered from ∼4.6 to ∼3.8. However modifying the parameters by such a large amount is outside the expected errors and does not agree with parameters determined via other methods. NLTE effects could explain the discrepancy in Fe, as for cooler stars it is expected that the Fe II lines are prone to NLTE alterations and can differ by up to 0.6 dex.

Therefore, spectroscopic $\log g$ values should not be trusted at all for stars below 5000 K, and alternate methods of determining $\log g$ should be sought. For example, Woolf & Wallerstein (2005) determined the $\log g$ of their sample of K and M dwarfs via a calculation, rather than directly from the mid resolution (∼33,000) spectra. The masses were obtained from the mass-luminosity diagram using H and $K_{\rm S}$ magnitudes determined from parallax distances. The bolometric magnitude ($M_{\rm bol}$) was found from the parallax, the $K_{\rm S}$ magnitude and the bolometric correction $BC_{\rm K}$. The $\log g$ was then determined from $M_{\rm bol}$, mass and $T_{\rm eff}$ via $\log g = \log M + 4 \log(T_{\rm eff}/5770) + 0.4$ ($M_{\rm bol}$ - 4.65) + 4.44. Bean et al. (2006) used a similar approach for M dwarfs using a $\log g$ and stellar mass calibration. The masses of several M dwarfs were determined from binaries and from the $M_{\rm K}$ and mass relationship of Delfosse et al. (2000) for single stars. The $M_{\rm K}$ magnitude was obtained from K magnitudes and parallaxes from 2MASS and *Hipparcos* respectively. Unfortunately, there are no parallaxes available for the sample of WASP stars studied here, so these methods cannot be employed to determine $\log g$, however future *Gaia* measurements could resolve this issue.

Table 3.8: $\log g$ for individual pressure broadened lines.

Star	Na 5889	Na 5893	Ca 6122	Ca 6162	Ca 6439	Mg 5167	Mg 5172	Mg 5183
WASP-2	4.45 ± 0.10	4.48 ± 0.09	>5	4.75 ± 0.10	4.45 ± 0.12	4.55 ± 0.05	4.45 ± 0.05	4.35 ± 0.05
WASP-4	4.37 ± 0.05	4.41 ± 0.04	>5	4.70 ± 0.18	4.65 ± 0.17	4.40 ± 0.10	4.20 ± 0.10	4.20 ± 0.05
WASP-5	4.25 ± 0.02	4.23 ± 0.02	∼5	4.44 ± 0.16	4.28 ± 0.10	4.05 ± 0.14	3.90 ± 0.14	3.90 ± 0.14
WASP-6	4.63 ± 0.04	4.69 ± 0.04	>5	4.83 ± 0.15	4.63 ± 0.13	4.60 ± 0.03	4.40 ± 0.03	4.30 ± 0.03
WASP-7	4.21 ± 0.04	4.33 ± 0.08	>5	4.35 ± 0.02	4.30 ± 0.02	4.25 ± 0.05	4.05 ± 0.05	4.05 ± 0.05
WASP-8	4.20 ± 0.10	4.20 ± 0.10	>5	4.50 ± 0.15	4.40 ± 0.05	4.10 ± 0.10	3.70 ± 0.10	3.80 ± 0.10
WASP-15	4.40 ± 0.12	4.43 ± 0.08	>5	4.50 ± 0.07	4.40 ± 0.14	4.35 ± 0.05	4.10 ± 0.13	4.10 ± 0.13
WASP-16	4.15 ± 0.07	4.15 ± 0.07	4.75 ± 0.25	4.37 ± 0.19	4.20 ± 0.17	4.05 ± 0.15	3.95 ± 0.20	3.95 ± 0.20
WASP-17	4.15 ± 0.07	4.15 ± 0.10	>5	4.40 ± 0.35	4.50 ± 0.50	4.40 ± 0.15	4.05 ± 0.20	4.10 ± 0.20
WASP-18	4.28 ± 0.07	4.32 ± 0.07	>5	4.45 ± 0.12	4.40 ± 0.12	4.50 ± 0.10	4.20 ± 0.10	4.20 ± 0.10
WASP-19	4.25 ± 0.05	4.25 ± 0.08	>5	4.45 ± 0.30	4.35 ± 0.25	4.10 ± 0.12	3.85 ± 0.10	3.85 ± 0.10

3.6.2 Determination of $T_{\rm eff}$

The temperatures from the HARPS spectra are compared with the IRFM values in Figure 3.6. The solid line is a linear regression to the data, m = 1.10 ± 0.06 and c = -579.66 ± 325.89. The rms difference between the two methods is 113 K, which is reasonable given the $T_{\rm eff}$ errors. If both measures of $T_{\rm eff}$ were in perfect agreement, r^2 would be 1 and here it has a value of 0.97, indicating that there is a strong linear relationship between the two methods of determining $T_{\rm eff}$.

It is possible that the spectroscopic temperatures are higher than the IRFM values for the hotter stars due to NLTE effects, particularly for WASP-17. Using the method outlined in Section 3.5, I found that the $T_{\rm eff}$ of WASP-17 derived from the excitation balance was now reduced from 6700 ± 105 to 6630 ± 100 K. In the case of WASP-17, the strong interstellar reddening present could affect the IRFM $T_{\rm eff}$.

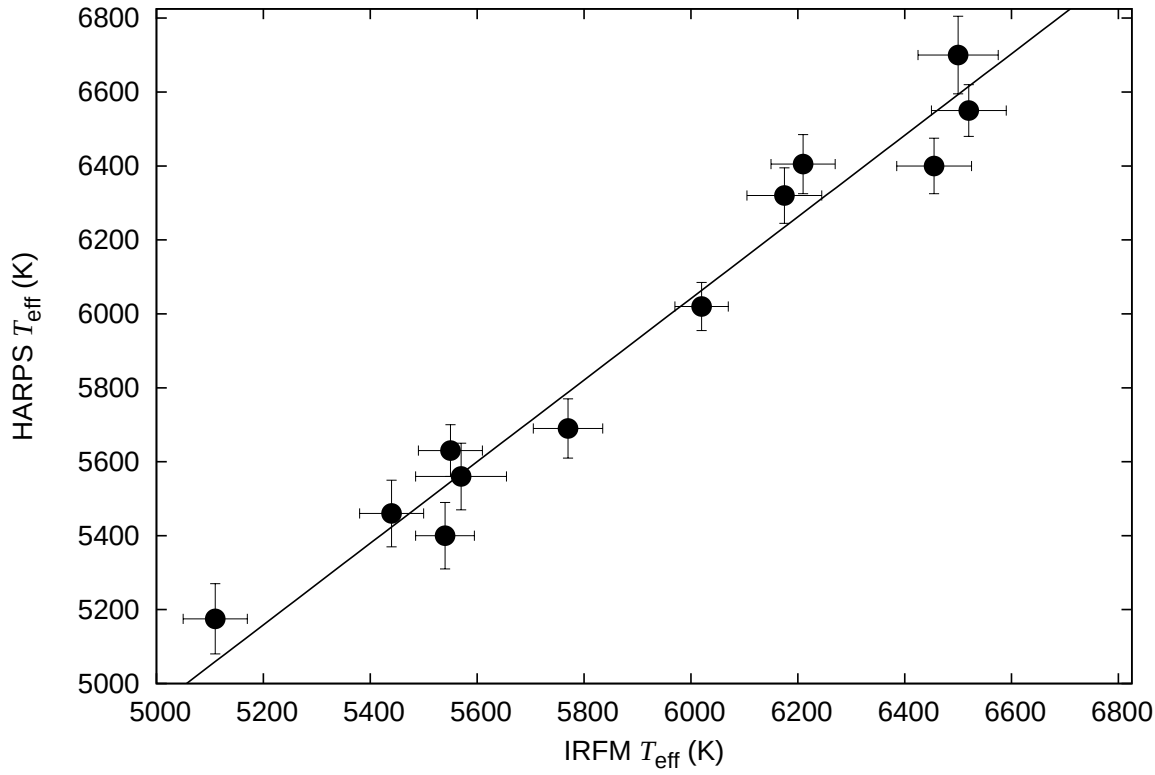

Figure 3.6: Comparison of $T_{\rm eff}$ from the HARPS spectra with the IRFM. The solid line depicts the linear regression.

3.6.3 Microturbulence

Obtaining the appropriate $v_{\rm mic}$ value depends strongly on knowing the correct value of $T_{\rm eff}$ and $\log g$. If one of these two parameters is incorrect then the $v_{\rm mic}$ will be skewed. For instance, a change in $T_{\rm eff}$ or $\log g$ by 100 K or 0.1 dex respectively will result in a change in $v_{\rm mic}$ of around 0.1 $\rm km\,s^{-1}$. In addition, the scatter in abundances makes it difficult to get a precision in $v_{\rm mic}$ any better than 0.08 $\rm km\,s^{-1}$.

I also considered using Blackwell diagrams to determine the $v_{\rm mic}$. However, there can be ambiguity as to the position of the intersection of the lines, as seen in Figure 3.7 for WASP-15 using the Fe I lines from Gray & Griffin (2007). As the Blackwell diagrams are also dependent on an input $T_{\rm eff}$, I found no advantage to using this method.

I found that the $v_{\rm mic}$ increases with $T_{\rm eff}$, in agreement with Bruntt et al. (2010a), Landstreet et al. (2009), and Smalley (2004). Valenti & Fischer (2005) suggested that $v_{\rm mic}$ should be fixed to the solar value of 0.85 $\rm km\,s^{-1}$ based on the fact that they found a correlation between [M/H] and $v_{\rm mic}$ when they let $v_{\rm mic}$ vary. They also found no significant dependence between $v_{\rm mic}$ and $T_{\rm eff}$. However, while fixing $v_{\rm mic}$ is valid for stars of similar $T_{\rm eff}$ to the Sun, it is not appropriate for hotter stars. The resulting $v_{\rm mic}$ is plotted against $T_{\rm eff}$ in Figure 3.9 and the second order polynomial fit is given in Equation 3.1:

$$v_{\rm mic} = 0.89 + 4.16 \times 10^{-4}(T_{\rm eff} - 5777) + 9.25 \times 10^{-8}(T_{\rm eff} - 5777)^2 \ \rm km\,s^{-1}. \quad (3.1)$$

An error of 0.18 $\rm km\,s^{-1}$ is determined by adding in quadrature the rms scatter of the fit (0.13 $\rm km\,s^{-1}$) and the average $v_{\rm mic}$ error (0.13 $\rm km\,s^{-1}$). As others (e.g. Edvardsson et al. 1993; Reddy et al. 2003; Bruntt et al. 2012; Tsantaki et al. 2013) have determined the relationship of $v_{\rm mic}$ with both $T_{\rm eff}$ and $\log g$, I also plotted the $\log g$ dependence in Figure 3.9. Unlike for $v_{\rm mac}$ in Figure 5.12, there is no indication of a $\log g$ dependence. However, the calibrations in the literature that include $\log g$ usually do so for a sample of stars that includes both dwarfs and more evolved stars, so it is possible that the $\log g$ dependence just isn't obvious among the dwarf stars.

The Bruntt et al. (2010a) calibration is also shown in Figure 3.9, and clearly returns higher $v_{\rm mic}$ values, particularly for the hotter stars. In fact, this is also true of the calibrations of Edvardsson et al. (1993), Reddy et al. (2003), Gómez Maqueo Chew et al. (2013) and Tsantaki et al. (2013). The reason for this is not clear, however it is possible that my use of the Magain method can partially explain the higher $v_{\rm mic}$ values

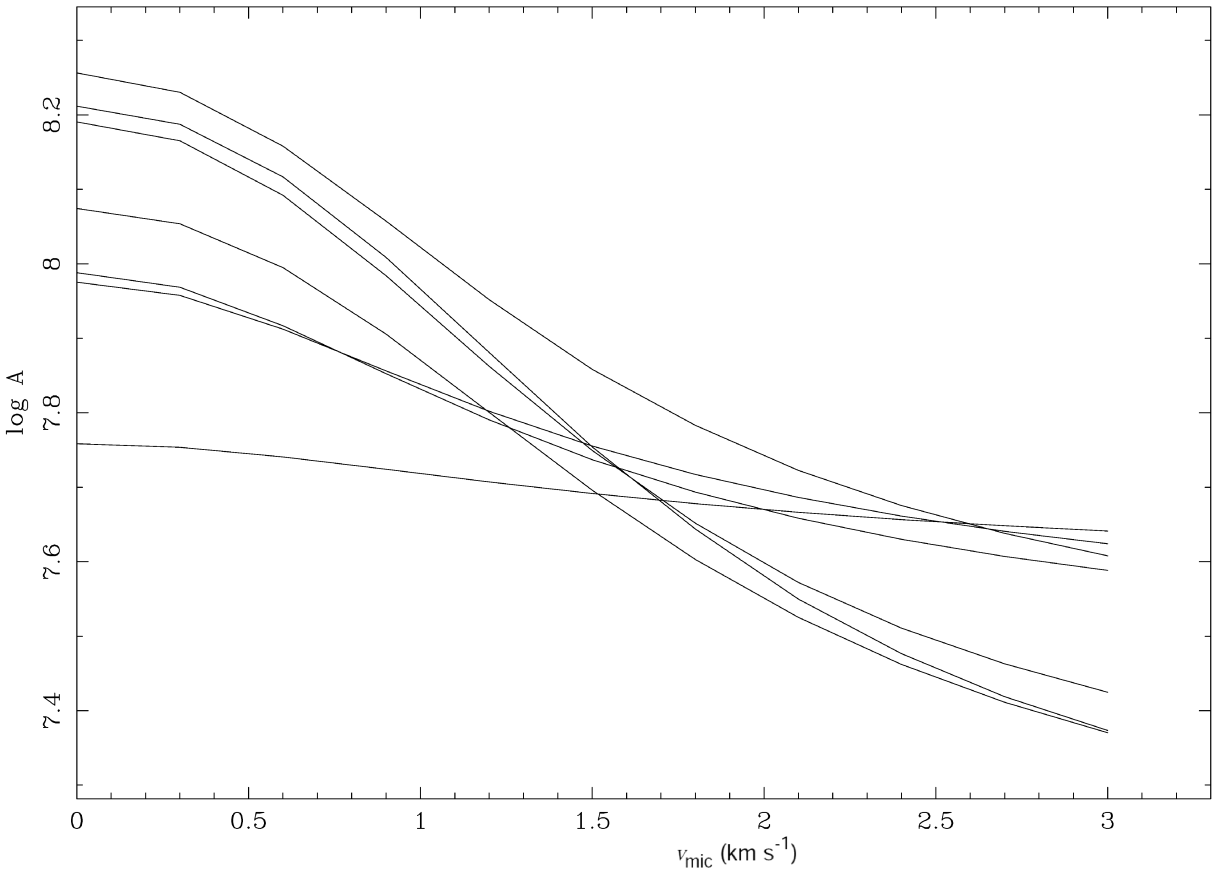

Figure 3.7: Blackwell diagram for WASP-15 using the selection of Fe I lines from Gray & Griffin (2007). Ideally, the lines should all intersect at one point which reveals the optimum $v_{\rm mic}$, but it is unclear from the diagram what the $v_{\rm mic}$ should be.

of other works. As expected, the use of the calculated EWs of the Magain method will result in lower $v_{\rm mic}$ values, as can be seen in Figure 3.8.

It is possible that the difference in line lists could contribute to the differences in $v_{\rm mic}$ determined, in both the number of lines used and the specific lines selected. In order to see how the number of lines used might affect the $v_{\rm mic}$, I chose a hot star with the most measured Fe lines (WASP-15; see Table 3.7) and randomly deleted lines until there were only 40 remaining. This did not result in a change in the $v_{\rm mic}$. The cutoff imposed for strong lines could also be a factor in the $v_{\rm mic}$ obtained, as additional broadening in the form of damping parameters will also be dominant in strong lines. I did not use lines stronger than ∼110 mÅ, although other authors use different limits. For example, Mucciarelli (2011) do not use lines stronger than 78 mÅ at 5500 Å. I found that deleting lines stronger than this in WASP-15 only serves to reduce the $v_{\rm mic}$ by 0.05 km s^{-1}.

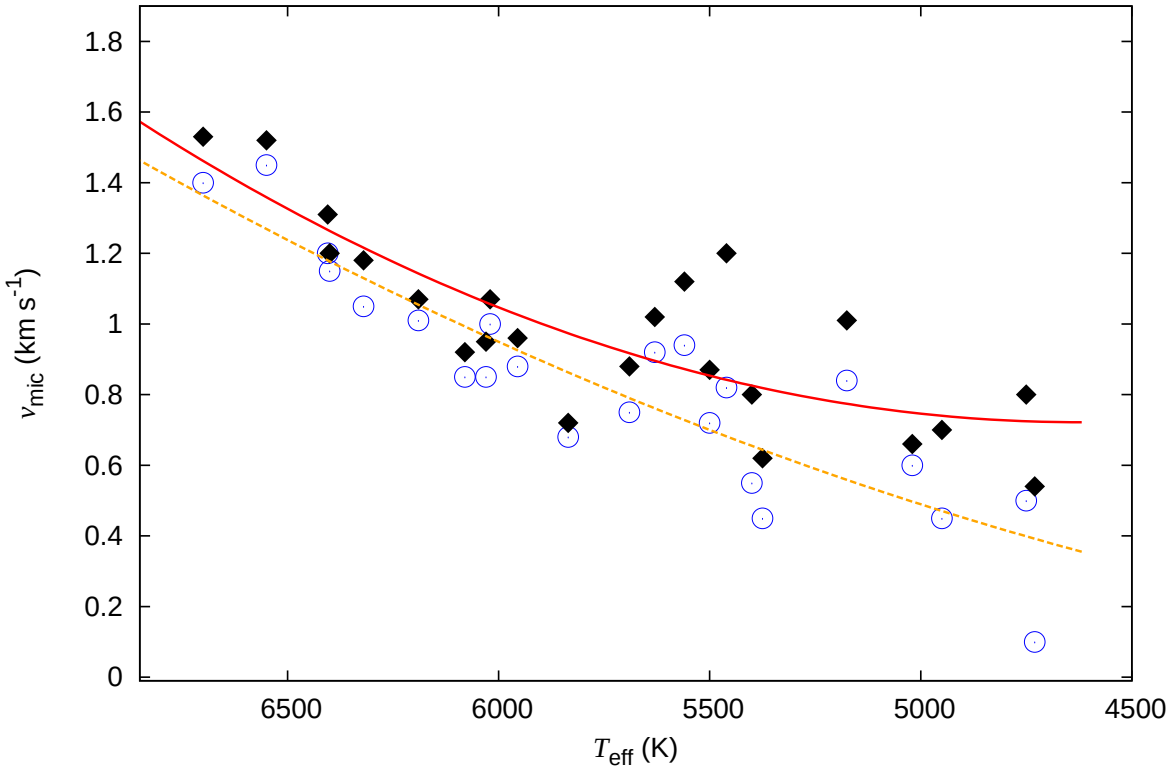

Figure 3.8: The $v_{\rm mic}$ calculated for the HARPS spectra via the Magain method is given by the blue circles, and the standard method is given by the black diamonds. The dashed and solid curves are fits to the respective data. The errors are the same as for Figure 3.9.

3.6.4 Fitting lines

The synthetic line based on the measured EW will not be as broad as the observed line, because damping parameters are a major factor for strong lines and strong lines begin to deviate from a Gaussian profile and develop Lorentzian wings. For example, Figure 3.10 shows the difference between the EW and fitting methods for the HARPS solar spectrum. The underestimation of the EW method for strong lines is obvious from the residuals between the fitting and EW values. For lines stronger than 0.08 Å, measuring the EW will underestimate the value of the line by up to 0.02 Å. As such, many authors choose to exclude strong lines from their analyses, although Mucciarelli (2011) advises that these lines can still be used for an abundance analysis, just not in microturbulence calculations.

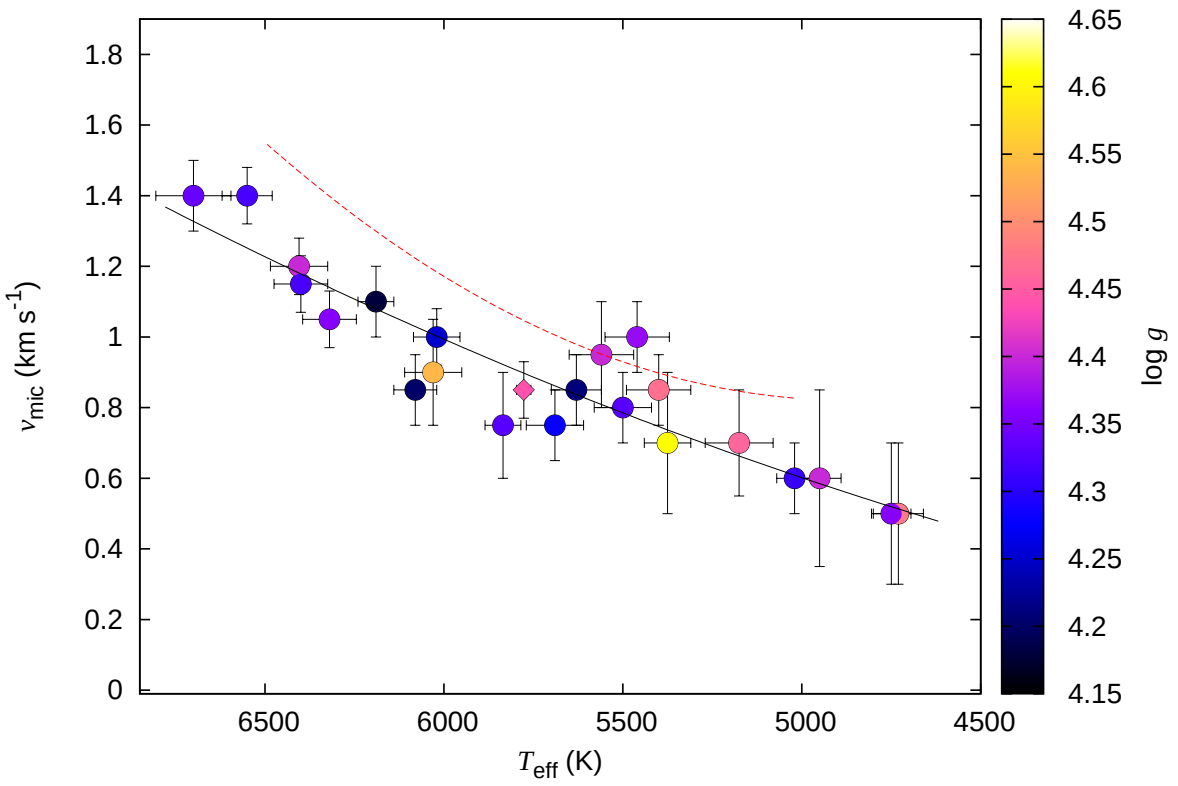

Figure 3.9: Microturbulence is seen to increase with $T_{\rm eff}$. The circles are the HARPS spectra and the diamond is the Sun. The solid black line is the fit to the points, and the red dashed line is the calibration from Bruntt et al. (2010a). There is no obvious dependence on $\log g$ among the dwarfs.

3.6.5 Continuum placement

Determining the points at which the wings of a line reach the continuum can be difficult and often results in an underestimate of the EW and thus the abundance.

I found that in spectra with low S/N (such as the CORALIE spectra), the noise makes the continuum placement difficult. In addition, the wings of the lines become lost in the noise, leading to an underestimation of the line strength. An example is shown in Figure 3.11 for a line in the CORALIE WASP-16 spectrum (S/N of 70), as well as for the same line in the HARPS spectrum which has S/N of 175.

A high S/N spectrum doesn't necessarily eliminate all problems associated with determining where the line wings meet the continuum. Extremely weak lines that are ordinarily lost in the noise at the continuum become evident, but these are often unidentified lines which makes them difficult to synthesise, as is shown in Figure 3.12 for the Kitt Peak Solar Atlas.

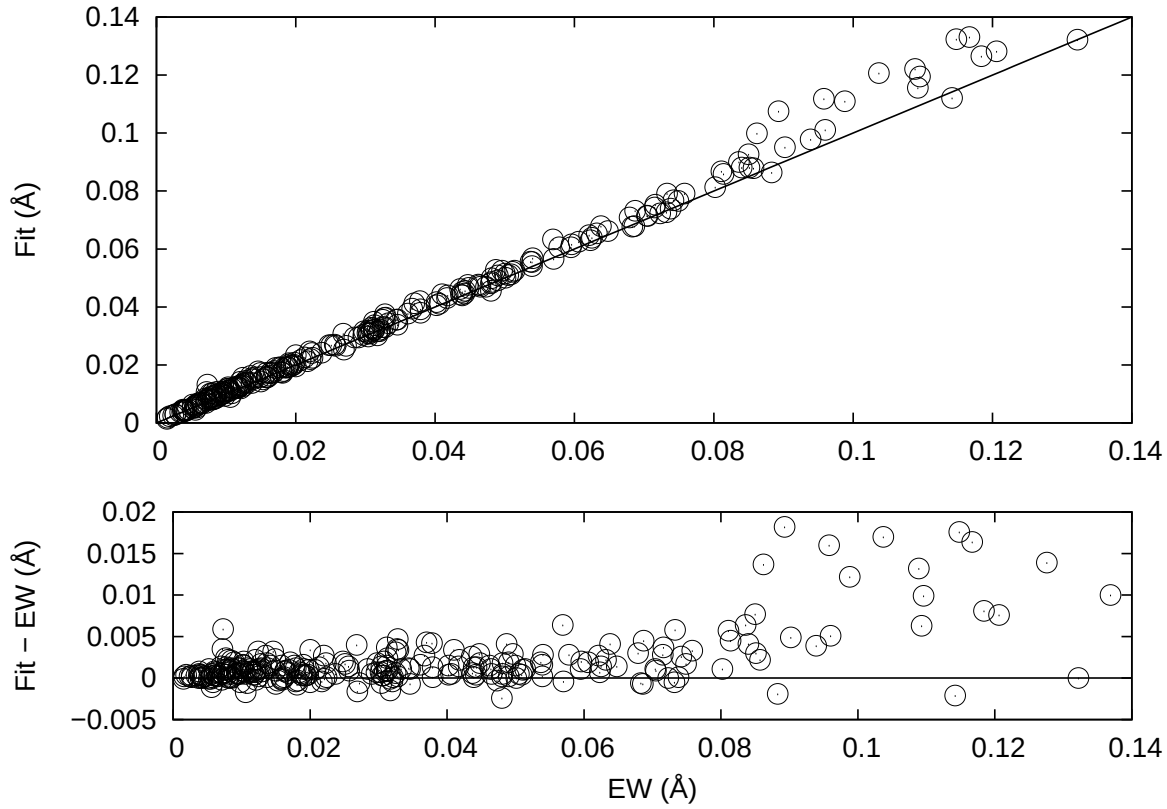

Figure 3.10: EW measurements compared with fitting for the HARPS solar spectrum. The solid line in the top panel is a 1:1 relationship. The residuals show that the fitting method can produce an EW error of up to 0.02 Å compared to just measuring the EWs for lines stronger than 0.08 Å.

3.6.6 Spectral comparison

Spectral comparison can be useful when there are some uncertainties in the parameters. While this method does not yield actual values for the parameters, it is useful to compare the spectra of stars to ascertain which set of parameters are the most likely. My initial analysis of the HARPS spectrum of WASP-23 yielded the parameters from the Fe lines of $T_{\rm eff} = 4975 \pm 50$ K and ionisation balance $\log g = 4.20 \pm 0.10$ dex. While this solution looked perfectly viable at first based purely on the spectroscopic analysis, the stellar radius derived from the $\log g$ is 1.24 $R_\odot$, which would make this a slightly evolved star. This is inconsistent with the radii derived from the discovery paper spectral analysis and from the statistical analysis, which are 0.97 $R_\odot$ and 0.77 $R_\odot$ respectively (Triaud et al. 2011). After a further inspection, and removal of three Fe lines, I found that the parameters of $T_{\rm eff} = 5020 \pm 50$ K and $\log g = 4.35 \pm 0.08$ dex also appeared to be a reasonable solution from the Fe lines, and a higher $\log g$ would be more consistent with previous results. While the latter appears to be the better solution, I decided to try

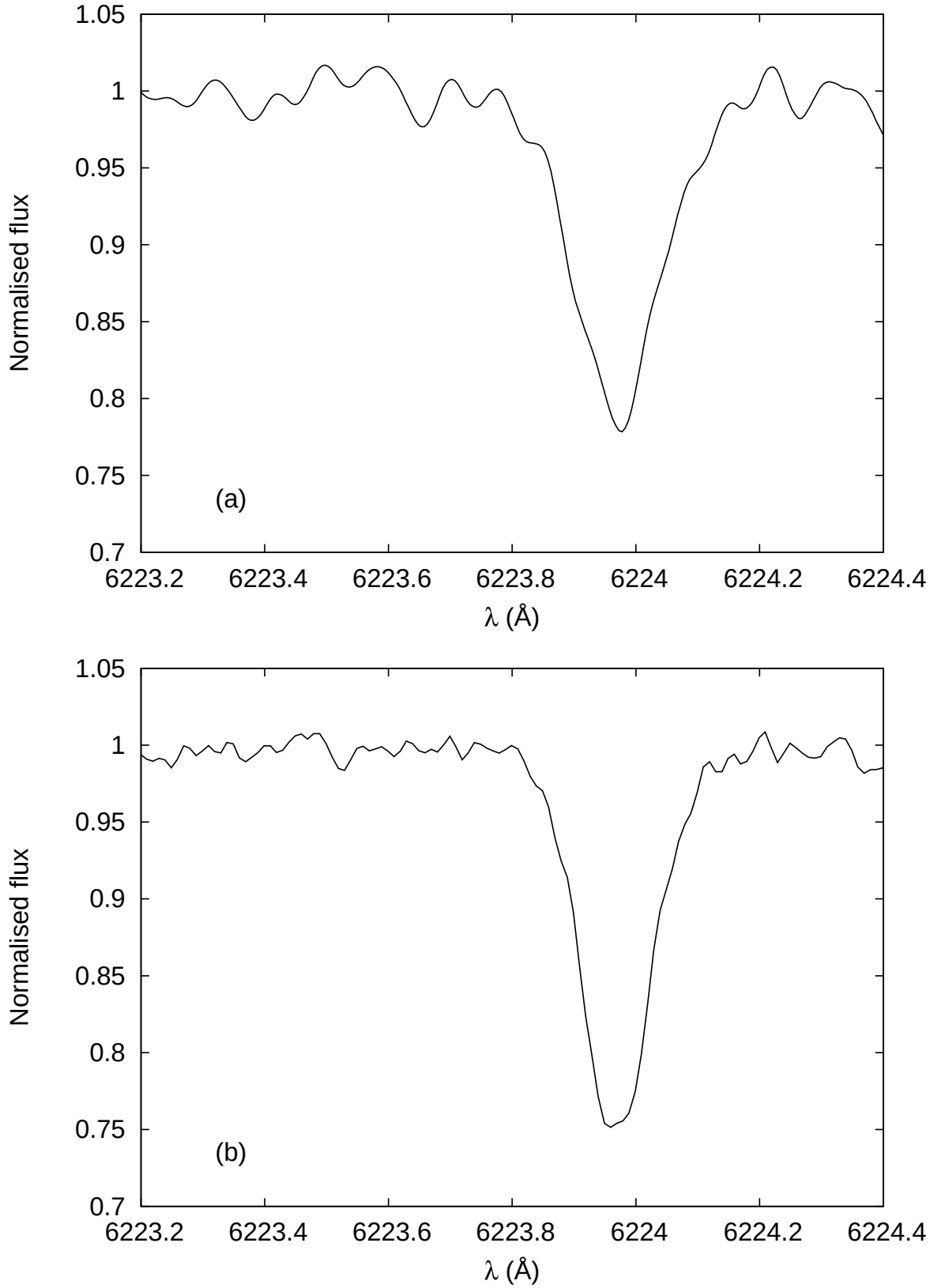

Figure 3.11: A Ni I line in a CORALIE spectrum of WASP-16 with S/N of 70 is shown in the top panel. The noise in the continuum makes it difficult to normalise the spectrum, as well as creating problems with fitting the wings of the line. The same line is shown in the bottom panel with the HARPS spectrum (S/N 175) for comparison.

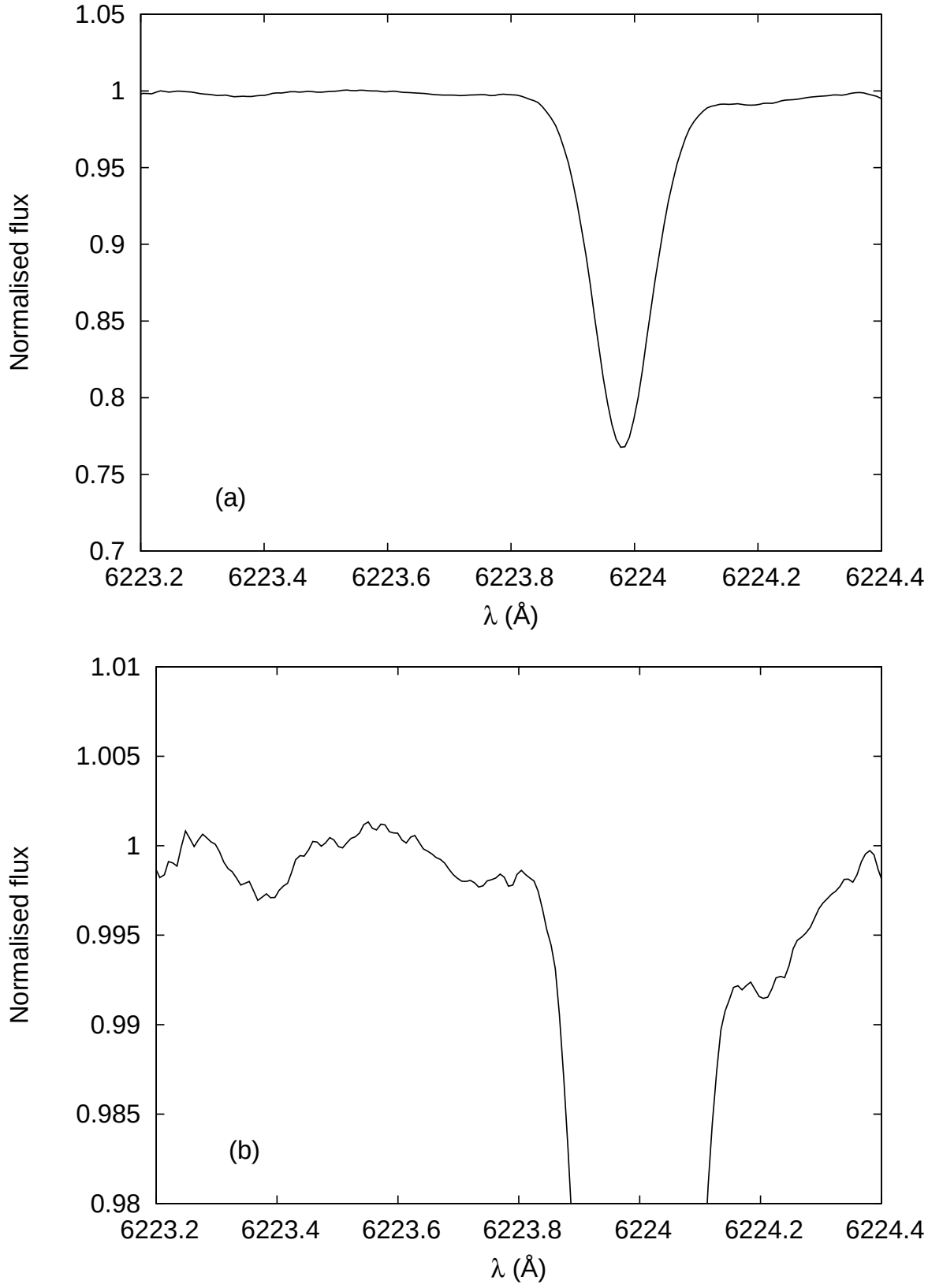

Figure 3.12: The top panel shows the same Ni I line as Fig. 3.11, but in the Kitt Peak Solar Atlas (S/N of 3000). The lower panel is a close up of the continuum showing that unidentified weak lines can cause normalisation issues even in high S/N spectra.

and verify this using spectral comparison.

Figure 3.13 shows several spectra in likely decreasing $T_{\rm eff}$ order; σ Dra (5282 K), WASP-23 (5020 K), WASP-53 (4950 K), WASP-29 (4730 K), and 61 Cyg A (4442 K). All additional spectra were obtained from the ELODIE archive at Observatoire de Haute-Provence (Moultaka et al. 2004). The spectra chosen were of similar $v \sin i$, as this can affect the spectral classification (Gray 1988). The spectral region shown in Figure 3.13 is sensitive to $T_{\rm eff}$ changes, with the Ca I 4226 Å line strengthening towards later spectral types. Of course the Ca abundance itself can affect the line strength, but for stars of similar metallicity it is the $T_{\rm eff}$ changes that dominate the variations in the line strength. The line ratios of Cr I 4275 / Fe I 4271 Å and Cr I 4254 / Fe I 4260 Å are also sensitive to temperature changes. As the Cr abundance generally scales with Fe, these ratios can be used for metal-poor and metal-rich stars. Line ratios between Fe and H are only suitable for solar metallicity stars (Gray & Corbally 2009). A visual inspection shows that WASP-23 is very similar to WASP-53, however when the line ratios are measured there is a clear difference that places the spectral type of WASP-23 between WASP-53 and σ Dra, which is consistent with the $T_{\rm eff}$ of WASP-23 being 5020 rather than 4975 K, and thus favours the second solution from the spectral analysis. It is quite difficult to measure the line ratios as all the lines are blended, and it is impossible to measure the EW of the line to the full extent of the wings due to the presence of many other strong lines. However, a consistent measurement towards the core of the line does result in a viable set of line ratios. These should be used with caution, but can provide an indication of spectral type.

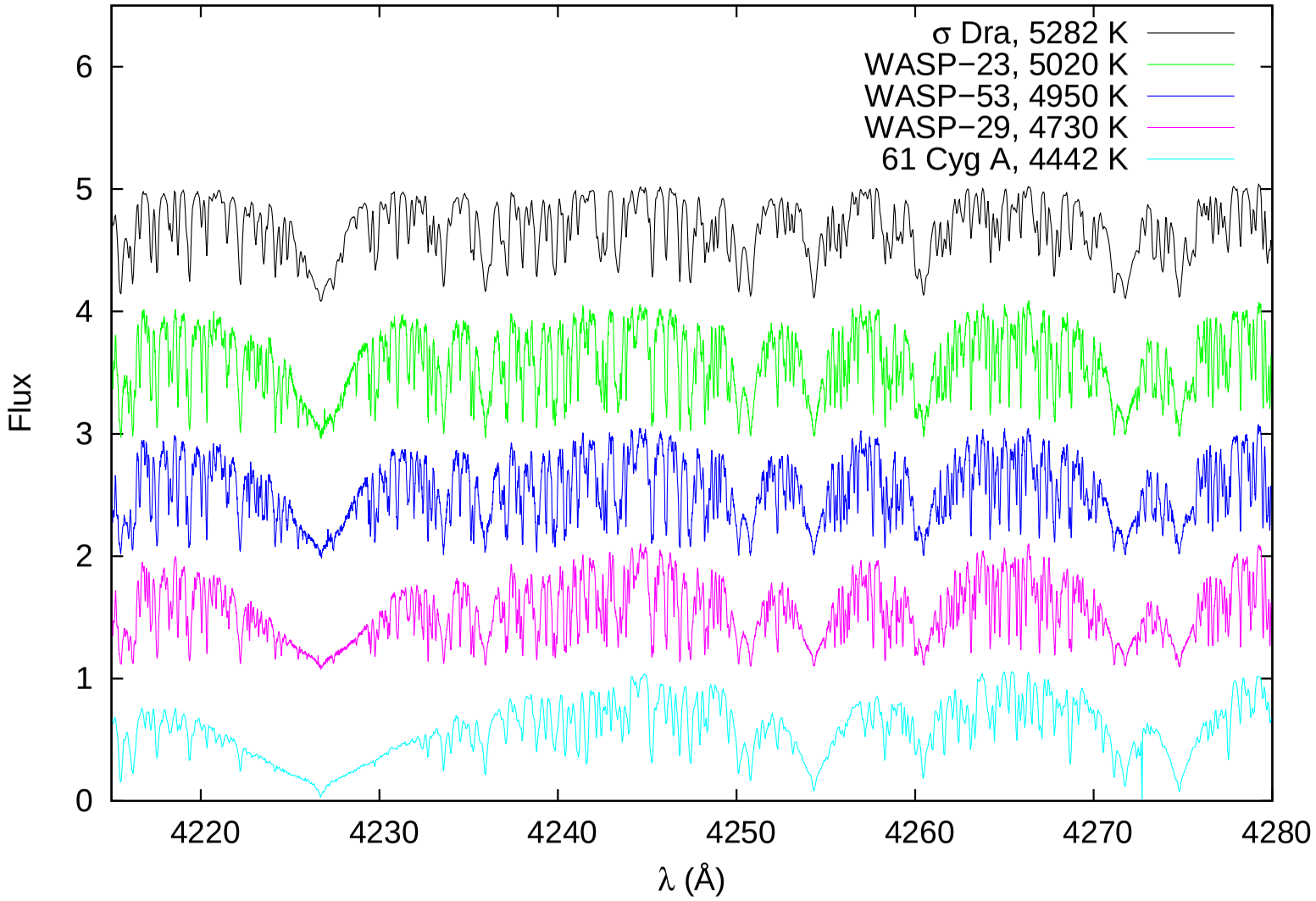

Figure 3.13: Spectral comparison for WASP-23

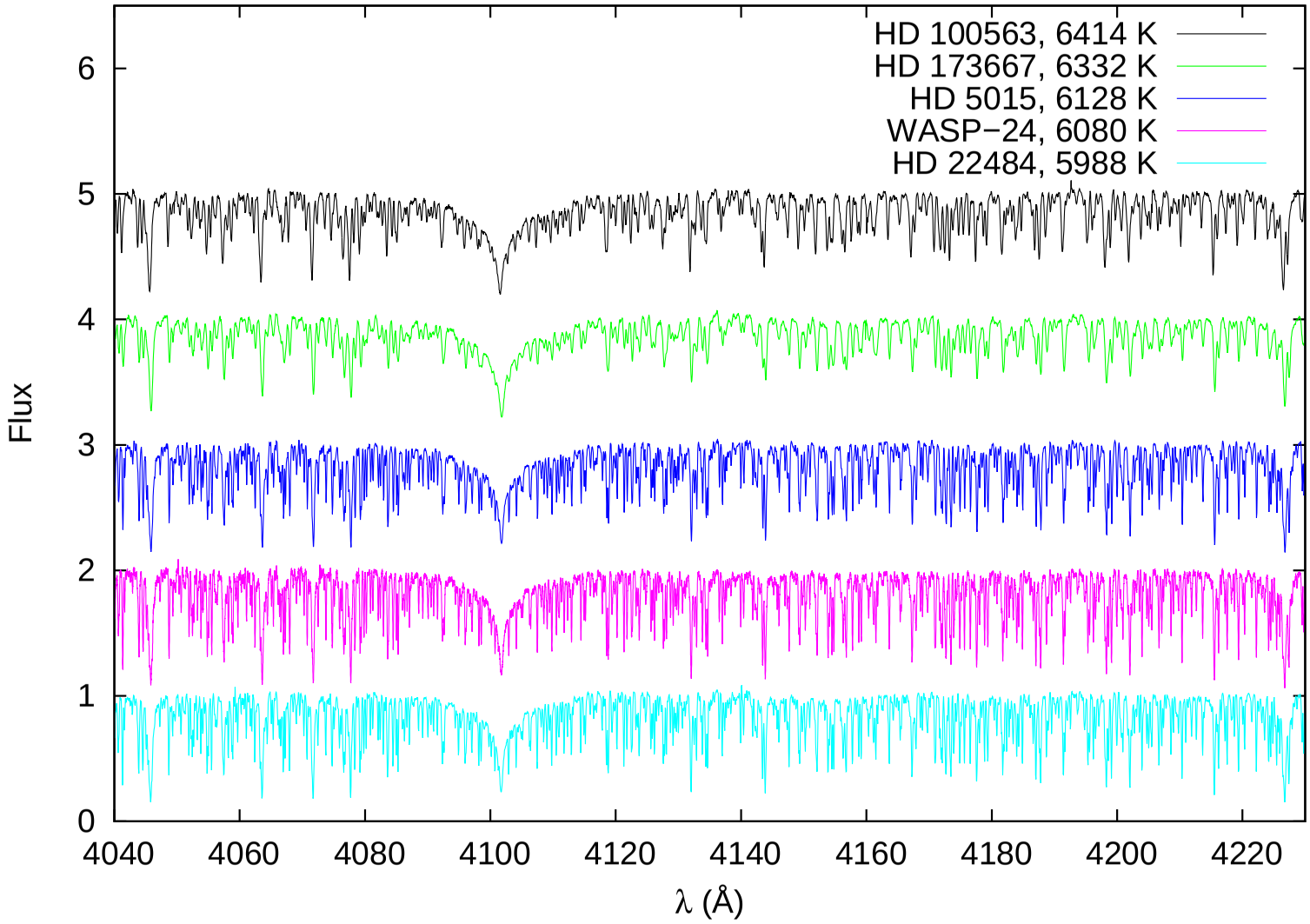

Figure 3.14: Spectral comparison for WASP-24

WASP-24 is a hotter star of $T_{\rm eff}$ = 6080 K, and as such different lines bear the temperature sensitivity. The spectral comparison of WASP-24 with the spectra of HD 22484 ($T_{\rm eff}$ 5988 K), HD 5015 ($T_{\rm eff}$ 6128 K), HD 173667 ($T_{\rm eff}$ 6332 K) and HD 100563 ($T_{\rm eff}$ 6414 K) is shown in Figure 3.14. The Ca I 4226 Å line is no longer useful as a standalone temperature indicator, however it can be used in a ratio with the Hδ line. The Fe I 4046 Å line can also be used with Hδ, however these ratios can only be used for solar metallicity stars. The Balmer lines can be used alone to decipher temperature as they grow towards increasing temperatures until mid-A type stars, however the comparison at this temperature range is not as clear cut as it was for WASP-23, because as mentioned in Section 2.1.3, the Balmer lines are difficult to normalise in echelle spectra and it is likely that there are continuum errors. As such, this should only be used as a guideline. The line ratios also indicate that HD 22484 is hotter than WASP-24, while a direct comparison of the Hδ lines between the two indicates otherwise. Other than this discrepancy, the line ratios agree with the general trend of temperature.

3.6.7 Constraining $\log g$ from planetary transits

Some WASP stars have $\log g$ values available that had been calculated from the stellar density, which are given in Table 3.6. For the values in common between Southworth and Mortier, there is good agreement for most stars, except for WASP-13 and WASP-16. This is most likely due to the fact that the transit $\log g$ requires isochrones to be computed, and is thus model dependent. Southworth used the mean of different values computed with five different models, and Mortier has used one model.

In Figure 3.15, I plot the Mortier transit $\log g$ values against my own spectroscopic $\log g$ values, including the HIRES analysis of WASP-13 (see Section 4.1 for more details). The linear regression gives m = 0.85 ± 0.31 and c = 0.68 ± 1.34. r^2 gives a value of 0.32, indicating that there isn't a relationship between these values. This is also obvious from the scatter of the values on the plot and the rms difference of 0.15 dex between the two methods. Therefore, there is no systematic difference between the spectroscopic and transit $\log g$ measurements and a comparison between the two doesn't show which is the best method.

As it is recommended by Torres et al. (2012) to redetermine the spectroscopic parameters with the $\log g$ fixed to the transit value, I re-derived the $T_{\rm eff}$ with priority given to the Southworth $\log g$. These values are given in Table 3.7. The comparison

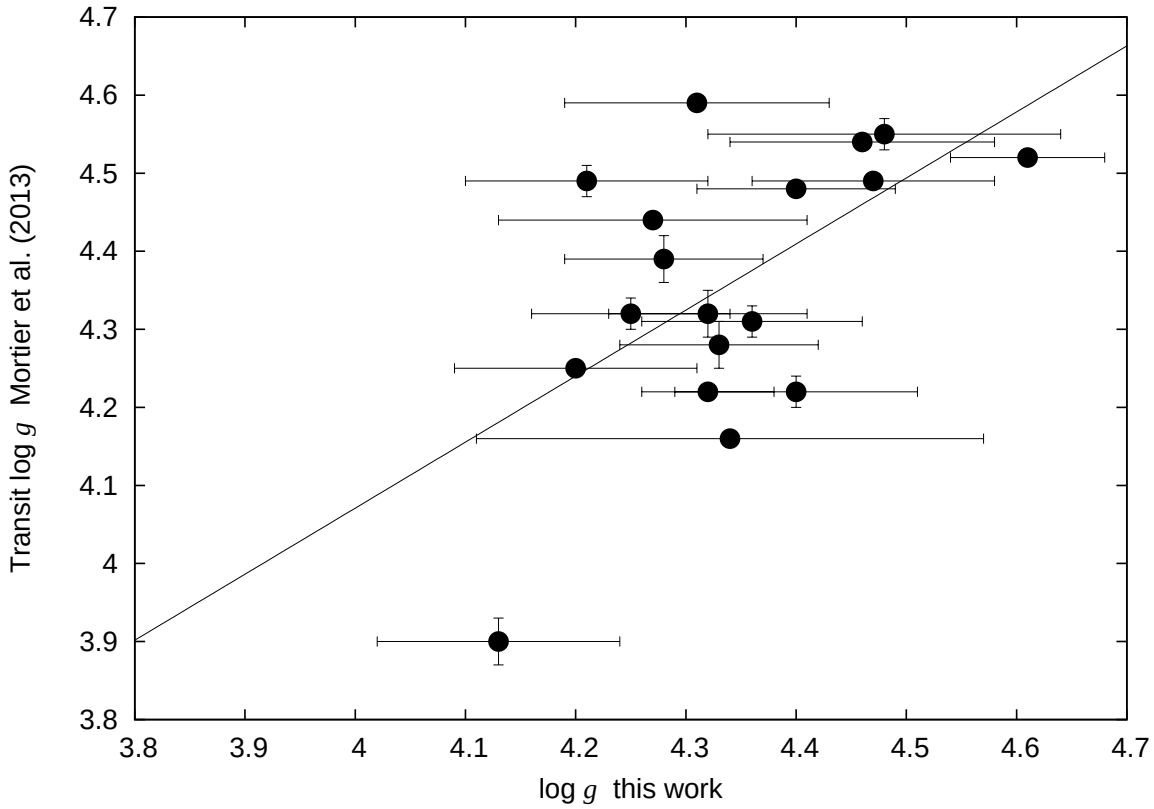

Figure 3.15: Comparison between the spectroscopic $\log g$ from this work and the transit $\log g$ from Mortier et al. (2013b). The solid line is the linear regression, and it is obvious that the spectroscopic and transit $\log g$ values don't compare well.

between constrained and unconstrained $T_{\rm eff}$ is shown in Figure 3.16. The solid line is the linear regression with m = 1.03 ± 0.03 and c = -204.61 ± 160.77. The rms difference is 62 K, which indicates that there is better agreement between the unconstrained and constrained $T_{\rm eff}$ values than there is between the unconstrained and IRFM values. r^2 is 0.99, which further indicates good agreement between the unconstrained and constrained values, and therefore that the constrained $T_{\rm eff}$ isn't any better than the unconstrained value.

For individual cases, the results still seem somewhat inconclusive. For example, the constrained $T_{\rm eff}$ is in disagreement with the IRFM $T_{\rm eff}$ for WASP-2, but in others the constrained $T_{\rm eff}$ seems to be better. The most striking example is that of WASP-15, where the unconstrained $T_{\rm eff}$ of 6405 ± 80 K is reduced to 6260 ± 80 K when the $\log g$ is fixed, in better agreement with the IRFM $T_{\rm eff}$ of 6210 ± 60 K.

As WASP-17 has a $T_{\rm eff}$ that is suspiciously high, it might be expected that constraining the $\log g$ would reduce the $T_{\rm eff}$, especially since the spectroscopic $\log g$ for this star is particularly unreliable. However, the $T_{\rm eff}$ is only reduced by 30 K, meaning that other factors are at work pushing the $T_{\rm eff}$ higher.

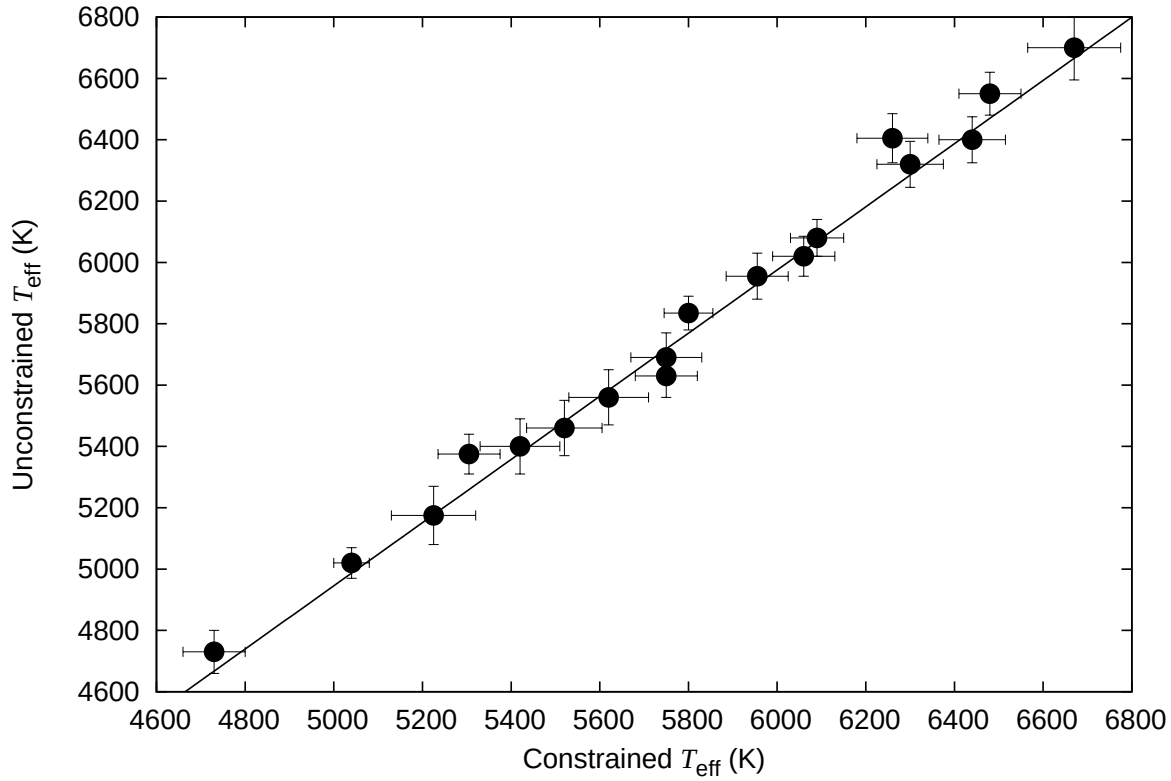

Figure 3.16: The unconstrained $T_{\rm eff}$ values are those determined with no prior for $\log g$. The constrained values are those that are determined when the $\log g$ is fixed to the transit value. The solid line is the linear regression.

3.6.8 Abundances

The abundances I determined are given in Table 3.9 for all elements that have three or more usable spectral lines. The abundances obtained from the HARPS solar spectrum are consistent with the Asplund et al. (2009) solar values, as seen in Figure 3.17. However, there is a discrepancy with Co, and the error on Mn is large compared to the other elements. This may be due to hyperfine splitting as discussed in Section 3.7. Overall, I found that the $\log A$(Fe) values derived from the HARPS spectra of the WASP stars were an average of 0.10 ± 0.05 dex higher than the previous analyses, and this can be seen in Figure 3.18. This is excluding WASP-2, WASP-4, and WASP-5, as there are large uncertainties in the initial values. Some of the initial analyses were also of HARPS spectra, which explains the data points which are in agreement. Higher abundances are to be expected from the high S/N HARPS spectra, as the line profile wings are less likely to be underestimated due to noise on the continuum.

There is evidence that the CORALIE spectrograph is prone to scattered light, which can weaken spectral lines and could also contribute to the underestimated abun-

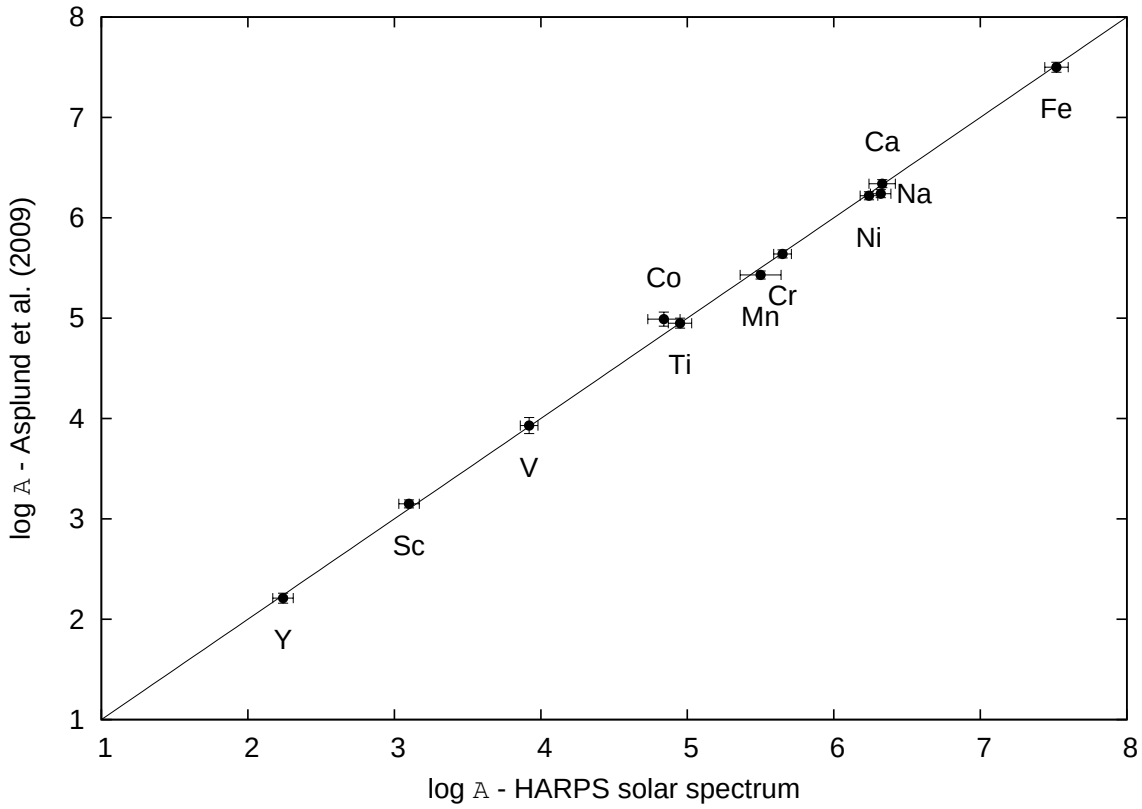

Figure 3.17: Comparison between Asplund et al. (2009) abundances and the HARPS solar spectrum analysis. There is a good agreement except for Co, which may be due to hyperfine splitting.

dances. This can be shown when looking at the EWs of the CORALIE and HARPS spectra of WASP-69 in Figure 3.19. The spectra are both of similar S/N, and this enabled a good comparison between the EWs of the lines, which is not possible with other stars within the WASP data sets or with the Sun. For example, the CORALIE spectrum of the Sun has S/N of 60, whereas the HARPS spectrum as S/N of 1000, and the S/N difference here is the major contributor to the CORALIE solar abundances being underestimated by $\sim$0.2 dex. In the case of WASP-69, there is an rms difference of 0.006 Å between both spectrographs. This small but systematic difference indicates that there is an additional discrepancy between the two spectrographs, possibly due to scattered light in the CORALIE spectrum.

3.6.8.1 Differential analysis

In addition to using abundances determined from the EWs measured with UCLSYN, I also performed a line-by-line differential analysis with the Sun. I found that the UCLSYN abundances agree with the differential abundances to within 0.04 dex. However, as there

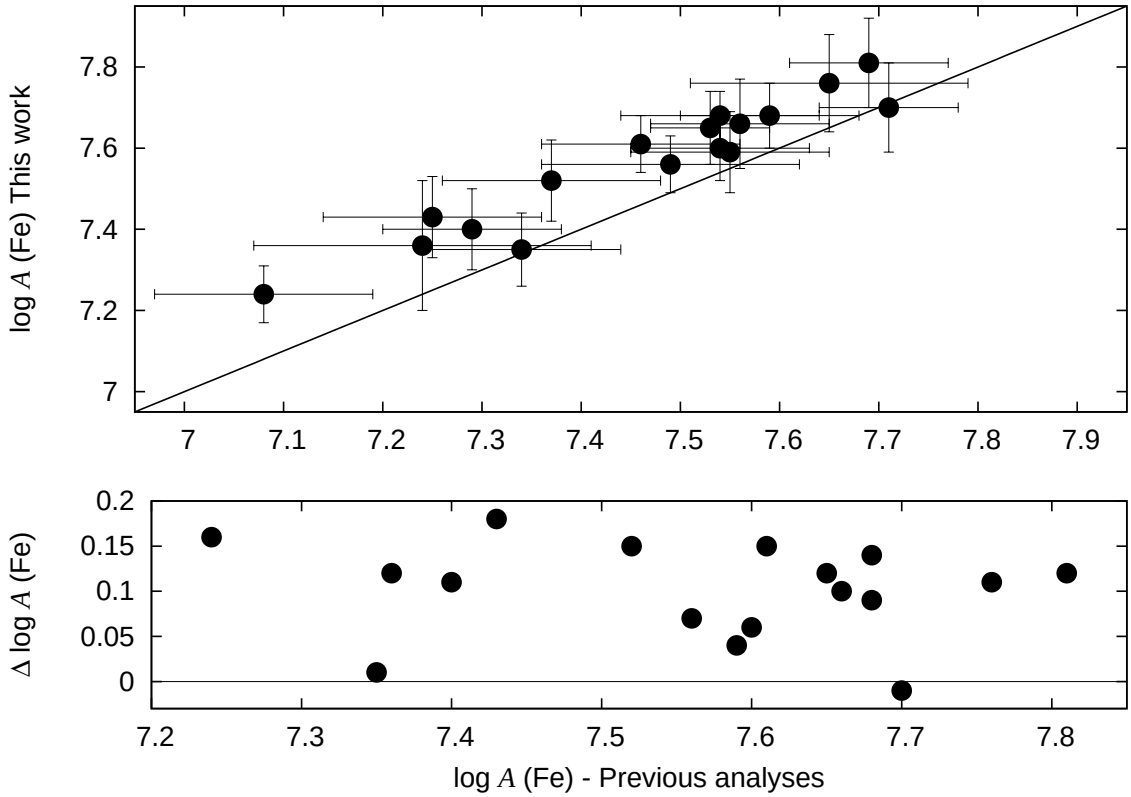

Figure 3.18: Comparison of Fe abundances between this work and previous analyses, where $\Delta \log A$ (Fe) = $\log A$ (Fe) this work - $\log A$ (Fe) previous analyses and the solid line is a 1:1 relationship. The abundances from this work are systematically higher by 0.10 ± 0.05 dex.

is a large range in the stellar parameters, I decided it was best not to use these values. As such, the abundances obtained from the non-differential analyses were retained for most elements.

For some elements, the abundances obtained are highly anomalous, even in the Sun, or there is an unusual scatter in the abundances, such as with Si. In these cases, I looked for suitable alternate values of $\log gf$ but found none. As such, the only way to obtain any sort of abundance values for these elements was to use a differential analysis, and the results of this is shown in Table 3.10 for Si, Cu, Sr, Sm, Gd, Dy and W. It should be noted that most of these elements have very few lines, which could introduce further errors. For instance, the precision of some of the abundances in Table 3.10 is as low as 0.01 dex and this is most likely due to the fact that there are very few lines. A larger number of lines, such as used for Fe, will have a larger scatter in the values. If there are only three lines measured for an element, they do not give an accurate representation of the possible spread in abundances, and could be biased towards as

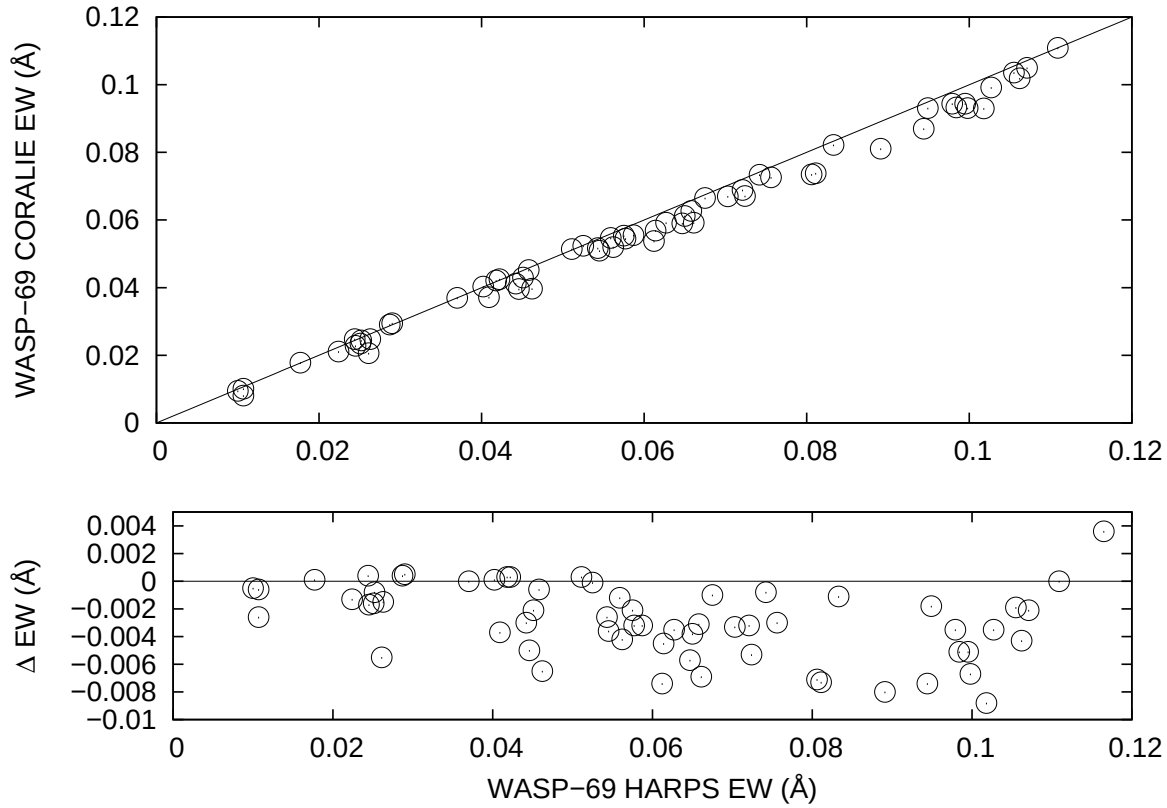

Figure 3.19: EW comparison between CORALIE and HARPS for WASP-69, where Δ EW = CORALIE - HARPS. The solid line depicts a 1:1 relationship. The EWs of the CORALIE spectrum of WASP-69 are systematically lower than the HARPS spectrum, which is of similar S/N. This indicates that scattered light could be an issue in CORALIE spectra.

higher or lower abundance, as is the case for too few Fe II lines in Section 3.6.1.

3.6.9 Mass and radius

The mass and radius for each star are obtained from the $T_{\rm eff}$, $\log g$, and [Fe/H], based on the Torres, Andersen & Giménez (2010) calibration and given in Table 3.11. However, it should be noted that these masses and radii are only given as an example, and that stellar evolutionary models may give different results based on the same spectroscopic parameters.

Table 3.9: Abundances for the HARPS solar spectrum, Procyon and the WASP stars.

Star	$\log A$ (Fe)	$\log A$(Na)	$\log A$(Ca)	$\log A$(Sc)	$\log A$(Ti)	$\log A$(V)	$\log A$(Cr)	$\log A$(Mn)	$\log A$(Co)	$\log A$(Ni)	$\log A$(Y)
Sun	7.52 ± 0.08	6.32 ± 0.07	6.33 ± 0.09	3.10 ± 0.07	4.95 ± 0.08	3.92 ± 0.06	5.65 ± 0.06	5.50 ± 0.14	4.84 ± 0.11	6.24 ± 0.06	2.24 ± 0.07
Procyon	7.48 ± 0.09	6.31 ± 0.03	6.37 ± 0.09	3.12 ± 0.12	4.98 ± 0.10	3.93 ± 0.03	5.65 ± 0.11	5.23 ± 0.06	4.83 ± 0.10	6.20 ± 0.08	2.28 ± 0.07
WASP-2	7.46 ± 0.10	6.40 ± 0.06	6.36 ± 0.08	3.15 ± 0.07	5.00 ± 0.08	4.07 ± 0.08	5.64 ± 0.09	5.53 ± 0.11	5.08 ± 0.20	6.18 ± 0.09	
WASP-4	7.42 ± 0.13	6.27 ± 0.07	6.25 ± 0.12	3.09 ± 0.14	4.87 ± 0.09	3.86 ± 0.06	5.59 ± 0.09	5.53 ± 0.13	4.87 ± 0.06	6.14 ± 0.13	2.14 ± 0.09
WASP-5	7.63 ± 0.10	6.54 ± 0.11	6.49 ± 0.09	3.32 ± 0.16	5.07 ± 0.12	4.07 ± 0.08	5.77 ± 0.08	5.84 ± 0.09	5.11 ± 0.07	6.37 ± 0.10	2.30 ± 0.14
WASP-6	7.35 ± 0.09	6.18 ± 0.09	6.19 ± 0.12	3.02 ± 0.10	4.83 ± 0.08	3.80 ± 0.09	5.50 ± 0.10	5.27 ± 0.12	4.67 ± 0.14	6.04 ± 0.12	
WASP-7	7.68 ± 0.06	6.50 ± 0.03			5.26 ± 0.24		5.77 ± 0.05			6.37 ± 0.10	
WASP-8	7.70 ± 0.11	6.59 ± 0.11	6.56 ± 0.08	3.23 ± 0.06	5.14 ± 0.10	4.19 ± 0.09	5.84 ± 0.05	5.66 ± 0.06	5.21 ± 0.17	6.49 ± 0.11	2.37 ± 0.09
WASP-15	7.52 ± 0.10	6.23 ± 0.03	6.31 ± 0.09	3.17 ± 0.10	4.97 ± 0.07		5.62 ± 0.08	5.30 ± 0.08	4.77 ± 0.10	6.12 ± 0.07	2.29 ± 0.08
WASP-16	7.59 ± 0.10	6.47 ± 0.05	6.44 ± 0.12	3.14 ± 0.13	5.03 ± 0.10	4.00 ± 0.11	5.73 ± 0.10	5.67 ± 0.16	5.10 ± 0.16	6.41 ± 0.11	2.12 ± 0.05
WASP-17	7.40 ± 0.10	6.19 ± 0.04	6.27 ± 0.19		4.91 ± 0.06		5.53 ± 0.05	5.19 ± 0.09		6.06 ± 0.10	2.20 ± 0.11
WASP-18	7.60 ± 0.08	6.22 ± 0.04	6.48 ± 0.12		5.07 ± 0.06	3.94 ± 0.08	5.75 ± 0.10	5.51 ± 0.15		6.24 ± 0.06	2.41 ± 0.10
WASP-19	7.66 ± 0.11	6.52 ± 0.08	6.51 ± 0.13	3.29 ± 0.09	5.15 ± 0.11	4.16 ± 0.08	5.81 ± 0.08	5.78 ± 0.21	5.12 ± 0.10	6.40 ± 0.08	2.39 ± 0.16
WASP-20	7.65 ± 0.09	6.40 ± 0.09	6.42 ± 0.10	3.20 ± 0.09	5.09 ± 0.10	4.11 ± 0.06	5.80 ± 0.12	5.58 ± 0.12	4.98 ± 0.18	6.28 ± 0.09	2.42 ± 0.12
WASP-21	7.24 ± 0.07	5.92 ± 0.07	6.16 ± 0.09	3.09 ± 0.05	4.82 ± 0.11	3.57 ± 0.06	5.30 ± 0.12	4.89 ± 0.09	4.54 ± 0.12	5.87 ± 0.07	1.88 ± 0.06
WASP-22	7.68 ± 0.08	6.52 ± 0.09	6.50 ± 0.08	3.24 ± 0.13	5.10 ± 0.09	4.06 ± 0.09	5.79 ± 0.07	5.67 ± 0.16	5.07 ± 0.11	6.41 ± 0.05	2.31 ± 0.10
WASP-23	7.56 ± 0.07	6.34 ± 0.04	6.36 ± 0.19	3.10 ± 0.08	5.02 ± 0.11	4.09 ± 0.12	5.70 ± 0.13	5.46 ± 0.16	4.98 ± 0.13	6.21 ± 0.09	
WASP-24	7.54 ± 0.08	6.28 ± 0.09	6.37 ± 0.09	3.18 ± 0.12	4.97 ± 0.12	3.81 ± 0.05	5.58 ± 0.11	5.39 ± 0.12	4.85 ± 0.12	6.17 ± 0.06	2.31 ± 0.09
WASP-29	7.76 ± 0.12	6.68 ± 0.10	6.55 ± 0.13	3.43 ± 0.09	5.28 ± 0.13	4.49 ± 0.22	5.96 ± 0.18	5.78 ± 0.17	5.29 ± 0.19	6.44 ± 0.10	
WASP-30	7.61 ± 0.07	6.43 ± 0.09	6.47 ± 0.12		5.01 ± 0.10	3.85 ± 0.05	5.78 ± 0.10	5.61 ± 0.13		6.29 ± 0.08	
WASP-31	7.43 ± 0.10	6.10 ± 0.05	6.33 ± 0.05	3.13 ± 0.09	4.91 ± 0.08		5.49 ± 0.09	5.15 ± 0.12		6.07 ± 0.10	2.25 ± 0.10
WASP-53	7.72 ± 0.11	6.76 ± 0.11	6.50 ± 0.15	3.34 ± 0.11	5.21 ± 0.15	4.37 ± 0.20	5.86 ± 0.11	5.72 ± 0.20	5.23 ± 0.11	6.42 ± 0.12	
WASP-69	7.81 ± 0.11	6.76 ± 0.10	6.67 ± 0.16	3.47 ± 0.19	5.29 ± 0.14	4.61 ± 0.14	6.05 ± 0.17	5.93 ± 0.34	5.65 ± 0.31	6.57 ± 0.19	
WASP-77A	7.50 ± 0.10	6.32 ± 0.05	6.32 ± 0.13	3.12 ± 0.07	4.93 ± 0.09	3.90 ± 0.07	5.64 ± 0.06	5.57 ± 0.14	4.91 ± 0.10	6.21 ± 0.08	2.25 ± 0.09
WASP-77B	7.38 ± 0.19	6.53 ± 0.08	6.33 ± 0.09	3.29 ± 0.18	5.10 ± 0.15	4.32 ± 0.14	5.71 ± 0.22		5.23 ± 0.27	6.23 ± 0.19	
WASP-80	7.36 ± 0.16	6.30 ± 0.16	6.20 ± 0.32		4.93 ± 0.28	4.08 ± 0.15	5.41 ± 0.16		5.25 ± 0.16	6.00 ± 0.31	

Table 3.10: Differential abundance analysis.

Star	[Si/H]	[Cu/H]	[Sr/H]	[Sm/H]	[Gd/H]	[Dy/H]	[W/H]
WASP-2	0.07 ± 0.03	-0.04 ± 0.05			0.25 ± 0.03	0.10 ± 0.05	
WASP-4	-0.02 ± 0.02	0.07 ± 0.04			0.08 ± 0.05	0.00 ± 0.05	-0.13 ± 0.08
WASP-5	0.20 ± 0.01	0.23 ± 0.02		0.24 ± 0.04	0.06 ± 0.04	0.17 ± 0.04	0.04 ± 0.09
WASP-6	-0.08 ± 0.02	-0.06 ± 0.06		0.15 ± 0.03	-0.12 ± 0.03	-0.06 ± 0.03	-0.42 ± 0.06
WASP-7	0.25 ± 0.02		0.46 ± 0.03		-0.29 ± 0.04	0.03 ± 0.04	
WASP-8	0.25 ± 0.06	0.32 ± 0.29		0.38 ± 0.05	0.36 ± 0.04	0.48 ± 0.04	0.30 ± 0.09
WASP-15	-0.02 ± 0.03	0.02 ± 0.07		0.09 ± 0.05	-0.21 ± 0.05	-0.05 ± 0.05	0.22 ± 0.09
WASP-16	0.16 ± 0.02	0.21 ± 0.06	0.12 ± 0.04	0.17 ± 0.05	0.06 ± 0.04	0.15 ± 0.04	0.00 ± 0.08
WASP-17	-0.14 ± 0.04					-0.45 ± 0.09	
WASP-18	0.13 ± 0.02	-0.04 ± 0.07			-0.27 ± 0.04		
WASP-19	0.25 ± 0.02	0.25 ± 0.07		0.12 ± 0.06	0.34 ± 0.06	0.29 ± 0.07	0.06 ± 0.09
WASP-20	0.00 ± 0.03	0.08 ± 0.06	0.12 ± 0.04	0.17 ± 0.06	-0.08 ± 0.06	0.10 ± 0.06	0.30 ± 0.09
WASP-21	-0.31 ± 0.02	-0.43 ± 0.06		0.07 ± 0.04	-0.30 ± 0.04	-0.32 ± 0.04	
WASP-22	0.14 ± 0.02	0.14 ± 0.02	0.30 ± 0.04	0.09 ± 0.04	-0.03 ± 0.04	0.02 ± 0.04	0.30 ± 0.08
WASP-30	0.10 ± 0.02	-0.14 ± 0.06	0.20 ± 0.03				

Table 3.11: Stellar mass and radius determined from the Torres, Andersen & Giménez (2010) calibration

Star	Mass ($M_\odot$)	Radius ($R_\odot$)
WASP-2	0.87 ± 0.07	0.90 ± 0.14
WASP-4	0.92 ± 0.07	0.92 ± 0.13
WASP-5	1.10 ± 0.08	1.24 ± 0.15
WASP-6	0.87 ± 0.06	0.77 ± 0.07
WASP-7	1.34 ± 0.09	1.32 ± 0.11
WASP-8	1.04 ± 0.08	1.05 ± 0.12
WASP-15	1.23 ± 0.09	1.15 ± 0.16
WASP-16	1.09 ± 0.09	1.34 ± 0.20
WASP-17	1.29 ± 0.12	1.27 ± 0.38
WASP-18	1.28 ± 0.09	1.29 ± 0.1
WASP-19	1.01 ± 0.08	1.07 ± 0.19
WASP-20	1.12 ± 0.08	0.94 ± 0.15
WASP-21	1.02 ± 0.07	1.13 ± 0.14
WASP-22	1.22 ± 0.09	1.35 ± 0.17
WASP-23	0.88 ± 0.07	1.07 ± 0.17
WASP-24	1.22 ± 0.09	1.44 ± 0.22
WASP-29	0.80 ± 0.06	0.83 ± 0.17
WASP-30	1.28 ± 0.09	1.51 ± 0.1
WASP-31	1.19 ± 0.09	1.19 ± 0.16
WASP-53	0.87 ± 0.08	0.96 ± 0.24
WASP-69	0.84 ± 0.07	0.98 ± 0.24
WASP-77A	1.00 ± 0.07	1.12 ± 0.12
WASP-77B	0.71 ± 0.06	0.69 ± 0.12
WASP-80	0.57 ± 0.05	0.61 ± 0.15

3.7 Errors

The $T_{\rm eff}$, $\log g$ and [Fe/H] are correlated, and thus errors in one parameter will affect the determination of another. For example, if the $T_{\rm eff}$ of a hot star is overestimated, the [Fe/H] will also be overestimated (Holmberg, Nordström & Andersen 2007).

I calculated the $T_{\rm eff}$ errors from the 1-σ variation in the slope of abundance against excitation potential, and they range between 50 and 105 K. These values are consistent with Torres, Winn & Holman (2008), who suggest that $T_{\rm eff}$ errors should not fall below 50 K, despite the fact that some automated spectroscopic analyses often give errors that are much lower than this. To justify this decision they cite, for example, the difference of around 100 K between excitation equilibrium measurements and the IRFM determined by Ramírez & Meléndez (2004). Maxted, Koen & Smalley (2011) also performed a comparison between spectroscopic methods and the IRFM, which supports that temperature errors should not be any lower than 50 K.

A change in $T_{\rm eff}$ will affect the ionisation balance, for example an increase in $T_{\rm eff}$ of 100 K will result in $\log g$ increasing by 0.1 dex (Bruntt 2009). This was accounted for by varying the $T_{\rm eff}$ by 1-σ when using the ionisation balance method. The $\log g$ determined from the pressure-broadened lines is also dependent on the abundance, as an increased abundance will cause the line to be stronger. The abundances were thus varied by 1-σ when determining $\log g$ from fitting the Na I D and Ca I lines.

While there is some reduction in errors of stellar parameters from the original analyses with mostly lower S/N spectra, the errors are still large considering the high S/N of the HARPS spectra. I calculated the average errors in $T_{\rm eff}$, $\log g$, $v_{\rm mic}$ and $\log A$(Fe) to be 83 K, 0.11 dex, 0.11 km s^{-1} and 0.10 dex respectively for this sample of stars. The scatter in Fe abundances due to uncertainties in atomic data can influence the $\log A$(Fe) as well as $T_{\rm eff}$, $\log g$ and $v_{\rm mic}$.

Variations in $T_{\rm eff}$, $\log g$ and $v_{\rm mic}$ can affect the elemental abundances. Table 3.12 and Table 3.13 list the uncertainties when the stellar parameters are varied by their average errors for the HARPS solar spectrum and Procyon respectively. Elements such as V are more sensitive to changes in temperature than others due to a restricted range in excitation potential. Therefore a large error on $T_{\rm eff}$ will give V a more substantial error than the other elements. For certain elements, additional sources of uncertainty have to be considered. Abundances can be overestimated for Mn and Co, as the line profiles are altered due to hyperfine splitting (Schuler et al. 2011b) so that they have a

flat core. This could cause abundances uncertainties in Mn and Co to be higher than for other elements (Wahlgren 2005).

Table 3.12: Abundance uncertainties for the HARPS solar spectrum

Element	$\Delta\ T_{\rm eff}$ +83 K	$\Delta\ \log g$ +0.11 dex	$\Delta\ v_{\rm mic}$ +0.11 km s^{-1}
[Fe/H]	0.02	0.00	-0.02
[Ca/H]	0.05	-0.03	-0.02
[Sc/H]	0.01	0.04	0.00
[Ti/H]	0.05	0.01	-0.01
[V/H]	0.09	0.00	0.00
[Cr/H]	0.04	0.01	-0.01
[Mn/H]	0.07	0.00	-0.02
[Co/H]	0.06	0.01	0.00
[Ni/H]	0.04	0.00	-0.01
[Y/H]	0.00	0.05	-0.01

Table 3.13: Abundance uncertainties for Procyon

Element	$\Delta\ T_{\rm eff}$ +83 K	$\Delta\ \log g$ +0.11 dex	$\Delta\ v_{\rm mic}$ +0.11 km s^{-1}
[Fe/H]	0.03	0.01	-0.01
[Ca/H]	0.05	-0.01	-0.02
[Sc/H]	0.04	0.04	0.00
[Ti/H]	0.03	0.02	-0.01
[V/H]	0.05	0.01	0.00
[Cr/H]	0.02	0.02	-0.02
[Mn/H]	0.11	0.06	0.05
[Co/H]	0.05	0.00	0.00
[Ni/H]	0.05	0.00	0.00
[Y/H]	0.03	0.04	-0.01

Systematic errors in the EWs can be investigated by comparing the EWs of the same star between two different spectrographs (Gratton et al. 2007). Figure 3.20 shows the EWs of the Sun measured from the Kitt Peak Solar Atlas plotted against the EWs from the HARPS solar spectrum. The EWs agree between both spectra for weak lines, however the HARPS EWs seem to be lower than the Kitt Peak Solar Atlas for lines stronger than 0.06 Å. However, there is no significant offset evident in the solar parameters when comparing the results between the HARPS solar spectrum and the Kitt Peak Solar Atlas, as seen in Table 3.5. In addition the strongest lines, where the largest deviations are seen, are culled prior to the final analyses. Therefore any systematic errors present should have a negligible effect on the stellar parameters.

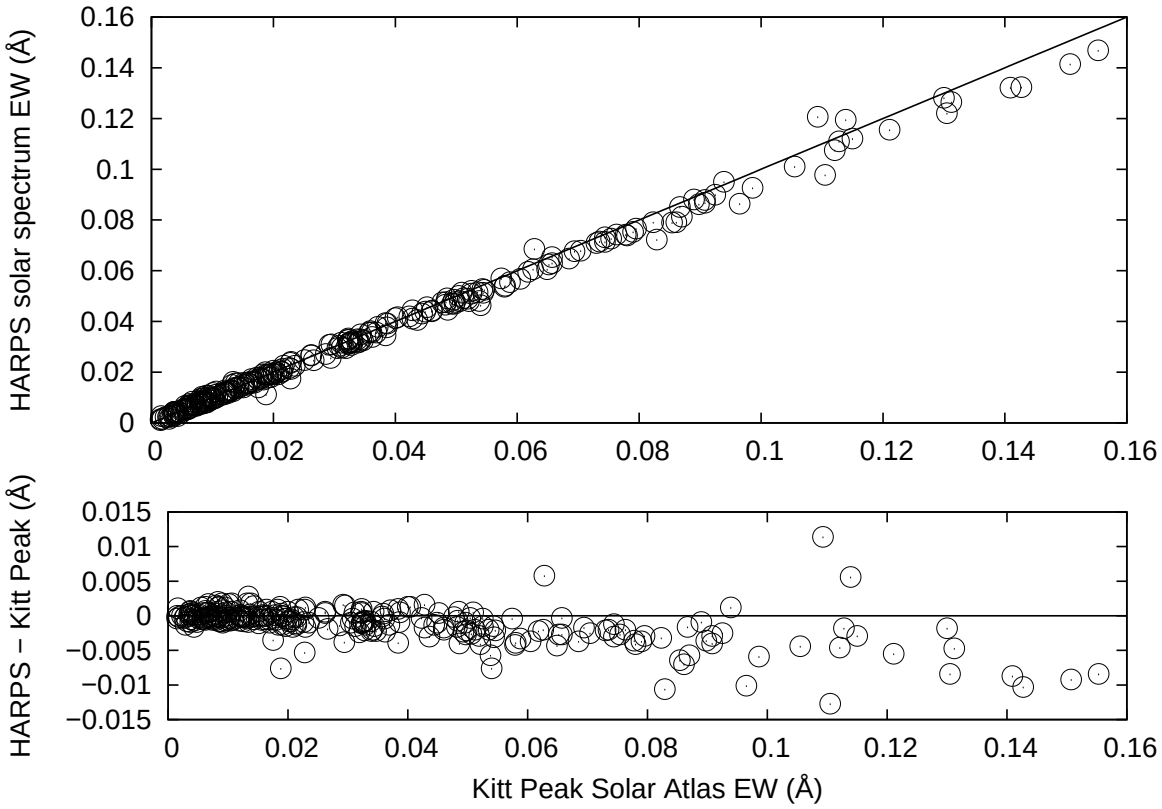

Figure 3.20: Comparison of EWs measured in two different solar spectra. The solid line depicts the 1:1 relationship.

4 Comparison with other methods

The investigation of the nature of the fixed stars by a prismatic analysis of the light which comes to us from them, however, is surrounded with no ordinary difficulties.

- William Huggins and William Allen Miller, 1864

It has been recognised that the use of different methods and software for analysing spectra can cause a scatter in the derived parameters, and in turn affect the planetary parameters if the star is a known planet host. In addition, the different S/N and resolution of the spectra, as well as the treatment of errors, can affect the results. In this chapter I compare my method in Chapter 3 with others in the literature.

4.1 WASP-13

4.1.1 The HoSTS Project

The Homogeneous Study of Transiting Systems (HoSTS) project aims to characterise planets and their host stars consistently, and to use a homogeneous, high quality set of stellar spectra. Previous studies of planet host stars include Torres, Winn & Holman (2008), who critically evaluated the spectral analyses procedures of multiple results for a set of planet host stars, and determined the best value by combining results from different studies. Ammler-von Eiff et al. (2009) redetermined the spectral properties of 13 planet host stars using spectra obtained from several different spectrographs, and compared this with other results from the literature. They noted some discrepancies, including the Fe abundance being systematically higher in their analysis compared to previous results.

I thought it would be pertinent to contribute to HoSTS, and compare my method with three others for the pilot study of WASP-13 (Gómez Maqueo Chew et al. 2013). Each of the four spectral analysis methods performed an unconstrained analysis to obtain $T_{\rm eff}$, $\log g$ and $\log A$ (Fe), an analysis with the $T_{\rm eff}$ fixed from the Hα line (5950 $\pm$ 70 K) , and an analysis with $\log g$ fixed from the transit value (4.10 $\pm$ 0.04 dex). The Hα $T_{\rm eff}$ was determined from a long-slit spectrum obtained with the IDS (R = 10,000). The spectrum used for general analysis was a HIRES (R = 72,000) spectrum.

Method A used SME (Valenti & Piskunov 1996), which adjusts parameters of a synthetic spectrum until it fits the observed spectrum. Method B was my analysis

based on the methods in Chapter 3. Method C used MOOG/ARES to measure EWs with a line list from Schuler et al. (2011b) and Method D used MOOG/ARES with a line list from Sousa et al. (2008). MOOG (Sneden 1973) uses the same equivalent width based methods as UCLSYN, and ARES (Sousa et al. 2007) automatically measures EWs of spectra.

All methods except mine utilised a differential abundance analysis. For the UCLSYN analysis, there wasn't much difference for the three different constraints, as the $T_{\rm eff}$ and $\log g$ determined from the unconstrained analysis already agreed well with the fixed $T_{\rm eff}$ and $\log g$. The results for the unconstrained analyses are given in Table 4.1.

Table 4.1: Results from unconstrained HoSTS analyses of WASP-13

Parameter	A	B	C	D	Weighted mean
$T_{\rm eff}$ (K)	6003 ± 65	5955 ± 75	5919 ± 30	6025 ± 21	5989 ± 48
$\log g$	4.16 ± 0.08	4.13 ± 0.11	4.02 ± 0.06	4.19 ± 0.03	4.16 ± 0.07
$\log A$ (Fe)	7.54 ± 0.05	7.60 ± 0.09	7.54 ± 0.05	7.58 ± 0.05	7.56 ± 0.03
$v_{\rm mic}$ (km s^{-1})	1.01 ± 0.17	0.95 ± 0.10	1.53 ± 0.09	1.28 ± 0.10	1.27 ± 0.29

The paper concludes that the results from the unconstrained analysis agreed well between all four methods and are consistent with the transit $\log g$ and the Hα $T_{\rm eff}$, leading to the conclusion that the four different methods of spectral analysis have no systematic differences between them. This is in disagreement with Torres et al. (2012), who find that the $\log g$ should be fixed to the transit value. However, our methods differ from Torres et al. (2012) in line lists, treatment of microturbulence and the parameters space. A final conclusion on this cannot be drawn until more stars are analysed for the HoSTS project.

While the results from the four different spectral analysis methods used do mostly agree within the errors, I was still concerned about the range of values. Methods B, C and D are essentially the same method; they all rely on the excitation and ionisation balance of Fe lines to determine the parameters, and they all assume LTE and use ATLAS 9 models. Yet there are significant differences in $T_{\rm eff}$ and $v_{\rm mic}$. As such, I decided to look into these discrepancies further as part of my thesis.

4.1.2 Comparison to Method A

The SME analysis fixed the $v_{\rm mic}$ to a value of 1.01 km s^{-1} based on the calibration of $T_{\rm eff}$ and $v_{\rm mic}$ from a sample of HARPS stars analysed in Sousa et al. (2011). However, this value of $v_{\rm mic}$ was determined based on the $T_{\rm eff}$ of 5825 ± 100 K from Skillen et al.

(2009). This was also an SME analysis, but this $T_{\rm eff}$ was derived from fixing the $v_{\rm mic}$ to 0.85 km s^{-1}. Using the Hα $T_{\rm eff}$ gives a $v_{\rm mic}$ of 1.23 km s^{-1} from the same calibration. I used SME to determine the parameters of WASP-13 using both $v_{\rm mic}$ values, and the results are presented in Table 4.2. I did one unconstrained and one constrained run for each $v_{\rm mic}$ value. The values are different from the ones in the paper due to different line lists and different assumptions, but the results in the table are self consistent. I also included the $v_{\rm mic}$ value of 0.85 km s^{-1}, as SME analyses often have $v_{\rm mic}$ fixed to this value based on the Valenti & Fischer (2005) recommendation.

Table 4.2: SME parameters for WASP-13 with fixed $v_{\rm mic}$

Parameter	$v_{\rm mic}$ 1.01 km s^{-1}		$v_{\rm mic}$ 1.23 km s^{-1}		$v_{\rm mic}$ 0.85 km s^{-1}	
$T_{\rm eff}$ (K)	6092	6011	6078	6017	6081	5999
$\log g$	4.22	4.10*	4.19	4.10*	4.21	4.10*
[M/H]	0.059	0.017	0.039	0.008	0.069	0.026

* Fixed from transit value

It is clear from Table 4.2 that fixing the $v_{\rm mic}$ to a value that is too low doesn't have much effect on the parameters in SME, whereas such a $v_{\rm mic}$ adjustment would have much more influence on parameters determined from the Fe excitation and ionisation balance. Also, fixing $\log g$ has much more of an impact than fixing $v_{\rm mic}$ in SME.

4.1.3 Comparison to Method D

The $\log g$ and $\log A$(Fe) are in good agreement between Methods B and D. However, the $T_{\rm eff}$ and $v_{\rm mic}$ are notably higher in Method D than Method B. When I plot the excitation balance using the lines and EWs of Method D in UCLSYN, I get the same $T_{\rm eff}$ and $v_{\rm mic}$ as they do, showing that it is not a difference in software that causes the discrepancies in parameters.

When I measured the EWs using the line list of Sousa et al. (2008) in UCLSYN, I noticed that a significant number of the lines were badly blended. In Figure 4.1 I have plotted the EWs that I measured against those measured via ARES in Method D, which shows that many of the ARES EWs are overestimated. The EWs that I measured do not included the blended component. If I do included the blended component in the EW, then there is a much better agreement with the ARES EWs, as seen in Figure 4.2. This figure shows a linear regression, with m = 1.01 $\pm$ 0.01, c = $-6.11 \times 10^{-4} \pm 3.03 \times 10^{-3}$ and $r^2 = 0.99$. The r^2 value of 0.99 indicates excellent agreement between these EW measurements. The inclusion of so many badly blended lines in Method D is possibly

because the line list was created from the Sun, and at the solar $T_{\rm eff}$ the lines aren't blended. The effect of including lines with overestimated EWs is to increase the $T_{\rm eff}$ determined from the excitation balance, which explains why the Method D $T_{\rm eff}$ is 70 K hotter than Method B.

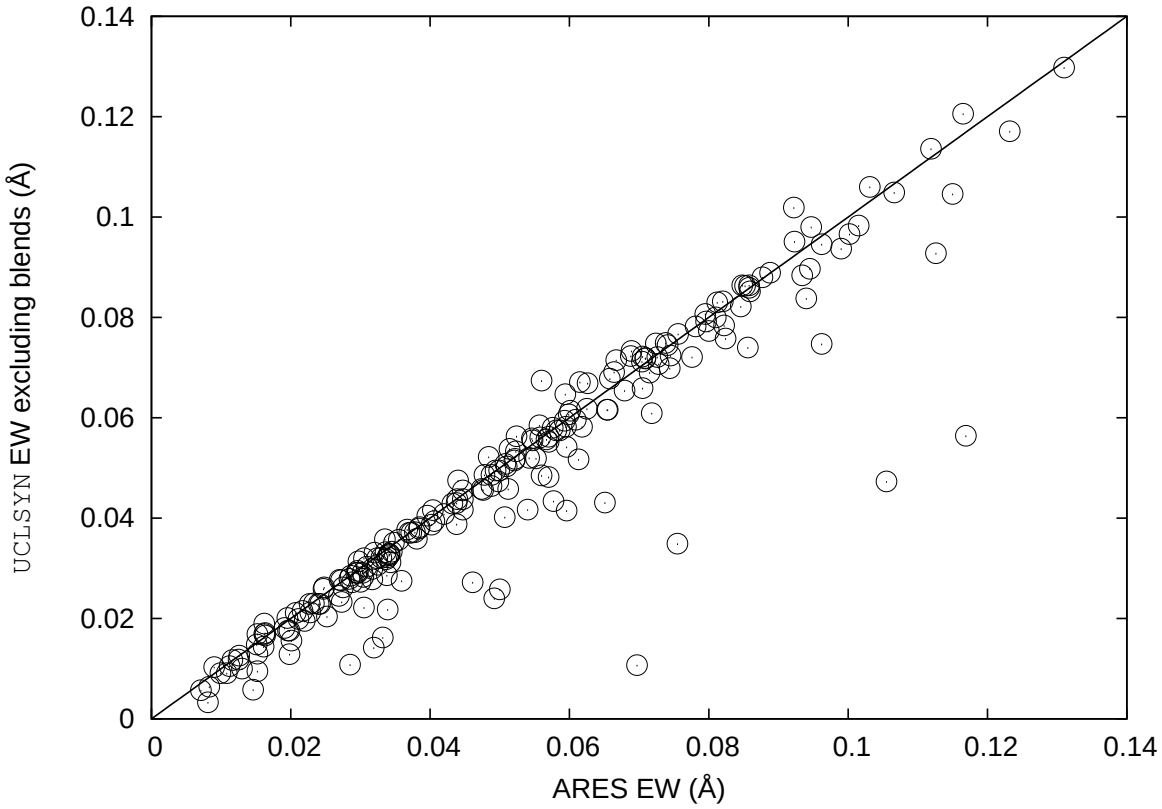

Figure 4.1: Comparison between measured EWs for WASP-13. The solid line depicts a 1:1 relationship. The EWs from this work are only for the line of interest and do not include the blended component. This results in many of the ARES lines being overestimated compared to the UCLSYN EWs.

Taking the lines in common between both line lists and using the same EWs, I found that using the Sousa et al. (2008) list gives a $v_{\rm mic}$ that is 0.25 km s^{-1} higher for the same value of $T_{\rm eff}$ and $\log g$. This indicates that the difference in $v_{\rm mic}$ is purely a factor of the different atomic data in the line lists, rather than the different EW measurements. Figure 4.3 compares the $\log gf$ between the two line lists for the lines in common, showing that there is an rms difference of 0.12 dex between the different values of $\log gf$.

The Sousa et al. (2008) line list was created differentially to the Sun. To determine the effect that this has on $v_{\rm mic}$ measurements, I adjusted my own line list to the Sun, assuming a solar $v_{\rm mic}$ of 0.85 km s^{-1}. Using the $T_{\rm eff}$ of 5955 K and $\log g$ of 4.13, I now

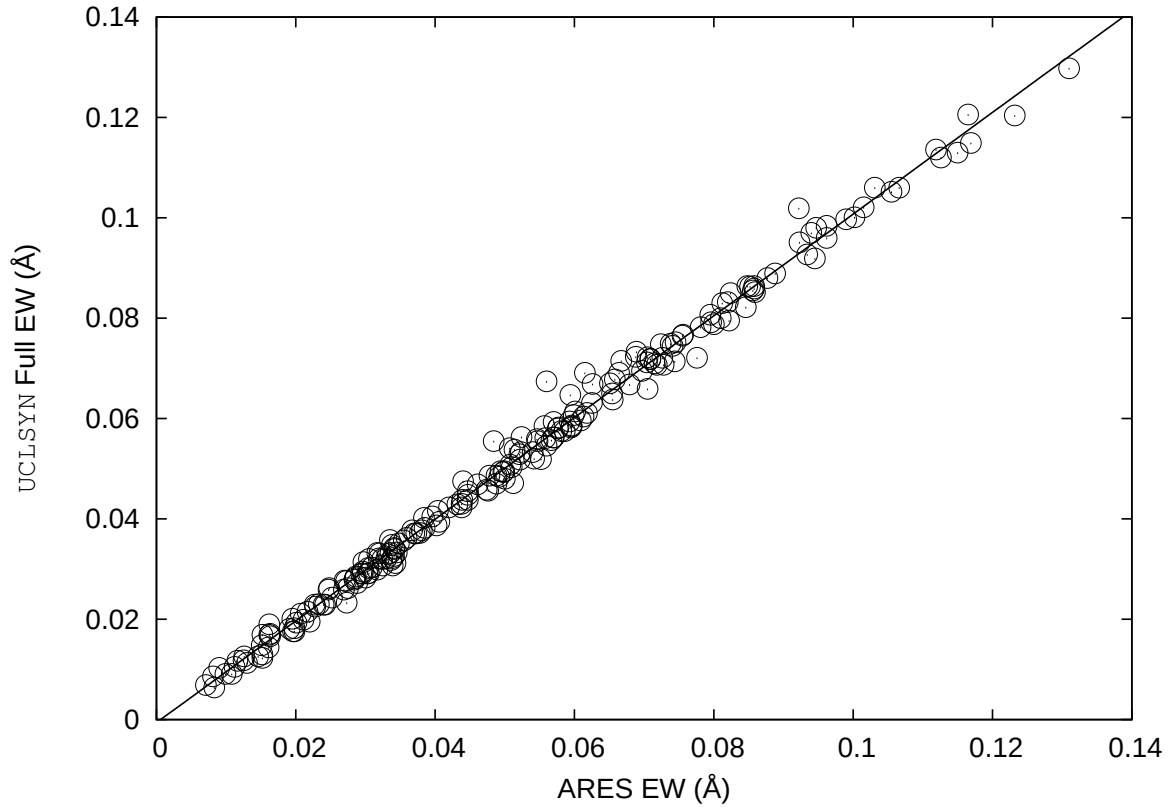

Figure 4.2: Same as for Figure 4.1 but this time the UCLSYN EWs measure the full EW of the line, including the blended component. The solid line is a linear regression to the data. The EWs are now in much better agreement.

get a $v_{\rm mic}$ of 1.2 km s^{-1} using my own line list. If I create a line list differentially to the Sun with a solar $v_{\rm mic}$ of 1 km s^{-1}, the resulting $v_{\rm mic}$ for WASP-13 is now 1.3 km s^{-1}, in agreement with Method D. Therefore using $\log gf$ values calculated from the Sun will create a significant bias when trying to determine the $v_{\rm mic}$ for another star.

4.1.4 Comparison to Method C

Using the Schuler et al. (2011b) line list, 45 Fe I and 5 Fe II lines were measured in the Method C analysis of WASP-13. The low number of Fe II lines might explain why the $\log g$ from Method C is $\sim$0.1 dex lower than the other methods, as discussed in Section 3.6.1. Using my own line list with only those five Fe II lines, I obtain an ionisation balance $\log g$ of 4.0.

The $v_{\rm mic}$ determined via this method is 1.53 $\pm$ 0.09 km s^{-1}, which is the highest of all four methods. Using their line list and EW values, along with their values of $T_{\rm eff}$ and $\log g$, I find it impossible to get a $v_{\rm mic}$ of 1.53 km s^{-1}. Instead, I find a value of 1.2 km s^{-1} eliminates the slope in the line. Similarly, I cannot recreate their excitation

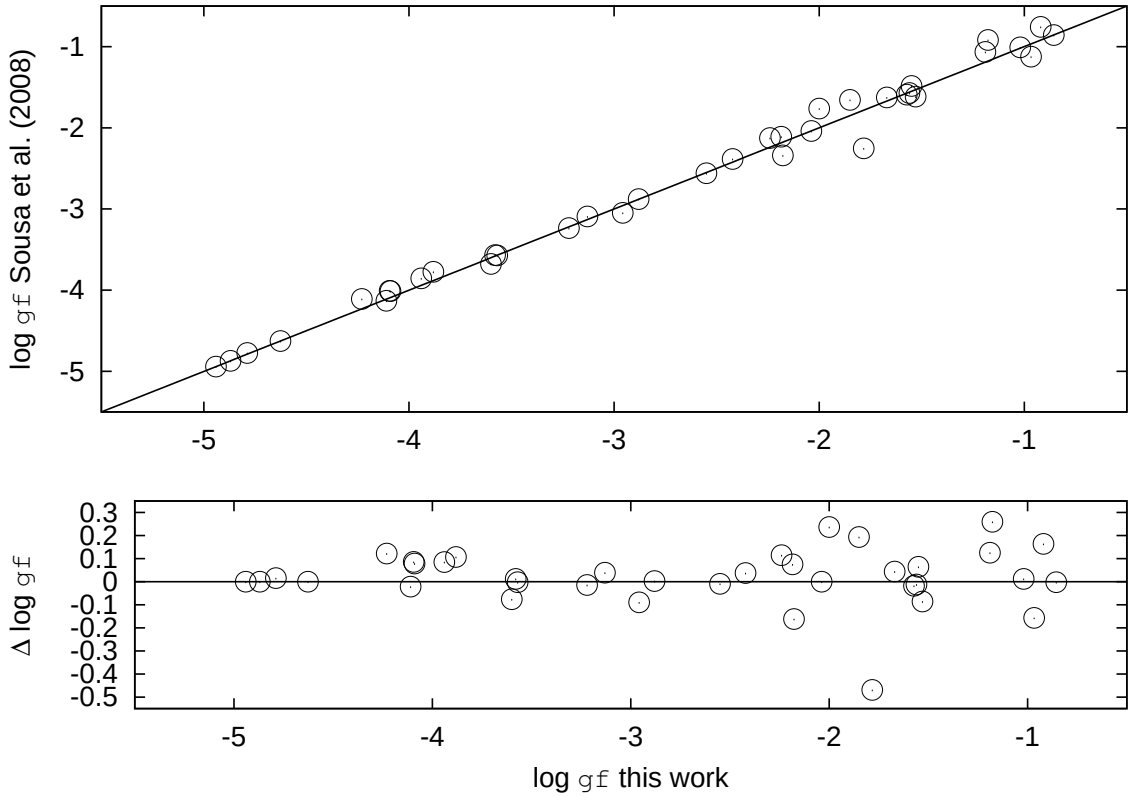

Figure 4.3: The top panel shows the comparison between the $\log gf$ values from my line list and the Sousa et al. (2008) line list. The solid line is a 1:1 relationship. The bottom panel shows the residuals, where $\Delta \log gf = \log gf$ (Sousa et al. 2008) - $\log gf$ (this work)

balance $T_{\rm eff}$, and I find a $T_{\rm eff}$ of 6239 $\pm$ 85 K is needed when using their values for $\log g$ and $v_{\rm mic}$.

The $\log gf$ values used in the Schuler et al. (2011b) line list were obtained from VALD, so should not contribute to the increase in $v_{\rm mic}$ as was found with the line list in Section 4.1.3. There are also very few lines in common between the Schuler list and my own, making a comparison of the $\log gf$ values (as was done for Method D) impossible.

They use the Unsöld values for VDW, increased by a factor of 2.2. Using their line list with the scaled Unsöld values does make a difference to the abundance of some of the lines, and this affects the $v_{\rm mic}$. However, it has the opposite effect in that the $v_{\rm mic}$ is lowered to 1.1 km s^{-1} using these values. This can be seen in Figure 4.4 where both sets of values are displayed for $T_{\rm eff}$ = 5919 K, $\log g$ = 4.02 and $v_{\rm mic}$ = 1.53 km s^{-1}. The VALD VDW values have higher abundances for the stronger lines and the slope of this fit has a correlation coefficient of -0.27. The fit to the Unsöld values has a correlation coefficient of -0.35.

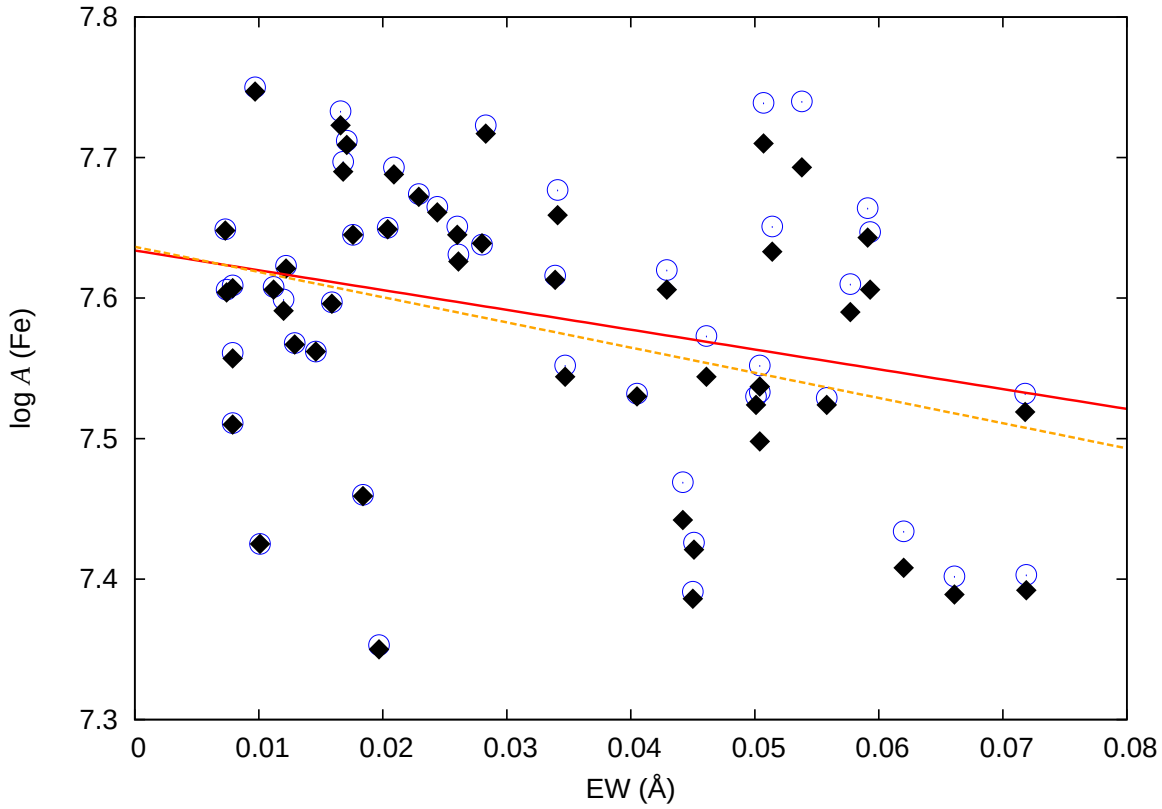

Figure 4.4: The Schuler et al. (2011b) lines are shown for WASP-13 using $T_{\rm eff}$ = 5919 K, $\log g = 4.02$ and $v_{\rm mic} = 1.53$ km s^{-1}. It is impossible to obtain their microturbulence value as evident by the slopes. The blue circle are using the VALD VDW values, and the black diamonds are using the Unsöld values scaled by 2.2. The solid red line and orange dashed are the fits to the respective data, and have correlation coefficients of -0.27 and -0.35. The slope is higher for the Unsöld values, which means that $v_{\rm mic}$ needs to be decreased compared to the VALD values.

Using the same line list for the Sun, along with the EWs measured in Schuler et al. (2011a), shows that the same problems with $T_{\rm eff}$ and $v_{\rm mic}$ exist as in WASP-13. The solar excitation $T_{\rm eff}$ I get is 6079 ± 88 K, and the $v_{\rm mic}$ is 1.2 km s^{-1}, compared to their value of 1.38 km s^{-1}. Method C used the overshooting models of Castelli & Kurucz (2004), however using these models in UCLSYN only changes the solar $T_{\rm eff}$ to 6103 ± 90 K and the $v_{\rm mic}$ to 1.1 km s^{-1}. This suggests that the problem may be due to differences in the codes used.

Both Method C and D use MOOG to calculate abundances, however I am able to recreate the parameters obtained by Method D once the line list is corrected for blends and differential analysis. Method C used the 2010 version of MOOG, and Method D likely used the 2002 version (as stated in Sousa et al. (2011)), so it is possible that there the differences between the two versions cause the abundance discrepancies as seen with Method C.

4.2 Comparison to SME abundances for Procyon

An analysis of Procyon by Piskunov et al. (2013) using SME resulted in excellent agreement with the abundances I published in Doyle et al. (2013), which is shown in Figure 4.5. However, the notable exception to this was Mn, where my value was 0.16 dex lower than theirs. As I had cautioned in my paper, Mn can be sensitive to HFS. As UCLSYN had recently been updated to include HFS with the Kurucz & Bell (1995) hyperfine list, I was able to recalculate my Mn abundance while including this. I obtained a value of 5.38 ± 0.12, which agreed well with the SME result of 5.39 ± 0.07. However, Piskunov et al. (2013) used more recent laboratory $\log gf$ values in their line list than I did, so I then used this updated line list, along with the HFS, to get the Mn abundance. The inclusion of the updated $\log gf$ values pushes the Mn abundance too high, but using either HFS or the new $\log gf$ values gives a result consistent with other elements. It is possible that the HFS is the actual cause of the problem, especially since some of the Mn lines are obviously affected by this, and that the new $\log gf$ values didn't account for HFS. As such, my new result for Mn only includes the HFS.

It is interesting to note that while the inclusion of HFS improves the Mn abundance for Procyon, it does the opposite in the Sun. My solar Mn abundance of 5.50 ± 0.14 is already 0.07 dex higher than the Asplund et al. (2009) result, and including HFS pushes this higher to 5.53 ± 0.14. A NLTE correction to Mn in the Sun is positive (Bergemann & Gehren 2007) which would also increase the abundance, so this is unlikely the cause of the discrepancy between the Sun and Procyon. However, Blackwell-Whitehead & Bergemann (2007) noted that strong lines are more sensitive than others to an adjustment in the VDW damping parameters. As VDW broadening would be stronger in a cooler star, it is possible that this could explain the overabundance of Mn in the Sun compared to Procyon.

I also performed a HFS analysis of Co and V in both the Sun and Procyon. There is no difference in the V abundance for both stars. The abundance of Co in the Sun is increased to 5.03 ± 0.15, which is in better agreement with Asplund et al. (2009). However, the Co abundance in Procyon is now 4.94 ± 0.04 meaning it is no longer in agreement with the Piskunov value of 4.85 ± 0.07. Therefore including the HFS for Co seems to have the opposite effect to Mn, in that the solar value is improved but the Procyon value is made worse.

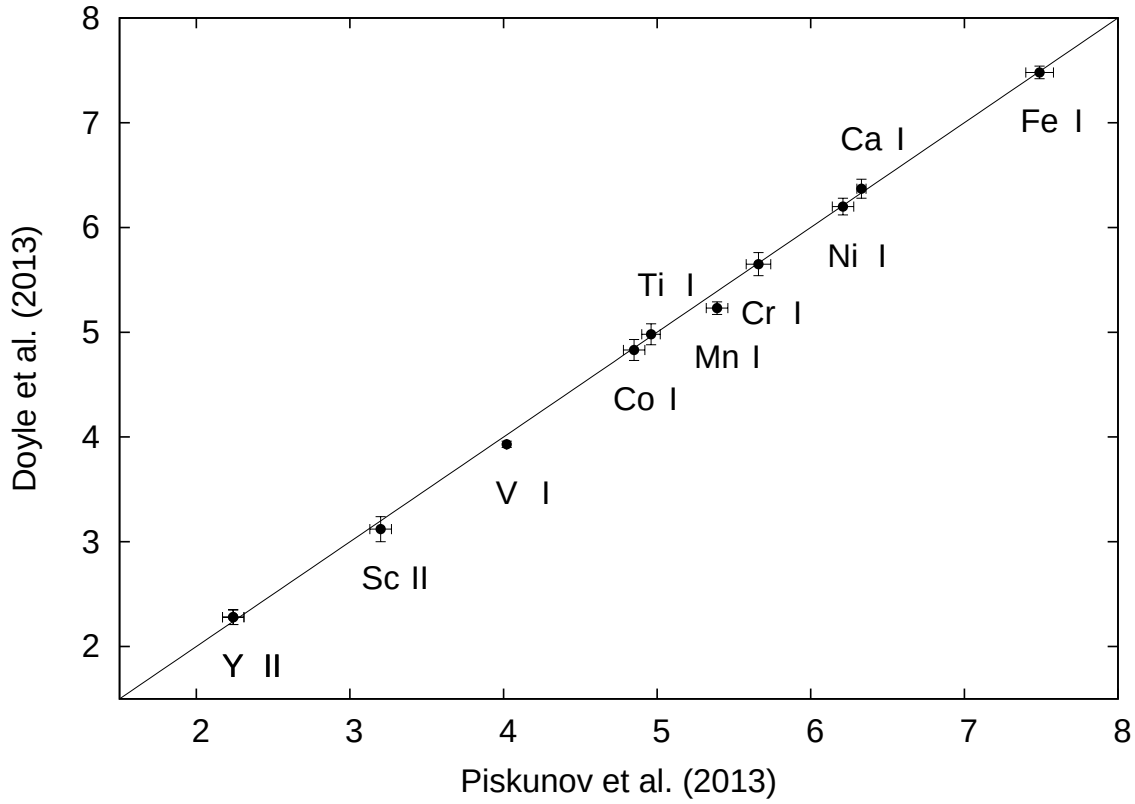

Figure 4.5: Comparison between SME and my method for Procyon abundances. The solid line is a 1:1 relationship. The abundances agree well except for Mn, likely because of HFS.

4.3 θ Cyg

The F4V star θ Cyg has a visual magnitude of 4.48, making it the brightest star that can be observed by the *Kepler* spacecraft. As it exhibits solar-like oscillations, asteroseismology can be used to determine an accurate and precise $\log g$ of 4.23 ± 0.03 dex. The star also has an M-dwarf companion, but unfortunately the orbital period is $\sim$230 years, making it currently impossible to derive the dynamical mass. Nonetheless, the brightness and proximity of the star allow detailed analyses to be performed, which is perfect for comparing methods. To determine the spectroscopic parameters of this star six different analyses were performed by different people, including my analysis (Guzik et al. 2014, in prep).

While the high resolution (85,000) HERMES spectrum of θ Cyg is more than adequate for measuring lines, a problem arose in my analyses when trying to interpret the results from the lines. The $T_{\rm eff}$ obtained from the excitation balance of the Fe I lines is $\sim$6900 K, which is anomalously high compared to the mean of previous literature values and the IRFM $T_{\rm eff}$, both of which are $\sim$6700 K. To confirm this, I also obtained a

$T_{\rm eff}$ estimate from the Balmer lines. As usual, the Hα line was very difficult to normalise, but even considering this obstacle the Hα line still line hints at a temperature around 6600 or 6700 K. The Hβ line was more obliging and was easier to normalise, giving a $T_{\rm eff}$ of 6700 K. The fits to the Balmer lines are shown in Figure 4.6. If the temperature is lowered to 6700 K, the excitation plot shows an obvious trend, with the low EP lines having lower abundances than their high EP counterparts. Mashonkina et al. (2011) find that lines with EP $<$ 1 eV need larger NLTE corrections than higher EP lines, however the INSPECT database gives the same NLTE correction for lines of low and high EP. Excluding all lines below 1 eV still results in an excitation balance $T_{\rm eff}$ of $\sim$6900 K. Including an NLTE correction for all the Fe I lines as was done for Procyon in Section 3.5 also didn't help and no change was seen in the $T_{\rm eff}$.

As there were enough Fe II lines present, I thought perhaps using these lines instead of Fe I might work, since they have a different temperature dependence. However, this has the opposite effect as the $T_{\rm eff}$ is then increased to 6970 K.

I thus chose to ignore the excitation $T_{\rm eff}$ and try to determine the parameters via the ionisation balance. The $\log g$ was determined in the usual manner, by combining the ionisation balance, and the fits to the Na and Ca lines, and these values are in good agreement giving 4.35 $\pm$ 0.08 overall. By adjusting both the $T_{\rm eff}$ and the $v_{\rm mic}$ so as to minimise the scatter in Fe, I obtained a best solution of $T_{\rm eff}$ = 6800 K and $v_{\rm mic}$ = 1.48 $\pm$ 0.08 km s^{-1}. To calculate the error on the $T_{\rm eff}$, I changed the $\log g$ and $v_{\rm mic}$ by their subsequent errors to see the effect on the $T_{\rm eff}$ thus arriving at an error of 108 K.

I fixed the $\log g$ to the asteroseismic value to see if a constrained analysis would improve the parameters. Using the excitation balance still produced a $T_{\rm eff}$ of 6900 K, so once again I just used the ionisation balance. However, this time I also kept the $v_{\rm mic}$ fixed to the value I had obtained from my best spectroscopic solution. The end result was that the $T_{\rm eff}$ was lowered to 6715 $\pm$ 92 K.

I performed a similar analysis using the NLTE corrected Fe I lines, and determined a $T_{\rm eff}$ of 6750 $\pm$ 108 K for the unconstrained analysis and 6670 $\pm$ 92 K when fixing $\log g$. All results are presented in Table 4.3.

Figure 4.7 shows the comparison of all the different methods in a $T_{\rm eff}$ - $\log g$ plot, and there is clearly a wide spread in the values. Bruntt and Sousa used the method based on the Fe lines, Frasca compared the spectrum to a grid of stellar spectra with well known parameters, and Lehmann and Latham used a grid of synthetic spectra. The dashed line represents the approximate location of the Fe ionisation balance. Also

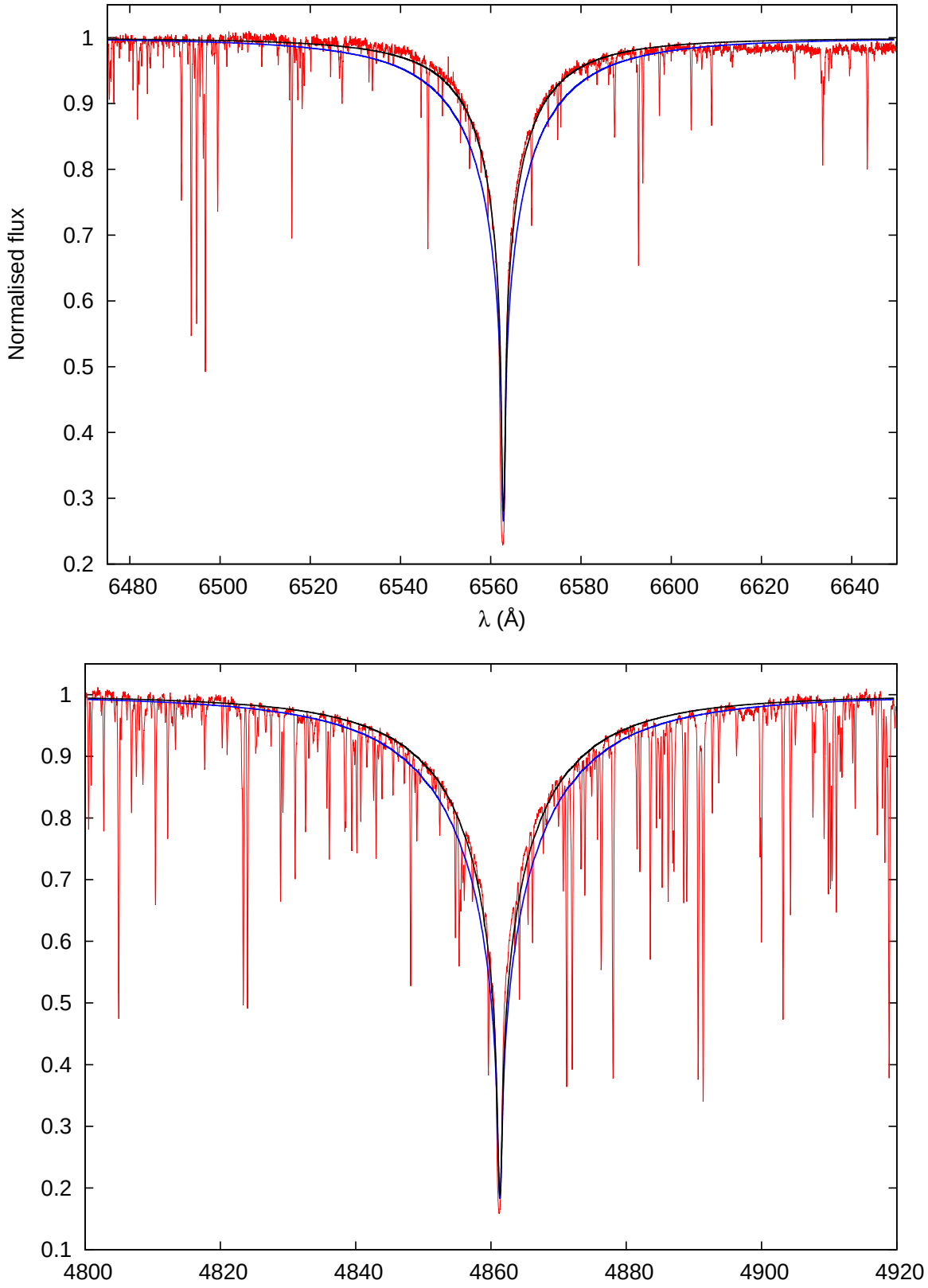

Figure 4.6: Top: The Hα show the observed spectrum in red, and synthetic fits at 6500 K (black) and 6900 K (blue). Bottom: The synthetic fits for Hβ are for 6700 K (black) and 6900 K (blue). The fits to the Balmer lines suggest the $T_{\rm eff}$ is a couple of hundred K lower than the 6900 K suggested by the excitation balance.

Table 4.3: Results from analysis of θ Cyg

	Unconstrained	Fixed $\log g$	Unconstrained; NLTE	Fixed $\log g$; NLTE
$T_{\rm eff}$	6800 ± 108	6715 ± 92	6750 ± 108	6670 ± 92
$\log g$	4.35 ± 0.08	4.23 ± 0.03	4.35 ± 0.08	4.23 ± 0.03
$v_{\rm mic}$	1.48 ± 0.08	1.48 ± 0.08	1.51 ± 0.08	1.51 ± 0.08
$\log A$ (Fe)	7.52 ± 0.08	7.47 ± 0.09	7.52 ± 0.09	7.52 ± 0.09

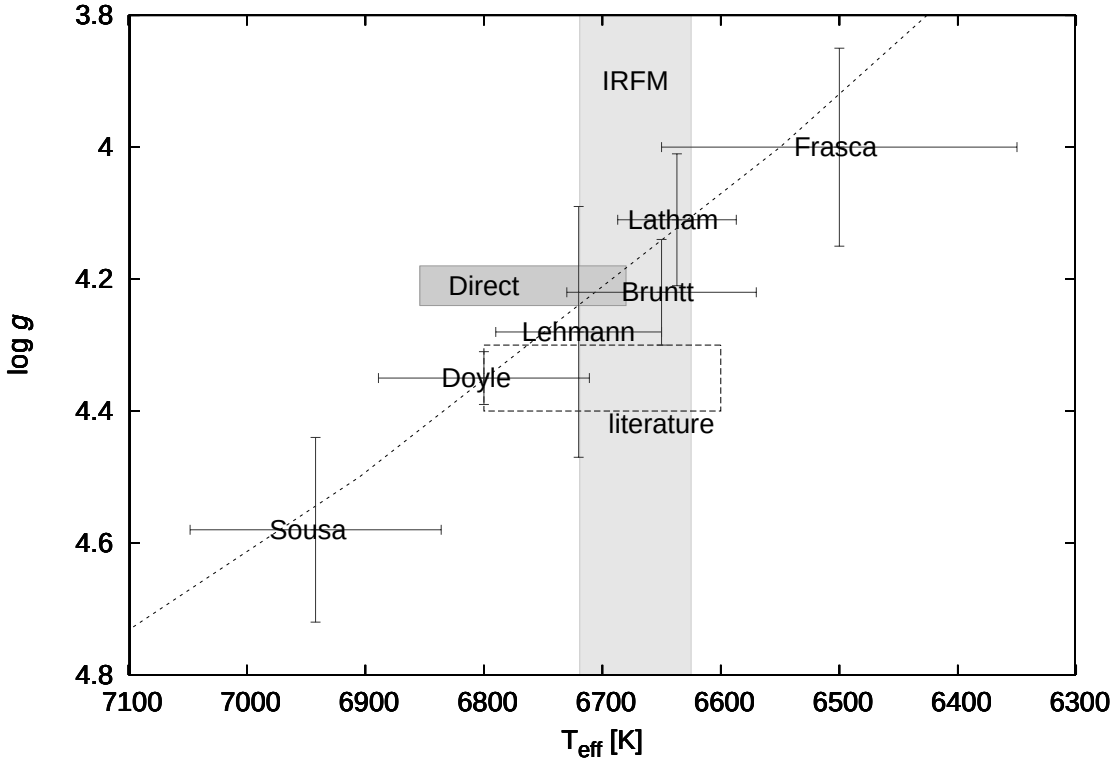

Figure 4.7: The $T_{\rm eff}$ and $\log g$ from the different methods are displayed, along with the direct, IRFM and best literature values. The dashed line represents the approximate location of the Fe ionisation balance. Credit: Guzik et al. 2014 (in prep).

shown are the location of the previous literature values, the IRFM $T_{\rm eff}$ (Blackwell & Lynas-Gray 1998), as well as the direct observations of $\log g$ from asteroseismology and the interferometric $T_{\rm eff}$ of Ligi et al. (2012).

4.4 Comparisons with other analyses in the literature

4.4.1 Tsantaki et al. (2013)

Tsantaki et al. (2013) aimed to improve the Fe line list used for the excitation and

ionisation balance, particularly for cool stars. They note that the spectroscopic $T_{\rm eff}$ of Sousa et al. (2008) is systematically higher than the IRFM $T_{\rm eff}$ for stars cooler than 5000 K, which they say could be due to line blending. Tsantaki et al. (2013) thus optimised their line list for cool stars by only selecting lines from the Sousa et al. (2008) list that were free of blends in a late K-dwarf. A comparison between both line lists showed that there is agreement above 5000 K, but below this the $T_{\rm eff}$ will be overestimated for cool stars with the Sousa et al. (2008) list.

However, given the discussion in Section 4.1.3, the Sousa et al. (2008) line list will still result in an overestimation of $T_{\rm eff}$ even for hotter stars. A solution to the blending problem might be to optimise a range of different line lists that are free of blends at a particular $T_{\rm eff}$.

Tsantaki et al. (2013) also note that $\log g$ and metallicity are not as sensitive to line selection as $T_{\rm eff}$. This is consistent with Method B and D from the WASP-13 analyses having similar $\log g$ and metallicity despite the different line lists. This also agrees with the fact that the Fe abundance is the same for the cool stars and solar lines lists given in Section 3.4.3, while the effect on $T_{\rm eff}$ is noticeable between these two lists.

They compared their spectroscopic $\log g$ values from the ionisation balance to the "trigonometric" $\log g$ based on *Hipparcos* parallaxes. The find that the spectroscopic $\log g$ values are underestimated for stars below 5000 K. They note that it is difficult to explain this discrepancy, but that the lack of Fe II lines in solar-like stars could lead to uncertainties in the spectroscopic $\log g$. This is in agreement with the discussion in Section 3.6.1.4.

4.4.2 Mortier et al. (2013b)

Mortier et al. (2013b) analysed 90 transiting planet host stars using spectra from a range of different spectrographs with the aim of homogeneously determining the parameters of the stars. They used ARES to measure EWs, and MOOG to perform the usual analysis with Fe lines to determine $T_{\rm eff}$, $\log g$, and $v_{\rm mic}$. They used the Sousa et al. (2008) line list for stars above 5200 K, and the Tsantaki et al. (2013) line list for cooler stars.

Figure 4.8 compares the $T_{\rm eff}$ for stars in common with the WASP analyses in Chapter 3, including WASP-13. It is clear that their $T_{\rm eff}$ is systematically higher, with an rms difference of 105 K. This is most likely due to the blends in the Sousa et al. (2008) line list. Mortier et al. (2013b) also noted that their $T_{\rm eff}$ values are on average

93 K hotter than those from the TEPCat catalogue of transiting planets (Southworth 2011).

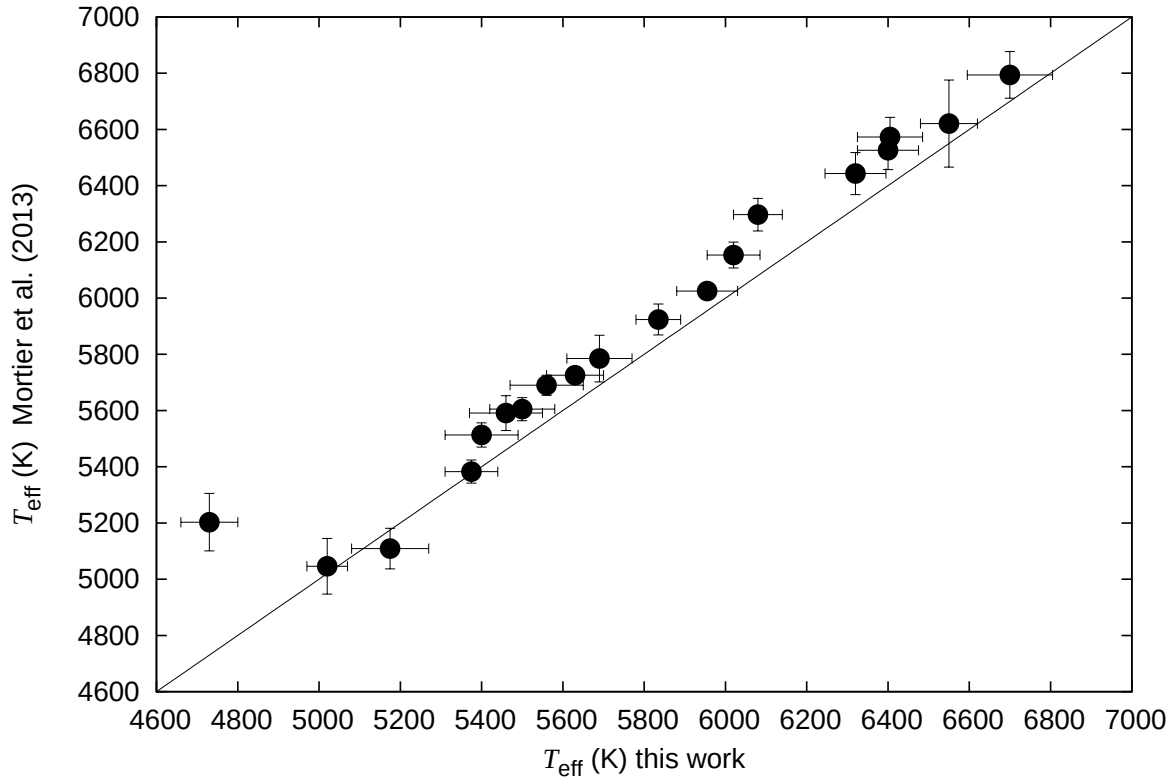

Figure 4.8: Comparison with the $T_{\rm eff}$ of Mortier et al. (2013b), which is systematically higher than the $T_{\rm eff}$ determined here. The solid line is the 1:1 relationship.

Their $v_{\rm mic}$ is also higher, as shown in Figure 4.9, and the difference between the two methods increases for higher values of $v_{\rm mic}$. This is most likely due the use of $\log gf$ values adjusted to the Sun as discussed in Section 4.1.3. However, as discussed in Section 3.6.3, the $v_{\rm mic}$ determined in this thesis is lower than other calibrations.

Their spectroscopic $\log g$, from the ionisation balance, is higher than this work as seen in Figure 4.10. This is probably because the $T_{\rm eff}$ and $v_{\rm mic}$ are also higher, and thus the $\log g$ is forced to larger values to compensate for this. However, as with the transit $\log g$, there is no systematic difference and they do not compare well, making it difficult to offer a suggestion as to why the values are different.

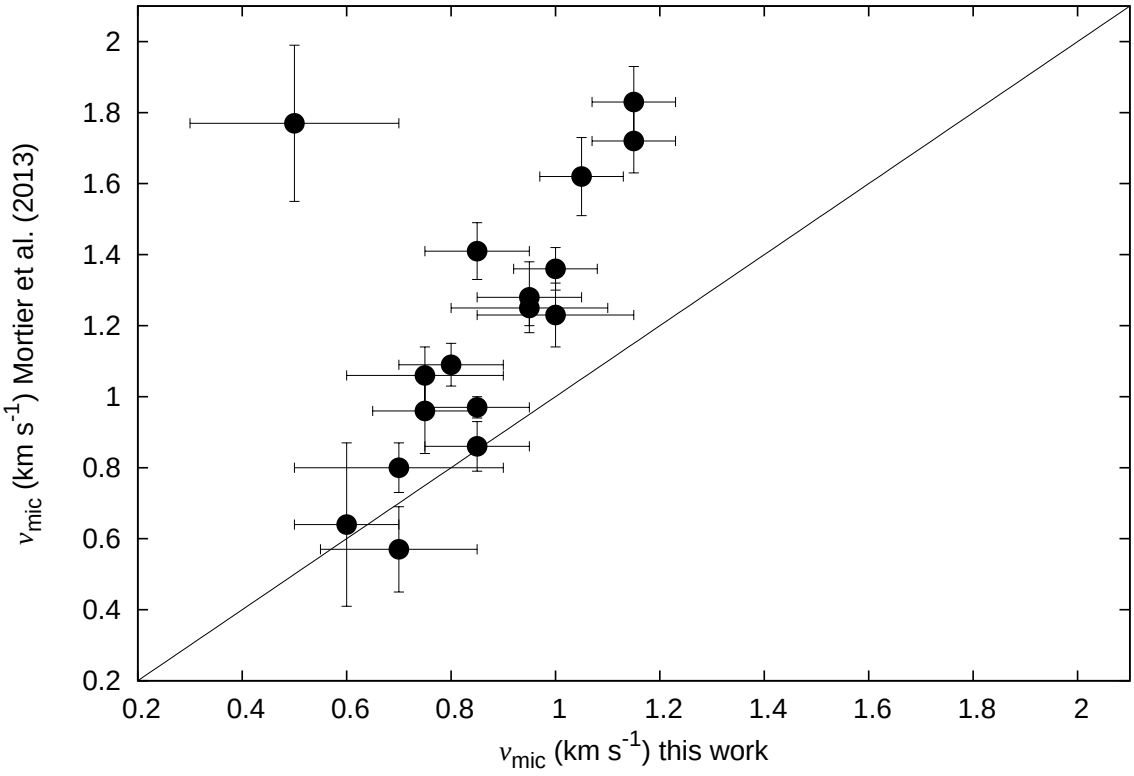

Figure 4.9: Comparison with the $v_{\rm mic}$ of Mortier et al. (2013b), showing that their $v_{\rm mic}$ are higher. The solid line is the 1:1 relationship.

4.4.3 Torres et al. (2012)

Torres et al. (2012) performed a comparison between different spectral analysis methods for 56 transiting planet host stars. They used SPC (Buchhave et al. 2012), which compares the spectrum to a grid of synthetic spectra, SME and MOOG. I have seven stars in common with Torres et al. (2012), however not all were analysed with all three of their methods. Interestingly, it is the MOOG results that disagree most strongly with my results. For instance, their $T_{\rm eff}$ for WASP-2 is 225 K hotter than mine. The MOOG $T_{\rm eff}$ for WASP-17 is 6300 $\pm$ 100 K, which is significantly lower than my NLTE $T_{\rm eff}$ of 6630 $\pm$ 100 K, as well as being 230 K lower than the SPC and SME methods. This is unexpected given that it is the method that is most similar to mine. This might be due to the use of a different line list, however they do not provide details of the lines they used. It is unclear from the paper which version of MOOG they use, but if it is the 2010 version then this may be a similar problem as was seen in Section 4.1.4.

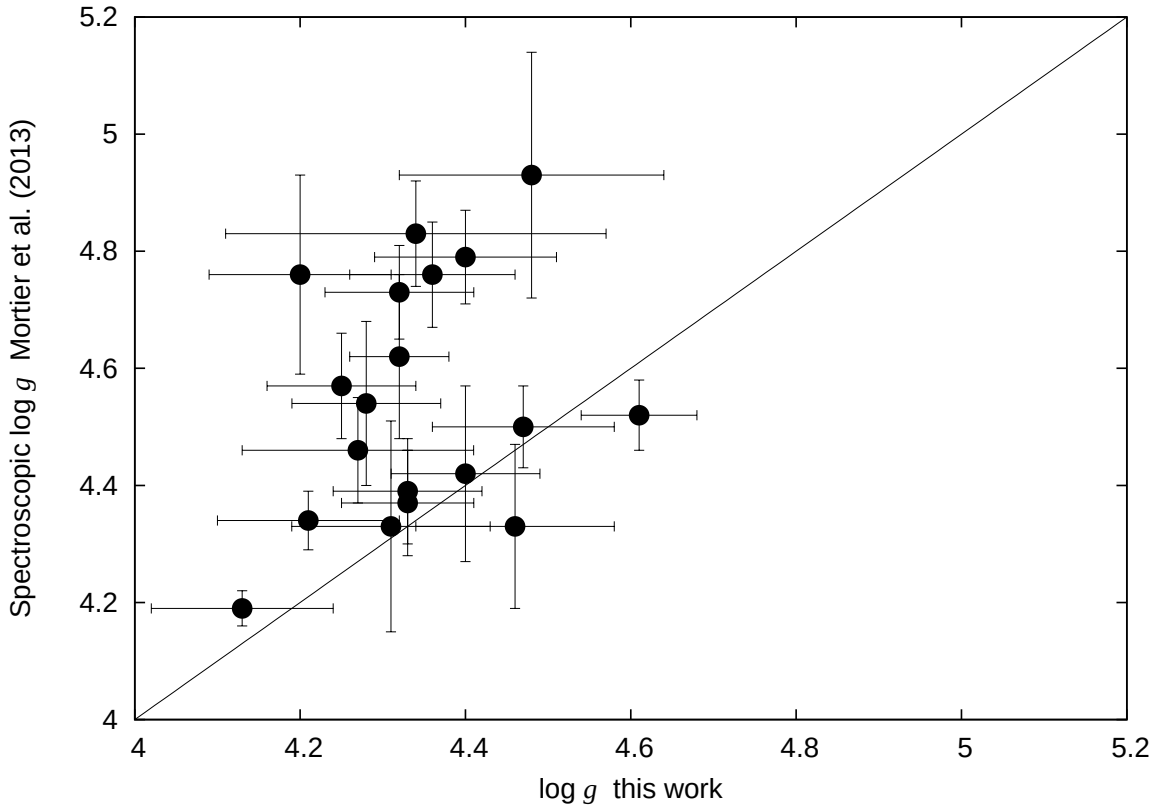

Figure 4.10: Comparison with the spectroscopic $\log g$ of Mortier et al. (2013b). Overall, their values are higher, but there is no systematic difference.

5 Disentangling projected rotational velocity from macroturbulence

It appears also that, other conditions being known, the mean velocity of rotation might be calculated.

- William de Wiveleslie Abney, 1877

The periodical obscuration or total disappearance of the star may arise from transits of the star by its attendant planets.

- Dionysius Lardner, 1858

Much can be ascertained about a star from the rate at which it spins. The rotation rate of a low-mass star decreases as it evolves due to magnetized winds carrying away the angular momentum (Schatzman 1962) and this spindown can be used to place constraints on the star's age (Skumanich 1972; Barnes 2007). The stellar rotation rate also depends on the star's mass (Meibom et al. 2011) and thus it is a key parameter when studying stellar evolution (Ekström et al. 2012; Gallet & Bouvier 2013). The rotation rate is also important for investigating how interactions with close-in planets can change stellar rotation rates (Bolmont et al. 2012). Knowledge of the stellar rotation rate is also essential in order to understand the obliquities of transiting planets, which is the motivation of this work. Some of the results in the this chapter have been published in Doyle et al. (2014).

5.1 Differential rotation

In 1630, Christoph Scheiner observed equatorial sunspots moving faster than those nearer to the poles. This phenomenon was attributed to differential rotation by Carrington (1860), who made detailed observations of the rotation rate of sunspots.

When angular rotational velocity varies with distance from the stellar centre it is known as radial differential rotation, and when it varies with latitude it is called latitudinal differential rotation. The former is detected on the Sun via helioseismology, and spots are used on the Sun and other solar-like stars to trace the latter (Ammler-von Eiff & Reiners 2012).

Differential rotation is modelled by

$$\Omega(\theta) = \Omega_{\rm equator}(1 - \alpha \sin^2 \theta), \tag{5.1}$$

where θ is latitude, $\Omega_{\rm equator}$ is the angular velocity at the equator, and α is a variable given by

$$\alpha = (\Omega_{\rm equator} - \Omega_{\rm pole})/\Omega_{\rm equator} = \Delta\Omega/\Omega. \quad (5.2)$$

The parameter α is called the differential rotation, while $\Delta\Omega$ is the absolute shear and has units of radians per day. However, $\Delta\Omega$ is also sometimes referred to as the absolute differential rotation, in which case α is known as the relative differential rotation. For the Sun, α is found to be 0.2, meaning that the equator rotates 20 per cent faster than the poles. α can be measured directly, but $\Delta\Omega$ requires a rotation period measurement, and thus a radius measurement (Reiners & Schmitt 2003; Reiners 2006).

Differential rotation leads to a sharper line profile, so that if $v \sin i$ is fit to the profile assuming it is a rigid rotator, the resulting $v \sin i$ value will be smaller than it should be and can differ by around 10 per cent from the true value for the solar case (Hirano et al. 2012). It is not just differential rotation that can change the shape of a line profile. In the wavelength domain, low inclination and high limb darkening have a similar effect on the line profile. These changes are very subtle and require high S/N before they can be recognised (Reiners & Schmitt 2002).

Differential rotation can be detected via Fourier analysis, where it is evident from the position of the zeros (Gray 1977a; Bruning 1981; Garcia-Alegre, Vazquez & Woehl 1982; Reiners & Schmitt 2002). Differential rotation can be inferred from starspot periodograms, as a second period adjacent to the primary one indicating spots at different latitudes have different rotation rates (Ballot et al. 2011; Reinhold & Reiners 2013; Reinhold, Reiners & Basri 2013). Planetary transits can also sometimes reveal differential rotation (Gaudi & Winn 2007; Hirano et al. 2011), as can Doppler imaging (Donati & Collier Cameron 1997; Collier Cameron, Donati & Semel 2002; Barnes et al. 2005).

5.2 The Rossiter-McLaughlin effect

When a planet transits a star, it casts part of the star into shadow, and this periodic reduction in flux is what allows transiting planets to be detected. When transits are viewed via spectroscopy, not only can the Doppler effect be observed, but it can also be possible to view an anomalous Doppler effect. With no transiting object, half of the star

will be blueshifted as it approaches us, and half will be redshifted as it recedes. However, a planet passing in front of the blueshifted half will weaken this signal and temporarily cause it to be slightly redshifted, and vice versa. This is called the Rossiter-McLaughlin (RM) effect and was first observed by Rossiter (1924) and McLaughlin (1924) for binary stars, and first observed in a transiting exoplanet system by Queloz et al. (2000).

The changing radial velocity as the planet transits the star depends on the angle at which the planet crosses the star. The true spin-orbit angle between the stellar spin axis and the orbital axis of the planet, ψ, is not directly measurable. However it is possible to measure λ, which is the angle in the plane of the sky between the projection of the stellar spin axis and the projection of the orbital angular momentum vector of the planet. The observer-orientated and orbit-orientated co-ordinate systems are depicted in Figure 5.1.

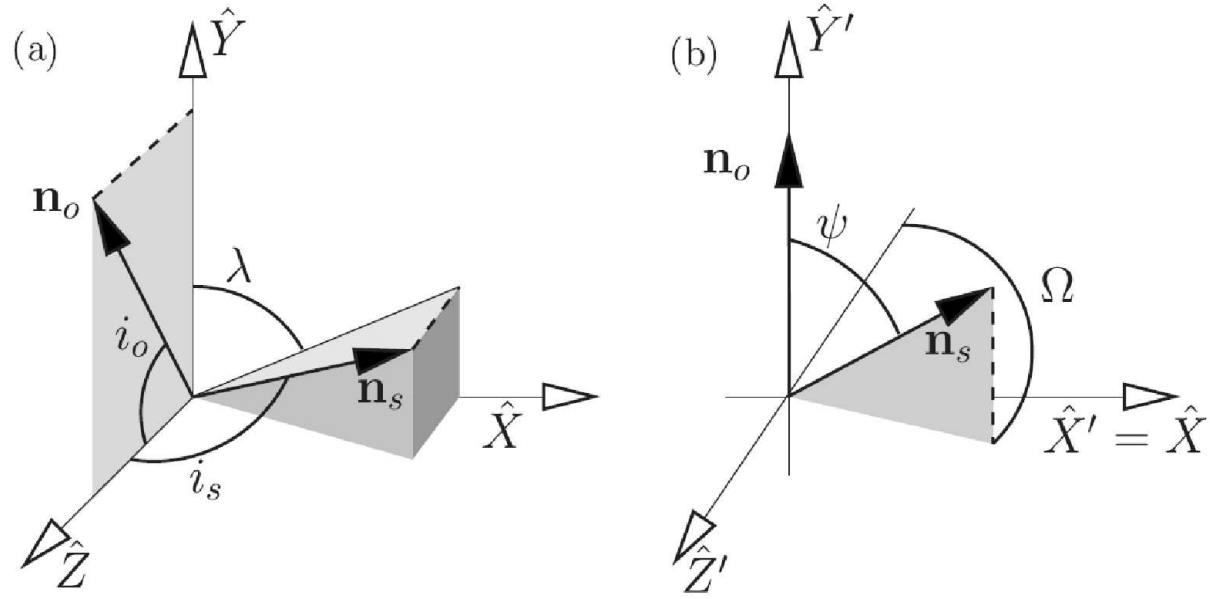

Figure 5.1: The observer-orientated co-ordinate system is shown in (a), where λ is the sky-projected spin-orbit angle, $\mathbf{n}_o$ is the orbital angular momentum vector of the planet, $\mathbf{n}_s$ is the stellar spin axis, i_o and i_s are the planetary orbital inclination and inclination of the stellar rotation axis relative to the line of sight respectively. The $\hat{X}$-$\hat{Y}$ plane is the sky plane and $\hat{Z}$ points towards the observer. The orbit-orientated system is shown in (b), where ψ is the actual spin-orbit angle of the system. Here, $\hat{Y}'$ is the orbital axis and the $\hat{X}'$-$\hat{Z}'$ plane is the orbital plane. Credit: Fabrycky & Winn (2009). Reproduced with permission.

The angle λ is determined from the asymmetry of the RM waveform, as shown in Figure 5.2. Three different possible paths of a planet across the star are depicted, each with the same closest approach of the planet to the centre of the star, known as the

impact parameter b. This means that the photometric signal from each transit will be the same. However, there are obvious differences in the systems when the RM effect is viewed. When the obliquity of the planet is negligible, the redshifted and blueshifted components are symmetric. However, when the planet is misaligned an asymmetric signal is produced as it only transits part of the redshifted part of the star, or doesn't transit this half at all (Gaudi & Winn 2007).

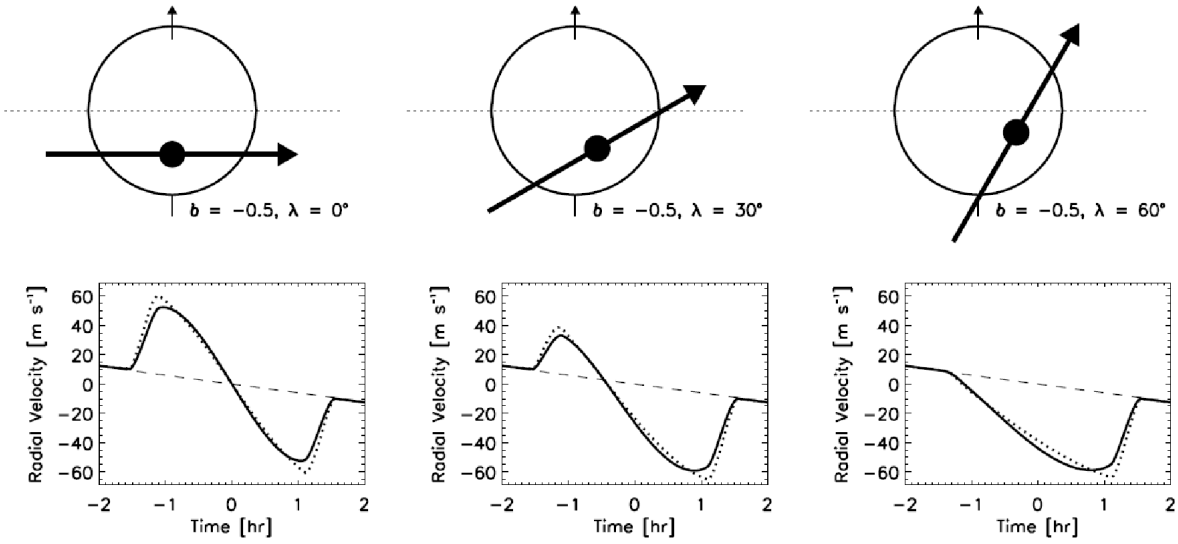

Figure 5.2: Different trajectories will change the RM signal, so that a misaligned planet will create an asymmetric signal. Credit: Gaudi & Winn (2007). Reproduced with permission.

If the orbital inclination of the planet $i_{\rm o}$, the inclination of the stellar rotation axis relative to the plane of the sky[1] $i_{\rm s}$, and λ are known, then ψ can be determined from (Chaplin et al. 2013)

$$\cos\psi = \cos i_{\rm s} \cos i_{\rm o} + \sin i_{\rm s} \sin i_{\rm o} \cos\lambda. \tag{5.3}$$

Unfortunately, while $i_{\rm o}$ and λ are constrained from the transit, $i_{\rm s}$ is not as straightforward to measure, and as such the spin-orbit angle is represented by λ instead of ψ. If the star has $i_{\rm s} = 90$, then the λ will be equivalent to ψ. A large value of λ indicates a large ψ, however the reverse is not true; in fact the value of ψ is quite uncertain for small values of λ (Fabrycky & Winn 2009; Schlaufman 2010).

[1]This is given as i throughout the rest of the thesis, but given as $i_{\rm s}$ here to distinguish it from the planetary inclination.

5.2.1 Misaligned planets

The presence of giant planets in short period orbits can be explained via migration (Lin, Bodenheimer & Richardson 1996). Gas giants are formed in the outer solar system, but tidal interactions with the protoplanetary disc cause the planets to lose angular momentum and migrate inwards towards the star. These motions damp the eccentricity and the inclination of the planets. Therefore, the discovery of misaligned planets (Hébrard et al. 2008) meant it was time to go back to the drawing board.

RM observations can possibly be used to distinguish between planets that underwent "ordinary" migration and those that underwent other processes that caused them to be misaligned. Therefore, by studying the distribution of λ with the properties of the host star, such as $T_{\rm eff}$, mass and age, it is possible to uncover clues as to the origin of these planets (Barker & Ogilvie 2009; Hirano et al. 2011).

The origin of misaligned planets is still not fully understood, and there are various theories involving few-body dynamics to explain them. Planet-planet scattering involves the dynamical interaction of a number of planets which can end with one being ejected and another migrating inwards (Rasio & Ford 1996; Chatterjee et al. 2008). Planet scattering combined with tidal circularisation can account for planets with high eccentricities or high inclinations (Nagasawa, Ida & Bessho 2008; Nagasawa & Ida 2011; Beaugé & Nesvorný 2012).

It is also possible that Kozai cycles (Kozai 1962) could generate highly inclined planets. Kozai cycles can occur when a close binary – in this case a star with a planet in a tight orbit – is influenced by a third object on a distant, inclined orbit. The perturber causes the eccentricity and inclination of the close binary to oscillate which can ultimately increase the obliquity of the planet (Fabrycky & Tremaine 2007; Nagasawa, Ida & Bessho 2008; Morton & Johnson 2011). The perturber can be either a star or a planet, however no stellar perturber has been observed so far in the hot Jupiter exoplanet systems (Beaugé & Nesvorný 2012).

5.2.2 The need for prior knowledge of $v \sin i$

In order to see why a $v \sin i$ prior can be important for the RM effect, and thus understand the motivation of this work, the amplitude and asymmetry of the RM effect need to be described.

The distance between the centre of the planet and the rotation axis of the star on the sky plane is given as x, and this is separated into x_1 and x_2 for the blueshifted and redshifted components. From the geometry shown in Figure 5.3, x_1 and x_2 are given as

$$x_1 = (\sqrt{1-b^2} - b\tan\lambda)\cos\lambda = \sqrt{1-b^2}\cos\lambda - b\sin\lambda, \tag{5.4}$$

and

$$x_2 = (\sqrt{1-b^2} + b\tan\lambda)\cos\lambda = \sqrt{1-b^2}\cos\lambda + b\sin\lambda. \tag{5.5}$$

The apparent velocity of a point across the surface of a star can be related to $v\sin i$ via $v(x) = x(v\sin i)$. Therefore the sum of x_1 and x_2 gives the mean amplitude of the RM effect, as shown in the right hand side of Figure 5.3, while the difference between x_1 and x_2 will give the asymmetry:

$$v\sin i\,(x_1 + x_2) = 2\sqrt{1-b^2}\,v\sin i\cos\lambda, \tag{5.6}$$

$$v\sin i\,(x_1 - x_2) = 2b\,v\sin i\sin\lambda. \tag{5.7}$$

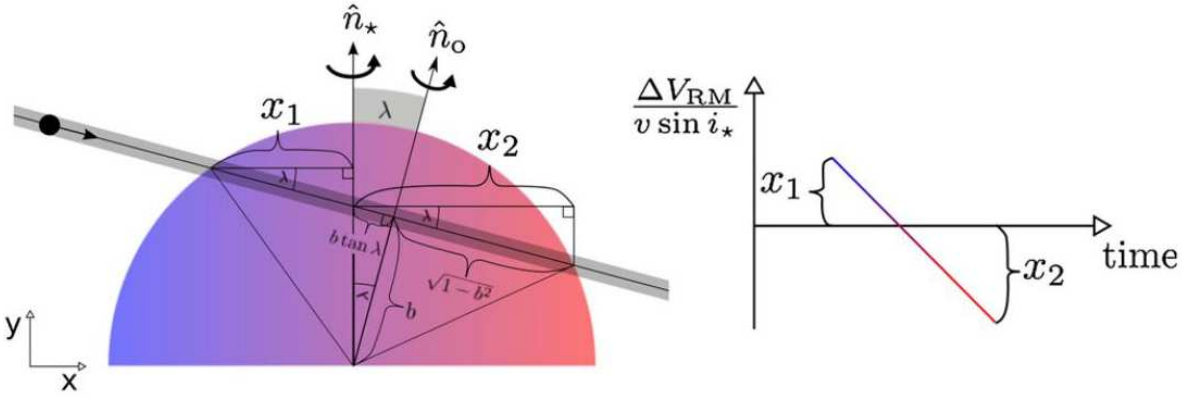

Figure 5.3: The geometry of the RM effect. The sum of x_1 and x_2 gives the amplitude, while their difference will give the asymmetry. Credit: Albrecht et al. (2011). Reproduced with permission.

The impact parameter has an important role to play in the asymmetry. If $b \approx 0$, then Equation 5.7 will also go to 0, meaning that the asymmetry, and thus the planet misalignment, can no longer be determined and only the mean amplitude can be measured. This is illustrated in Figure 5.4. WASP-2 has a high impact parameter, so the asymmetry is obvious in the RM waveform. In contrast, WASP-1 has a negligible

impact parameter, and therefore the RM waveform looks symmetric even when λ is high (Albrecht et al. 2011; Triaud 2011).

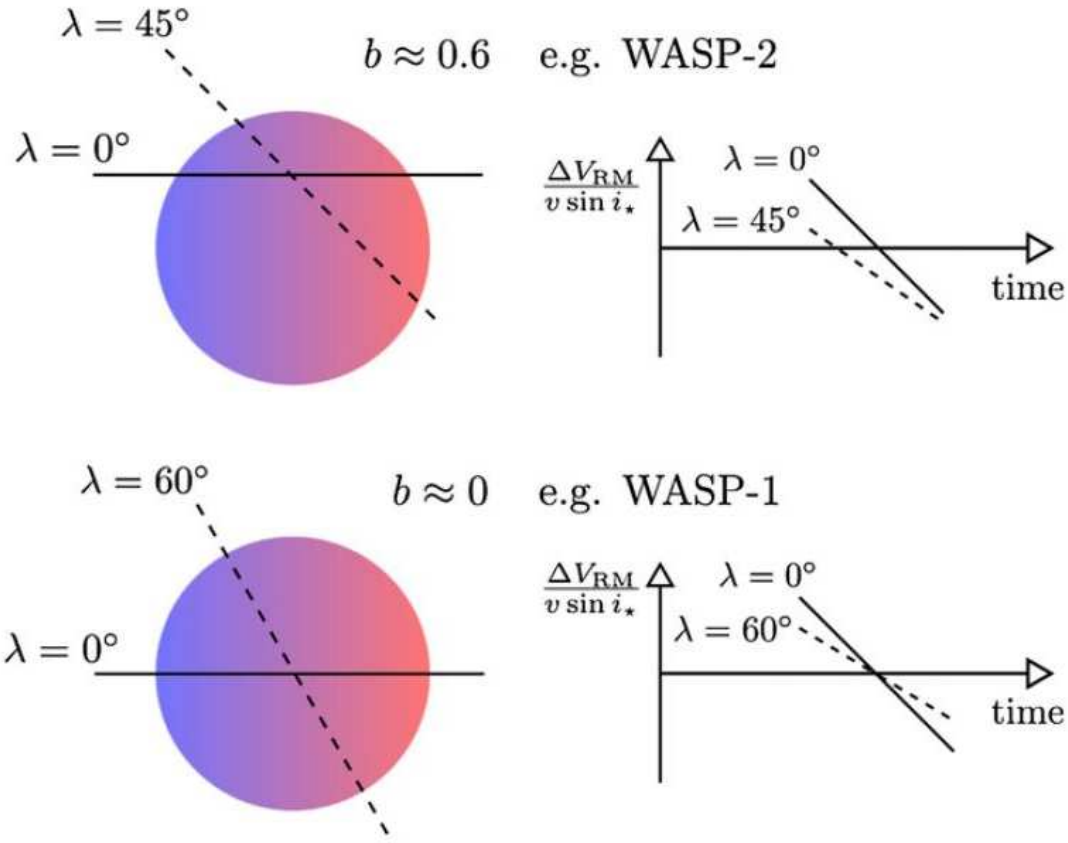

Figure 5.4: The low impact parameter of WASP-1 means that the asymmetry in the signal can no longer be detected for different values of λ. WASP-2 has a higher value of b, so that there is now an obvious difference in the signals. Credit: Albrecht et al. (2011). Reproduced with permission.

Thus, there is a degeneracy between $v \sin i$ and λ for $b \approx 0$, which can only be broken if there is prior knowledge of $v \sin i$. In most cases, the $v \sin i$ prior is obtained from the rotational broadening of the spectra, meaning that the value of macroturbulence chosen will influence the results (Albrecht et al. 2012b).

5.3 Rotation from asteroseismology

The rotation of a star will ultimately influence the frequencies obtained via asteroseismology, and this can be directly related to the $v \sin i$, allowing an independent determination of the rotational velocity. As discussed in Section 2.6.2, a mode is described by n, l and m. The azimuthal order m is given as $(2l + 1)$, however in the absence of

rotation the m frequencies will all be the same and the frequency of the mode is given as $\nu_{\rm nl}$. For a rotating star, this degeneracy is lifted, so that the non-radial mode is now split into a multiplet described by the m components. The frequency of the mode can then be given as

$$\nu_{\rm nlm} \equiv \nu_{\rm nl} + \delta\nu_{\rm nlm}. \tag{5.8}$$

If significant latitudinal differential rotation was present, then there would be a variation of the frequency splittings between modes. The Sun-as-a-star data shows miniscule variations in $l = 3$ and $l = 4$ modes, but even this is difficult to detect (Chaplin 2011). Thus solid body rotation can safely be assumed for solar-like stars and $\delta\nu_{\rm nlm}$ can be written as $\delta\nu_{\rm s}$ as all frequency splittings have the same value. The frequency splitting is related to the rotation of the star via $\delta\nu_{\rm s} = \Omega/2\pi$ where Ω is the angular velocity (Ballot, García & Lambert 2006; Chaplin et al. 2013).

As non-radial modes are not spherically symmetric, the angle at which they are viewed is a factor in detecting the frequency splitting. For example, as shown in Figure 5.5, an $l = 1$ mode at $i = 90°$ has $m = \pm 1$ components that can quite clearly be seen, and the $m = 0$ component does not contribute to the line profile at all. This is because at $i = 90$, the intensity perturbations from the northern and southern hemispheres cancel out for $m = 0$. As i diminishes, the splitting evident from the $m = \pm 1$ modes will become less evident as blending becomes more prominent. At $i = 0$, the contribution from the $m = \pm 1$ components has vanished completely, leaving only the $m = 0$ component, which presents itself as a single, unsplit line profile (Chaplin et al. 2013). Therefore it is possible to estimate the inclination from the ratio of the amplitudes of the m components, assuming the data have a sufficiently high S/N (Gizon & Solanki 2003).

If the multiplet components are blended, then the measured values of i and $\delta\nu_{\rm s}$ are highly correlated, even though physically the two parameters are independent of each other. This can make it difficult to disentangle the two parameters, and can create significant errors. It is possible for there to be different couples of i and $\delta\nu_{\rm s}$, so that there is no unique solution. Using their combination, $\delta\nu_{\rm s} \sin i$, reduces the correlation for stars with low rotation rates, and also reduces the uncertainty (Ballot, García & Lambert 2006; Ballot et al. 2008; Chaplin et al. 2013).

Figure 5.5 shows example of $l = 1$ modes that all have the same linewidth, Γ, of 3 μHz. However, changing the linewidth will also have an effect on the ability to detect

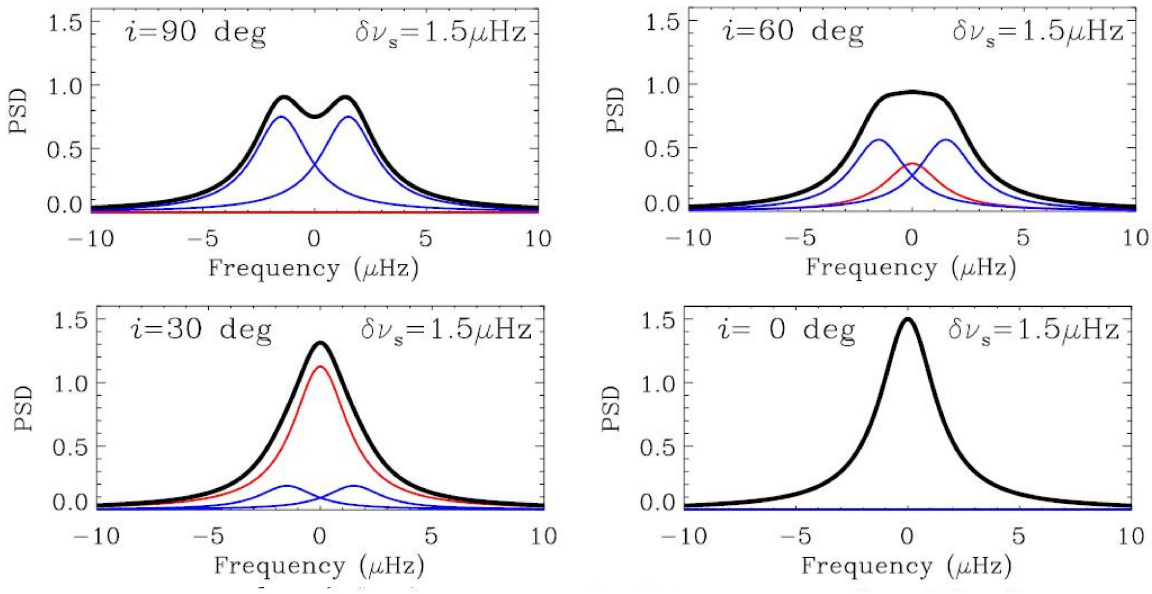

Figure 5.5: For an inclination of 90°, the $m = \pm 1$ components (in blue) are visible, while the $m = 0$ component (in red) does not contribute to the line profile. For low inclinations, the $m = 0$ component becomes prominent while the $m = \pm 1$ component diminish. Therefore there is no frequency splitting evident for low inclinations. Credit: Chaplin et al. (2013). Reproduced with permission.

frequency splitting. Linewidth increases with $T_{\rm eff}$ (Appourchaux et al. 2012), which makes $\delta\nu_{\rm s} \sin i$ harder to determine for hotter stars as blending increases. For instance if the linewidth or the splitting is similar to the small frequency separation, it can make it difficult to distinguish between $l = 0$ and $l = 2$ modes, thus hampering the ability to fit a unique solution (Barban et al. 2009).

For stars with a rotation several times that of the Sun, it is easier to extract the splitting and inclination as $\delta\nu_{\rm s}$ will be greater than Γ. At lower rotation rates, $\delta\nu_{\rm s} < \Gamma$ creates blending of the multiplet, making it difficult to resolve (Gizon & Solanki 2003; Ballot, García & Lambert 2006). However, it is still possible to measure $\delta\nu_{\rm s} \sin i$ even when the splitting isn't resolved, as the m components will broaden the line profile, and this broadening can be measured. This is more likely for the $l = 2$ mode, which has more m components and thus greater broadening (Gizon et al. 2013).

By using $\delta\nu_{\rm s} \sin i$ along with an accurate determination of stellar radius, the $v \sin i$ of the star can be determined via (Chaplin et al. 2013)

$$v \sin i \equiv 2\pi R \, \delta\nu_{\rm s} \sin i. \tag{5.9}$$

The asteroseismic $v \sin i$ values used for this work were kindly provided by Guy Davies and Bill Chaplin of the University of Birmingham.

5.4 Instrumental broadening

The resolution of a spectrograph is given as $R = \lambda/\Delta\lambda$, and in order to truly disentangle the rotational and macroturbulent broadening in the line profiles, it is imperative to know how the spectrograph itself broadens the lines. Unfortunately, the resolution of a spectrograph isn't a value that's set in stone. It can vary with time (Ramírez, Allende Prieto & Lambert 2008), and even for the highly stable HARPS spectrograph, different literature sources can quote vastly different values. For example Queloz et al. (2001) give the HARPS resolution as 90,000, Pepe et al. (2002) determine R to be 98,000 while in Mayor et al. (2003) R is 115,000.

The spectra of the *Kepler* stars used for this work were obtained by Bruntt et al. (2012) using the ESPaDOnS spectrograph at the 3.6 m Canada-France-Hawaii Telescope, and the Narval spectrograph at the 2 m Bernard Lyot Telescope. ESPaDOnS has a resolving power of ∼81,000 (Donati et al. 2006) and Narval, which is an almost identical spectrograph, has a resolving power of ∼75,000. High resolution spectra were required in order to distinguish between different types of broadening in the spectral lines. Bruntt et al. (2012) selected 93 stars that showed evidence of solar-like oscillations in the *Kepler* data. A subset of these stars was chosen for this work with the criteria that they must not have mixed modes, and that the asteroseismic S/N should be high enough to clearly detect splitting.

The instrumental broadening can be measured using the telluric lines for a spectrum that hasn't been coadded with others, assuming the S/N is high enough. This method isn't appropriate for the ESPaDOnS spectra, as the telluric lines only suggest that the resolution is between 75,000 and 81,000, and do not give a clear result. I therefore determined the instrumental broadening using ThAr spectra. The ThAr spectra were coadded to increase the S/N and wavelength calibration was performed using the IRAF ecidentify package.

By using the programme *SPLAT* to fit a Gaussian to a number of lines in each order, I was able to determine the FWHM ($\Delta\lambda$) for those lines. As expected, the FWHM increases with wavelength as seen in Figure 5.6. However, there is still a significant amount of scatter in the FWHM values which could be due to blending or misidentification of the lines (Murphy et al. 2007). Ramírez, Allende Prieto & Lambert (2008) and Ramírez et al. (2009) noted that Th lines are sharper than Ar lines due to differences in thermal broadening, although this isn't significant enough to explain

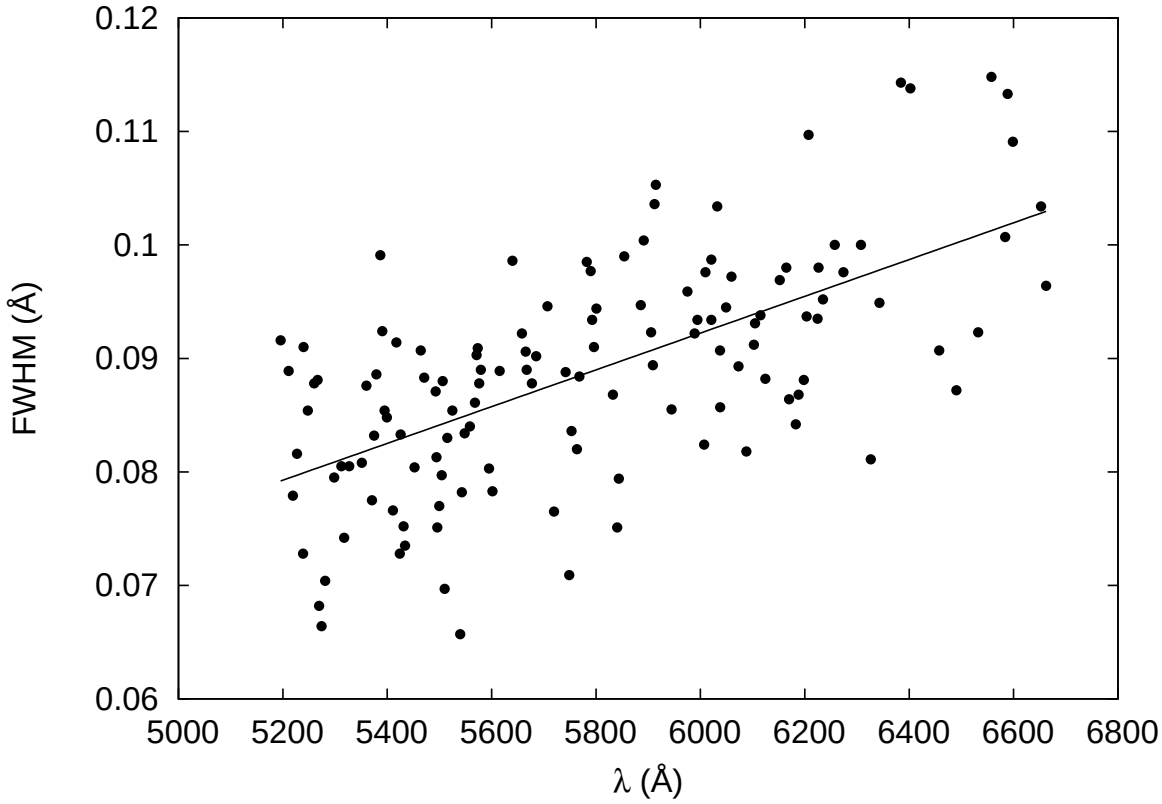

Figure 5.6: The FWHM of the ThAr lines as a function of λ shows the expected increase in FWHM with increasing λ. The solid line is a best fit to the points.

the scatter in the FWHM values. They also found their ThAr lines from the 2dcoudé spectrograph (R $\gtrsim$ 150,000) on the 2.7 m telescope at McDonald Observatory were slightly asymmetric, and there was a slight deviation from a Gaussian profile. However, this asymmetry isn't detectable for the lower resolution ESPaDOnS spectrograph. In addition, the binning (discussed further below) makes it difficult to notice any subtle deviations in the line profile shapes. A Gaussian is therefore still the best fit for the instrumental profile, as can be seen in Figure 5.7.

Figure 5.8 shows the resolution as a function of wavelength, with a linear fit to the data showing that the resolution is approximately 65,500. This is clearly in disagreement with the published value. However, it later came to light that the CCD on ESPaDOnS had been updated not long after the ThAr spectrum was taken. Therefore, the resolution obtained from the ThAr spectrum is also not useful for determining the resolution of the stellar spectra.

The ESPaDOnS pipeline rebins the stellar spectra using bin sizes of 1.8 $\mathrm{km\,s^{-1}}$ (Donati 2004), therefore it was necessary to also bin the synthetic spectrum in UCLSYN. This was done by binning the synthetic spectrum into 2.6 $\mathrm{km\,s^{-1}}$ bins, and then inter-

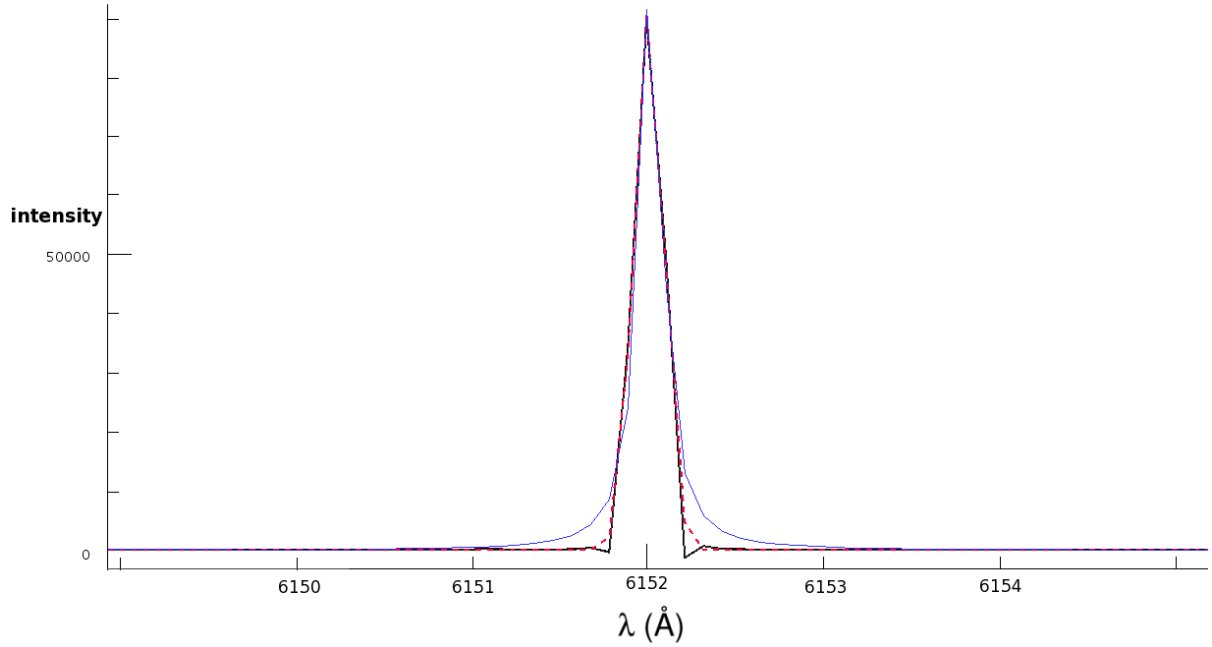

Figure 5.7: The Th line at 6151.993 Å for the ESPaDOnS spectrograph is shown along with the Gaussian (red dashed) and Lorentzian (blue solid) fits.

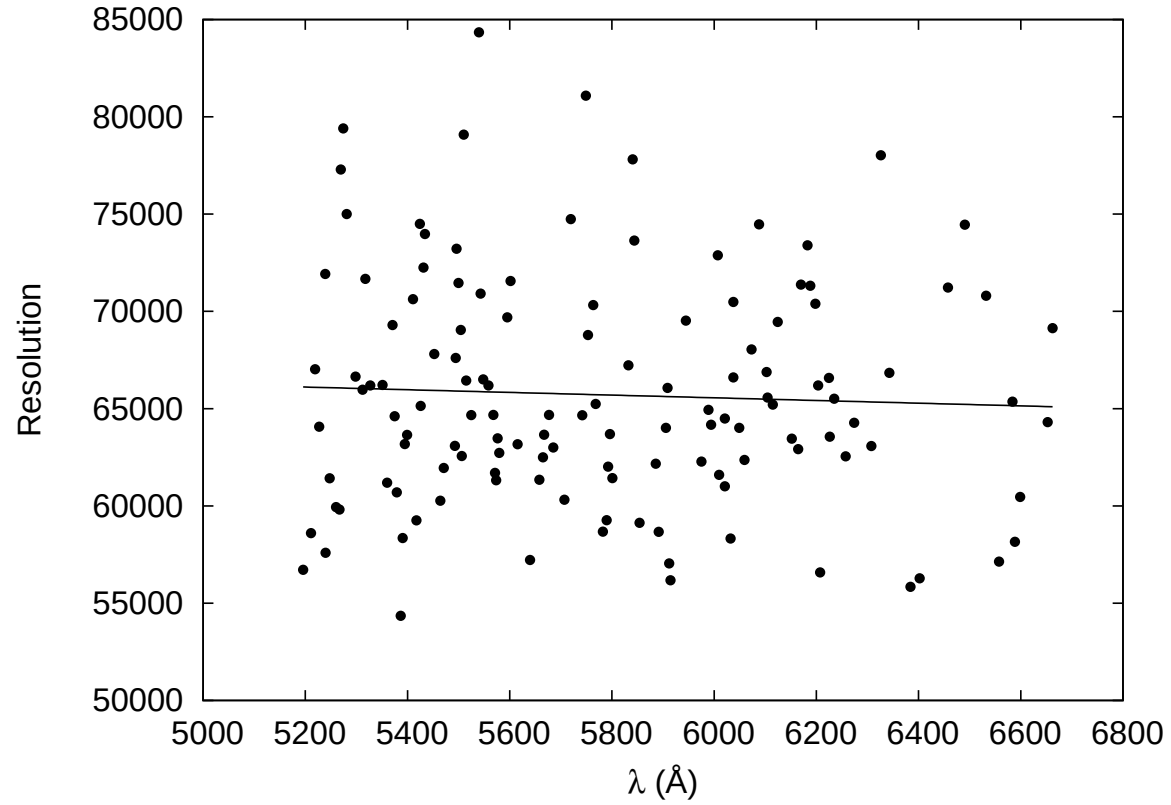

Figure 5.8: Resolution as a function of λ shows the resolution is constant, however there is a lot of scatter.

polating over the 1.8 km s^{-1} bins of the observed spectra. A Gaussian with R = 81,000 can then be fit to the binned synthetic spectrum. As the Narval spectrograph is almost identical to ESPaDOnS, the same binning process was used for those spectra. The final value for R for each spectrograph was chosen based on the binned solar spectra, as discussed in the next section.

5.5 Measuring macroturbulence

Before measuring the macroturbulence, I had to choose a subset of lines from Section 3.4 which could be used with reasonable confidence, i.e. those that are unblended over as large a $T_{\rm eff}$ range as possible. These lines are are listed in Table 5.1 and the table also includes four Fe I lines which weren't used in the calibration, and this will be discussed in Section 5.9. In cooler stars blending will become an issue for some of these lines, in which case they are rejected. Stars that are slightly metal-poor will also have fewer measurable lines. In stars with a relatively high $v \sin i$ ($\gtrsim$ 12 km s^{-1}), blending also becomes an issue as the selected lines will become broadened and encroach on other nearby lines. Unresolved blends were rejected in these stars, however due to the paucity of suitable lines in high $v \sin i$ stars, resolved blends were still used. While line asymmetries should only be evident for a resolution greater than 100,000 (Gray 2008), there does appear to be some asymmetric lines in these spectra. In such cases, lines were rejected as it was impossible to fit the $v_{\rm mac}$ to both wings. I selected a range of elements, line strengths, and excitation potentials in order to see if macroturbulence affected the various lines in different ways. I excluded Mn, Co and V as these lines are prone to broadening from HFS, and Si as the lines are difficult to fit.

I first determined the radial-tangential $v_{\rm mac}$ for the Kitt Peak Solar Atlas, HARPS, ESPaDOnS and Narval solar spectra by using a least squares fit for each spectral line. The $v \sin i$ was fixed to 1.9 km s^{-1} (Gray 1977b), and $v_{\rm mic}$ was assumed to be 1.0 km s^{-1}. I checked all lines individually by eye to ensure that the fitting was correct and to eliminate any lines with bad fits. The final $v_{\rm mac}$ value given is the average of all the lines used. The $v_{\rm mac}$ determined for the Kitt Peak Solar Atlas is 3.21 $\pm$ 0.27 km s^{-1}, and as the resolution of 300,000 means that the instrumental broadening is negligible in this spectrum, this $v_{\rm mac}$ value was deemed to be the solar value for the purpose of this work. This is reasonably consistent with the range of values (3.1 km s^{-1} for strong lines and 3.8 km s^{-1} for weak lines) determined from the Fourier analysis of Gray (1977b).

Table 5.1: Spectral lines used to fit macroturbulence. The EWs and $v_{\rm mac}$ for the Kitt Peak Solar Atlas are also given.

Element	λ (Å)	EP (eV)	$\log gf$	Effective Landé g	Sun EW (Å)	Sun $v_{\rm mac}$ (km s^{-1})
Cr I	5238.964	2.709	-1.305	1.43	0.0163	3.71
Ti I	5295.780	1.067	-1.633	1.23	0.0278	3.54
Y II	5402.774	1.839	-0.510	0.89	0.0106	3.29
Ti II	5418.751	1.582	-2.110	1.04	0.0493	3.46
Fe II	5425.257	3.199	-3.220	1.24	0.0404	3.81
Fe I	5538.517	4.218	-3.244	1.96	0.0383	3.39
Fe I	5576.090	3.430	-1.000	0.00	0.1330	2.77
Fe I	5651.470	4.473	-2.000	1.88	0.0183	3.25
Fe I*	5732.275	4.991	-1.560	1.40	0.0146	3.92
Ca I	5867.563	2.933	-1.570	1.00	0.0243	3.22
Fe I*	5956.692	0.859	-4.605	0.71	0.0531	3.05
Fe I*	6055.992	4.733	-0.460	0.87	0.0759	2.92
Ni I	6111.066	4.088	-0.870	1.22	0.0347	3.55
Fe I	6151.617	2.176	-3.299	1.84	0.0502	2.93
Fe I	6200.319	2.609	-2.437	1.51	0.0736	3.08
Ni I	6204.600	4.088	-1.100	1.28	0.0226	3.47
Ni I	6223.980	4.105	-0.910	0.84	0.0286	3.39
Fe I	6252.554	2.404	-1.687	0.95	0.1246	3.03
Ti I	6258.104	1.443	-0.355	1.00	0.0525	2.89
Ni I	6378.247	4.154	-0.830	0.83	0.0326	3.51
Fe I*	6710.319	1.485	-4.880	1.69	0.0151	2.98
Ni I	6772.313	3.658	-0.980	0.92	0.0496	3.08
Fe I	6810.257	4.607	-0.986	1.49	0.0511	3.09
Fe I	6857.249	4.076	-2.150	1.14	0.0225	3.51

* Lines not used in the final calibration

Using the nominal resolution of 81,000 for the ESPaDOnS solar spectrum gave $v_{\rm mac} = 3.48 \pm 0.40$ km s^{-1}. Similarly, the nominal resolution of 75,000 for Narval gave $v_{\rm mac} = 3.04 \pm 0.50$ km s^{-1}. Although these values agree with the Kitt Peak Solar Atlas within the errors, the discrepancies can be ascribed to a slightly incorrect value of the spectral resolution adopted for ESPaDOnS and Narval. As a check on the resolution values, I varied the average resolution of the synthetic spectra until the $v_{\rm mac}$ equal to the Kitt Peak Solar Atlas value. The HARPS solar spectrum was also included, although binning is not required for HARPS. The resolution and $v_{\rm mac}$ for each solar spectrum are given in Table 5.2.

For the *Kepler* stars, I used the $T_{\rm eff}$, $\log g$ and $v_{\rm mic}$ from Bruntt et al. (2012), where $\log g$ was determined from asteroseismology. The errors are given as 60 K, 0.03 dex and 0.05 km s^{-1} for $T_{\rm eff}$, $\log g$ and $v_{\rm mic}$ respectively. Including the resolution de-

termined from the solar spectra and fixing the $v \sin i$ to the asteroseismic value, the radial-tangential $v_{\rm mac}$ was determined for each star using the binned spectra. The individual $v_{\rm mac}$ measurements for each line of each star are given in Table 5.3.

Table 5.2: Resolution and $v_{\rm mac}$ for each solar spectrum

Spectrograph	Resolution	$v_{\rm mac}$ (km s^{-1})
Solar Atlas	300 000	3.21 ± 0.27
HARPS (day sky)	98 000	3.21 ± 0.19
ESPaDOnS (twilight sky)	76 000	3.21 ± 0.53
Narval (Moon)	80 000	3.20 ± 0.49

Table 5.3: $v_{\rm mac}$ (km s^{-1}) measurements of individual lines. Line wavelengths are given in Å.

KIC	Cr I 5238	Ti I 5295	Y II 5402	Ti II 5418	Fe II 5425	Fe I 5538	Fe I 5576	Fe I 5651	Ca I 5867	Ni I 6111
1435467			5.47	5.58	5.45	6.07	5.09	4.88		6.12
2837475				11.17			13.00			
3427720	3.73	2.88	2.11	3.50	4.10	4.03	4.56		3.24	4.43
3632418			4.39	4.59	4.49	4.95	5.22	4.53	5.51	4.61
3656476	3.09			3.61	3.88	3.30	3.58	3.29	3.40	3.18
4914923	4.09		4.08	4.04	3.78	4.13	4.44	4.55	4.82	4.01
5184732	3.77	3.76	2.66	3.54	4.17	2.70	4.13	3.43	3.96	3.57
6106415	4.90	4.53	4.25	3.82	3.82	3.35	4.28	4.19	5.54	3.42
6116048			3.99	3.52	3.90		4.52		3.72	3.80
6508366				9.00	8.44		10.69			
6933899			3.41	4.03	4.35	3.89	4.27	2.47		4.58
7680114				3.37	3.59	3.47	3.58		5.08	3.55
7871531				2.52	3.11	3.46	3.11	1.99	3.31	2.77
7970740	2.26	2.43		1.19			3.28	1.89	3.55	2.43
8006161	2.14	2.39		2.67	3.26	2.19			2.85	2.34
8228742				3.25	3.52	3.86	4.85		4.52	4.40
8394589				5.54	5.20		5.47			4.69
8694723				5.94	5.72		6.89			
9098294				4.76	3.83		3.98		4.20	
9139151	3.96			3.32	3.84	3.78	4.44		4.01	3.19
9812850			5.68		5.83		6.47			
9955598	2.34	2.03		2.59	3.25	2.12	3.21	1.32	2.72	1.99
10355856				5.62	4.40	4.28	5.92			
10454113			5.85	4.04	4.67	4.56	5.51	4.64	5.14	4.46
10644253	3.62		3.22	3.96	4.68	3.56	4.17	4.01	4.45	3.35
10963065			4.55	4.15	3.86	3.55	4.48		4.46	4.33
11244118	3.46	4.13	3.66	3.65	4.05	2.97	3.68	2.96	4.01	2.81
12009504				4.33	4.09		4.69			5.05

Table 5.3: $v_{\rm mac}$ (km s^{-1}) measurements of individual lines (continued).

KIC	Fe I 6151	Fe I 6200	Ni I 6204	Ni I 6223	Fe I 6252	Ti I 6258	Ni I 6378	Ni I 6772	Fe I 6810	Fe I 6857
1435467	5.54	5.89	5.34	5.18	6.19		5.62		6.19	
2837475		11.55			12.55					
3427720	3.72	4.51		3.89	3.75	4.36	4.41	3.77	3.86	3.59
3632418	5.97		4.70		3.59	6.01		4.84	4.79	
3656476		3.59	4.00	4.16	2.90	3.75	4.53		3.21	3.52
4914923		3.86	4.25	4.52	3.91	3.56		4.20	3.91	
5184732	2.82	3.97	3.55	4.98	2.95	3.48	4.46	4.43	3.44	3.66
6106415	4.06	4.52	3.35	3.82	4.02	3.83	4.41	4.46	4.50	3.81
6116048	4.38	4.63	3.10		3.96	4.03	4.82	4.62	3.28	
6508366		9.81			11.24					
6933899	3.90	4.51	4.72	4.18	4.30	4.32	4.55	4.30	4.22	5.18
7680114	3.44	3.89		3.33	3.06	3.42	3.94	4.08	3.30	
7871531	2.58	3.04	3.09	1.95	2.88	2.89	3.02	3.27	2.98	1.79
7970740	1.34	3.02			2.53	1.95	2.42	3.27	2.78	
8006161	1.34	2.49	2.52		1.74	1.57		3.11	1.69	2.06
8228742	3.36	5.05		5.02	3.94		4.28		4.53	
8394589	4.91	5.72			4.37		4.82			
8694723	4.11	8.20			6.31				6.76	
9098294	3.50	3.50			2.64	3.08		3.36	4.29	
9139151	3.65	4.40	4.34		4.06		4.28	4.56	4.29	3.57
9812850		6.00			6.26			6.14		
9955598	1.51	3.18	3.10	3.38	2.31	2.18	3.68	3.41	2.13	1.31
10355856		7.23			5.94	6.01			5.75	
10454113	4.31	5.52	4.85	4.75	4.78	4.62	4.77	5.02	4.21	
10644253	2.65	4.47		4.07	3.99	3.86	3.78	3.59	3.67	4.18
10963065	4.52	4.88	4.59	4.29	4.10	4.86	3.86	4.52	4.58	
11244118	2.53	3.94	4.46	5.29	3.13	3.08	4.84	4.02	3.32	3.17
12009504					3.67	4.09	5.19		4.13	

5.5.1 Errors in computing $v_{\rm mac}$

The main contribution to the $v_{\rm mac}$ error is from the scatter in the $v_{\rm mac}$ values for the different lines. The spectra have a S/N of 100 or less, meaning that noise at the continuum level makes continuum placement difficult. Adjusting the continuum by even 0.5 per cent will result in a different macroturbulence, and by performing two different normalisations for several lines in a selection of stars, I found that the average difference in the $v_{\rm mac}$ for the two normalisations was $\sim$0.5 km s^{-1}. An example is shown in Figure 5.9 for a Fe II line in KIC 8228742, with the corresponding $v_{\rm mac}$ fits for the two different normalisations shown in Figure 5.10. The two different $v_{\rm mac}$ values in this example are 3.34 and 3.76 km s^{-1}. This is obviously one of the largest factors

contributing to the errors. However, there is also a genuine difference in $v_{\rm mac}$ in some lines, as discussed in Section 5.9.

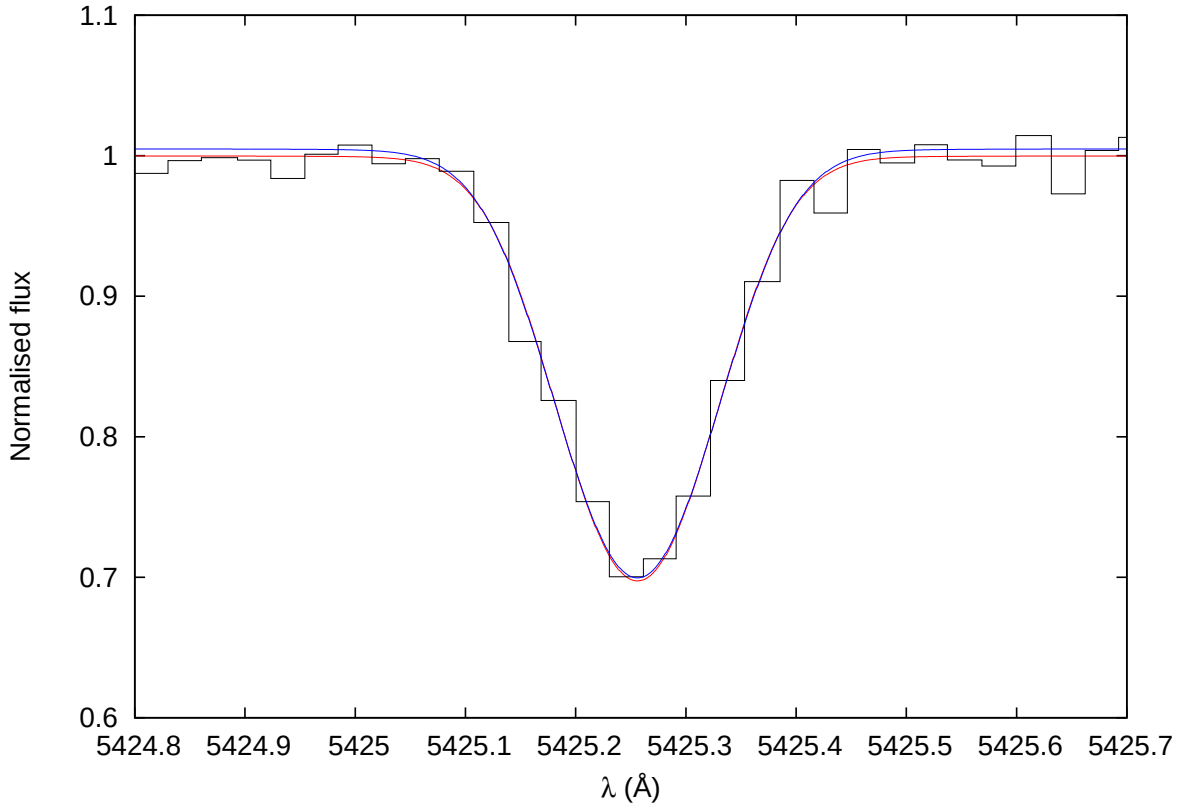

Figure 5.9: A Fe II line in KIC 8228742. The S/N of ∼100 makes continuum placement ambiguous, as indicated by two different synthetic lines (in red and blue) which differ by 0.5 percent at the continuum level. The solid black line is the observed spectrum. The synthetic lines were first binned before a Gaussian was fit, but the binned synthetic lines are left out of the image for clarity.

The $v \sin i$ error is included in the $v_{\rm mac}$ error. The $v_{\rm mac}$ was calculated based on the given $v \sin i$ value, and then recalculated with the $v \sin i$ increased by the error. The difference between the two $v_{\rm mac}$ values was then added in quadrature in the $v_{\rm mac}$ error. The errors on the $v \sin i$ have a negligible impact on the $v_{\rm mac}$ except for KIC 10355856 where the large $v \sin i$ error propagates into the $v_{\rm mac}$ error.

Different spectral analysis techniques can yield different values of $v_{\rm mic}$ for the same spectrum, and the choice of $v_{\rm mic}$ can affect the resulting $v_{\rm mac}$. For instance, using a $v_{\rm mic}$ of 1.00 and 0.85 in the Kitt Peak solar atlas yields a $v_{\rm mac}$ of 3.21 ± 0.27 and 3.33 ± 0.28 respectively. Thus, the choice of $v_{\rm mic}$ can have a subtle influence on $v_{\rm mac}$. In order to account for this, a $v_{\rm mic}$ error of 0.15 km s^{-1} was added in quadrature to the $v_{\rm mac}$ error.

The metallicity can potentially influence the derived $v_{\rm mac}$, as $v_{\rm mac}$ is fit while also

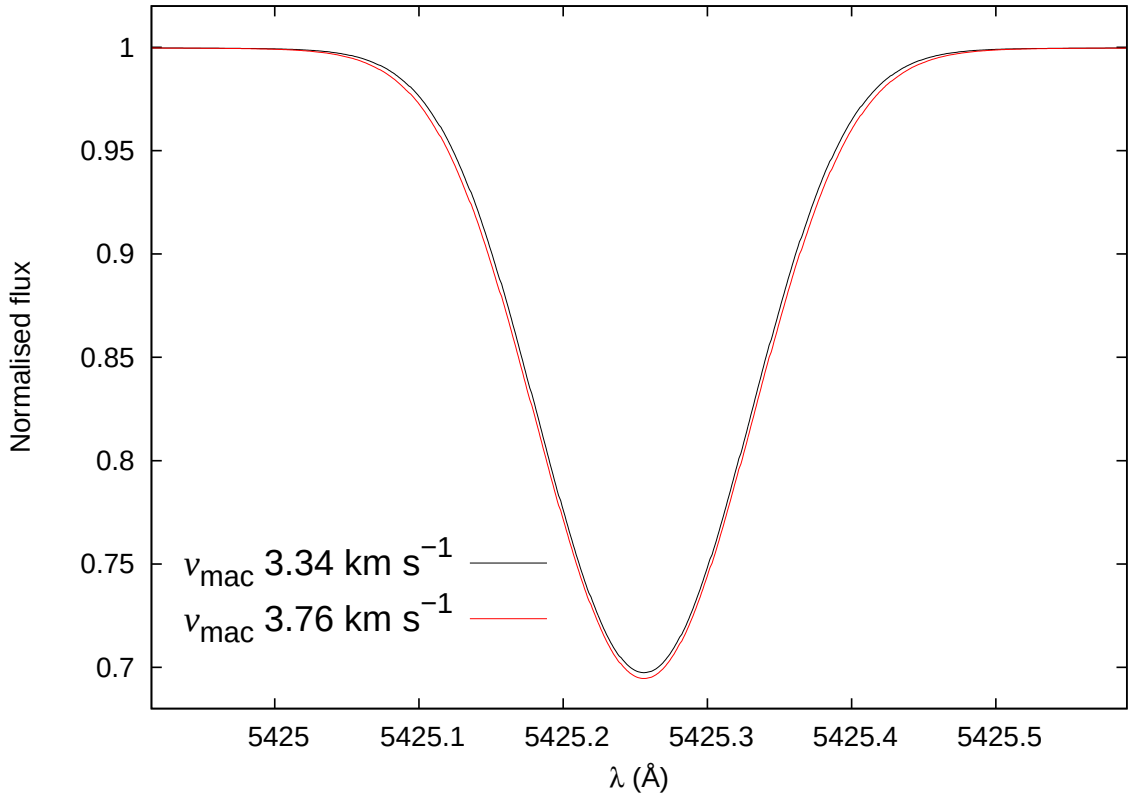

Figure 5.10: The two synthetic lines shown in Figure 5.9 for KIC 8228742 are normalised to 1 show the difference in the $v_{\rm mac}$ fit for the same spectral line.

adjusting the $\log A$ of the line, and assuming the solar values as a starting point. There is a subtle difference for KIC 8760414, which Bruntt et al. (2012) gives as $\log A$(Fe) = 6.36. Using a $v \sin i$ of 0 km s^{-1} (as no $\delta\nu_{\rm s} \sin i$ is available; see Section 5.6.3) and assuming a solar abundance when fitting the lines gives a $v_{\rm mac}$ of 3.62 $\pm$ 0.75 km s^{-1}. Using the lower abundance given in Bruntt et al. (2012) results in a $v_{\rm mac}$ of 3.65 $\pm$ 0.71. This could create a small error if solar metallicity was assumed for a very metal-poor or metal-rich star. However, most stars in this sample are not deviant from solar metallicity, and even if the metallicity was wrong by $\sim$0.3 dex, the difference in the $v_{\rm mac}$ would be negligible.

The instrumental broadening needs to be input before the $v_{\rm mac}$ can be determined, but since the resolution of a spectrograph can vary, an additional error can be introduced to the $v_{\rm mac}$ if the wrong resolution is used. Increasing the resolution of the ESPaDOnS and Narval solar spectra by 5000 increases the $v_{\rm mac}$ by 0.19 and 0.14 km s^{-1} respectively and this was accounted for in the $v_{\rm mac}$ errors.

As VDW broadening is a prominent broadening factor in strong lines, then an incorrect VDW value could introduce an error in the $v_{\rm mac}$, particularly if it has not

been computed from ABO theory. For example, if VDW is assumed to be zero for the strong line Fe I 6252 Å in the Kitt Peak Solar Atlas, the $v_{\rm mac}$ increases from 3.02 to 3.95 km s^{-1}. In this case, it is still impossible to fit the wings of the lines, showing that VDW is clearly needed. However, when VDW is included and $v_{\rm mac}$ is fixed to 3.5 km s^{-1} (the average Gray value), it is impossible to fit the core of the line as the $v_{\rm mac}$ is now too high. Varying the VDW does not rectify this, which suggests that both the VDW and $v_{\rm mac}$ are correct for this particular line. This is shown in Figure 5.11.

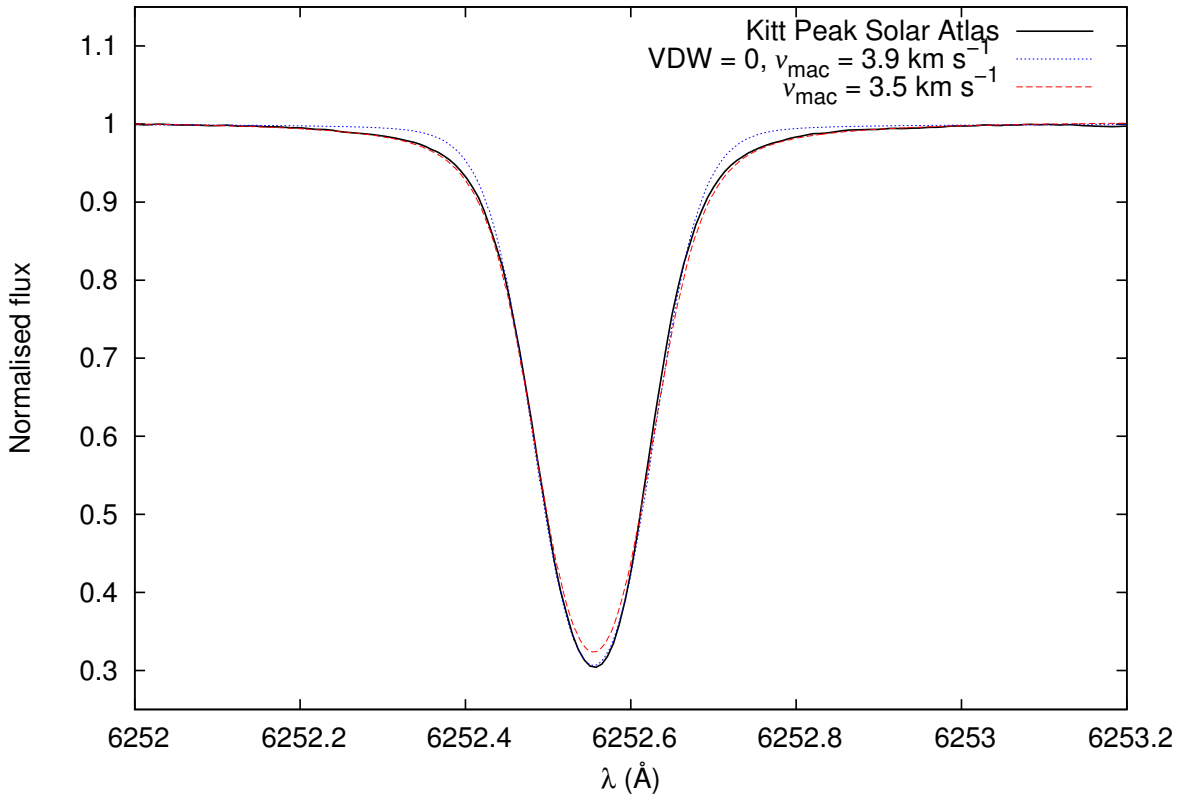

Figure 5.11: The Fe I 6252 Å in the Kitt Peak Solar Atlas has a $v_{\rm mac}$ of 3.02 km s^{-1}. This fit matches the observed spectral line exactly and is not shown on the plot. If the VDW is set to 0 (the blue dotted line), the $v_{\rm mac}$ is pushed higher to compensate, but the wings clearly do not fit, showing that an accurate VDW is needed. If the VDW broadening is used and the $v_{\rm mac}$ set to 3.5 km s^{-1} (red dashed line), it is still not possible to get a proper fit even when varying the VDW, indicating that the $v_{\rm mac}$ is too high.

5.6 Results

The asteroseismic rotational velocity ($v \sin i_{\rm astero}$) and the derived $v_{\rm mac}$ are listed in Table 5.4, and stars are identified with their *Kepler* Input Catalog (KIC) numbers. The $v_{\rm mac}$ is plotted against $T_{\rm eff}$ in Figure 5.12, showing a clear increase in $v_{\rm mac}$ with

increasing $T_{\rm eff}$. The plot also shows that there is a dependency on $\log g$ among the dwarfs, indicating that $\log g$ should be accounted for even within the same luminosity class. There are two young red giants and one subgiant from Deheuvels et al. (2014) also included on the plot, but not included in the calibration. These show that $v_{\rm mac}$ is higher for the giants as expected (Gray 2008), although it should be noted that the $\delta\nu_{\rm s} \sin i$ values for these stars are upper limits. The fit to the data is expressed as a function of $T_{\rm eff}$ and $\log g$ via

$$\begin{aligned} v_{\rm mac} \ &= 3.21 + 2.33 \times 10^{-3}(T_{\rm eff} - 5777) \\ +2.00 \times 10^{-6}&(T_{\rm eff} - 5777)^2 - 2.00(\log g - 4.44). \end{aligned} \tag{5.10}$$

The zero points were set to yield the $v_{\rm mac}$ value for the Sun and the gradient was determined from a polynomial fit. This calibration is valid for the $T_{\rm eff}$ range 5200 to 6400 K, and the $\log g$ range 4.0 to 4.6. The observed values were compared to the value predicted from the calibration. Taking the difference between these and then obtaining the standard deviation gives the rms scatter of the fit 0.37 $\rm km\,s^{-1}$. The mean of the $v_{\rm mac}$ errors with a 3-σ clipping rejection criterion is 0.62 $\rm km\,s^{-1}$. Adding these two errors in quadrature gives a total error of 0.73 $\rm km\,s^{-1}$ for the calibration.

The $v_{\rm mac}$ values obtained from the calibration will be affected by errors in the $T_{\rm eff}$ and $\log g$. For instance, if the $T_{\rm eff}$ of a star is increased by 100 K, the $v_{\rm mac}$ will be 0.31 $\rm km\,s^{-1}$ greater on average. Similarily, an increase of 0.1 dex in $\log g$ will increase the average $v_{\rm mac}$ by 0.17 $\rm km\,s^{-1}$.

There are two outliers, KIC 2837475 and KIC 6508366 which have abnormally high $v_{\rm mac}$. These are not shown on the plot and are not included in the calibration. Judging by the extent that the wings of the lines are broadened, it is possible that this effect could be real. However, both stars also have high $v \sin i$ ($\sim$20 $\rm km\,s^{-1}$), meaning that only a few lines are available to fit $v_{\rm mac}$ and it is quite difficult to obtain a reasonable fit. Interestingly, KIC 2837475 has a large discrepancy between the spectroscopic and asteroseismic $\log g$ with the former being 0.35 dex higher than the latter. Bruntt et al. (2012) finds that the spectroscopic $\log g$ is on average 0.08 $\pm$ 0.07 dex higher than the asteroseismic values, but cannot explain the discrepancy of KIC 2837475.

Table 5.4: The asteroseismic $v \sin i$ and $v_{\rm mac}$ as determined in this work. The asteroseismic $v \sin i$ is too high to fit the line profiles in some stars, in which case no $v_{\rm mac}$ is given. The $T_{\rm eff}$, $\log g$ and $v_{\rm mic}$ are from Bruntt et al. (2012), with errors of 60 K, 0.03 dex and 0.05 km s^{-1} respectively. The number of lines (out of 20) used to determine the average $v_{\rm mac}$ for each star is also given.

KIC	HD	HIP	$T_{\rm eff}$ K	$\log g$	$v_{\rm mic}$ km s^{-1}	$v \sin i_{\rm astero}$ km s^{-1}	$v_{\rm mac}$ km s^{-1}	No. of lines
1435467			6264	4.09	1.45	10.58 ± 0.70	5.61 ± 1.35	14
2837475	179260		6700	4.16	2.35	21.50 ± 0.96	12.07 ± 2.31*	4
3427720			6040	4.38	1.16	1.07 ± 0.63	3.80 ± 0.82	18
3456181			6270	3.93	1.53	10.89 ± 0.52		
3632418	179070	94112	6190	4.00	1.42	7.75 ± 0.46	4.87 ± 0.87	14
3656476			5710	4.23	1.02	1.13 ± 0.18	3.56 ± 0.49	16
4914923		94734	5905	4.21	1.19	2.46 ± 0.39	4.13 ± 0.42	16
5184732			5840	4.26	1.13	3.11 ± 0.19	3.67 ± 0.64	20
6106415	177153	93427	5990	4.31	1.15	3.66 ± 0.14	4.14 ± 0.59	20
6116048			5935	4.28	1.02	3.47 ± 0.16	4.02 ± 0.57	14
6225718	187637	97527	6230	4.32	1.38	15.46 ± 1.13		
6508366			6354	3.94	1.52	20.59 ± 0.95	9.83 ± 1.35*	5
6679371			6260	3.92	1.62	18.53 ± 0.92		
6933899			5860	4.09	1.15	1.99 ± 0.30	4.19 ± 0.63	17
7103006			6394	4.01	1.58	13.46 ± 1.04		
7206837			6304	4.17	1.29	7.82 ± 1.06		
7680114			5855	4.18	1.10	2.49 ± 0.27	3.65 ± 0.53	14
7871531			5400	4.49	0.71	1.22 ± 0.27	2.81 ± 0.52	17
7940546	175226	92615	6264	3.99	1.56	9.17 ± 0.42		
7970740	183606		5290	4.58	0.68	0.70 ± 0.20	2.50 ± 0.74	13
8006161		91949	5390	4.49	1.07	1.20 ± 0.08	2.22 ± 0.58	16
8228742		95098	6042	4.02	1.30	5.15 ± 0.59	4.22 ± 0.85	13
8394589			6114	4.32	1.23	4.92 ± 0.33	5.09 ± 0.65	8
8694723			6120	4.10	1.39	4.19 ± 0.78	6.28 ± 1.27	7
9098294			5840	4.30	1.01	2.11 ± 0.36	3.71 ± 0.69	10
9139151		92961	6125	4.38	1.22	4.75 ± 0.31	3.98 ± 0.74	15
9139163	176071	92962	6400	4.18	1.31	10.15 ± 0.81		
9812850			6325	4.05	1.61	12.04 ± 0.96	6.06 ± 1.27	7
9955598			5410	4.48	0.87	1.29 ± 0.12	2.51 ± 0.76	19
10355856			6350	4.08	1.55	5.74 ± 2.72	5.75 ± 2.56	11
10454113		92983	6120	4.31	1.21	3.83 ± 0.51	4.81 ± 0.64	17
10644253			6030	4.40	1.14	0.62 ± 0.81	3.85 ± 0.56	18
10963065			6060	4.29	1.06	3.61 ± 0.25	4.35 ± 0.46	16
11244118			5745	4.09	1.16	1.67 ± 0.22	3.66 ± 0.73	20
12009504			6065	4.21	1.13	7.36 ± 0.37	4.41 ± 0.60	8

* Not included in the calibration.

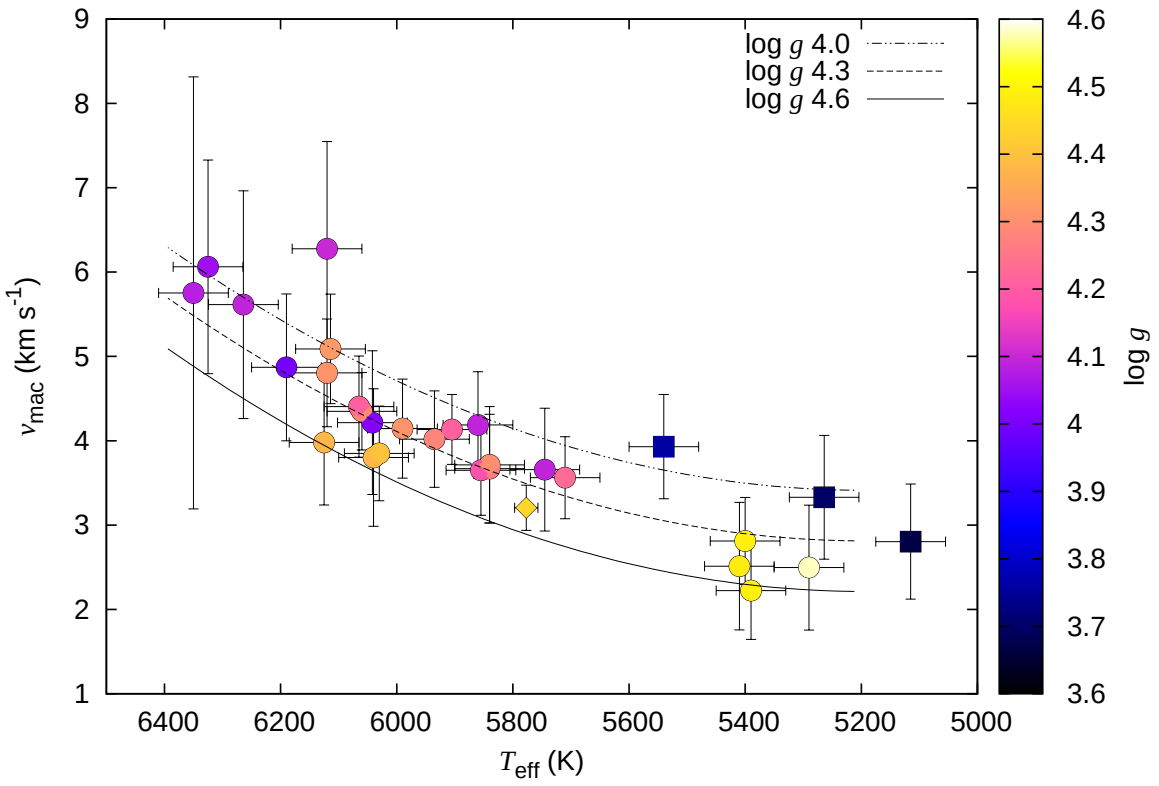

Figure 5.12: Macroturbulence is seen to increase with increasing $T_{\rm eff}$, however there also seems to be some $\log g$ dependence. The circles represent the stars used in this study, the diamond represents the Sun, and the squares are the red giants from Deheuvels et al. (2014). The red giants are not included in the calibration.

5.6.1 Stars with $v \sin i_{\rm astero}$ too high

Seven of the stars have an asteroseismic $v \sin i$ that is clearly too high to fit the spectra, and an example is shown in Figure 5.13. The $v \sin i$ is too high to allow for any $v_{\rm mac}$ broadening, which means that the wings cannot be fit and the core of the synthetic profile is too shallow. If the $v_{\rm mac}$ is fixed to 4.92 km s^{-1} from the calibration, the $v \sin i$ fits with a value of 3.25 km s^{-1}.

This implies that another mechanism is changing the shape of the line profiles. Differential rotation, low inclination and limb darkening have the effect of narrowing line profiles (Reiners & Schmitt 2002), which could explain why the $v \sin i$ will not fit. However, limb darkening would not explain why this effect is only seen in some stars and not others with similar parameters. As $\delta\nu_{\rm s} \sin i$ cannot be well constrained for stars with a low inclination, the discrepancy in the line profiles cannot be caused by low inclination. While there is some correlation between i and $\delta\nu_{\rm s} \sin i$, it is still possible to infer lower limits on the inclination from the posterior distribution plots, which show

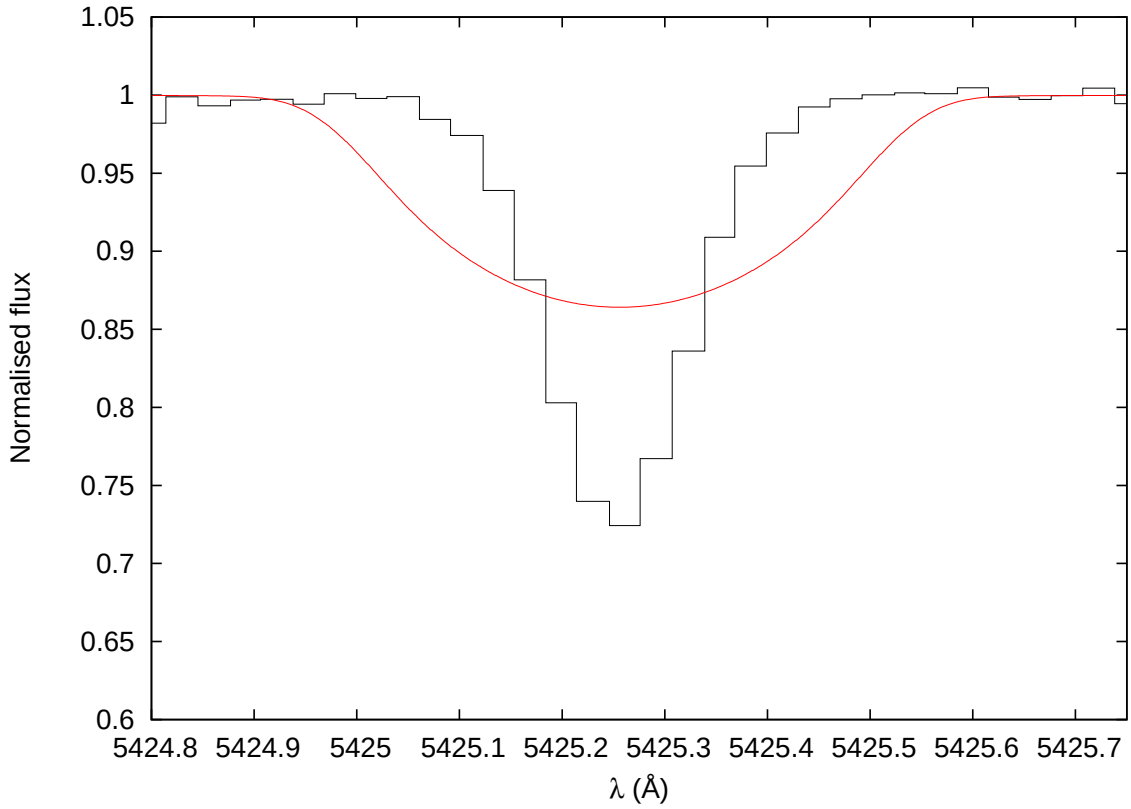

Figure 5.13: The synthetic spectrum clearly doesn't fit the observed spectrum of KIC 6225718. The synthetic line, in red, has $v \sin i_{\text{astero}}$ of 15.46 ± 1.13 and no v_{mac}.

that $i \gtrsim 40$ for these stars and most have $i \gtrsim 60$. This suggests that the most likely explanation for the shapes of these line profiles is latitudinal differential rotation.

However, including solar-like latitudinal differential rotation (i.e. $\alpha = 0.2$) in the synthetic line profile only solves the problem for KIC 7940546. For the other six stars, a reduction in inclination is needed along with differential rotation. This can be as low as $i = 10$ degrees. Even with these adjustments to the line profiles, there are still some lines that cannot be fit. This is complicated by the fact that v_{mac} is different for every line due to depth dependence (see Section 5.9). For example, in KIC 7206837 the strong lines seem to fit with $v \sin i_{\text{astero}}$, while the weaker lines do not fit. This is because the stronger lines have lower v_{mac} values, which allows them to compensate for the high $v \sin i_{\text{astero}}$. No conclusive explanation can be offered as to why the line profiles of these stars do not agree with $v \sin i_{\text{astero}}$. It is possible that undetected mixed modes could be interfering with the $\delta\nu_{\text{s}} \sin i$ measurements for the stars with $\log g < 4.0$, however this needs further investigation with asteroseismic modelling. In addition, higher quality spectra might help in understanding these stars as it would allow the line profiles to be fit with much better precision.

5.6.2 Comparison with $P_{\rm rot}$

It would be useful to compare the asteroseismic $v \sin i$ values to the upper limit $v \sin i$ derived from the rotation period and the stellar radius. The rotation period can be determined from the light curve, as any existing spots will cause periodic modulations in the light curve as they pass in and out of view. However, there are no stars in common with the $P_{\rm rot}$ values of Reinhold, Reiners & Basri (2013) and only five stars have a $P_{\rm rot}$ value from Nielsen et al. (2013). It is not expected that many stars in this sample will have $P_{\rm rot}$ values from starspots, as most of the stars are too old ($\gtrsim 2$ Gyr) to have sufficient activity (Chaplin et al. 2014). Table 5.5 compares $v \sin i_{\rm astero}$ with the upper limit $v \sin i$ determined from the $P_{\rm rot}$ values of Nielsen et al. (2013), showing that the latter are systematically higher than the $v \sin i_{\rm astero}$ values. This is expected, since the $v \sin i$ determined from $P_{\rm rot}$ is an upper limit, but it is possible that this discrepancy could be from period measurements of spots at high latitudes.

Table 5.5: Comparison between $v \sin i_{\rm astero}$ and the $v \sin i$ determined from $P_{\rm rot}$

KIC	$v \sin i_{\rm astero}$ ($\rm km\,s^{-1}$)	$v \sin i$ from $P_{\rm rot}$ ($\rm km\,s^{-1}$) (upper limit)
1435467	10.58 ± 0.70	$\leq 11.89 \pm 0.81$
7206837	7.82 ± 1.06	$\leq 9.27 \pm 1.18$
9098294	2.11 ± 0.36	$\leq 2.90 \pm 0.12$
9812850	12.04 ± 0.96	$\leq 13.98 \pm 0.53$
10454113	3.83 ± 0.51	$\leq 4.33 \pm 0.21$

5.6.3 Stars with no obvious splitting

There are three stars (KIC 6603624, 8760414 and 8938364) where $\delta\nu_{\rm s} \sin i$ couldn't be determined as there was no splitting evident. It is possible that this is simply because these stars have negligible rotation. All three stars show no signs of Li and the asteroseismic ages are given as $7.9\ ^{+2.4}_{-2.2}$, 13.6 ± 1.5 and $13.0\ ^{+2.8}_{-2.7}$ respectively (Chaplin et al. 2014).

Using $v \sin i = 0$ to obtain the upper limit of $v_{\rm mac}$, I saw that these stars fit in with the general trend seen in Figure 5.12, indicating that the $v \sin i$ is probably not much more than 0. I also placed an estimated upper limit on $v \sin i$, by obtaining the rotation periods via the gyrochronology calibration of Mamajek & Hillenbrand (2008) and using the ages from Chaplin et al. (2014). However, these estimated $v \sin i$ values are inconsistent with the asteroseismic $v \sin i$ values for the stars that do have a detectable

$\delta\nu_{\rm s} \sin i$, so the estimated values should be used as a guideline only. As such, I did not include these three stars in the calibration. Both sets of parameters are given in Table 5.6.

Table 5.6: Estimated $v \sin i$ and $v_{\rm mac}$ for stars with no splitting

KIC	$v \sin i$ (km s^{-1})	$v_{\rm mac}$ (km s^{-1})	$v \sin i$ (km s^{-1}) (estimated)	$v_{\rm mac}$ (km s^{-1})
6603624	0	$\leq 3.35 \pm 0.80$	$\leq 1.32 \pm 0.20$	$\geq 2.96 \pm 0.76$
8760414	0	$\leq 3.62 \pm 0.75$	$\leq 1.90 \pm 0.25$	$\geq 3.05 \pm 1.17$
8938364	0	$\leq 3.77 \pm 0.57$	$\leq 1.36 \pm 0.12$	$\geq 3.50 \pm 0.74$

5.7 Comparison with other $v_{\rm mac}$ relationships

Figure 5.14 shows my data overplotted with three other calibrations which are often cited in the literature: Gray (1984a), Valenti & Fischer (2005) and Bruntt et al. (2010a). My calibration is plotted at $\log g = 4.44$. The observed values were compared with the values predicted from the calibrations, and a linear regression was performed to see which calibration predicted values that agreed with the observed values. My calibration has the highest r^2 value of 0.87 as seen in Table 5.7. This suggests a relatively good agreement, however the r^2 values for the other calibrations aren't much lower so they also agree well with the observed values. My calibration also has the lower rms scatter. The linear regression and the rms scatter for my calibration are shown in Figure 5.15. It is difficult to make a satisfactory comparison between the observed and predicted values due to the scatter and large errors in the observed $v_{\rm mac}$ values.

Table 5.7: Parameters from the linear regressions between the observed $v_{\rm mac}$ values and those predicted from each calibration.

Calibration	r^2	rms scatter
Doyle	0.87	0.37
Gray	0.81	0.50
Bruntt	0.82	0.44
Valenti & Fischer	0.81	0.67

5.7.1 Gray (1984a)

The difference in line profiles shapes due to varying broadening parameters is very subtle in the wavelength domain. However, in the Fourier domain the broadening parameters

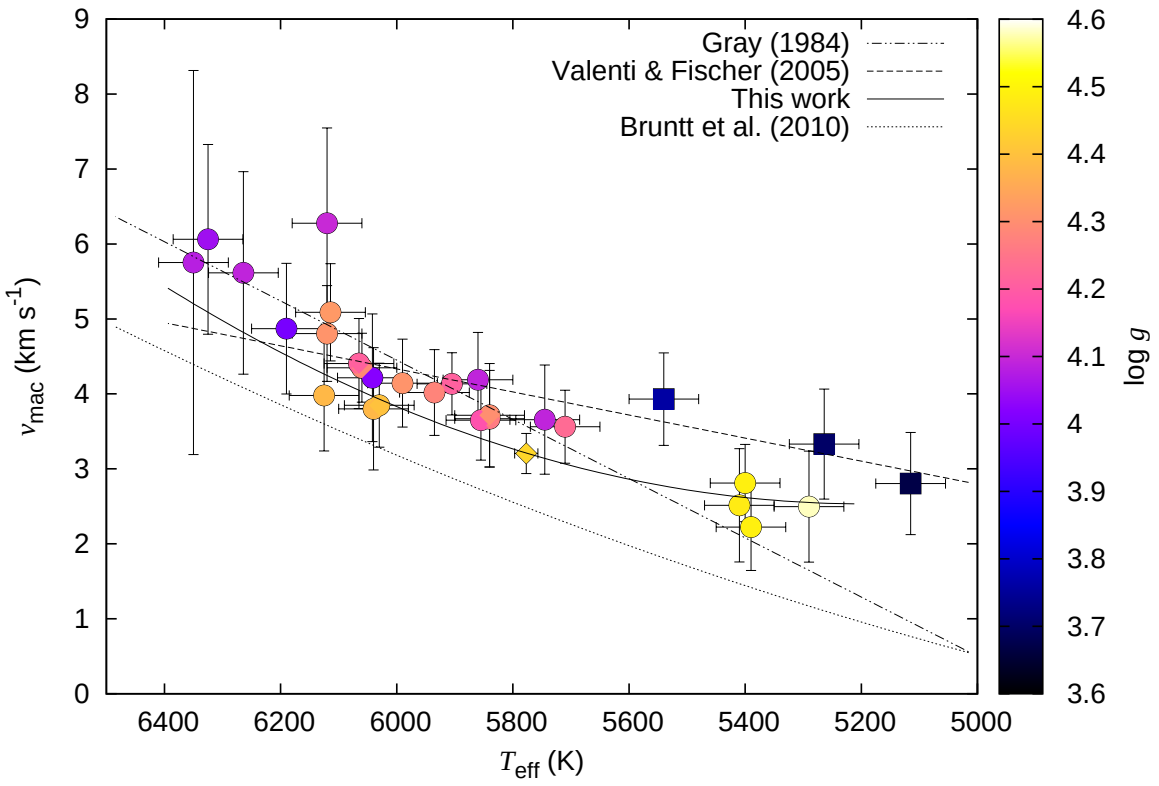

Figure 5.14: Same as for Figure 5.12, but with the calibrations of Gray (1984a), Bruntt et al. (2010a) and the upper limit of Valenti & Fischer (2005) also plotted. The fit for this work is given at $\log g = 4.44$.

have more distinct shapes, meaning that they can be distinguished from each other more easily. The observed line profile $D(\lambda)$ in the wavelength domain is a convolution with the instrumental profile $I(\lambda)$, the thermal profile $H(\lambda)$ (including microturbulence) and the total non-thermal broadening profile $M(\lambda)$.

$$D(\lambda) = M(\lambda) * I(\lambda) * H(\lambda). \tag{5.11}$$

The thermal profile is computed from a model atmosphere. The thermal profile also includes the microturbulence, even though microturbulence is non-thermal. $M(\lambda)$ includes both radial-tangential $v_{\rm mac}$ and rotation, which have been combined via disc integration and not via a convolution. Pressure broadening is not included, however only lines that are not prone to significant pressure broadening should be selected for the Fourier analysis. The Fourier transform of the observed profile is written with lower case letters as

$$d(\sigma) = m(\sigma)i(\sigma)h(\sigma). \tag{5.12}$$

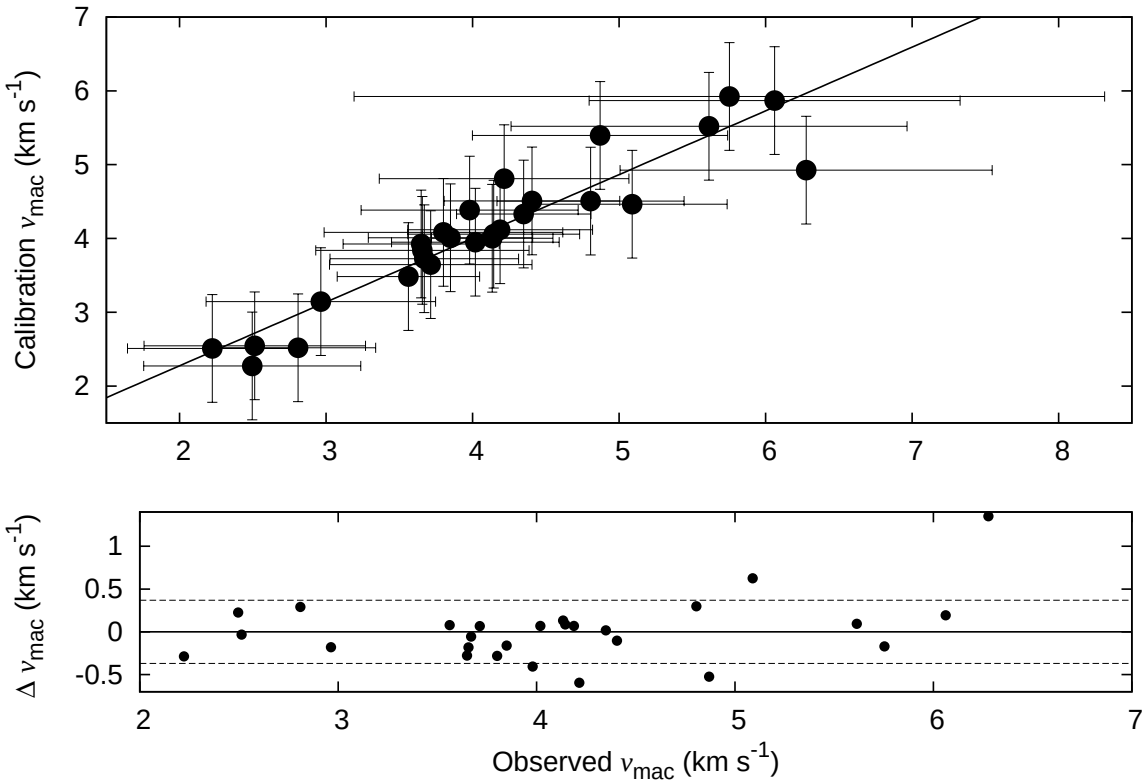

Figure 5.15: The observed $v_{\rm mac}$ is plotted against the $v_{\rm mac}$ predicted from Equation 5.10 and a linear regression was performed, giving an r^2 of 0.87 km s^{-1}. The lower plot shows the difference between the observed and predicted values, and the dashed liness mark the rms scatter of 0.37 km s^{-1}.

The instrumental profile and thermal profile can now be divided out, leaving a residual transform that represents the combination of $v_{\rm mac}$ and $v \sin i$. It is now possible to disentangle $v_{\rm mac}$ and $v \sin i$ as the shape of the sidelobes of the profiles in the Fourier domain are distinctly different for both. This means that different ratios of the two broadening parameters will also have unique shapes. Therefore, both $v_{\rm mac}$ and $v \sin i$ can be extracted by comparing the shape of m(σ) to a grid of model values.

This type of analysis requires high resolution spectra in order to obtain high Fourier frequencies and thus distinguish between the transforms, as the top of the transform has a similar shape for various combinations of $v_{\rm mac}$ and $v \sin i$. It is also essential to have high S/N, as the crucial part of the transform needed for disentangling the broadening occurs at low Fourier amplitudes (Gray 2008).

Gray (1984a) uses the Fourier method to determine the radial-tangential $v_{\rm mac}$ for a selection of stars with high S/N spectra (100 to 300). He plots this against spectral type, and then converts spectral type to $T_{\rm eff}$ to obtain the relation

$$v_{\rm mac} = 3.95\ T_{\rm eff} - 19.25\ \ {\rm km\,s^{-1}}, \tag{5.13}$$

where $T_{\rm eff}$ is given in 10^3 K. The calibration has an error of $\sim$0.2 km s^{-1}, and there is an approximate change of 4 km s^{-1} per thousand degrees, which is similar to that found for giant stars.

Zeeman broadening was approximated as a convolution with the non-thermal profile, so that it could ultimately be removed. The Zeeman broadening had been calculated in a previous paper (Gray 1984b), so that the actual $v_{\rm mac}$ could be obtained for these cooler stars, albeit with added uncertainties. Gray (1984a) provides $v_{\rm mac}$ values both with and without Zeeman broadening included in the profile, and there is a noticeable difference in the calibration in the cool end depending on which value is used.

A $v_{\rm mac}$ calibration from Gray (2008) is also cited in the literature, however this is obtained via a linear fit to the $v_{\rm mac}$ values given for a typical star of each spectral type, rather than a specific set of stars. This fit is almost the same as for Gray (1984a) and it is probably the same calibration, albeit slightly different due to different $T_{\rm eff}$ values used. A visual inspection of Figure 3 in Gray (1984a) shows that the $v_{\rm mac}$ values given in Gray (2008) are consistent with that fit, except for the hottest star. As the Gray (1984a) paper details the actual stars used in the calibration, it is more accurate to use this one when comparing the different calibrations.

5.7.2 Valenti & Fischer (2005)

Valenti & Fischer (2005) initially tried using Gray's macroturbulence calibration, however the resulting $v \sin i$ values suggested that the 1040 stars in their sample would have a minimum rotational velocity of 3 km s^{-1}, which disagrees with measured rotation periods of inactive stars from Noyes et al. (1984).

They set $v \sin i = 0$ and determined the upper limit radial-tangential $v_{\rm mac}$ for each star by fitting a synthetic spectrum to an observed spectrum with the programme SME. The $v_{\rm mac}$ derived is thus an upper limit as it is a combination of $v_{\rm mac}$ and $v \sin i$. Their plot of the $v_{\rm mac}$ against $T_{\rm eff}$ shows that below 5800 K, the slope changes by 1 km s^{-1} every 650 K. Using this, they then fit their linear relationship by fixing the solar $v_{\rm mac}$ value to 3.98 (the value obtained by Gray (1984a) for weak lines) and the solar $v \sin i$ value to 1.63 km s^{-1} (Valenti & Piskunov 1996) to obtain the relationship

$$v_{\rm mac} = \left(3.98 + \frac{T_{\rm eff} - 5770\ K}{650\ K}\right)\ {\rm km\,s^{-1}}. \quad (5.14)$$

They note that as stars below 5800 K should have negligible $v \sin i$, then the resulting $v_{\rm mac}$ is the true value rather than an upper limit. To determine if setting $v \sin i = 0$ has an effect on the $v_{\rm mac}$ of stars below 5800 K, I compared $v_{\rm mac}$ upper limits obtained using $v \sin i = 0$ to the $v_{\rm mac}$ obtained when using the $v \sin i_{\rm astero}$ ($0.7 < v \sin i < 1.9$ km s^{-1}) for the *Kepler* stars with $T_{\rm eff}$ below 5800 K, as well as for the Sun. The results show that using $v \sin i = 0$ for stars below 5800 K will overestimate the $v_{\rm mac}$ by 0.41 ± 0.13 km s^{-1}, as can be seen in Fig. 5.16. Therefore, there is a small systematic error in the Valenti & Fischer (2005) calibration for these stars. However from Fig. 5.14 it is clear that it is still valid as an upper limit for dwarf stars below 5800 K.

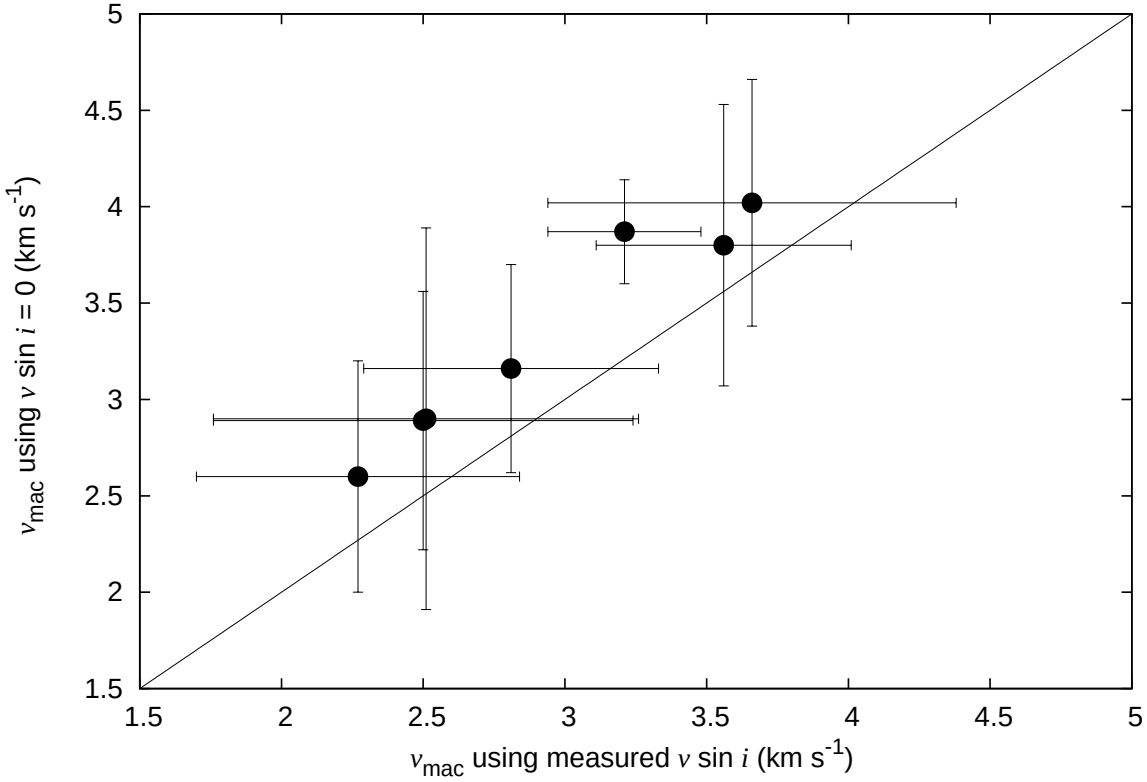

Figure 5.16: Comparing the $v_{\rm mac}$ obtained using $v \sin i_{\rm astero}$ with the $v_{\rm mac}$ obtained with $v \sin i = 0$ shows that the latter will be overestimated. The solid line depicts a 1:1 relationship.

For stars with $T_{\rm eff}$ greater than 5800 K, they note that the $v_{\rm mac}$ points rise sharply above the linear relationship. They attribute this to the fact that $v \sin i$ will increase with $T_{\rm eff}$, but do acknowledge that some of this might be due to $v_{\rm mac}$. In fact, it is interesting to note that the turn off point for the increased $v_{\rm mac}$ occurs at a similar $T_{\rm eff}$

(∼6000 K) in my own plot. This indicates that the sharp increase seen in their plot for the hotter stars is likely due to a combination of both $v \sin i$ and $v_{\rm mac}$. Therefore their relationship will underestimate the $v_{\rm mac}$ of stars above 5800 K, and explains why the $v_{\rm mac}$ values I obtained are greater than the "upper limit" for the hotter stars.

5.7.3 Bruntt et al. (2010a)

Bruntt et al. (2010a) analysed a sample of 22 stars using 10 to 30 lines with a line strength of between 20 and 100 mÅ using the software VWA (Bruntt et al. 2002). They assumed $v_{\rm mac}$ with a Gaussian profile, and convolved the synthetic spectrum with different combinations of $v \sin i$ and $v_{\rm mac}$ in a grid with steps of 0.15 km s^{-1} until the best fit was found. They fit a polynomial to their data to determine their $v_{\rm mac}$ calibration

$$v_{\rm mac} \ = 2.26 + 2.90 \times 10^{-3} \Delta T + 5.86 \times 10^{-7} \Delta T^2 \ \ {\rm km\,s^{-1}}, \tag{5.15}$$

where ΔT = $T_{\rm eff}$ − 5700 K.

The Bruntt calibration gives $v_{\rm mac}$ values that are systematically lower than this work. A line profile in VWA with a given value of $v_{\rm mac}$ is broader than in UCLSYN for the same value of $v_{\rm mac}$. In order for the two line profiles to agree, the $v_{\rm mac}$ in VWA needs to be increased by $\sqrt{2}$. For example, the solar $v_{\rm mac}$ from the Bruntt calibration is 2.48 km s^{-1}, but when this is multiplied by $\sqrt{2}$ it gives 3.50 km s^{-1}, which is in agreement with Gray (1984a). This will also move the Bruntt calibration up on Figure 5.14. The $\sqrt{2}$ difference is probably due to the method of modelling $v_{\rm mac}$ within the software, however the exact reason for this is unclear even to the authors of the code (Bruntt 2014, private communication).

If the Bruntt $v_{\rm mac}$ values are used as computed in Equation 5.15, it would be expected that the $v \sin i$ will be pushed higher to compensate for this. In fact, this can be seen in Figure 5.17, where the $v \sin i$ values from Bruntt et al. (2012) are seen to be systematically higher than the $v \sin i_{\rm astero}$ values. The stars that have $v \sin i_{\rm astero}$ too high (Section 5.6.1) are also included on the plot.

However, even when including the $\sqrt{2}$ factor, the $v \sin i$ still seems to be too high. For example, when I assume that the $v_{\rm mac}$ of KIC 3427720 is 4.66 km s^{-1} (Bruntt value increased by $\sqrt{2}$), I obtain a $v \sin i$ of 0.95 ± 0.95 km s^{-1}. This is in agreement with the $v \sin i_{\rm astero}$ of 1.07 ± 0.63, but in disagreement with the Bruntt et al. (2012) value of 4 km s^{-1}. It is not possible to fit the line profiles with that $v_{\rm mac}$ and a $v \sin i$ of 4 km s^{-1}.

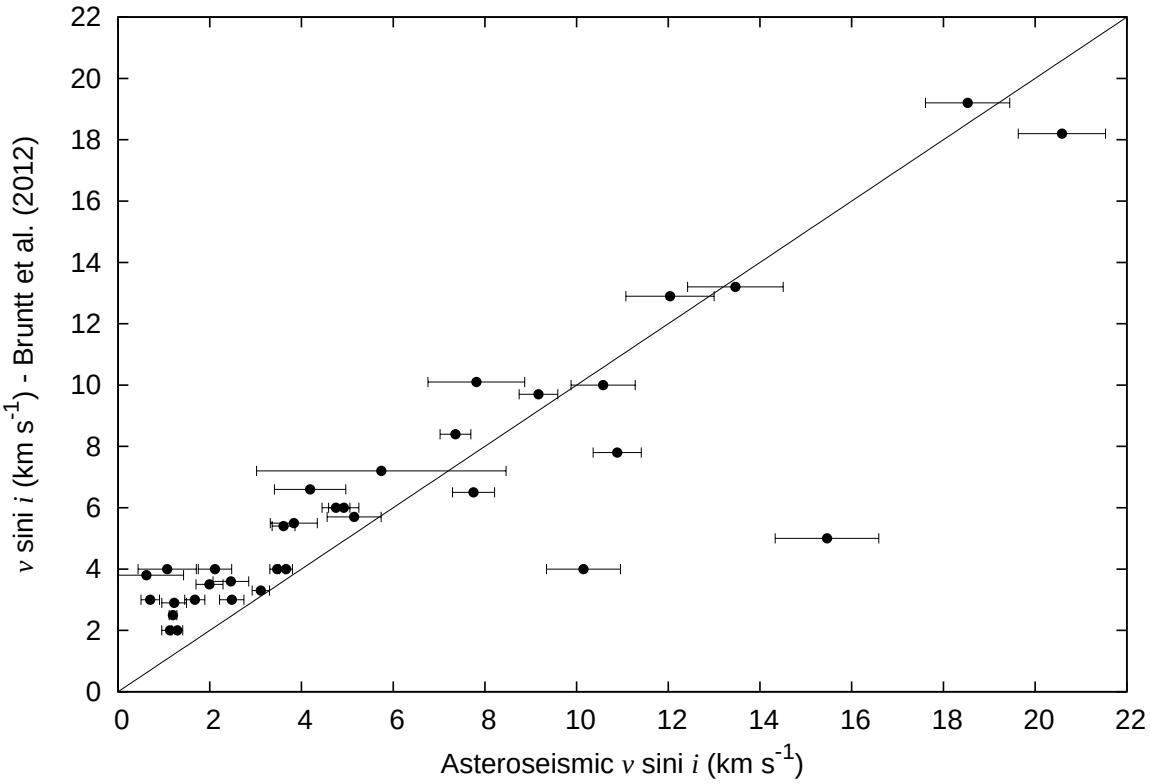

Figure 5.17: Comparing the Bruntt et al. (2012) $v \sin i$ values with the $v \sin i_{\rm astero}$ values show that the Bruntt values are systematically higher. The outliers that have $v \sin i_{\rm astero}$ too high for the line profiles are also shown on the plot. The solid line is a 1:1 relationship.

5.8 Implications for the RM effect

5.8.1 The influence of different $v_{\rm mac}$ calibrations on $v \sin i$.

The choice of macroturbulence calibration has a significant effect on the $v \sin i$ value that is obtained. To demonstrate this, I determined the solar $v \sin i$ from the Kitt Peak Solar Atlas using the same set of lines as I did for measuring $v_{\rm mac}$. I used the $v_{\rm mac}$ values of 3.98 (Valenti & Fischer 2005), 3.5 (Gray 1984a) and 2.5 km s^{-1} (Bruntt et al. 2010a), which resulted in a $v \sin i$ of 0.59 $\pm$ 0.45, 1.62 $\pm$ 0.32 and 2.67 $\pm$ 0.18 km s^{-1} respectively. However, when the Bruntt value is corrected for the $\sqrt{2}$ difference, it is in better agreement with Gray. Clearly, using the Gray $v_{\rm mac}$ obtains the most realistic solar value, compared to the synodic solar $v \sin i$ which is given as 1.73 $\pm$ 0.25 in Soderblom (1982), 1.85 $\pm$ 0.1 in Bruning (1984), 1.9 km s^{-1} in Takeda (1995) and Gray (2008).

The Valenti & Fischer (2005) $v_{\rm mac}$ value is too high for the solar lines and it makes the cores of the lines too shallow. This inevitably makes it difficult to fit $v \sin i$,

Table 5.8: Pairs of Fe I lines used to infer Zeeman broadening

High Landé g lines (Å)	Low Landé g lines (Å)
6173.34	6240.65
6302.50	6408.03
6733.16	6627.55
6842.70	6810.27

which is why $v \sin i$ is too low for the Sun using this calibration. The Gray (1984a) macroturbulence value returns reasonable fits for most lines, although there are still some subtle differences in the line profiles.

I also noticed that while for some lines the different combinations of $v_{\rm mac}$ and $v \sin i$ are visually indistinguishable, there are other lines that show clear differences in the shape of the line profile depending on the $v_{\rm mac}$ value used. This indicates that different lines have varying sensitivities to macroturbulence, which is discussed in Section 5.9.

5.8.2 New $v \sin i$ values for the WASP stars

Using Equation 5.10 to yield the $v_{\rm mac}$, I redetermined the $v \sin i$ for the WASP planet host stars using HARPS spectra. The resolution was determined individually for these spectra from the telluric lines, as the spectra were of a S/N high enough to do so. The typical resolution is ∼112,000, in agreement with Mayor et al. (2003), where the resolution is given as 115,000. These new $v \sin i$ values ($v \sin i_{\rm spec}$) are given in Table 5.9. Two different errors are listed in the table; σ_{sd} is the standard deviation of $v \sin i_{\rm spec}$, and σ_{mac} is the standard deviation added in quadrature to the error on the $v_{\rm mac}$ calibration.

Also give in the table are the original spectroscopic $v \sin i$ ($v \sin i_{\rm original}$) and the $v \sin i$ determined from the RM effect ($v \sin i_{\rm RM}$). The $v \sin i_{\rm original}$ values are typically those determined in the discovery papers, and are the values given in the RM papers.

A direct comparison with $v \sin i_{\rm original}$ (and the RM values that used a spectroscopic prior) is difficult, as the $v_{\rm mac}$ determination is inconsistent. However, there are some interesting comparisons to be made with the $v \sin i_{\rm RM}$ values that did not require a spectroscopic prior. For example, $v \sin i_{\rm spec}$ for WASP-40 seems to be higher than $v \sin i_{\rm RM}$. The Zeeman effect can cause additional line broadening in cooler stars, so I checked to see if any such broadening was present using pairs of lines with high and low Landé g-factors as determined by Robinson (1980). The pairs of lines are given in Table 5.8.

Table 5.9: The $v_{\rm mac}$ has been calculated from Equation 5.10 and has an error of 0.73 km s^{-1}. The $v \sin i$ values redetermined for this work are given as $v \sin i_{\rm spec}$, and the previous spectroscopic values ($v \sin i_{\rm original}$) and the values obtained from the RM effect are also given. σ_{sd} is the standard deviation of $v \sin i_{\rm spec}$, and σ_{mac} is the standard deviation added in quadrature to the error on the $v_{\rm mac}$ calibration. The $T_{\rm eff}$ and $\log g$ are determined from spectroscopic analyses from the given references.

Star	$T_{\rm eff}$ K	$\log g$	$v_{\rm mac}$ km s^{-1}	$v \sin i_{\rm original}$ km s^{-1}	$v \sin i_{\rm RM}$ km s^{-1}	$v \sin i_{\rm spec}$ km s^{-1}	σ_{sd} km s^{-1}	σ_{mac} km s^{-1}	Ref.
WASP-2	5175 ± 95	4.46 ± 0.12	2.49	1.60 ± 0.70	0.99 $^{+0.27}_{-0.32}$	0.88	0.61	0.95	1,2
				1.30 ± 0.50	< 0.5				3
WASP-4	5400 ± 90	4.47 ± 0.11	2.56	2.00 ± 1.00	2.14 $^{+0.38}_{-0.35}$	2.43	0.37	0.82	1,2
WASP-5	5690 ± 80	4.28 ± 0.09	3.34	3.50 ± 1.00	3.24 $^{+0.35}_{-0.27}$	3.45	0.37	0.82	1,2
WASP-6	5375 ± 65	4.61 ± 0.07	2.26	1.40 ± 1.00	1.6 $^{+0.27}_{-0.17}$	2.36	0.31	0.79	1,4
WASP-7*	6550 ± 70	4.32 ± 0.06	6.45	17.00 ± 2.00	14.00 ± 2.00	17.89	0.68	0.99	1,5
WASP-8	5560 ± 90	4.40 ± 0.11	2.88	2.00 ± 0.60	1.59 $^{+0.08}_{-0.09}$	1.84	0.38	0.82	1,6
WASP-15	6405 ± 80	4.40 ± 0.11	5.54	4.00 ± 2.00	4.27 $^{+0.26}_{-0.36}$	4.52	0.46	0.86	1,2
WASP-16	5630 ± 70	4.21 ± 0.11	3.37	2.3 ± 0.4	1.20 ± 0.3	1.90	0.53	0.89	1,7
					3.20 ± 0.90				8
WASP-17*	6700 ± 105	4.34 ± 0.23	7.27	9.80 ± 0.50	9.82 $^{+0.40}_{-0.45}$	9.36	0.73	1.03	1,2
				9.0 ± 1.5	8.61 ± 0.45				9
				9.0 ± 1.5	20.0 $^{+69.2}_{-5.2}$				10
WASP-18	6400 ± 75	4.32 ± 0.09	5.68	11.00 ± 1.50	11.20 ± 0.60	10.96	0.43	0.85	1,2,8
WASP-19	5460 ± 90	4.37 ± 0.14	2.81	5.0 ± 0.3	4.63 ± 0.26	4.86	0.17	0.75	1,11
				4.0 ± 2.0	4.40 ± 0.90				8
WASP-20	6000 ± 100	4.40 ± 0.15	3.91	3.5 ± 0.5	4.71 ± 0.50	3.92	0.28	0.78	12
WASP-21	5800 ± 100	4.2 ± 0.1	3.57	1.5± 0.6		1.88	0.42	0.84	13
WASP-22	6000 ± 100	4.5 ± 0.2	4.28	4.5 ± 0.4	4.42 ± 0.34	3.97	0.30	0.79	14,15
WASP-24	6075 ± 100	4.15 ± 0.10	4.58	7.0 ± 1.0	7.32 ± 0.88	5.95	0.28	0.78	16,17
WASP-25	5750 ± 100	4.5 ± 0.15	3.03	2.6 ± 0.4	2.90 ± 0.3	2.35	0.41	0.84	18,7
WASP-26	5950 ± 100	4.3 ± 0.2	3.95	3.90 ± 0.4	2.20 ± 0.70	3.31	0.31	0.79	8,19,15
WASP-28	6100 ± 150	4.5 ± 0.2	4.05	3.1 ± 0.6	3.25 ± 0.34	3.54	0.49	0.88	12
WASP-30	6190 ± 50	4.18 ± 0.08	5.03	12.1 ± 0.5	12.1 $^{+0.4}_{-0.5}$	11.84	0.26	0.78	20
WASP-31	6300 ± 100	4.4 ± 0.1	5.23	7.6 ± 0.4	7.50 ± 0.7	7.56	0.38	0.82	21,7
					6.80 ± 0.60				8
WASP-32	6100 ± 100	4.4 ± 0.2	4.25	5.5 ± 0.4	3.9 $^{+0.4}_{-0.5}$	5.18	0.27	0.78	22,23
WASP-38	6150 ± 80	4.3 ± 0.1	4.64	8.3 ± 0.4	7.7 $^{+0.1}_{-0.2}$	7.97	0.25	0.77	24,23
				8.60 ± 0.40					17
WASP-40	5200 ± 150	4.5 ± 0.2	2.41	2.4 ± 0.5	0.6 $^{+0.7}_{-0.4}$	1.71	0.39	0.83	25,23
WASP-41	5450 ± 100	4.4 ± 0.2	2.74	1.6 ± 1.1		2.74	0.24	0.77	26
WASP-50	5400 ± 100	4.5 ± 0.1	2.50	2.6 ± 0.5		2.65	0.29	0.78	27
WASP-54	6100 ± 100	4.2 ± 0.1	4.65	4.0 ± 0.8		3.49	0.42	0.84	28
WASP-55	5900 ± 100	4.3 ± 0.1	3.81	3.1 ± 1.0		2.42	0.48	0.87	29
WASP-61	6250 ± 150	4.3 ± 0.1	5.04	10.3 ± 0.5		10.29	0.36	0.81	29
WASP-62	6230 ± 80	4.45 ± 0.10	4.66	8.7 ± 0.4		8.38	0.35	0.81	29
WASP-71	6050 ± 100	4.3 ± 0.1	4.28	9.4 ± 0.5	9.89 ± 0.48	9.06	0.36	0.82	30
WASP-76	6250 ± 100	4.4 ± 0.1	4.84	3.3 ± 0.6		2.33	0.36	0.82	31
WASP-77A	5500 ± 80	4.33 ± 0.08	2.94	4.0 ± 0.2		3.17	0.34	0.81	32
WASP-78	6100 ± 150	4.10 ± 0.20	4.85	4.1 ± 0.2		6.63	0.16	0.75	33
WASP-79*	6600 ± 100	4.2 ± 0.15	6.96	19.1 ± 0.7	17.5 $^{+3.1}_{-3.0}$	18.53	0.40	0.83	33,34

* Extrapolating the calibration beyond 6400 K.

References: 1. Doyle et al. (2013), 2. Triaud et al. (2010) , 3. Albrecht et al. (2011), 4. Gillon et al. (2009), 5. Albrecht et al. (2012a), 6. Queloz et al. (2010), 7. Brown et al. (2012a), 8. Albrecht et al. (2012b), 9. Bayliss et al. (2010), 10. Anderson et al. (2010), 11. Hellier et al. (2011), 12. Anderson et al. (2014b), 13. Bouchy et al. (2010), 14. Maxted et al. (2010b), 15. Anderson et al. (2011b), 16. Street et al. (2010), 17. Simpson et al. (2011), 18. Enoch et al. (2011), 19. Smalley et al. (2010), 20. Triaud et al. (2013b), 21. Anderson et al. (2011c), 22. Maxted et al. (2010a), 23. Brown et al. (2012b), 24. Barros et al. (2011), 25. Anderson et al. (2011a), 26. Maxted et al. (2011), 27. Gillon et al. (2011), 28. Faedi et al. (2013), 29. Hellier et al. (2012), 30. Smith et al. (2013), 31. West et al. (2013), 32. Maxted et al. (2013), 33. Smalley et al. (2012), 34. Addison et al. (2013)

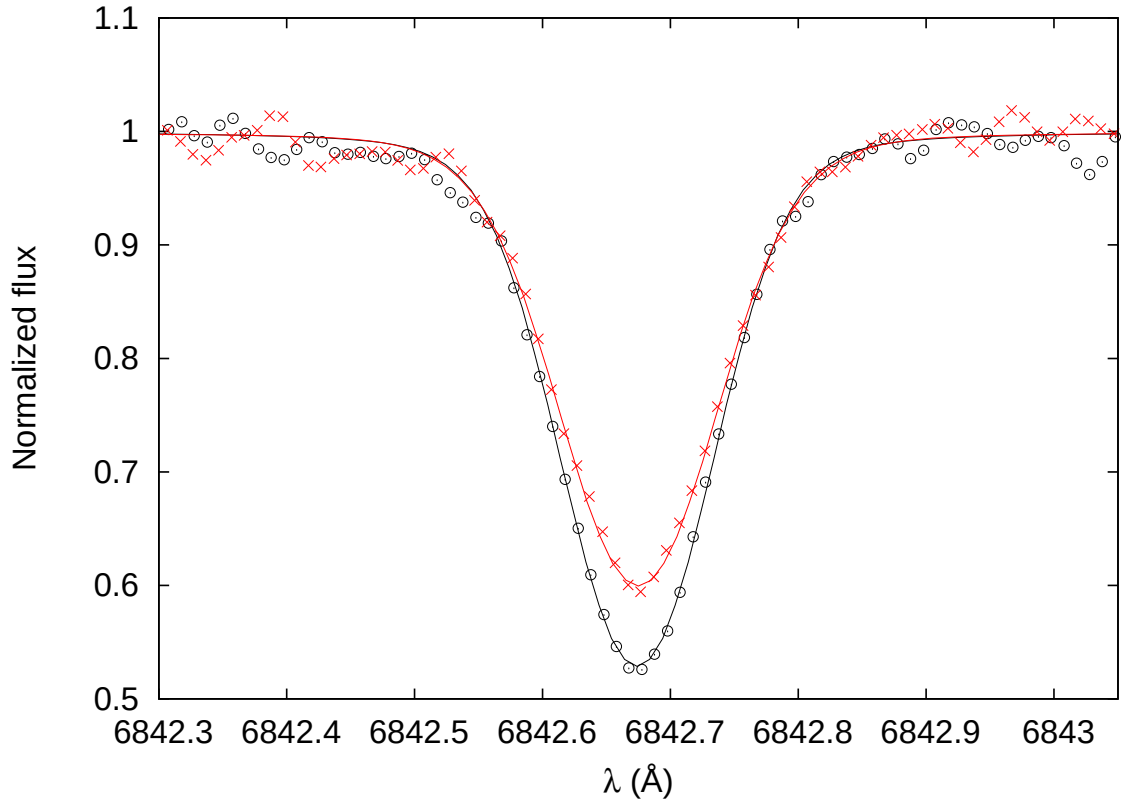

Figure 5.18: The magnetically sensitive Fe line at 6842 Å (red crosses) is overplotted with the non-magnetically sensitive Fe line at 6810 Å (black circles) for WASP-40, showing that 6842 Å exhibits stronger broadening which is likely due to Zeeman broadening. The solid lines are the synthetic fits to the observed spectrum.

The lines should have similar depth of formation and line strength, so that when the $v \sin i$ is fixed to 1.71 km s^{-1}, the $v_{\rm mac}$ measured from both lines should be the same if there is no additional broadening. In this sense, $v_{\rm mac}$ was fitted to test for additional broadening of the lines, rather than to obtain the actual macroturbulent broadening. If Zeeman broadening was affecting the line profiles, I would expect that the macroturbulence determined from the magnetically sensitive line would be higher than the reference line. WASP-40 does show evidence of Zeeman broadening, as seen in Figure 5.18, which shows the Fe line at 6842 Å which has a Landé g-factor of 2.5 overplotted with the Fe line at 6810 Å which has lower Landé g-factor of 0.86. It is clear that the magnetically sensitive line at 6842 Å exhibits stronger broadening. The $v_{\rm mac}$ for this line is 3.15 km s^{-1}, while the $v_{\rm mac}$ for the line at 6810 Å is 2.10 km s^{-1}. This implies that $v \sin i_{\rm spec}$ is overestimated for WASP-40 because the rotational broadening is used to erroneously fit also the Zeeman broadening.

WASP-6 also shows some evidence of Zeeman broadening, although it is not

as clear as for WASP-40 and in this case the $v \sin i_{\rm RM}$ used a spectroscopic prior. The $v \sin i_{\rm spec}$ is still higher than $v \sin i_{\rm original}$, however the latter was obtained from a CORALIE spectrum. The $v \sin i_{\rm spec}$ is still consistent with the value of 2.4 ± 0.5 km s^{-1} that I had previously determined in Section 3.6.

There is a small discrepancy in the fits to the lines of WASP-4. Adjusting both the $v_{\rm mac}$ and $v \sin i$ suggests that $v_{\rm mac}$ should be higher and $v \sin i$ lower for a precise fit to the spectral lines. The test for Zeeman broadening is inconclusive in this star, however as it would explain why a higher $v_{\rm mac}$ is needed to fit the lines, it is a plausible solution. Therefore, if a spectroscopic prior is required for a cool star, it should be noted that if there is Zeeman broadening present, then the $v \sin i$ could be wrong.

There are also some discrepancies for hotter stars, for example WASP-20, WASP-24 and WASP-32. WASP-20 has similar discrepancies in the line fits as WASP-4 and it once again seems that $v_{\rm mac}$ should be higher and $v \sin i$ lower, however it can't be Zeeman broadening in this case. As differential rotation makes the line profile more "pointed", it is possible that the $v \sin i$ isn't fitting properly due to the presence of differential rotation. The $v \sin i_{\rm RM}$ for WASP-24 is too high to fit the spectrum, which also suggests that differential rotation could be present. While it can be possible to detect differential rotation via the RM effect for misaligned planets that transit a range of latitudes (Gaudi & Winn 2007), these three systems are all well aligned.

There is one WASP star not included in Table 5.9. WASP-42, although having a published $T_{\rm eff}$ of 5200 ± 150 (Lendl et al. 2012), is actually beyond the range of the calibration. The initial analysis was performed with a poor S/N CORALIE spectrum and so I performed a spectral comparison with the HARPS spectrum and that of other cool stars as described in Section 3.6.6. This indicated that WASP-42 is more similar in $T_{\rm eff}$ to WASP-23 (5020 K), as shown in Figure 5.19, and thus should not be used. While the calibration could be extrapolated to lower temperatures, the lack of data points in this region and the problems with Zeeman broadening introduce too much uncertainty. I also checked the other stars with $T_{\rm eff}$ $\sim$5200 K, but there were no other inconsistencies.

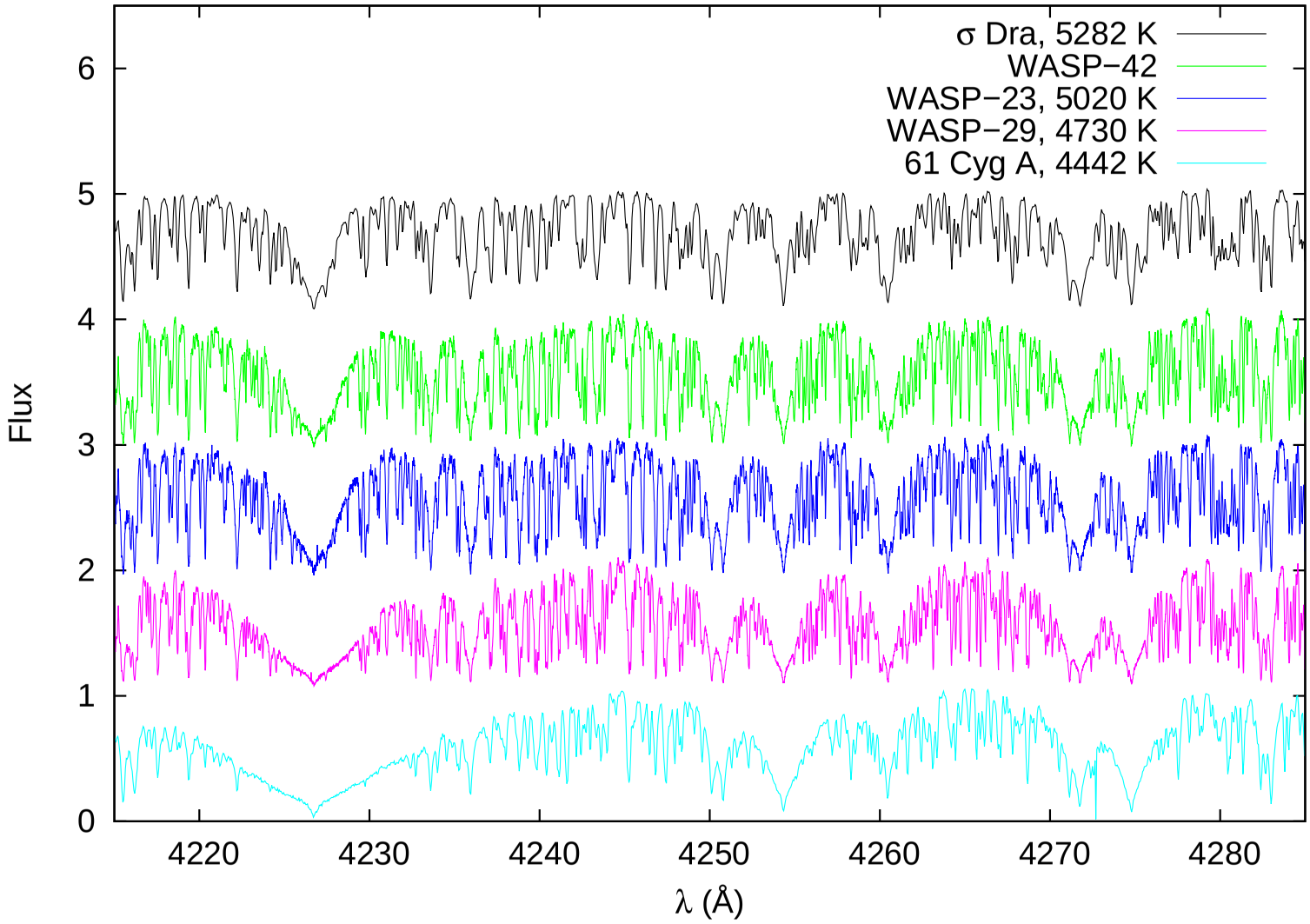

Figure 5.19: Spectral comparison for WASP-42.

I did extrapolate the calibration at the hotter end to measure the $v \sin i$ of WASP-7, WASP-17 and WASP-79. The $v \sin i_{\rm spec}$ of WASP-7 is notably higher than the $v \sin i_{\rm RM}$, which did not need a prior. This might imply differential rotation; indeed Albrecht et al. (2012a) also suggest that differential rotation could be present in this star. The $v \sin i_{\rm spec}$ of WASP-17 is in agreement with both $v \sin i_{\rm original}$ and $v \sin i_{\rm RM}$, suggesting that the calibration can still be used at this $T_{\rm eff}$ range. However it should be emphasised that there is a lot of uncertainty in both the $T_{\rm eff}$ and $\log g$ of this star, so the $v \sin i$ might not be an accurate representation. It is also possible that the extrapolation is invalid at hotter temperatures. The comparison of $v \sin i_{\rm spec}$ to $v \sin i_{\rm RM}$ for WASP-79 is inconclusive, given the large error in the latter.

Overall, the use of Equation 5.10 to determine $v_{\rm mac}$, and thus $v \sin i$, has the advantage of having improved accuracy over the original spectroscopic values. However, they should still be used with caution as other factors such as Zeeman broadening and differential rotation can also potentially influence the line broadening.

5.9 Depth dependence

Macroturbulence is usually assumed to be independent of depth in the photosphere, possibly because it is a large-scale phenomenon. However, the $v_{\rm mac}$ velocity is mostly due to granulation, and the granulation velocity in the Sun diminishes with height (Gray 2008; Lefebvre et al. 2008).

Gray (1977b) finds that the RT $v_{\rm mac}$ is larger for weak lines compared to the strong lines, i.e. it is larger deeper in the photosphere where the weak lines are formed. If it is assumed that $v_{\rm mac}$ doesn't vary with depth, then it is impossible to reproduce the Fourier transform of the intrinsic flux profile using the $v_{\rm mac}$ obtained from only the strong lines in the Sun. The same is true regardless of whether $v_{\rm mic}$ is constant or depth-dependent. Simply increasing the microturbulence with depth will make the Fourier profile more Gaussian in shape than radial-tangential, and this does not match the observed profile which is dominated by the radial-tangential function. The model profile will have a lower Fourier amplitude than the observed data unless the $v_{\rm mac}$ is higher for the weak lines (Gray 1977b).

The results of Takeda (1995) agree with Gray (1977b), and also show that when $v_{\rm mac}$ is plotted as a function of depth of line formation, it appears that $v_{\rm mac}$ increases with depth. Takeda also shows that $v_{\rm mac}$ decreases as EW increases, and increases as

EP increases. This is because the range of depths at which a line is formed depends on the EP. For Fe I lines with higher EPs, greater temperatures are needed to maintain the same population of atoms in the lower energy level. This means that the lines can only be formed deeper in the photosphere where the temperature is high enough, and thus the range of formation is decreased. The dependence of $v_{\rm mac}$ on line strength is still governed by EP, as the higher EP lines are generally weak because of the decreased population of the lower energy level (Grossmann-Doerth 1994).

I have also verified this using the Fe I lines from Table 5.1 for the Sun. Four additional Fe I lines were used, which were not used in the calibration. Figure 5.20 shows $v_{\rm mac}$ as a function of the optical depth $\log \tau$ at 5000 Å at which the core of each line is formed. It is clear that $v_{\rm mac}$ is higher in the lower layers of the photosphere, however it should be cautioned that an incorrect $\log gf$ will result in an incorrect value of $\log \tau$. The bottom panel of the figure also shows variation of $v_{\rm mac}$ with EP. The high EP lines are formed deeper in the atmosphere. The trends with $v_{\rm mac}$ are not the exact same for $\log \tau$ and EP because the lines strength will also play a small role in the depth of formation.

The difference in $v_{\rm mac}$ for lines of low and high EP can be seen across all of the *Kepler* stars. Figure 5.21 shows the relationship between $v_{\rm mac}$ and $T_{\rm eff}$ for the Fe I lines 5956 and 6055 Å. These lines have EP of 0.859 and 4.733 eV respectively. The line with higher EP is formed deeper in the photosphere and thus has higher $v_{\rm mac}$.

As different lines will have different values of $v_{\rm mac}$, assuming an average $v_{\rm mac}$ for a star will increase the errors in the $v \sin i$. For example, using the average $v_{\rm mac}$ of 3.21 $\rm km\,s^{-1}$ for the Sun returns a $v \sin i$ value of 1.84 $\pm$ 0.35 in the Kitt Peak Solar Atlas. Alternatively, using each individual $v_{\rm mac}$ value for each line gives a $v \sin i$ of 1.88 $\pm$ 0.11. Therefore a depth-dependent $v_{\rm mac}$ calibration would improve the precision of the $v \sin i$.

I attempted to fit individual relationships between $v_{\rm mac}$ and $T_{\rm eff}$ for each of the lines used in the final calibration. The results for the Fe I lines are shown in Figure 5.22. The points shown in the plot are the average $v_{\rm mac}$ values as depicted in Figure 5.12, however there can be a significant amount of scatter for individual lines, so that the fits shown in Figure 5.22 don't necessarily accurately represent the $v_{\rm mac}$ relationship with $T_{\rm eff}$. It is particularly difficult to include a $\log g$ component for most of the individual lines, therefore only $T_{\rm eff}$ was used. In addition, some lines required a linear rather than a polynomial fit. Nonetheless, it is still clear that different lines will have different relationships with $T_{\rm eff}$.

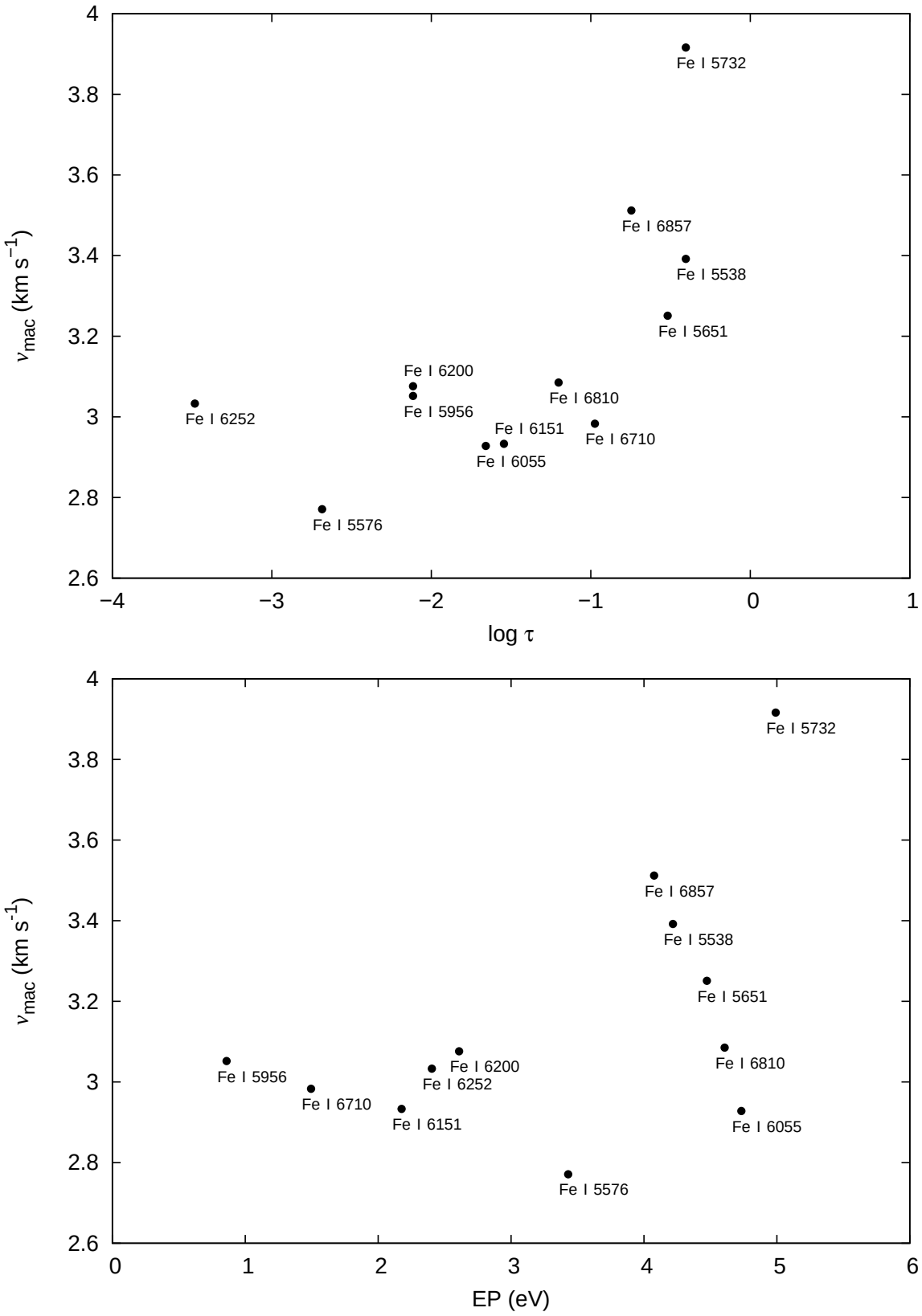

Figure 5.20: The top panel shows that the $v_{\rm mac}$ increases with optical depth in the Sun, and the bottom panel shows that the $v_{\rm mac}$ increases with EP.

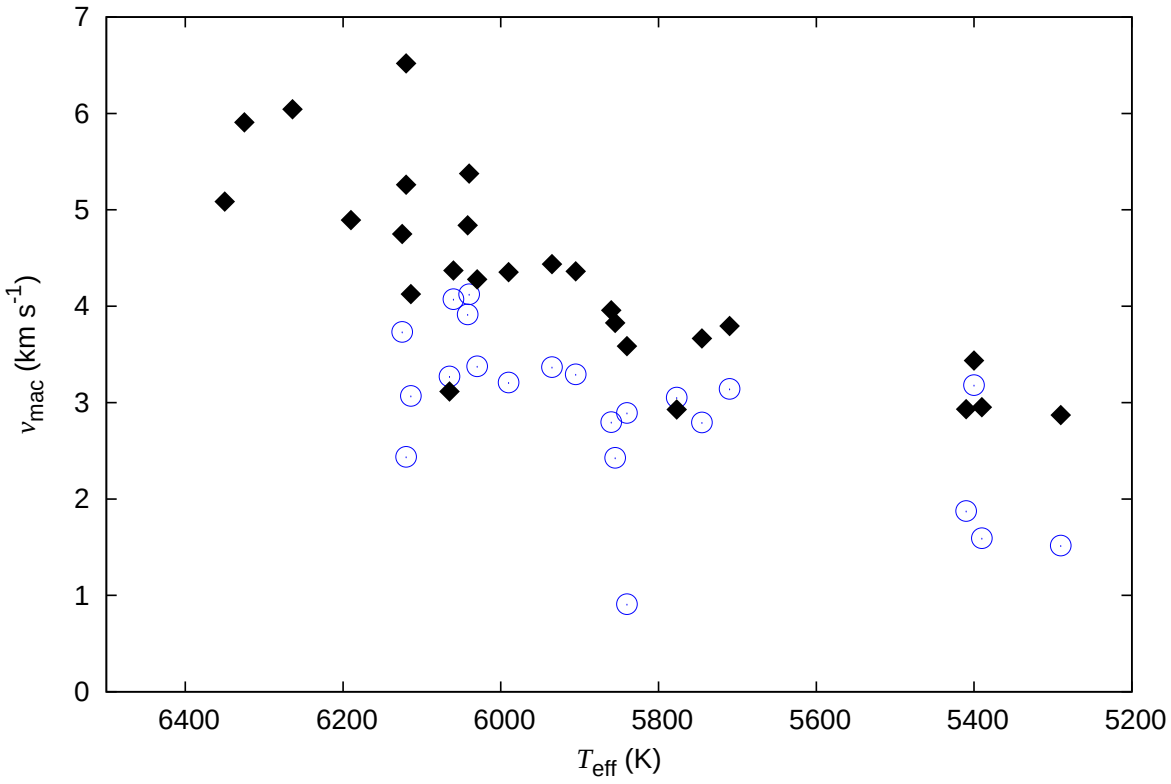

Figure 5.21: The black diamonds are the high EP line Fe 6055 Å and the blue circles are the low EP line Fe 5956 Å.

5.9.1 Fitting Si lines

In Section 3.4 I mentioned that it is often difficult to fit the Si lines due to unusually broad wings and asymmetries in the lines. Shi et al. (2008) suggest that the asymmetries are not due to line blends, but are a direct result of the velocity fields in the photosphere and cannot be modelled adequately with 1D models. They propose that the use of 3D models will result in improvement of the line profile fitting. Nonetheless, Shaltout et al. (2013) used 3D NLTE models and still found that some line profiles were discrepant. As such, they cited uncertainties in collisional broadening, $\log gf$, and possible blending as the source of the error.

As the Si lines have high EPs and are formed deep in the photosphere, they will experience stronger velocity fields compared to lines of other elements, which might explain why the lines are so difficult to fit. The solar $v_{\rm mac}$ and depth of formation of the line core are given in Table 5.10.

However Sheminova (1993) notes that Si is particularly sensitive to pressure compared to other elements and Shaltout et al. (2013) state that Si lines are notably influenced by VDW broadening. For the 6721 Å line, I originally obtained a best-fit $v_{\rm mac}$ of

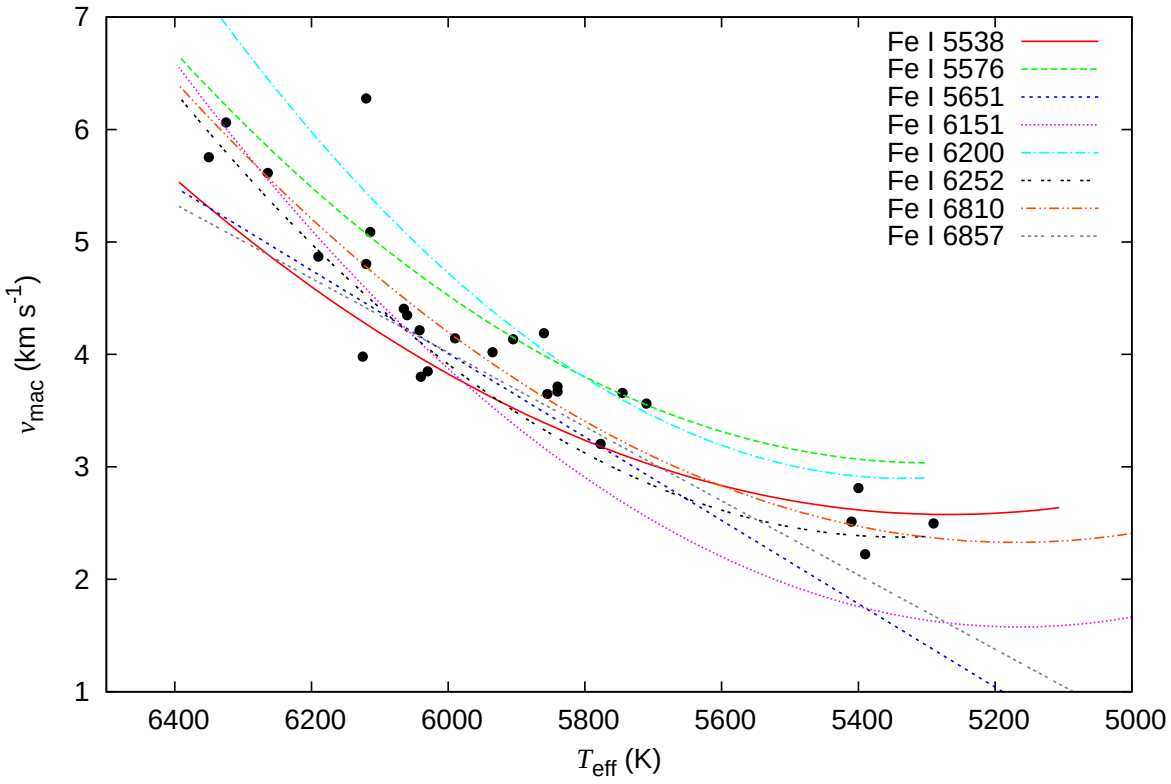

Figure 5.22: Individual calibrations for each of the Fe I lines used in the final calibration. The points are the same as in Figure 5.12.

Table 5.10: $v_{\rm mac}$ of Si lines in the Kitt Peak Solar Atlas

λ (Å)	EP (eV)	$\log gf$	Solar EW (Å)	$\log \tau$	$v_{\rm mac}$ (km s^{-1})
5488.983	5.614	-2.420	0.0215	-0.29	6.944
5517.533	5.082	-2.611	0.0134	-0.29	4.304
5701.104	4.930	-1.581	0.0399	-1.08	3.828
6721.848	5.863	-1.516	0.0488	-0.52	4.984

4.98 km s^{-1} for the Kitt Peak Solar Atlas. This is shown in Figure 5.23 and it is clear that the synthetic line is not broadened enough compared to the observed line. Fixing the $v_{\rm mac}$ of the 6721 Å line to 3.5 km s^{-1}, I found that significantly increasing the VDW value will result in an improved fit to the line, although it is still not possible to fit it perfectly. Using this value of VDW and then fitting the $v_{\rm mac}$ again gives a value of 3.83 km s^{-1}, which fits better than the original value of 4.98 km s^{-1}. It is possible that the $v_{\rm mac}$ given in Table 5.10 is not actually that high due to errors in VDW broadening, however it is still not possible to precisely fit any of the Si lines.

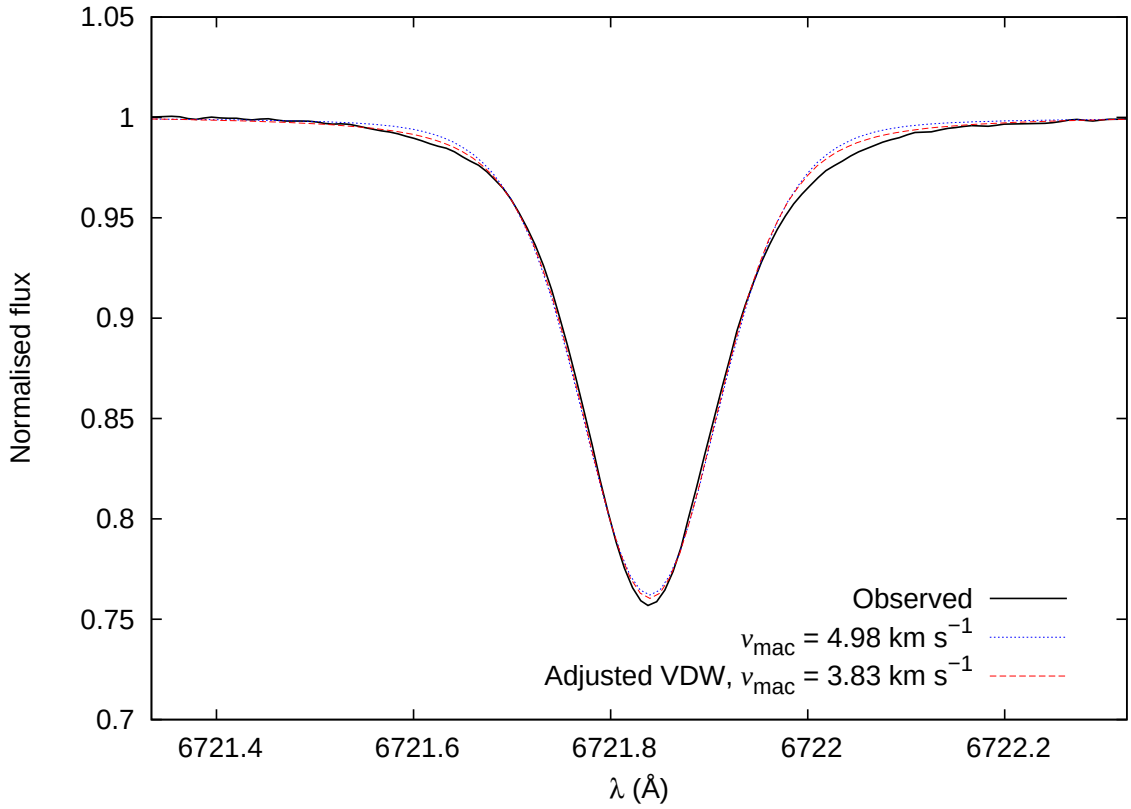

Figure 5.23: The black solid line is the observed Si 6721 Å in the Kitt Peak Solar Atlas. The blue dotted line is the original $v_{\rm mac}$ fit the line, which does not have broad enough wings. The red dashed line is the fit when the VDW is increased and the $v_{\rm mac}$ is refit. The latter results in a better fit, although it is still impossible to fit the line perfectly.

5.10 Comparison with other indicators of velocity fields

Macroturbulence is not the only signature of granulation that can be detected in stellar line profiles. Line asymmetries and line shifts are also an indication of velocity fields in the photosphere and both of these vary across the HR diagram in a similar manner to $v_{\rm mac}$ (Gray 2009; Ramírez et al. 2009).

There is a Doppler shift introduced by the upflowing material in the granules and the downflowing material in the intergranular lanes. The bright, hot material of the upward moving granule causes the spectral line to be blueshifted as the rising material approaches the observer. The dark, cool intergranular lanes cause line profiles to be redshifted. When granulation is unresolved, the net effect is that the line is blueshifted, but the red wing is broadened from the intergranular material. This causes the spectral line to be asymmetric in shape (Gray 2008; Ramírez et al. 2009).

If the line profile is sliced up into horizontal segments, plotting the midpoint of

each horizontal line will reveal the bisector of the line. In a solar-like star the bisector is a "c" shape, although this shape will be reversed in early-type stars (Gray 2008).

The blueshifting of the line means that the core wavelength is displaced from its rest wavelength, and this is known as convective blueshift. Weak lines exhibit the strongest shift as they are formed deeper in the atmosphere where the velocity fields are stronger. The amount of line shift decreases with increasing line strength, and lines stronger than 100 mÅ in the Sun do not exhibit any line shifts (Allende Prieto & Garcia Lopez 1998; Ramírez, Allende Prieto & Lambert 2008).

Obtaining line bisectors requires very high resolution and high S/N spectra, so is not possible with the ESPaDOnS and Narval spectra. It is possible to measure line shifts with lesser quality spectra, however there are still uncertainties in the laboratory wavelengths, the gravitational redshift and radial velocity of the star. Line shifts for the Sun were available for most of the Fe I lines that I have in Allende Prieto & Garcia Lopez (1998). They compared the wavelengths of the lines in the Kitt Peak Solar Atlas to the laboratory wavelengths of Nave et al. (1994). These line shifts are plotted against the $v_{\rm mac}$ for each Fe I line in Figure 5.24. The zero velocity shift takes into account the gravitational redshift of the Sun of 636 $\rm ms^{-1}$.

The strongest lines have the highest $v_{\rm mac}$ and also the lowest velocity shifts as expected, showing that these both represent the same phenomenon. The line shifts also show a similar dependence with $\log \tau$ as $v_{\rm mac}$, and this is shown in Figure 5.25. There is no real trend seen between line shift and EP.

As mentioned in Section 1.8.3.3, 3D models have no need for either $v_{\rm mac}$ or $v_{\rm mic}$ in order to fit the line profiles as modelling convection in 3D is sufficient to broaden the lines. Line bisectors and shifts can be successfully measured using 3D models (Asplund et al. 2000), although as mentioned earlier in this section they are not easy to measure. Macroturbulence, on the other hand, is much easier to measure and it can be measured even for spectra of moderate quality, as shown here. While it has been described as an "fudge factor," macroturbulence is still a measure of the velocity dispersion of granulation. Therefore, measuring $v_{\rm mac}$ using 1D models can still be of use for studying convection in stellar photospheres.

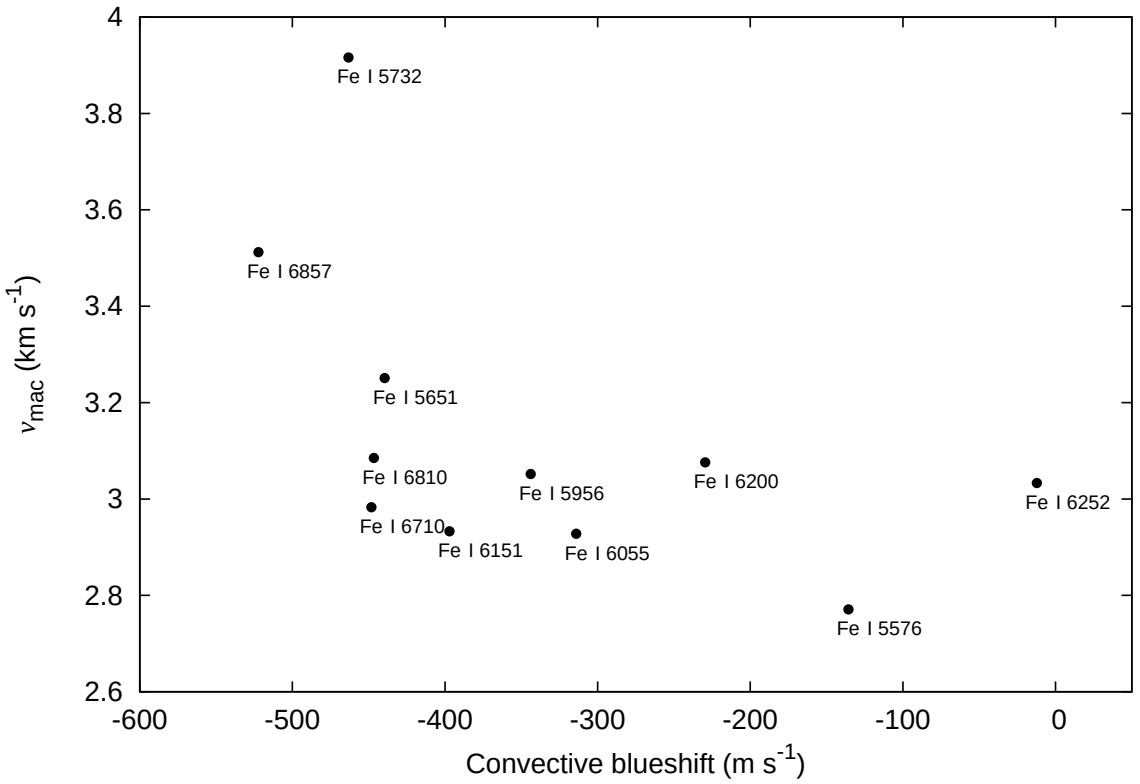

Figure 5.24: The $v_{\rm mac}$ versus convective blueshift for the Sun. The zero line shift takes the gravitational redshift of 636 ms^{-1} into account. Weak lines have the largest blueshift and also the highest $v_{\rm mac}$.

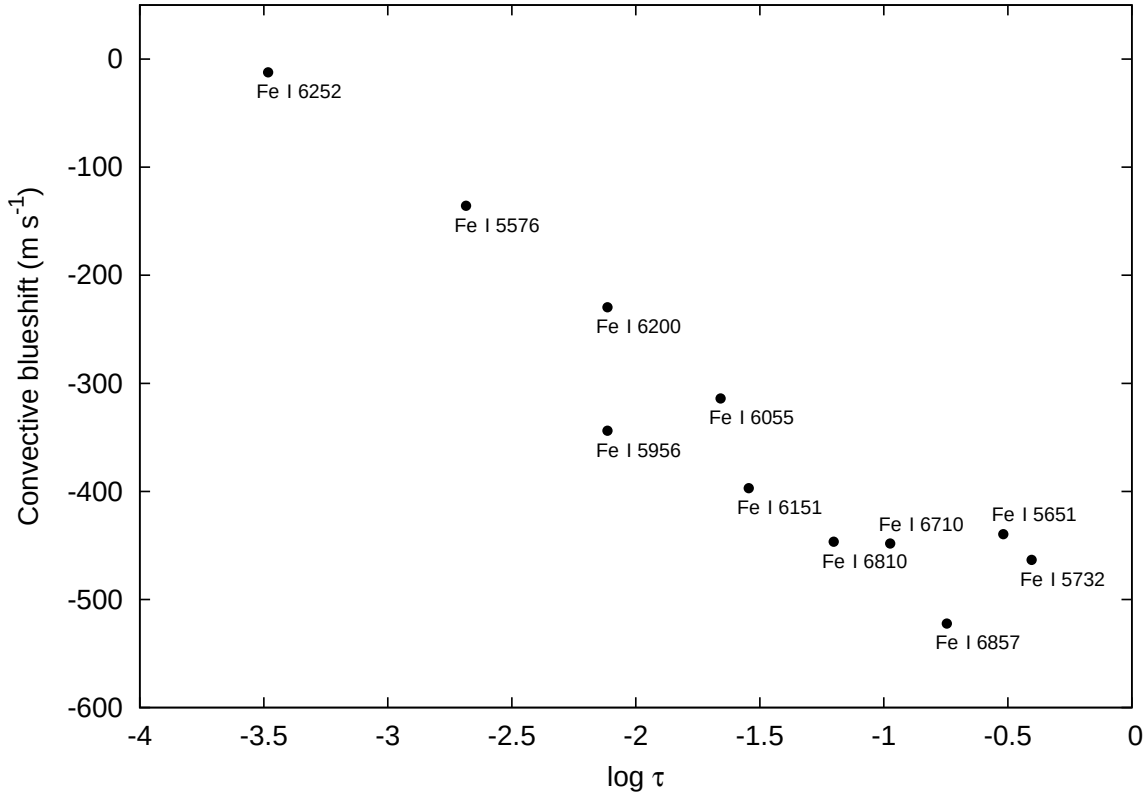

Figure 5.25: Convective blueshift versus $\log\tau$ with for the Sun. The depth dependence is more obvious for the blueshifts than for $v_{\rm mac}$.

6 Summary, discussion, and future work

The future of a subject is the product of its past, and the hopes of astrophysics should be implicit in what the science has already achieved.

- Cecilia Payne, 1925

In this thesis, I have investigated the "traditional" spectral analysis method in depth, highlighted flaws that are often ignored, and offered suggestions on how to improve these methods. By comparing my own thorough analyses with other, supposedly similar methods I have revealed a worrying amount of differences in the stellar parameters derived by different methods. Finally, my in-depth analysis of spectra of solar-like stars led me to disentangle two of the more prominent broadening factors in spectral lines; macroturbulence and projected rotational velocity. In this chapter I will summarise my work, as well as discuss where it could lead next.

6.1 The finer points of spectral analysis

I first checked my spectral analysis method on the Sun and Procyon, to verify that it returned reasonable parameters. I then applied this method to the HARPS spectra of 22 WASP stars to determine $T_{\rm eff}$, $\log g$, $v_{\rm mic}$, $v_{\rm mac}$, $v \sin i$ and elemental abundances. Despite the high resolution, high S/N HARPS spectra, the overall errors in these parameters are still quite high, showing that there is only so much that can be done with high quality spectra. In order to minimise these errors, improvements in laboratory atomic data need to made first.

6.1.1 Line lists and elemental abundances

All of the stellar parameters listed above rely on the selection of spectral lines for the method based on EWs, and even methods that fit the entire spectrum still require accurate atomic data to be sourced. The selection of a good line list is crucial, as it forms the foundation for the EW method, and is a task that a considerable amount of thought must go into. There is a misconception in the literature that using hundreds of Fe lines will automatically make the stellar parameters more reliable, however this is only true if they are hundreds of *good* lines.

In Section 3.4, I described how to select a good line list and also how different line lists should be constructed from stars of different temperatures. A solar line list will not

return the best results for stars of different $T_{\rm eff}$ to the Sun. A line list should have lines with a low Landé g-factor, so that there there will be some lines that aren't affected by Zeeman broadening. Comparing these lines with lines of a high Landé g-factor can indicate the presence of Zeeman broadening, and thus activity, although this method isn't the most reliable due to the difficulties in fitting lines. It might still be useful when it isn't possible to check the Ca II H and K lines for activity (if the spectral range isn't covered by the spectrograph), or if no rotation period from spots is available. A knowledge of Zeeman broadening is also important as it can affect $v_{\rm mac}$ measurements. It is also imperative to have a wide range in EP, and in particular to include as many low EP lines as possible. This is important for the excitation balance $T_{\rm eff}$, as well as for investigating depth dependent macroturbulence.

Despite a careful selection of lines, the frustrating lack of accurate laboratory $\log gf$ values hinders the determination of stellar parameters. It is important not to accept the default atomic data in VALD as the best available without first looking for alternate sources. It might be helpful to liaise with laboratory physicists to obtain accurate $\log gf$ values. For instance, many of the highest rated lines in the NIST database are not detectable in the spectra of solar-like stars. Similarly, some of the most prominent lines in the stellar spectra do not have laboratory measurements.

When measuring the EWs of lines, strong lines should be fit using a least squares method as the EW measurements will be underestimated due to broad wings. Spectra with low S/N tend to make continuum placement difficult, which can lead to abundance errors, and even with high S/N unidentified weak lines can cause problems with normalisation and thus EW measurements.

Differential analysis to the Sun is frequently used in spectral analysis in order to eliminate the errors associated with the oscillator strength. This is only applicable to stars with similar parameters to the Sun, yet it is often applied to stars that are not in the correct parameter space. In such cases, a line-by-line differential analysis won't be appropriate as different $T_{\rm eff}$ conditions will mean that the lines no longer simply scale with the Sun. My analysis did show that the abundances obtained from UCLSYN agreed with the differential analyses to within 0.04 dex, however given the range of parameters of the WASP stars I would rather use the direct abundances than the differential ones. Differential analysis can also create a problem for $v_{\rm mic}$ determination, as seen in Section 4.1.3. The choice of solar $v_{\rm mic}$ used when creating the astrophysical $\log gf$ values will ultimately bias the $v_{\rm mic}$ determined for other stars. Ultimately the

solution once again relies on better laboratory atomic data.

In Section 5.10, I discussed the difficulties involved in fitting Si lines due to their exceptionally broad wings. This is likely a combination of the fact that Si lines are formed deeper in the photosphere than any other elements that are commonly used in the analysis of solar-like stars, and due to the fact that there are uncertainties in their VDW values. Even if the lines could be fit perfectly, it is still difficult to get an accurate Si abundance. As discussed in Section 3.4.1, there are few reliable $\log gf$ values available for this element. This is a matter of concern in relation to planetary studies. Si is an important element for planet formation due to its presence in silicates, and it has been suggested that Si is enriched in planet host stars (Robinson et al. 2006; Brugamyer et al. 2011). This supposed Si enrichment needs to be looked at more carefully.

Ideally, abundance analyses should be performed with 3D NLTE models, and it is likely that this will become more common in the future as computing power increases.

6.1.2 Microturbulence

Microturbulence is one of the trickiest parameters to measure. I determined a relationship between $v_{\rm mic}$ and $T_{\rm eff}$ for the WASP stars in Section 3.6.3. There is a lot of scatter in the $v_{\rm mic}$ values, but this does not appear to be partially caused by a $\log g$ dependence as was found with $v_{\rm mac}$. Unlike $v_{\rm mac}$, $v_{\rm mic}$ can not easily be fit to the spectral lines because it is a very subtle effect. It is also possible that $v_{\rm mic}$ is depth dependent, meaning that it will not be the same for every line of similar strength. Plotting $\log A$ (Fe) against EW to determine the $v_{\rm mic}$ depends on many other factors, so it is understandable that the $v_{\rm mic}$ values vary so much between different analysis methods. I also investigated the use of Blackwell diagrams, but found no advantage to using this method as it still relies on a knowledge of $T_{\rm eff}$.

Comparing my calibration to others showed that my values are underestimated. Part of this can be explained by my use of the Magain (1984) method to determine $v_{\rm mic}$, but this does not fully explain the discrepancy. However, it should be borne in mind that there is still no definite answer as to what the $v_{\rm mic}$ of the Sun is, as can be seen in the literature values given in Table 1.1.

Perhaps with high S/N and high resolution spectra, accurate atomic data, accurate damping parameters, a proper knowledge of the depth-dependent $v_{\rm mac}$, and an external measurement of the $v \sin i$, it might be possible to measure the $v_{\rm mic}$ accurately

from fitting the line profiles, but we are still a long way from that. Similarly, the method of reducing the slope between $\log A$ (Fe) and EW will not improve until the atomic data does.

6.1.3 Fixing $\log g$ to the transit or asteroseismic values

The use of a spectroscopic $\log g$ is often frowned upon in the literature when there are values available from planet transits or from asteroseismology. Indeed, in this thesis I highlighted a number of issues with determining the spectroscopic $\log g$. For instance, it is crucial to include as many Fe II lines as possible for the ionisation balance, as using only a handful of Fe II lines will give the wrong $\log g$. It is also vital to know the Na abundance before determining $\log g$ from the Na D lines. However, the abundance of Na with respect to Fe is abnormally high for stars with $T_{\rm eff} < 5000$ K which results in an underestimation of $\log g$.

It is often suggested that the transit $\log g$ should be used in spectral analysis so that the other spectroscopic parameters are determined while keeping $\log g$ fixed. Figure 3.15 shows that no real comparison can be made between the spectroscopic and transit $\log g$ and from this perspective there is no reason to think that one method should be preferred over the other. In addition, using a $\log g$ fixed from the transit can mean that the spectral analysis is no longer self consistent. However, in this analysis the "unconstrained" $T_{\rm eff}$ from the excitation balance agreed well with the "constrained" $T_{\rm eff}$ determined while keeping the $\log g$ fixed. Although as Torres et al. (2012) point out, fixing $\log g$ is more likely to effect the $T_{\rm eff}$ for spectral fitting methods, rather than methods based on Fe line EWs. Without having an obvious answer as to which $\log g$ value is better, it is probably best to show both sets of parameters.

The $\log g$ can also be fixed to the asteroseismic value, which is more reliable than the transit $\log g$ as it is not dependent on isochrone models. Unlike a comparison between the spectroscopic and transit $\log g$, there is a systematic difference between the spectroscopic and asteroseismic values as shown by Bruntt et al. (2012). They find that the spectroscopic values are higher by 0.08 dex, with the exception of a few outliers, but are unable to offer an explanation why. It should be emphasised that this difference between the $\log g$ values is for one spectral analysis method, and there will likely be a variation in the discrepancy depending on the spectral analysis method used. It should also be borne in mind that the spectra used for the Bruntt et al. (2012) analysis were of poor quality. Spectra with higher S/N which are properly sampled might allow

for a more thorough investigation into the differences between the spectroscopic and asteroseismic $\log g$ values. After all, the spectroscopic $\log g$ values I determined for the Sun and Procyon were accurate, and these were very high S/N, high quality spectra.

If the asteroseismic values are indeed an accurate fundamental value, then a detailed comparison between them and the spectroscopic values might reveal problems with the latter. Looking at θ Cyg, where my spectroscopic $\log g$ is 0.12 dex higher than the asteroseismic value, does not currently offer any insight as to why the values are different. The ionisation balance, Na D lines and 6439 Å Ca line all agree well and none of them are responsible for pulling the spectroscopic value higher. Perhaps for this particular example, the star is simply too hot to be appropriate for such an analysis.

6.2 The need for homogeneous studies

We don't just need to compare stars using different methods, we need to understand why those methods give different results, how we can improve the methods, and ultimately what is the best possible way of doing it. My additional work on the HoSTS study of WASP-13 has highlighted some of the differences between spectral analysis methods.

It is difficult to make a comprehensive comparison to SME as this is based on fitting sections of the spectrum by varying the parameters. However the comparison with Procyon in Section 4.2 does show good agreement of the abundances between SME and UCLSYN. For WASP-13, it does appear that fixing the $v_{\rm mic}$ has a minimal effect on the parameters determined by SME, while fixing $\log g$ can have a notable effect on the $T_{\rm eff}$. This is the opposite to the Fe line based methods, where $v_{\rm mic}$ needs to be left as a variable.

Theoretically, the three analyses for WASP-13 based on the EWs of Fe lines should return the same result. In reality, there are some substantial differences between these results. The 70 K difference in $T_{\rm eff}$ and the 0.33 $\rm km\,s^{-1}$ difference in $v_{\rm mic}$ for Method D can both be explained by the use of different line lists. This was explored in detail, and revealed that the increased $T_{\rm eff}$ of Method D is due to numerous blended lines in the list and that the increased $v_{\rm mic}$ is due to the line list being created differentially to the Sun. The low $\log g$ of Method C was also explained by the use of only five Fe II lines for the ionisation balance. This one again highlights the importance of carefully selecting a line list and also that we should be aware of how these different lists can influence the parameters obtained. Each person or group involved in spectral analysis

will have their own preferred line list, and while it would be impossible to choose one line list to suit everyone's needs, it is important to realise just how much the line list is responsible for differences between methods.

This work has also indicated that there might be some differences between the codes UCLSYN and MOOG which are creating significant differences in abundances. This deserves further investigation, as well as comparison with other codes that are used in spectral analysis.

Many studies use different spectrographs, without taking the potential differences into account. I found a difference of 0.10 ± 0.05 dex between the HARPS spectral analyses and the previous analyses, which were mostly performed using CORALIE spectra. The CORALIE spectra typically have lower S/N than their HARPS counterparts, so that the wings of the lines become lost in the noise and the abundances are underestimated. Even for spectra of similar S/N, there is still a small systematic difference which may be due to scattered light in CORALIE. These differences between spectrographs need to be studied in more detail, and to include other high resolution spectrographs frequently used for the analysis of solar-like stars so that corrections can be made for the spectrograph used.

Figure 4.7 showing the θ Cyg results is an eye-opener as to the discrepancies that still exist between different methods for the one star. While this was a particularly difficult star to analyse with the traditional Fe line method due to its high $T_{\rm eff}$, this does not explain why such large differences exist when spectrum fitting methods are also included. It is clear that more work is needed in order to resolve the discrepancies between different spectral analysis methods, and ultimately determine reliable stellar parameters.

6.3 The study of macroturbulence

In Chapter 5, I used $v \sin i_{\rm astero}$ values to determine the $v_{\rm mac}$ for a number of *Kepler* stars, and ultimately a relationship between $v_{\rm mac}$, $T_{\rm eff}$ and $\log g$. A statistical comparison between my $v_{\rm mac}$ calibration and those of Gray (1984a), Valenti & Fischer (2005) and Bruntt et al. (2010a) show that while mine agrees best with the observed data, the other calibrations also offer reasonable agreement. However, as there is obviously a $\log g$ dependence in $v_{\rm mac}$, my calibration will ultimately return more accurate values compared to the others. The Gray (1984a) calibration also proves to be a good cali-

bration, although it does not include a $\log g$ component. The Valenti & Fischer (2005) calibration should only be used to obtain the upper limit on $v_{\rm mac}$ for stars with $T_{\rm eff} <$ 5800 K, and the Bruntt et al. (2010a) calibration needs to be corrected by a factor of $\sqrt{2}$ before it can be used reliably. There is still room for improvement in my calibration if better spectra are obtained, and it will be interesting to see just how prominent the $\log g$ dependence actually is.

I used this calibration to remeasure the $v \sin i$ for the WASP stars so that there are now more accurate and consistent $v \sin i$ values available for these stars, which is important when the spectroscopic $v \sin i$ prior is needed for the RM analysis. I also highlighted how comparing these new spectroscopic $v \sin i$ values with those obtained from the RM effect (without a prior) can be used to indicate if Zeeman broadening or differential rotation might be present.

6.3.1 What could be achieved with better spectra

The results presented in Chapter 5 on $v_{\rm mac}$ are based on spectra that are barely appropriate for a detailed analysis of line profile shapes, particularly as the spectra are undersampled. Ideally spectra of much higher quality, for example those that could be obtained from HARPS-N, are needed for these stars. Such spectra would have the resolution and S/N high enough to study the line profiles in great detail. Errors in continuum placement dominate the current $v_{\rm mac}$ errors but with a S/N $\gtrsim$ 200, the continuum errors will diminish and it will be possible to get much greater precision. This will be particularly helpful for the stars KIC 2837475 and 6508366, which as mentioned in Section 5.6 have curiously high values of $v_{\rm mac}$. As both stars also have relatively high $v \sin i$ values, there are few lines that can be used and the $v_{\rm mac}$ signal is starting to become washed out by the rotational broadening. With better spectra, it would be possible to verify if the $v_{\rm mac}$ is indeed this high and in turn investigate the implications of this.

For high resolution (R >100,000), high S/N spectra, Fourier methods can also be used to disentangle $v_{\rm mac}$ and $v \sin i$ (Gray 2008). The $v_{\rm mac}$ relationship determined here is in reasonable agreement with that of Gray (1984a), which uses Fourier methods to determine a relationship between $v_{\rm mac}$ and $T_{\rm eff}$. Asteroseismology can only be used to obtain reliable $v \sin i$ values in the range of $\sim$5100 $< T_{\rm eff} <$ 6700 K. With higher resolution spectra, it might be possible to confirm that the Fourier method produces $v_{\rm mac}$ values in agreement with the values obtained using the asteroseismic $v \sin i$ values

for this sample of stars. This would allow for the $v_{\rm mac}$ calibration to be extended to higher and lower temperatures, which would be of greater use to those requiring $v \sin i$ values for the RM studies. Fourier methods can also be used to determine differential rotation (Reiners & Schmitt 2002), which could help to understand the stars that appear to have $v \sin i_{\rm astero}$ too high for the spectra, as discussed in Section 5.6.1.

Another advantage of higher quality spectra would be the ability to thoroughly investigate depth dependent $v_{\rm mac}$ in stars other than the Sun. Section 5.9 discusses how $v_{\rm mac}$ varies with depth in the Sun, and Figure 5.22 suggests that there could be different $v_{\rm mac}$ relationship with $T_{\rm eff}$ for each line, depending on its properties. A depth dependant $v_{\rm mac}$ calibration would enable incredibly precise measurements of $v \sin i$ values for particular lines, as well as revealing how the velocity fields change with height in stars of different spectral type.

It may also be possible to measure line shifts and bisectors for higher quality spectra, which would compliment the $v_{\rm mac}$ measurements and allow for a thorough analysis of the velocity fields.

6.3.2 Extending the macroturbulence work

Saar & Osten (1997) found evidence that active stars have enhanced $v_{\rm mac}$ and it would be interesting to investigate this further. Unfortunately, only five stars in the sample used in this work show evidence of activity but it may be possible to explore this if the sample is ever extended.

Figure 5.12 shows the upper limit values of three giants from Deheuvels et al. (2014), which have a higher $v_{\rm mac}$ than the dwarf star equivalents, as expected. Asteroseismic data is much more plentiful for red giants than it is for solar-like stars. While it is more difficult to determine $\delta\nu_{\rm s} \sin i$ for these stars due to the mixed modes, it might be possible to extend the $v_{\rm mac}$ calibration for stars with $\log g$ between 3.0 and 4.0 dex if the $\delta\nu_{\rm s} \sin i$ measurements became available. Even an upper limit for more giants would allow for an investigation of velocity fields in these stars.

It is also possible to study granulation via asteroseismology. Granulation creates a background signal at low frequencies and this signal can be modelled to yield the timescale and amplitude of the granulation (Harvey 1985). Mathur et al. (2011) analysed the granulation signals for 1000 red giants from *Kepler* data where they showed that the characteristic timescale of granulation is proportional to $\sqrt{T_{\rm eff}}/g$. When the granulation signals have been studied for the dwarf stars used in this thesis, it will be

interesting to see if this granulation timescale follows the same trend with $T_{\rm eff}$ and $\log g$ as $v_{\rm mac}$ does.

Very few stars have accurate $v \sin i$ measurements. Stellar rotation is frequently determined from the rotation period measurements, but this is dependent on the latitude of the spots. The stars here represent the best available for asteroseismic analysis of solar-like stars, and the $v \sin i_{\rm astero}$ values have opened up a new window in the study of stellar velocity fields, with room for more analysis in the years to come.

Publications

As lead author

Doyle, A.P., Davies, G.R., Smalley, B., Chaplin, W.J., & Elsworth, Y., 2014, Determining stellar macroturbulence using asteroseismic rotational velocities from *Kepler*, MNRAS, 444, 3592

Doyle, A.P. et al., 2013, Accurate spectroscopic parameters of WASP planet host stars, MNRAS, 428, 3164

As co-author

Anderson, D.R.A. et al., 2014, Three newly discovered sub-Jupiter-mass planets: WASP-69b and WASP-84b transit active K dwarfs and WASP-70Ab transits the evolved primary of a G4+K3 binary, MNRAS, 445, 1114

Brothwell, R.D. et al., 2014, A Window on Exoplanet Dynamical Histories: Rossiter-McLaughlin Observations of WASP-13b and WASP-32b, MNRAS, 440, 3392

Brown, D.J.A. et al., 2012, Analysis of Spin-Orbit Alignment in the WASP-32, WASP-38, and HAT-P-27/WASP-40 Systems, ApJ, 760, 139

Delrez, L. et al., 2014, Transiting planets from WASP-South, Euler and TRAPPIST: WASP-68 b, WASP-73 b and WASP-88 b, three hot Jupiters transiting evolved solar-type stars, A&A, 563, A143

Faedi, F. et al., 2013, WASP-54b, WASP-56b and WASP-57b: Three new sub-Jupiter mass planets from SuperWASP, A&A, 551, A73

Gillon, M. et al., 2011, WASP-50b: a hot Jupiter transiting a moderately active solar-type star, A&A, 533, A88

Gillon, M. et al., 2013, WASP-64b and WASP-72b: two new transiting highly irradiated giant planets, A&A, 552, A82

Gomez Maqueo Chew, Y. et al., 2013, Discovery of WASP-65b and WASP-75b: Two Hot Jupiters Without Highly Inflated Radii, A&A, 559, A36

Gomez Maqueo Chew, Y. et al., 2013, The Homogeneous Study of Transiting Systems (HoSTS) I. The Pilot Study of WASP-13, ApJ, 768, 79

Hebrard, G. et al., 2013, WASP-52b, WASP-58b, WASP-59b, and WASP-60b: four new transiting close-in giant planets, A&A, 549, A134

Hellier, C. et al., 2012, Seven transiting hot-Jupiters from WASP-South, Euler and TRAPPIST: WASP-47b, WASP-55b, WASP-61b, WASP-62b, WASP-63b, WASP-66b & WASP-67b, MNRAS, 426, 739

Lendl, M. et al., 2012, WASP-42 b and WASP-49 b: two new transiting sub-Jupiters, A&A, 544, A72

Lendl, M. et al., 2014, WASP-117b: a 10-day-period Saturn in an eccentric and misaligned orbit, A&A, 568, A81

Maxted, P.F.L. et al., 2012, WASP-77 Ab: A transiting hot Jupiter planet in a wide binary system, PASP, 125, 923

Maxted, P.F.L. et al., 2013, Spitzer 3.6 micron and 4.5 micron full-orbit lightcurves of WASP-18, MNRAS, 428, 2645

Smalley, B. et al., 2012, WASP-78b and WASP-79b: Two highly-bloated hot Jupiter-mass exoplanets orbiting F-type stars in Eridanus, A&A, 547, A61

Smith, A.M.S. et al., 2013, WASP-71b: a bloated hot Jupiter in an 2.9-day, prograde orbit around an evolved F8 star, A&A, 552, A120

Triaud, A.H.M.J. et al., 2013, WASP-80b: a gas giant transiting a cool dwarf, A&A, 551, A80

Triaud, A.H.M.J. et al., 2013, The EBLM Project I-Physical and orbital parameters, including spin-orbit angles, of two low-mass eclipsing binaries on opposite sides of the Brown Dwarf limit, A&A, 549, A18

A Line list

Table A.1: Combined line lists. "Star" refers to the star the line was selected from; P = Procyon, S = Sun, W = WASP-29. The $\log gf$ source is given if a $\log gf$ value was selected outside of VALD.

El.	Ion	λ (Å)	EP (eV)	$\log gf$	Star	$\log gf$ ref.
Al	1	5557.063	3.143	-2.110	P	
Al	1	6698.673	3.143	-1.647	S	
Ba	2	6496.897	0.604	-0.377	S	
C	1	4775.897	7.488	-2.163	S	
C	1	5052.167	7.685	-1.648	S	
C	1	5053.515	8.537	-2.980	P	
C	1	5800.602	7.946	-2.338	P	
C	1	6014.830	8.643	-1.585	P	
C	1	6587.610	8.537	-1.596	S	
Ca	1	4578.551	2.521	-0.697	S	
Ca	1	5260.387	2.521	-1.719	S, W	
Ca	1	5512.979	2.933	-0.464	S	
Ca	1	5715.821	2.709	-3.256	W	
Ca	1	5857.451	2.933	0.240	S	
Ca	1	5867.563	2.933	-1.570	S, W	
Ca	1	6097.266	2.521	-2.754	W	
Ca	1	6162.173	1.899	-0.090	S	
Ca	1	6166.439	2.521	-1.142	S, W	
Ca	1	6424.585	4.443	-1.242	W	
Ca	1	6449.806	2.521	-0.502	P	
Ca	1	6455.598	2.523	-1.557	S, W	
Ca	1	6471.662	2.526	-0.686	W	
Ca	1	6493.781	2.521	-0.109	S, W	
Ca	1	6499.650	2.521	-0.818	S, W	
Ca	1	6654.973	4.735	-0.755	W	
Ca	1	6709.893	2.932	-3.165	W	
Ca	1	6798.479	2.709	-2.320	W	
Ce	2	4418.780	0.864	0.270	S	Lawler et al. (2009)
Ce	2	4511.641	1.212	-0.870	S	
Ce	2	4544.953	0.417	-0.790	S	Lawler et al. (2009)
Ce	2	4550.293	1.123	-0.300	S	
Ce	2	4562.359	0.478	0.210	S	Lawler et al. (2009)
Ce	2	4572.278	0.684	0.220	S	Lawler et al. (2009)
Ce	2	4591.116	1.107	-0.410	S	
Ce	2	4612.965	1.048	-1.060	S	
Ce	2	4694.871	0.808	-1.110	S	Lawler et al. (2009)
Ce	2	4717.881	0.701	-1.140	S	Lawler et al. (2009)

Table A.1: Line list (continued)

El.	Ion	λ (Å)	EP (eV)	$\log gf$	Star	$\log gf$ ref.
Ce	2	4725.069	0.521	-1.440	S	
Ce	2	4773.941	0.924	-0.390	S	Lawler et al. (2009)
Co	1	4594.626	3.363	-0.376	W	Lobel (2008)
Co	1	5156.356	4.058	0.037	S	
Co	1	5212.691	3.514	-0.110	S	
Co	1	5230.202	1.740	-1.840	S	
Co	1	5280.629	3.629	-0.030	S	
Co	1	5342.695	4.021	0.690	S	
Co	1	5359.192	4.149	0.340	S, W	
Co	1	5381.768	4.240	-0.032	W	
Co	1	5483.344	1.710	-1.490	S, W	
Co	1	5530.774	1.710	-2.060	S	
Co	1	5647.234	2.280	-1.560	S, W	
Co	1	5915.552	2.137	-2.000	W	
Co	1	6000.663	3.622	-0.990	W	
Co	1	6005.025	1.710	-3.320	W	
Co	1	6093.143	1.740	-2.440	W	
Co	1	6116.996	1.785	-2.490	W	
Co	1	6444.675	3.629	-1.410	W	
Co	1	6454.990	3.632	-0.250	S	
Co	1	6722.759	4.504	-0.808	W	
Co	1	6814.942	1.956	-1.900	S	
Cr	2	4558.650	4.073	-0.449	W	
Cr	1	4576.801	3.079	-1.817	W	
Cr	1	4578.298	3.850	-0.860	W	
Cr	2	4588.199	4.071	-0.627	S, W	
Cr	2	4592.049	4.074	-1.221	S, W	
Cr	1	4614.728	3.369	-1.609	W	
Cr	1	4641.961	3.850	-0.670	W	
Cr	1	4676.358	3.556	-1.589	W	
Cr	1	4695.149	2.983	-1.180	W	
Cr	1	4700.597	2.710	-1.255	W	
Cr	1	4801.047	3.122	-0.131	W	
Cr	1	5068.280	1.004	-3.127	P	
Cr	1	5072.917	0.941	-2.734	S	
Cr	1	5091.875	1.004	-3.039	S	
Cr	1	5093.423	1.030	-4.081	W	
Cr	1	5123.450	1.030	-2.960	S	
Cr	1	5214.140	3.369	-0.740	S, W	
Cr	1	5220.912	3.385	-1.034	W	
Cr	2	5232.496	4.071	-2.093	P	
Cr	1	5238.964	2.709	-1.305	S, W	
Cr	1	5241.453	2.710	-2.080	S	
Cr	2	5246.768	3.714	-2.466	S	
Cr	2	5279.876	4.073	-2.100	S, W	
Cr	1	5293.396	3.375	-1.360	W	
Cr	1	5296.691	0.983	-1.400	S	

Table A.1: Line list (continued)

El.	Ion	λ (Å)	EP (eV)	$\log gf$	Star	$\log gf$ ref.
Cr	1	5344.789	3.449	-1.060	W	
Cr	1	5348.312	1.004	-1.290	S	
Cr	2	5369.358	3.871	-3.045	P	
Cr	1	5628.621	3.422	-0.772	S, W	
Cr	1	5642.370	3.857	-0.830	W	
Cr	1	5648.230	3.826	-1.000	W	
Cr	1	5649.385	3.839	-1.160	W	
Cr	2	5678.390	6.484	-1.238	P	
Cr	1	5719.810	3.013	-1.660	W	
Cr	1	5736.605	3.556	-1.442	W	
Cr	1	5738.541	3.551	-1.468	W	
Cr	1	5772.678	3.556	-1.702	W	
Cr	1	5785.024	3.321	-0.380	S	
Cr	1	5787.037	3.013	-1.791	W	
Cr	1	5788.394	3.013	-1.834	W	
Cr	1	5792.184	0.961	-4.533	W	
Cr	1	5798.496	1.030	-3.939	W	
Cr	1	5824.085	3.111	-2.448	W	
Cr	1	5959.171	4.449	-1.180	W	
Cr	1	5982.880	3.168	-2.021	W	
Cr	1	6047.672	3.850	-1.811	W	
Cr	1	6135.734	4.824	-1.157	P	
Cr	1	6330.093	0.941	-2.920	W	
Cr	1	6501.194	0.983	-4.295	W	
Cr	1	6537.929	1.004	-4.069	W	
Cr	1	6612.158	4.159	-1.251	W	
Cr	1	6630.005	1.030	-3.560	W	
Cr	1	6636.317	4.144	-1.715	W	
Cr	1	6729.770	4.389	-0.713	W	
Cu	1	5105.537	1.389	-1.516	S	
Cu	1	5218.197	3.817	0.476	S	
Cu	1	4507.408	5.575	-0.340	S	
Dy	2	4829.690	2.589	-0.018	S	
Dy	2	4923.167	0.103	-2.384	S	
Dy	2	5272.249	0.538	-2.143	S	
Fe	1	4510.821	3.603	-2.097	W	
Fe	1	4546.467	4.186	-2.510	S	
Fe	2	4620.521	2.828	-3.210	S	Meléndez & Barbuy (2009)
Fe	2	4656.981	2.891	-3.600	S, W	Meléndez & Barbuy (2009)
Fe	2	4670.182	2.583	-4.090	S	
Fe	2	4720.149	3.197	-4.480	S	
Fe	2	4825.736	2.635	-4.829	S, W	Kurucz (1988)
Fe	2	4833.197	2.657	-4.640	S, W	
Fe	2	4923.927	2.891	-1.260	W	Meléndez & Barbuy (2009)

Table A.1: Line list (continued)

El.	Ion	λ (Å)	EP (eV)	$\log gf$	Star	$\log gf$ ref.
Fe	2	5000.743	2.778	-4.578	S	
Fe	1	5016.476	4.256	-1.690	S	
Fe	1	5029.621	3.415	-2.050	S	
Fe	1	5044.210	2.851	-2.038	S	
Fe	1	5058.496	3.642	-2.830	W	
Fe	1	5083.338	0.958	-2.958	S	
Fe	1	5088.188	4.154	-1.780	P	
Fe	1	5119.901	3.882	-3.050	W	
Fe	1	5124.602	3.301	-2.960	S	
Fe	1	5127.681	0.052	-6.125	S	
Fe	2	5132.669	2.807	-4.094	S, W	
Fe	1	5137.395	4.178	-0.400	S	
Fe	1	5141.739	2.424	-2.240	S	Fuhr & Wiese (2006)
Fe	2	5197.577	3.230	-2.220	W	Meléndez & Barbuy (2009)
Fe	1	5213.805	3.943	-2.760	S	
Fe	1	5217.389	3.211	-1.070	S	Fuhr & Wiese (2006)
Fe	1	5225.525	0.110	-4.789	S	
Fe	1	5236.205	4.186	-1.497	S	
Fe	1	5236.381	4.312	-2.430	W	
Fe	1	5242.491	3.634	-0.967	S, W	
Fe	1	5247.049	0.087	-4.946	W	
Fe	1	5253.023	2.279	-3.940	S	
Fe	1	5253.461	3.283	-1.573	S	
Fe	2	5264.812	3.230	-3.130	S	Meléndez & Barbuy (2009)
Fe	1	5365.396	3.573	-1.020	S	
Fe	1	5379.574	3.695	-1.514	W	
Fe	1	5405.340	4.386	-1.390	P	
Fe	2	5414.073	3.221	-3.580	S, W	Meléndez & Barbuy (2009)
Fe	1	5422.145	4.320	-2.260	P	
Fe	2	5425.257	3.199	-3.220	S	Meléndez & Barbuy (2009)
Fe	1	5434.522	1.011	-2.122	P	
Fe	1	5436.207	5.012	-4.272	P	
Fe	1	5445.042	4.386	-0.020	S	
Fe	1	5464.278	4.143	-1.402	W	
Fe	1	5483.098	4.154	-1.580	W	
Fe	1	5491.840	4.186	-2.188	W	
Fe	2	5525.125	3.267	-3.970	S	Meléndez & Barbuy (2009)
Fe	1	5538.517	4.218	-3.244	P	
Fe	1	5543.937	4.218	-1.140	W	
Fe	1	5546.500	4.371	-1.310	S	
Fe	1	5560.207	4.434	-1.190	S, W	
Fe	1	5568.072	4.154	-2.807	W	
Fe	1	5576.090	3.430	-1.000	S	
Fe	1	5577.031	5.033	-1.550	S	
Fe	1	5579.335	4.231	-2.400	P	
Fe	1	5587.573	4.143	-1.850	S	
Fe	2	5591.368	3.267	-4.590	P	
Fe	1	5592.646	4.294	-2.240	W	Kurucz (1988)

Table A.1: Line list (continued)

El.	Ion	λ (Å)	EP (eV)	$\log gf$	Star	$\log gf$ ref.
Fe	1	5609.962	3.640	-3.240	W	
Fe	1	5611.361	3.635	-2.990	W	
Fe	1	5622.947	3.640	-3.096	W	
Fe	1	5639.323	4.956	-2.733	W	Kurucz (1988)
Fe	1	5651.470	4.473	-2.000	S, W	
Fe	1	5672.267	4.584	-2.800	W	
Fe	1	5673.377	3.695	-3.674	W	
Fe	1	5679.025	4.652	-0.920	S, W	
Fe	1	5705.466	4.301	-1.355	P	
Fe	1	5715.470	4.154	-2.980	W	
Fe	1	5724.454	4.284	-2.640	S, W	
Fe	2	5725.963	3.425	-4.820	P	
Fe	1	5731.782	4.256	-1.300	P	
Fe	1	5732.275	4.991	-1.560	W	
Fe	1	5741.846	4.256	-1.670	S	Fuhr & Wiese (2006)
Fe	1	5759.261	4.652	-2.070	W	
Fe	1	5769.307	4.608	-2.257	W	
Fe	1	5776.225	3.695	-3.688	W	Lobel (2008)
Fe	1	5791.528	4.584	-1.876	W	
Fe	1	5796.433	4.607	-2.482	W	
Fe	1	5811.917	4.143	-2.430	W	
Fe	2	5813.677	5.571	-2.510	S	Meléndez & Barbuy (2009)
Fe	1	5844.917	4.154	-2.940	W	
Fe	1	5845.266	5.033	-1.820	W	
Fe	1	5849.682	3.695	-2.990	W	
Fe	1	5853.149	1.485	-5.280	W	
Fe	1	5856.083	4.294	-1.328	S	
Fe	1	5861.107	4.283	-2.450	W	
Fe	1	5871.304	4.154	-2.666	W	
Fe	1	5933.792	4.638	-2.230	W	
Fe	1	5943.577	2.198	-4.178	W	
Fe	1	5955.102	4.584	-3.021	P	
Fe	1	5956.692	0.859	-4.605	W	
Fe	1	5961.919	4.220	-3.160	W	
Fe	1	5969.559	4.283	-2.730	W	
Fe	1	5978.130	4.638	-3.053	W	Kurucz (1988)
Fe	1	5984.814	4.733	-0.196	P	
Fe	2	5991.376	3.153	-3.647	S	
Fe	1	6008.554	3.884	-0.986	P	
Fe	1	6012.206	2.223	-4.038	W	
Fe	1	6027.050	4.076	-1.089	S, W	
Fe	1	6027.959	4.608	-3.178	W	Kurucz (1988)
Fe	1	6034.033	4.312	-2.420	W	
Fe	2	6045.465	6.209	-2.549	P	
Fe	1	6050.996	2.559	-4.965	W	Lobel (2008)
Fe	1	6054.072	4.371	-2.310	W	
Fe	1	6055.992	4.733	-0.460	S, W	
Fe	1	6060.621	1.557	-5.524	W	Kurucz (1988)
Fe	1	6065.482	2.608	-1.530	S	

Table A.1: Line list (continued)

El.	Ion	λ (Å)	EP (eV)	$\log gf$	Star	$\log gf$ ref.
Fe	1	6078.999	4.652	-1.120	S, W	
Fe	1	6082.708	2.223	-3.573	W	
Fe	2	6084.111	3.199	-3.881	S, W	
Fe	1	6089.580	4.580	-3.112	W	Kurucz (1988)
Fe	1	6098.280	4.559	-1.880	W	
Fe	1	6105.152	4.549	-2.050	P	
Fe	2	6113.322	3.221	-4.230	S	
Fe	1	6139.648	2.588	-4.500	W	
Fe	1	6145.408	3.368	-3.700	W	
Fe	1	6151.617	2.176	-3.299	P	
Fe	1	6173.341	2.223	-2.880	S	
Fe	2	6179.384	5.569	-2.797	S	
Fe	1	6187.398	2.832	-4.148	W	
Fe	1	6199.507	2.559	-4.430	W	
Fe	1	6200.319	2.609	-2.437	P	
Fe	1	6209.713	3.960	-3.249	W	
Fe	1	6221.670	0.859	-6.613	W	
Fe	1	6226.729	3.884	-2.220	W	
Fe	2	6239.953	3.889	-3.573	S, W	
Fe	2	6247.557	3.892	-2.435	S, W	
Fe	1	6252.554	2.404	-1.687	S, W	
Fe	1	6265.131	2.176	-2.550	S	
Fe	1	6271.276	3.332	-2.703	W	
Fe	1	6290.545	2.588	-4.330	W	
Fe	1	6335.328	2.198	-2.177	S	
Fe	1	6336.823	3.686	-0.856	S	
Fe	1	6338.896	4.795	-1.060	W	
Fe	1	6339.948	3.397	-4.431	W	Kurucz (1988)
Fe	1	6351.270	4.312	-3.366	W	
Fe	2	6369.462	2.891	-4.110	S, W	Meléndez & Barbuy (2009)
Fe	2	6385.451	5.553	-2.715	S	
Fe	1	6392.538	2.279	-4.030	W	
Fe	2	6432.680	2.891	-3.570	S	Meléndez & Barbuy (2009)
Fe	2	6442.955	5.549	-2.440	S	
Fe	2	6446.410	6.223	-2.082	S	
Fe	2	6456.383	3.903	-2.185	S, W	
Fe	1	6464.661	0.958	-5.801	W	Lobel (2008)
Fe	2	6482.204	6.219	-1.853	S	
Fe	1	6483.943	1.485	-5.130	W	Lobel (2008)
Fe	2	6491.246	5.585	-2.899	S	
Fe	2	6493.035	5.585	-2.695	P	
Fe	2	6506.333	5.589	-2.680	S	
Fe	1	6574.225	0.990	-5.023	W	
Fe	1	6591.325	4.593	-2.070	W	
Fe	1	6593.871	2.433	-2.422	S	
Fe	1	6653.850	4.154	-2.520	W	
Fe	1	6699.162	4.593	-2.101	W	
Fe	1	6725.353	4.103	-2.300	P	

Table A.1: Line list (continued)

El.	Ion	λ (Å)	EP (eV)	$\log gf$	Star	$\log gf$ ref.
Fe	1	6733.151	4.638	-1.580	P	
Fe	1	6750.150	2.424	-2.621	S	
Fe	1	6801.864	1.608	-5.043	W	Kurucz (1988)
Fe	1	6810.257	4.607	-0.986	P	
Fe	1	6837.016	4.593	-1.687	W	
Fe	1	6857.243	4.076	-2.150	W	
Gd	2	5092.249	1.727	-0.230	S	
Gd	2	5098.366	1.621	-0.630	S	
Gd	2	5140.830	1.575	-0.840	S	
La	2	4662.498	0.000	-1.240	S	
La	2	4748.726	0.927	-0.540	S	
La	2	5122.988	0.321	-0.850	S	
La	2	6390.478	0.321	-1.410	S	
Mg	1	4571.096	0.000	-5.623	S	Fuhr & Wiese (2006)
Mg	1	4730.029	4.346	-2.347	S	Fuhr & Wiese (2006)
Mg	1	5528.405	4.346	-0.498	S	Fuhr & Wiese (2006)
Mg	1	5711.088	4.346	-1.724	S	Fuhr & Wiese (2006)
Mg	1	5785.313	5.108	-2.110	S	
Mg	1	6318.717	5.108	-2.103	S	Fuhr & Wiese (2006)
Mg	1	6319.237	5.108	-2.324	S	Fuhr & Wiese (2006)
Mn	1	4671.672	2.888	-1.668	W	
Mn	1	4739.087	2.941	-0.490	S	
Mn	1	4761.512	2.953	-0.138	S	
Mn	1	4765.846	2.941	-0.080	S	
Mn	1	4969.133	4.726	-1.205	W	
Mn	1	5004.892	2.920	-1.630	S, W	
Mn	1	5117.934	3.135	-1.140	W	
Mn	1	5255.326	3.133	-0.763	S	
Mn	1	5288.862	5.396	-0.577	W	
Mn	1	5377.637	3.844	-0.109	S	
Mn	1	5388.544	3.373	-1.690	S	
Mn	1	5399.499	3.853	-0.287	S	
Mn	1	5432.546	0.000	-3.795	S	
Mn	1	5470.637	2.164	-1.702	S	
Mn	1	5516.774	2.178	-1.847	S	
Mn	1	5551.977	5.491	0.607	W	
Mn	1	6265.612	4.233	-1.317	W	
Mn	1	6391.200	4.268	-1.546	W	
Mn	1	6440.971	3.772	-1.238	S, W	
Mn	1	6519.374	3.772	-1.958	W	
Na	1	4751.822	2.104	-2.090	W	
Na	1	5148.839	2.104	-2.060	W	
Na	1	5682.633	2.104	-0.700	W	
Na	1	6154.226	2.102	-1.560	S	
Na	1	6160.747	2.104	-1.260	S	
Nd	2	4567.605	0.205	-1.310	S	
Nd	2	4645.760	0.559	-0.760	S	
Nd	2	4914.382	0.380	-0.700	S	
Nd	2	4998.541	0.471	-1.166	S	

Table A.1: Line list (continued)

El.	Ion	λ (Å)	EP (eV)	$\log gf$	Star	$\log gf$ ref.
Nd	2	5130.586	1.304	0.450	S	
Nd	2	5132.328	0.559	-0.710	S	
Nd	2	5255.506	0.205	-0.670	S	
Nd	2	5276.869	0.859	-0.668	P	
Nd	2	5293.163	0.823	0.100	S	
Nd	2	5485.696	1.264	-0.120	P	
Ni	1	4567.407	3.453	-2.410	W	
Ni	1	4705.916	3.658	-1.387	W	
Ni	1	4829.016	3.542	-0.330	S	
Ni	1	5010.934	3.635	-0.870	S, W	
Ni	2	5066.328	6.329	-1.799	P	
Ni	1	5079.955	1.826	-2.750	S	
Ni	1	5082.339	3.658	-0.540	S	
Ni	1	5084.089	3.679	0.030	S	
Ni	1	5088.532	3.847	-0.980	S	
Ni	1	5088.953	3.679	-1.340	P	
Ni	1	5094.406	3.833	-1.080	S	
Ni	1	5115.389	3.834	-0.110	P	
Ni	1	5176.559	3.898	-0.440	S	
Ni	1	5347.705	3.796	-2.040	W	
Ni	1	5392.327	4.154	-1.320	S	
Ni	1	5494.876	4.105	-1.160	S	
Ni	1	5537.098	3.847	-2.200	W	
Ni	1	5578.711	1.676	-2.640	W	
Ni	1	5589.357	3.898	-1.140	P	
Ni	1	5593.733	3.898	-0.840	S	
Ni	1	5625.312	4.089	-0.700	S	
Ni	1	5641.880	4.105	-1.070	W	
Ni	1	5796.078	1.951	-3.942	S, W	
Ni	1	5805.213	4.167	-0.640	W	
Ni	1	5846.986	1.676	-3.210	S	
Ni	1	6007.306	1.676	-3.330	W	
Ni	1	6025.751	4.236	-1.760	W	
Ni	1	6053.679	4.236	-1.070	S	
Ni	1	6086.276	4.266	-0.530	W	
Ni	1	6108.107	1.676	-2.450	S	
Ni	1	6111.066	4.088	-0.870	S, W	
Ni	1	6119.749	4.266	-1.350	W	
Ni	1	6130.130	4.266	-0.986	S, W	
Ni	1	6176.807	4.088	-0.260	W	
Ni	1	6191.171	1.676	-2.353	S	
Ni	1	6204.600	4.088	-1.100	S	
Ni	1	6223.980	4.105	-0.910	P	
Ni	1	6322.164	4.154	-1.170	W	
Ni	1	6360.806	4.167	-1.790	P	
Ni	1	6370.341	3.542	-1.940	W	
Ni	1	6378.247	4.154	-0.830	S	
Ni	1	6414.581	4.154	-1.180	S	
Ni	1	6532.871	1.935	-3.390	S, W	

Table A.1: Line list (continued)

El.	Ion	λ (Å)	EP (eV)	$\log gf$	Star	$\log gf$ ref.
Ni	1	6598.593	4.236	-0.980	S	
Ni	1	6643.629	1.676	-2.300	P	
Ni	1	6767.768	1.826	-1.888	W	
Ni	1	6772.313	3.658	-0.980	S	
Ni	1	4512.986	3.706	-1.470	W	
Pr	2	5259.728	0.633	-0.038	S	
S	1	4695.443	6.525	-1.920	S	
Sc	1	4922.827	1.987	0.418	W	
Sc	1	5081.574	1.448	0.469	S	
Sc	2	5239.813	1.455	-0.765	S	
Sc	1	5356.091	1.865	0.168	W	
Sc	1	5484.626	1.851	0.148	S	
Sc	2	5526.790	1.768	0.024	W	
Sc	2	5552.224	1.455	-2.119	S	
Sc	2	5667.149	1.500	-1.309	S	
Sc	2	5684.202	1.507	-1.074	S	
Sc	1	5686.847	1.440	0.376	S	
Sc	1	5724.107	1.433	-0.661	W	
Sc	1	6193.666	0.000	-2.760	W	
Sc	1	6239.762	0.000	-1.780	W	
Sc	2	6245.637	1.507	-1.030	S, W	
Sc	1	6258.943	0.021	-1.800	W	
Sc	2	6300.698	1.507	-1.887	S, W	
Sc	1	6306.020	0.021	-2.150	W	
Sc	2	6309.920	1.497	-1.630	W	
Sc	2	6320.851	1.500	-1.819	S, W	
Sc	1	6413.324	0.021	-2.310	W	
Si	1	5258.842	5.616	-2.100	P	Lobel (2008)
Si	1	5413.099	5.616	-2.750	S	Lobel (2008)
Si	1	5488.983	5.614	-2.420	S	Lobel (2008)
Si	1	5517.533	5.082	-2.611	S	
Si	1	5621.608	5.082	-3.140	S	
Si	1	5645.613	4.930	-2.100	S	Brugamyer et al. (2011)
Si	1	5666.677	5.616	-1.650	P	
Si	1	5684.484	4.954	-1.620	S	Brugamyer et al. (2011)
Si	1	5701.104	4.930	-1.581	S	
Si	1	5772.146	5.082	-1.710	S	Brugamyer et al. (2011)
Si	1	5873.764	4.930	-2.910	S	Lobel (2008)
Si	1	6029.869	5.984	-1.550	P	
Si	1	6142.483	5.619	-0.920	S	Shi et al. (2008)
Si	1	6155.134	5.619	-0.400	S	Shi et al. (2008)
Si	1	6194.416	5.871	-1.540	P	
Si	1	6195.433	5.871	-1.540	S	
Si	1	6237.319	5.614	-0.530	S	Shi et al. (2008)
Si	1	6308.825	5.863	-1.792	P	
Si	1	6463.652	5.954	-3.483	P	
Si	1	6583.707	5.954	-1.740	P	
Si	1	6721.848	5.863	-1.516	S	

Table A.1: Line list (continued)

El.	Ion	λ (Å)	EP (eV)	$\log gf$	Star	$\log gf$ ref.
Si	1	6741.628	5.984	-1.750	P	Shi et al. (2008)
Si	1	6800.596	5.694	-1.967	P	
Sm	2	4318.927	0.277	-0.268	S	
Sm	2	4566.202	0.333	-0.590	S	
Sm	2	4577.688	0.248	-0.650	S	
Sm	2	4791.580	0.104	-1.440	S	
Sm	2	5100.258	1.493	-0.490	S	
Sr	1	5450.834	2.259	-0.340	S	
Ti	1	4562.625	0.021	-2.656	W	
Ti	2	4583.409	1.165	-2.870	S, W	
Ti	1	4747.666	2.249	-0.820	W	
Ti	1	4758.120	2.249	0.425	S	
Ti	2	4798.521	1.080	-2.670	S	
Ti	1	4811.032	1.887	-0.805	W	Lobel (2008)
Ti	2	4911.193	3.124	-0.650	S	
Ti	1	4926.147	0.818	-2.170	W	
Ti	1	4928.887	0.836	-3.547	W	
Ti	1	4963.760	3.583	-0.815	W	
Ti	1	5001.009	1.997	-0.034	S	
Ti	2	5005.157	1.566	-2.730	S	
Ti	1	5016.162	0.848	-0.574	S	
Ti	1	5062.112	2.160	-0.464	S	
Ti	1	5064.081	2.695	-0.484	S	
Ti	2	5069.090	3.124	-1.540	P	
Ti	1	5071.472	1.460	-1.063	P	
Ti	1	5113.448	1.443	-0.782	S	
Ti	2	5129.152	1.892	-1.300	S	
Ti	1	5152.185	0.021	-2.024	S	
Ti	2	5185.913	1.893	-1.370	P	
Ti	2	5211.536	2.590	-1.356	S, W	Kurucz (1994)
Ti	1	5231.021	2.239	-1.108	W	
Ti	1	5247.291	2.103	-0.727	S	
Ti	1	5260.001	2.738	-0.180	W	
Ti	1	5295.780	1.067	-1.633	S	
Ti	1	5351.080	2.778	0.010	W	
Ti	2	5396.226	1.584	-3.020	S	
Ti	2	5418.751	1.582	-2.110	S, W	
Ti	1	5453.643	1.443	-1.610	W	
Ti	1	5459.682	1.053	-3.513	W	
Ti	1	5465.775	1.067	-3.117	W	
Ti	1	5471.197	1.443	-1.400	S, W	
Ti	1	5490.150	1.460	-0.933	S	
Ti	2	5490.689	1.566	-2.650	S, W	Kurucz (1994)
Ti	2	5492.862	1.582	-3.310	S	
Ti	1	5514.537	1.443	-0.413	S	
Ti	1	5648.567	2.495	-0.260	S	
Ti	1	5662.161	2.318	-0.109	S	
Ti	1	5679.937	2.472	-0.570	S	
Ti	1	5689.488	2.297	-0.360	W	

Table A.1: Line list (continued)

El.	Ion	λ (Å)	EP (eV)	$\log gf$	Star	$\log gf$ ref.
Ti	1	5702.693	2.292	-0.590	W	
Ti	1	5720.478	2.292	-0.900	W	
Ti	1	5739.464	2.249	-0.600	S, W	
Ti	1	5741.201	2.506	-1.290	W	Lobel (2008)
Ti	1	5756.434	2.256	-2.025	W	
Ti	1	5766.330	3.294	0.389	S, W	
Ti	1	5813.944	1.067	-2.200	W	Lobel (2008)
Ti	1	5832.475	3.336	-0.967	W	
Ti	1	5866.452	1.067	-0.840	S	
Ti	1	5880.273	1.053	-2.045	W	
Ti	1	5899.297	1.053	-1.154	S	
Ti	1	5903.317	1.067	-2.145	W	
Ti	1	5913.709	0.021	-4.198	W	
Ti	1	5918.539	1.067	-1.460	W	
Ti	1	5922.110	1.046	-1.466	W	
Ti	1	5937.812	1.067	-1.890	W	
Ti	1	5944.650	0.000	-4.059	W	
Ti	1	5953.162	1.887	-0.329	S, W	
Ti	1	5982.556	2.408	-1.843	W	
Ti	1	5999.663	2.236	-1.479	W	
Ti	1	6018.636	1.053	-2.142	W	
Ti	1	6031.677	0.048	-4.199	W	
Ti	1	6058.730	1.067	-1.771	W	
Ti	1	6064.629	1.046	-1.944	S, W	
Ti	1	6069.272	1.879	-2.325	W	
Ti	1	6091.174	2.267	-0.423	S, W	
Ti	1	6126.217	1.067	-1.425	W	
Ti	1	6174.778	2.662	-1.605	W	
Ti	1	6205.248	1.460	-4.387	W	
Ti	2	6219.940	2.061	-2.819	W	
Ti	1	6258.104	1.443	-0.355	S	
Ti	1	6266.033	1.749	-2.501	W	
Ti	1	6273.386	0.021	-4.248	W	
Ti	1	6303.757	1.443	-1.566	S, W	
Ti	1	6325.179	0.021	-3.972	W	
Ti	1	6419.098	2.175	-1.656	W	
Ti	1	6497.684	1.443	-2.085	W	
Ti	2	6513.045	4.002	-1.310	P	
Ti	2	6559.588	2.048	-2.019	W	
Ti	1	6599.133	0.900	-2.085	W	
Ti	2	6606.949	2.061	-2.790	W	
Ti	1	6689.313	2.250	-1.988	W	
Ti	1	6716.707	2.487	-1.409	W	
Ti	1	6745.550	2.236	-1.752	W	Kurucz (1988)
V	1	4609.641	1.376	-1.956	W	
V	1	4635.177	0.069	-1.920	W	
V	1	4746.616	2.029	-0.590	W	
V	1	4784.467	0.017	-2.670	W	
V	1	4832.426	0.000	-1.505	S	

Table A.1: Line list (continued)

El.	Ion	λ (Å)	EP (eV)	$\log gf$	Star	$\log gf$ ref.
V	1	5290.286	1.893	-1.904	W	
V	1	5504.885	1.711	-0.882	W	
V	1	5592.972	0.040	-3.230	W	
V	1	5604.199	1.854	-1.591	W	
V	1	5646.108	1.051	-1.190	S, W	
V	1	5656.881	2.332	-1.064	W	
V	1	5657.436	1.064	-1.020	S, W	
V	1	5668.361	1.081	-1.030	S, W	
V	1	5670.854	1.081	-0.420	S	
V	1	5725.641	2.365	0.010	W	
V	1	5727.048	1.081	-0.012	S	
V	1	5737.059	1.064	-0.740	S, W	
V	1	5783.502	2.708	-0.377	W	
V	1	5807.085	3.087	0.293	W	
V	1	5817.490	3.099	0.434	W	
V	2	5928.862	2.522	-1.598	S	
V	1	6002.295	1.218	-1.780	W	
V	1	6039.722	1.064	-0.650	S, W	
V	1	6090.214	1.081	-0.062	S	
V	1	6128.328	1.051	-2.300	W	
V	1	6135.060	1.350	-1.790	W	
V	1	6135.361	1.051	-0.746	S, W	
V	1	6224.529	0.287	-2.010	W	
V	1	6243.105	0.301	-0.980	S	
V	1	6251.827	0.287	-1.340	S	
V	1	6266.307	0.275	-2.290	W	
V	1	6274.649	0.267	-1.670	S, W	
V	1	6285.150	0.275	-1.510	S, W	
V	1	6326.840	1.868	-0.810	W	
V	1	6349.475	1.854	-0.890	W	
V	1	6531.415	1.218	-0.840	W	
W	1	5015.309	0.599	-1.860	S	
Y	2	4883.684	1.084	0.070	S	
Y	2	5087.416	1.084	-0.170	S, W	
Y	2	5119.112	0.992	-1.360	S	
Y	2	5205.724	1.033	-0.340	S	
Y	2	5289.815	1.033	-1.850	S	
Y	2	5402.774	1.839	-0.510	S	
Y	2	5544.611	1.738	-1.090	S	
Y	2	5728.890	1.839	-1.120	S	
Y	2	6795.414	1.738	-1.190	S	
Zn	1	6362.338	5.796	0.150	S	
Zr	2	4629.079	2.490	-0.590	S	
Zr	1	4739.480	0.651	0.230	S	
Zr	1	4815.621	0.604	-0.030	S	
Zr	2	5350.089	1.827	-1.240	S	

References

Abney W. D. W., 1877, MNRAS, 37, 278

Addison B. C., Tinney C. G., Wright D. J., Bayliss D., Zhou G., Hartman J. D., Bakos G. Á., Schmidt B., 2013, ApJL, 774, L9

Adibekyan V. Z. et al., 2012a, A&A, 543, A89

Adibekyan V. Z., Sousa S. G., Santos N. C., Delgado Mena E., González Hernández J. I., Israelian G., Mayor M., Khachatryan G., 2012b, A&A, 545, A32

Aerts C., Christensen-Dalsgaard J., Kurtz D. W., 2010, Asteroseismology. Springer

Albrecht S., Winn J. N., Butler R. P., Crane J. D., Shectman S. A., Thompson I. B., Hirano T., Wittenmyer R. A., 2012a, ApJ, 744, 189

Albrecht S. et al., 2011, ApJ, 738, 50

Albrecht S. et al., 2012b, ApJ, 757, 18

Aldenius M., Tanner J. D., Johansson S., Lundberg H., Ryan S. G., 2007, A&A, 461, 767

Allard N. F., Kielkopf J. F., Cayrel R., van't Veer-Menneret C., 2008, A&A, 480, 581

Allende Prieto C., Asplund M., García López R. J., Lambert D. L., 2002, ApJ, 567, 544

Allende Prieto C., Barklem P. S., Lambert D. L., Cunha K., 2004, A&A, 420, 183

Allende Prieto C., Garcia Lopez R. J., 1998, A&AS, 129, 41

Ammler-von Eiff M., Reiners A., 2012, A&A, 542, A116

Ammler-von Eiff M., Santos N. C., Sousa S. G., Fernandes J., Guillot T., Israelian G., Mayor M., Melo C., 2009, A&A, 507, 523

Anders E., Grevesse N., 1989, Geochimica et Cosmochimica Acta, 53, 197

Andersen J., 1991, Astron. Astrophys. Rev., 3, 91

Anderson D. R. et al., 2011a, PASP, 123, 555

Anderson D. R. et al., 2014a, MNRAS, 445, 1114

Anderson D. R. et al., 2011b, A&A, 534, A16

Anderson D. R. et al., 2014b, preprint, arXiv:1402.1482

Anderson D. R. et al., 2011c, A&A, 531, A60

Anderson D. R. et al., 2011d, ApJL, 726, L19

Anderson D. R. et al., 2008, MNRAS, 387, L4

Anderson D. R. et al., 2010, ApJ, 709, 159

Anstee S. D., O'Mara B. J., 1991, MNRAS, 253, 549

Anstee S. D., O'Mara B. J., 1995a, MNRAS, 276, 859

Anstee S. D., O'Mara B. J., 1995b, MNRAS, 276, 859

Appourchaux T. et al., 2012, A&A, 537, A134

Árnadóttir A. S., Feltzing S., Lundström I., 2010, A&A, 521, A40

Arnone E., Ryan S. G., Argast D., Norris J. E., Beers T. C., 2005, A&A, 430, 507

Asplund M., 2005, ARA&A, 43, 481

Asplund M., 2007, in IAU Symposium, Vol. 239, Convection in Astrophysics, Kupka F., Roxburgh I., Chan K. L., eds., pp. 122–129

Asplund M., Grevesse N., Sauval A. J., Scott P., 2009, ARA&A, 47, 481

Asplund M., Nordlund Å., Trampedach R., Allende Prieto C., Stein R. F., 2000, A&A, 359, 729

Aufdenberg J. P., Ludwig H.-G., Kervella P., 2005, ApJ, 633, 424

Baglin A., Auvergne M., Barge P., Deleuil M., Michel E., CoRoT Exoplanet Science Team, 2009, in IAU Symposium, Vol. 253, Transiting Planets, Pont F., Sasselov D., Holman M. J., eds., pp. 71–81

Baines E. K., McAlister H. A., ten Brummelaar T. A., Turner N. H., Sturmann J., Sturmann L., Goldfinger P. J., Ridgway S. T., 2008, ApJ, 680, 728

Ballot J., Appourchaux T., Toutain T., Guittet M., 2008, A&A, 486, 867

Ballot J., García R. A., Lambert P., 2006, MNRAS, 369, 1281
Ballot J. et al., 2011, A&A, 530, A97
Barban C. et al., 2009, A&A, 506, 51
Barker A. J., Ogilvie G. I., 2009, MNRAS, 395, 2268
Barklem P. S., Anstee S. D., O'Mara B. J., 1998, PASA, 15, 336
Barklem P. S., Aspelund-Johansson J., 2005, A&A, 435, 373
Barklem P. S., O'Mara B. J., 1997, MNRAS, 290, 102
Barklem P. S., Piskunov N., O'Mara B. J., 2000, A&AS, 142, 467
Barnes J. R., Collier Cameron A., Donati J.-F., James D. J., Marsden S. C., Petit P., 2005, MNRAS, 357, L1
Barnes S. A., 2007, ApJ, 669, 1167
Barros S. C. C. et al., 2011, A&A, 525, A54
Basu S., Chaplin W. J., Elsworth Y., 2010, ApJ, 710, 1596
Bayliss D. D. R., Winn J. N., Mardling R. A., Sackett P. D., 2010, ApJL, 722, L224
Bean J. L., Sneden C., Hauschildt P. H., Johns-Krull C. M., Benedict G. F., 2006, APJ, 652, 1604
Beaugé C., Nesvorný D., 2012, ApJ, 751, 119
Bedding T. R., 2011, in Asteroseismology, Pallé P. L., Esteban C., eds., Canary Islands Winter School of Astrophysics, pp. 60–86
Bedding T. R. et al., 2011, Nature, 471, 608
Beirão P., Santos N. C., Israelian G., Mayor M., 2005, A&A, 438, 251
Belkacem K., 2012, in SF2A-2012: Proceedings of the Annual meeting of the French Society of Astronomy and Astrophysics, Boissier S., de Laverny P., Nardetto N., Samadi R., Valls-Gabaud D., Wozniak H., eds., pp. 173–188
Belkacem K., Goupil M. J., Dupret M. A., Samadi R., Baudin F., Noels A., Mosser B., 2011, A&A, 530, A142
Benomar O. et al., 2009, A&A, 507, L13
Bergemann M., 2011, in Uncertainties in Atomic Data and How They Propagate in Chemical Abundances, Luridiana V., García-Rojas C., Manchado A., eds., pp. 25–32
Bergemann M., Gehren T., 2007, A&A, 473, 291
Bergemann M., Lind K., Collet R., Magic Z., Asplund M., 2012, MNRAS, 427, 27
Bessell M. S., 2005, ARA&A, 43, 293
Biazzo K., Frasca A., Catalano S., Marilli E., 2007, Astronomische Nachrichten, 328, 938
Biemont E., Baudoux M., Kurucz R. L., Ansbacher W., Pinnington E. H., 1991, A&A, 249, 539
Bigot L., Thévenin F., 2006, MNRAS, 372, 609
Blackwell D. E., Booth A. J., Petford A. D., 1984, A&A, 132, 236
Blackwell D. E., Ibbetson P. A., Petford A. D., Willis R. B., 1976, MNRAS, 177, 227
Blackwell D. E., Lynas-Gray A. E., 1998, A&AS, 129, 505
Blackwell D. E., Petford A. D., Shallis M. J., 1980, A&A, 82, 249
Blackwell D. E., Shallis M. J., 1977, MNRAS, 180, 177
Blackwell D. E., Shallis M. J., 1979, MNRAS, 186, 673
Blackwell D. E., Shallis M. J., Selby M. J., 1979, MNRAS, 188, 847
Blackwell D. E., Shallis M. J., Simmons G. J., 1982, MNRAS, 199, 33
Blackwell-Whitehead R., Bergemann M., 2007, A&A, 472, L43
Böhm-Vitense E., 1958, Zeitschrift für Astrophysik, 46, 108
Bolmont E., Raymond S. N., Leconte J., Matt S. P., 2012, A&A, 544, A124
Bonifacio P., Caffau E., Ludwig H.-G., Steffen M., 2012, in IAU Symposium, Vol. 282, From Interacting Binaries to Exoplanets: Essential Modeling Tools, Richards M. T., Hubeny I., eds., pp. 213–220

Bonifacio P. et al., 2009, A&A, 501, 519
Borucki W. J. et al., 2010, Science, 327, 977
Bouchy F. et al., 2010, A&A, 519, A98
Boyajian T. S. et al., 2012, ApJ, 746, 101
Brown D. J. A. et al., 2012a, MNRAS, 423, 1503
Brown D. J. A. et al., 2012b, ApJ, 760, 139
Brown T. M., Gilliland R. L., Noyes R. W., Ramsey L. W., 1991, ApJ, 368, 599
Brugamyer E., Dodson-Robinson S. E., Cochran W. D., Sneden C., 2011, APJ, 738, 97
Bruning D. H., 1981, ApJ, 248, 274
Bruning D. H., 1984, ApJ, 281, 830
Bruntt H., 2009, A&A, 506, 235
Bruntt H. et al., 2012, MNRAS, 423, 122
Bruntt H. et al., 2010a, MNRAS, 405, 1907
Bruntt H. et al., 2002, A&A, 389, 345
Bruntt H., De Cat P., Aerts C., 2008, A&A, 478, 487
Bruntt H. et al., 2010b, A&A, 519, A51
Buchhave L. A. et al., 2012, Nature, 486, 375
Caffau E., Ludwig H.-G., Steffen M., Freytag B., Bonifacio P., 2011, Solar Physics, 268, 255
Cannon A. J., Pickering E. C., 1912, Annals of Harvard College Observatory, 56, 65
Canuto V. M., Mazzitelli I., 1991, ApJ, 370, 295
Canuto V. M., Mazzitelli I., 1992, ApJ, 389, 724
Cardini D., Cassatella A., 2007, ApJ, 666, 393
Carlsson M., Rutten R. J., Bruls J. H. M. J., Shchukina N. G., 1994, A&A, 288, 860
Carrington R. C., 1860, MNRAS, 20, 254
Carroll B., Ostlie D., 2006, An Introduction to Modern Astrophysics, 2nd edn. Addison-Wesley, San Francisco
Carter J. A. et al., 2012, Science, 337, 556
Casagrande L., Portinari L., Flynn C., 2006, MNRAS, 373, 13
Casagrande L., Ramírez I., Meléndez J., Bessell M., Asplund M., 2010, A&A, 512, A54
Castelli F., Gratton R. G., Kurucz R. L., 1997, A&A, 318, 841
Castelli F., Kurucz R. L., 2004, in IAU Symposium, Vol. 210, Modelling of Stellar Atmospheres, p. Poster A20
Chanamé J., Ramírez I., 2012, ApJ, 746, 102
Chaplin W. J., 2011, in Asteroseismology, Canary Islands Winter School of Astrophysics, pp. 1–31
Chaplin W. J. et al., 2010, ApJL, 713, L169
Chaplin W. J. et al., 2014, ApJS, 210, 1
Chaplin W. J. et al., 2011, Science, 332, 213
Chaplin W. J., Miglio A., 2013, ARA&A, 51, 353
Chaplin W. J. et al., 2013, ApJ, 766, 101
Charbonneau D., Brown T. M., Latham D. W., Mayor M., 2000, ApJL, 529, L45
Chatterjee S., Ford E. B., Matsumura S., Rasio F. A., 2008, ApJ, 686, 580
Chiavassa A., Bigot L., Kervella P., Matter A., Lopez B., Collet R., Magic Z., Asplund M., 2012, A&A, 540, A5
Christensen-Dalsgaard J., 2011, in Asteroseismology, Canary Islands Winter School of Astrophysics, p. 194
Christensen-Dalsgaard J. et al., 2010, ApJL, 713, L164
Collet R., Asplund M., Trampedach R., 2007, A&A, 469, 687
Collier Cameron A. et al., 2007, MNRAS, 375, 951
Collier Cameron A., Donati J.-F., Semel M., 2002, MNRAS, 330, 699

Collins G. I., 1989, The Fundamentals of Stellar Astrophysics. W.H.Freeman & Co Ltd
Corliss C. H., Bozman W. R., 1962, Experimental transition probabilities for spectral lines of seventy elements; derived from the NBS Tables of spectral-line intensities
Cunha M. S. et al., 2007, Astron Astrophys Rev, 14, 217
Dall T. H., Santos N. C., Arentoft T., Bedding T. R., Kjeldsen H., 2006, A&A, 454, 341
Deheuvels S. et al., 2014, A&A, 564, A27
Deheuvels S. et al., 2012, ApJ, 756, 19
Delfosse X., Forveille T., Ségransan D., Beuzit J.-L., Udry S., Perrier C., Mayor M., 2000, A&A, 364, 217
Demarque P., Woo J.-H., Kim Y.-C., Yi S. K., 2004, ApJS, 155, 667
Dodson-Robinson S. E., 2012, ApJ, 752, 72
Donati J.-F., 2004, http://www.ast.obs-mip.fr/projets/espadons/espadons_new/resol.html (accessed 26/05/2014)
Donati J.-F., Catala C., Landstreet J. D., Petit P., 2006, in Astronomical Society of the Pacific Conference Series, Vol. 358, Solar Polarization 4, Casini R., Lites B. W., eds., p. 362
Donati J.-F., Collier Cameron A., 1997, MNRAS, 291, 1
Doğan G., 2010, PhD Thesis, Aarhus University, Denmark
Doyle A. P., Davies G. R., Smalley B., Chaplin W. J., Elsworth Y., 2014, MNRAS, 444, 3592
Doyle A. P. et al., 2013, MNRAS, 428, 3164
Doyle M. T., O'Mara B. J., Ross J. E., Bessell M. S., 2005, PASA, 22, 6
Edvardsson B., Andersen J., Gustafsson B., Lambert D. L., Nissen P. E., Tomkin J., 1993, A&A, 275, 101
Ekström S. et al., 2012, A&A, 537, A146
Enoch B. et al., 2011, MNRAS, 410, 1631
Enoch B., Collier Cameron A., Horne K., 2012, A&A, 540, A99
Enoch B., Collier Cameron A., Parley N. R., Hebb L., 2010, A&A, 516, A33
Fabrycky D., Tremaine S., 2007, ApJ, 669, 1298
Fabrycky D. C., Winn J. N., 2009, ApJ, 696, 1230
Faedi F. et al., 2013, A&A, 551, A73
Feltzing S., Gustafsson B., 1998, A&AS, 129, 237
Fischer D. A., Valenti J., 2005, ApJ, 622, 1102
Fischer D. A., Valenti J. A., 2003, in Astronomical Society of the Pacific Conference Series, Vol. 294, Scientific Frontiers in Research on Extrasolar Planets, Deming D., Seager S., eds., pp. 117–128
Fortney J. J., Lodders K., Marley M. S., Freedman R. S., 2008, ApJ, 678, 1419
Fossati L., Ryabchikova T., Shulyak D. V., Haswell C. A., Elmasli A., Pandey C. P., Barnes T. G., Zwintz K., 2011, MNRAS, 417, 495
Fraunhofer J., 1817, in Denkschriften der Königlichen Akademie der Wissenschafter zu München für die Jarhe 1814 und 1815, p. 193
Fuhr J. R., Wiese W. L., 2006, Journal of Physical and Chemical Reference Data, 35, 1669
Fuhrmann K., 1998, A&A, 338, 161
Fuhrmann K., Pfeiffer M., Frank C., Reetz J., Gehren T., 1997, A&A, 323, 909
Gadun A. S., 1994, Astronomische Nachrichten, 315, 413
Gallet F., Bouvier J., 2013, A&A, 556, A36
Garcia-Alegre M. C., Vazquez M., Woehl H., 1982, A&A, 106, 261
Gardiner R. B., Kupka F., Smalley B., 1999, A&A, 347, 876
Gaudi B. S., Winn J. N., 2007, ApJ, 655, 550
Ghezzi L., Cunha K., Smith V. V., de Araújo F. X., Schuler S. C., de la Reza R., 2010, ApJ,

720, 1290
Gillon M. et al., 2009, A&A, 501, 785
Gillon M. et al., 2011, A&A, 533, A88
Girardi L., Bressan A., Bertelli G., Chiosi C., 2000, A&AS, 141, 371
Gizon L. et al., 2013, Proceedings of the National Academy of Science, 110, 13267
Gizon L., Solanki S. K., 2003, ApJ, 589, 1009
Gómez Maqueo Chew Y. et al., 2013, ApJ, 768, 79
Gonzalez G., 1998, A&A, 334, 221
Gonzalez G., 2006, PASP, 118, 1494
Gonzalez G., Carlson M. K., Tobin R. W., 2010, MNRAS, 407, 314
Gonzalez G., Laws C., 2000, AJ, 119, 390
Gonzalez G., Laws C., 2007, MNRAS, 378, 1141
Gonzalez G., Laws C., Tyagi S., Reddy B. E., 2001, AJ, 121, 432
González Hernández J. I., Israelian G., Santos N. C., Sousa S., Delgado-Mena E., Neves V., Udry S., 2010, ApJ, 720, 1592
Gratton R. G. et al., 2007, A&A, 464, 953
Gray D., 2008, The Observation and Analysis of Stellar Photospheres, 3rd edn. Cambridge University Press, Cambridge, UK
Gray D. F., 1975, ApJ, 202, 148
Gray D. F., 1977a, ApJ, 211, 198
Gray D. F., 1977b, ApJ, 218, 530
Gray D. F., 1978, Solar Physics, 59, 193
Gray D. F., 1984a, ApJ, 281, 719
Gray D. F., 1984b, ApJ, 277, 640
Gray D. F., 2009, ApJ, 697, 1032
Gray R. O., 1988, Journal of the Royal Astronomical Society of Canada, 82, 336
Gray R. O., Corbally, J. C., 2009, Stellar Spectral Classification. Princeton University Press, Princeton
Gray R. O., Griffin R. E. M., 2007, AJ, 134, 96
Grevesse N., 1991, in IAU Symposium, Vol. 145, Evolution of Stars: the Photospheric Abundance Connection, Michaud G., Tutukov A. V., eds., p. 63
Grossmann-Doerth U., 1994, A&A, 285, 1012
Guillot T., Santos N. C., Pont F., Iro N., Melo C., Ribas I., 2006, A&A, 453, L21
Gustafsson B., Bell R. A., Eriksson K., Nordlund A., 1975, A&A, 42, 407
Hartmann L., 1987, in Lecture Notes in Physics, Berlin Springer Verlag, Vol. 291, Cool Stars, Stellar Systems and the Sun, Linsky J. L., Stencel R. E., eds., p. 1
Harvey J., 1985, in ESA Special Publication, Vol. 235, Future Missions in Solar, Heliospheric & Space Plasma Physics, Rolfe E., Battrick B., eds., pp. 199–208
Hebb L. et al., 2010, ApJ, 708, 224
Hébrard G. et al., 2008, A&A, 488, 763
Hellier C. et al., 2012, MNRAS, 426, 739
Hellier C. et al., 2009a, Nature, 460, 1098
Hellier C. et al., 2010, ApJL, 723, L60
Hellier C., Anderson D. R., Collier-Cameron A., Miller G. R. M., Queloz D., Smalley B., Southworth J., Triaud A. H. M. J., 2011, ApJL, 730, L31
Hellier C. et al., 2009b, ApJL, 690, L89
Henry G. W., Marcy G. W., Butler R. P., Vogt S. S., 2000, ApJL, 529, L41
Hirano T., Sanchis-Ojeda R., Takeda Y., Narita N., Winn J. N., Taruya A., Suto Y., 2012, ApJ, 756, 66
Hirano T., Suto Y., Winn J. N., Taruya A., Narita N., Albrecht S., Sato B., 2011, ApJ, 742,

69
Holmberg J., Nordström B., Andersen J., 2007, A&A, 475, 519
Hoskin M., 1999, The Cambridge Concise History of Astronomy. Cambridge University Press, Cambridge
Huber D. et al., 2013, ApJ, 767, 127
Huggins W., Miller W. A., 1864, Royal Society of London Philosophical Transactions Series I, 154, 413
Hyde Wollaston W., 1802, Royal Society of London Philosophical Transactions Series I, 92, 365
Jenkins J. S., Jones H. R. A., Pavlenko Y., Pinfield D. J., Barnes J. R., Lyubchik Y., 2008, A&A, 485, 571
Johnson H. L., Morgan W. W., 1953, ApJ, 117, 313
Kirchhoff G., 1859, in Monatsberichte der Königlichen Preussische Akademie des Wissenschaften zu Berlin, p. 662
Kirchhoff G., Bunson R., 1860, Annalen der Physik, 186, 161
Kovtyukh V. V., Soubiran C., Belik S. I., Gorlova N. I., 2003, A&A, 411, 559
Kozai Y., 1962, AJ, 67, 591
Kupka F., Piskunov N., Ryabchikova T. A., Stempels H. C., Weiss W. W., 1999, A&AS, 138, 119
Kurucz R., 1988, Trans. IAU, Vol. XXB, ed. M. McNally (Dordrecht: Kluwer), 168
Kurucz R., 1993, Kurucz CD-ROM No. 13. Cambridge, Mass.: Smithsonian Astrophysical Observatory., 13
Kurucz R., 1994, Atomic Data for Fe and Ni. Kurucz CD-ROM No. 22. Cambridge, Mass.: Smithsonian Astrophysical Observatory, 22
Kurucz R., Bell B., 1995, Atomic Line Data (R.L. Kurucz and B. Bell) Kurucz CD-ROM No. 23. Cambridge, Mass.: Smithsonian Astrophysical Observatory, 1995., 23
Kurucz R. L., 2002, Baltic Astronomy, 11, 101
Kurucz R. L., Furenlid I., Brault J., Testerman L., 1984, Solar flux atlas from 296 to 1300 nm
Lachaume R., Dominik C., Lanz T., Habing H. J., 1999, A&A, 348, 897
Landstreet J. D., 2007, in IAU Symposium, Vol. 239, Observing convection in stellar atmospheres, Kupka F., Roxburgh I., Chan K. L., eds., pp. 103–112
Landstreet J. D., Kupka F., Ford H. A., Officer T., Sigut T. A. A., Silaj J., Strasser S., Townshend A., 2009, A&A, 503, 973
Lardner D., 1858, Handbooks of Natural Philosophy & Astronomy: Third Course, Meteorology - Astronomy . Blanchard and Lea, Philadelphia, chapter XXVII, p. 693
Lawler J. E., Sneden C., Cowan J. J., Ivans I. I., Den Hartog E. A., 2009, ApJS, 182, 51
Leavitt H. S., Pickering E. C., 1912, Harvard College Observatory Circular, 173, 1
Leblanc F., 2010, An Introduction to Stellar Astrophysics. Wiley
Lefebvre S., García R. A., Jiménez-Reyes S. J., Turck-Chièze S., Mathur S., 2008, A&A, 490, 1143
Leighton R. B., Noyes R. W., Simon G. W., 1962, ApJ, 135, 474
Lendl M. et al., 2012, A&A, 544, A72
Ligi R. et al., 2012, A&A, 545, A5
Lin D. N. C., Bodenheimer P., Richardson D. C., 1996, Nature, 380, 606
Lind K., Asplund M., Barklem P. S., 2009, A&A, 503, 541
Lind K., Asplund M., Barklem P. S., Belyaev A. K., 2011, A&A, 528, A103
Lind K., Bergemann M., Asplund M., 2012, MNRAS, 427, 50
Lister T. A. et al., 2009, ApJ, 703, 752
Lobel A., 2008, Journal of Physics Conference Series, 130, 012015

Lodders K., Palme H., Gail H.-P., 2009, Landolt Börnstein, 44
Magain P., 1984, A&A, 134, 189
Magic Z., 2014, PhD thesis, LudwigMaximiliansUniversität München.
Magic Z., Collet R., Asplund M., Trampedach R., Hayek W., Chiavassa A., Stein R. F., Nordlund Å., 2013, A&A, 557, A26
Malkov O. Y., Tamazian V. S., Docobo J. A., Chulkov D. A., 2012, A&A, 546, A69
Mamajek E. E., Hillenbrand L. A., 2008, ApJ, 687, 1264
Mashonkina L., 2010a, in EAS Publications Series, Vol. 43, Non-LTE Line Formation for Trace Elements in Stellar Atmospheres, Monier R., Smalley B., Wahlgren G., Stee P., eds., pp. 33–42
Mashonkina L., 2010b, in EAS Publications Series, Vol. 43, Non-LTE Line Formation for Trace Elements in Stellar Atmospheres, Monier R., Smalley B., Wahlgren G., Stee P., eds., pp. 223–229
Mashonkina L., 2010c, in EAS Publications Series, Vol. 43, Non-LTE Line Formation for Trace Elements in Stellar Atmospheres, Monier R., Smalley B., Wahlgren G., Stee P., eds., pp. 189–197
Mashonkina L., 2010d, in EAS Publications Series, Vol. 43, Non-LTE Line Formation for Trace Elements in Stellar Atmospheres, Monier R., Smalley B., Wahlgren G., Stee P., eds., pp. 135–141
Mashonkina L., 2013, A&A, 550, A28
Mashonkina L., Gehren T., Shi J.-R., Korn A. J., Grupp F., 2011, A&A, 528, A87
Mashonkina L. I., Shimanskiĭ V. V., Sakhibullin N. A., 2000, Astronomy Reports, 44, 790
Mathur S. et al., 2011, ApJ, 741, 119
Mathur S. et al., 2012, ApJ, 749, 152
Maxted P. F. L. et al., 2013, PASP, 125, 48
Maxted P. F. L. et al., 2010a, PASP, 122, 1465
Maxted P. F. L. et al., 2011, PASP, 123, 547
Maxted P. F. L. et al., 2010b, AJ, 140, 2007
Maxted P. F. L., Koen C., Smalley B., 2011, MNRAS, 418, 1039
Mayor M. et al., 2003, The Messenger, 114, 20
McLaughlin D. B., 1924, ApJ, 60, 22
Meibom S., Mathieu R. D., Stassun K. G., Liebesny P., Saar S. H., 2011, ApJ, 733, 115
Meléndez J., Asplund M., Gustafsson B., Yong D., 2009, ApJL, 704, L66
Meléndez J., Asplund M., Gustafsson B., Yong D., Ramírez I., 2010, in IAU Symposium, Vol. 265, Chemical Abundances in the Universe: Connecting First Stars to Planets, Cunha K., Spite M., Barbuy B., eds., pp. 412–415
Meléndez J., Barbuy B., 2009, A&A, 497, 611
Metcalfe T. S. et al., 2012, ApJL, 748, L10
Molisch A., Oehry B., 1998, Radiation trapping in atomic vapours. Oxford University Press, Oxford
Morel T., Miglio A., 2012, MNRAS, 419, L34
Mortier A., Santos N. C., Sousa S., Israelian G., Mayor M., Udry S., 2013a, A&A, 551, A112
Mortier A., Santos N. C., Sousa S. G., Fernandes J. M., Adibekyan V. Z., Delgado Mena E., Montalto M., Israelian G., 2013b, A&A, 558, A106
Morton T. D., Johnson J. A., 2011, ApJ, 729, 138
Moultaka J., Ilovaisky S. A., Prugniel P., Soubiran C., 2004, PASP, 116, 693
Mucciarelli A., 2011, A&A, 528, A44
Murphy M. T., Tzanavaris P., Webb J. K., Lovis C., 2007, MNRAS, 378, 221
Nagasawa M., Ida S., 2011, ApJ, 742, 72
Nagasawa M., Ida S., Bessho T., 2008, ApJ, 678, 498

Nave G., Johansson S., Learner R. C. M., Thorne A. P., Brault J. W., 1994, ApJS, 94, 221
Nielsen M. B., Gizon L., Schunker H., Karoff C., 2013, A&A, 557, L10
Nordlund Å., Stein R. F., Asplund M., 2009, Living Reviews in Solar Physics, 6, 2
Nordström B. et al., 2004, A&A, 418, 989
North J. R. et al., 2007, MNRAS, 380, L80
Noyes R. W., Hartmann L. W., Baliunas S. L., Duncan D. K., Vaughan A. H., 1984, ApJ, 279, 763
O'Malley-James J. T., Greaves J. S., Raven J. A., Cockell C. S., 2013, International Journal of Astrobiology, 12, 99
O'Mara B. J., Barklem P. S., 2003, in The Future of Cool-Star Astrophysics: 12th Cambridge Workshop on Cool Stars, Stellar Systems, and the Sun, Brown A., Harper G. M., Ayres T. R., eds., Vol. 12, pp. 1097–1102
Payne C. H., 1929, Harvard College Observatory Bulletin, 867, 1
Payne C. H., 1930, Harvard College Observatory Bulletin, 874, 2
Pepe F. et al., 2002, The Messenger, 110, 9
Perryman M. A. C. et al., 2001, A&A, 369, 339
Perryman M. A. C., ESA, eds., 1997, ESA Special Publication, Vol. 1200, The HIPPARCOS and TYCHO catalogues. Astrometric and photometric star catalogues derived from the ESA HIPPARCOS Space Astrometry Mission
Pickering E. C., Fleming M., 1897, Annals of Harvard College Observatory, 26, 193
Piskunov N., Titarenko A., Ryabchikova T., Pakhomov Y., B N., 2013, in Putting A Stars into Context: Evolution, Environment, and Related Stars
Queloz D. et al., 2010, A&A, 517, L1
Queloz D., Eggenberger A., Mayor M., Perrier C., Beuzit J. L., Naef D., Sivan J. P., Udry S., 2000, A&A, 359, L13
Queloz D. et al., 2001, The Messenger, 105, 1
Ramírez I., Allende Prieto C., Koesterke L., Lambert D. L., Asplund M., 2009, A&A, 501, 1087
Ramírez I., Allende Prieto C., Lambert D. L., 2008, A&A, 492, 841
Ramírez I., Asplund M., Baumann P., Meléndez J., Bensby T., 2010, A&A, 521, A33
Ramírez I., Meléndez J., 2004, ApJ, 609, 417
Ramírez I., Meléndez J., 2005, ApJ, 626, 446
Ramírez I., Meléndez J., Asplund M., 2009, A&A, 508, L17
Randich S., 2009, in IAU Symposium, Vol. 258, The Ages of Stars, Mamajek E. E., Soderblom D. R., Wyse R. F. G., eds., pp. 133–140
Rasio F. A., Ford E. B., 1996, Science, 274, 954
Reddy B. E., Tomkin J., Lambert D. L., Allende Prieto C., 2003, MNRAS, 340, 304
Reiners A., 2006, A&A, 446, 267
Reiners A., Schmitt J. H. M. M., 2002, A&A, 384, 155
Reiners A., Schmitt J. H. M. M., 2003, A&A, 398, 647
Reinhold T., Reiners A., 2013, A&A, 557, A11
Reinhold T., Reiners A., Basri G., 2013, A&A, 560, A4
Robinson K., 2007, Spectroscopy: The Key to the Stars. Springer
Robinson, Jr. R. D., 1980, ApJ, 239, 961
Robinson S. E., Laughlin G., Bodenheimer P., Fischer D., 2006, ApJ, 643, 484
Rocha-Pinto H. J., Maciel W. J., 1998, MNRAS, 298, 332
Rocha-Pinto H. J., Maciel W. J., Scalo J., Flynn C., 2000, A&A, 358, 850
Romanyuk I. I., 1997, in Stellar Magnetic Fields, Glagolevskij Y., Romanyuk I., eds., pp. 11–25
Rosseland S., 1928, MNRAS, 89, 49

Rossiter R. A., 1924, ApJ, 60, 15
Rowland H. A., 1895, ApJ, 1, 29
Rupprecht G. et al., 2004, in Proceedings of the SPIE, Vol. 5492, Ground-based Instrumentation for Astronomy, Moorwood A. F. M., Iye M., eds., pp. 148–159
Ryan S. G., 1998, A&A, 331, 1051
Saar S. H., Osten R. A., 1997, MNRAS, 284, 803
Saffe C., Levato H., 2004, A&A, 418, 1083
Saha M. N., 1921, Royal Society of London Proceedings Series A, 99, 135
Santos N. C., Israelian G., Mayor M., 2004, A&A, 415, 1153
Schatzman E., 1962, Annales d'Astrophysique, 25, 18
Schlaufman K. C., 2010, ApJ, 719, 602
Schuler S. C., Cunha K., Smith V. V., Ghezzi L., King J. R., Deliyannis C. P., Boesgaard A. M., 2011a, ApJL, 737, L32
Schuler S. C., Flateau D., Cunha K., King J. R., Ghezzi L., Smith V. V., 2011b, ApJ, 732, 55
Seager S., Mallén-Ornelas G., 2003, ApJ, 585, 1038
Sestito P., Randich S., 2005, A&A, 442, 615
Shaltout A. M. K., Beheary M. M., Bakry A., Ichimoto K., 2013, MNRAS, 430, 2979
Shapley H., 1914, ApJ, 40, 448
Sheminova V. A., 1993, Kinematics and Physics of Celestial Bodies, 9, 21
Sheminova V. A., Gadun A. S., 1998, Kinematics and Physics of Celestial Bodies, 14, 169
Shi J. R., Gehren T., Butler K., Mashonkina L. I., Zhao G., 2008, A&A, 486, 303
Shi J. R., Gehren T., Zhao G., 2004, A&A, 423, 683
Silva Aguirre V., Casagrande L., Basu S., Campante T. L., Chaplin W. J., Huber D., Miglio A., Serenelli A. M., 2013, Astronomische Nachrichten, 334, 22
Simpson E. K. et al., 2011, MNRAS, 414, 3023
Skillen I. et al., 2009, A&A, 502, 391
Skumanich A., 1972, ApJ, 171, 565
Smalley B., 2004, in IAU Symposium, Vol. 224, The A-Star Puzzle, Zverko J., Ziznovsky J., Adelman S. J., Weiss W. W., eds., pp. 131–138
Smalley B., 2005, Memorie della Societa Astronomica Italiana Supplementi, 8, 130
Smalley B. et al., 2012, A&A, 547, A61
Smalley B. et al., 2010, A&A, 520, A56
Smalley B., Gardiner R. B., Kupka F., Bessell M. S., 2002, A&A, 395, 601
Smalley B., Smith K. C., Dworetsky M. M., 2001, UCLSYN Userguide, http://www.astro.keele.ac.uk/∼bs/publs/uclsyn.pdf
Smith A. M. S. et al., 2013, A&A, 552, A120
Smith K. C., 1992, Ph.D. Thesis, University of London
Sneden C., Lawler J. E., 2005, in ASP Conference Series, Vol. 336, Cosmic Abundances as Records of Stellar Evolution and Nucleosynthesis, Barnes III T. G., Bash F. N., eds., p. 11
Sneden C. A., 1973, PhD thesis, The University of Texas at Austin.
Soderblom D. R., 1982, ApJ, 263, 239
Soderblom D. R., 2009, in IAU Symposium, Vol. 258, IAU Symposium, Mamajek E. E., Soderblom D. R., Wyse R. F. G., eds., pp. 1–10
Soderblom D. R., 2010, ARA&A, 48, 581
Sousa S. G., Santos N. C., Israelian G., Mayor M., Monteiro M. J. P. F. G., 2007, A&A, 469, 783
Sousa S. G., Santos N. C., Israelian G., Mayor M., Udry S., 2011, A&A, 533, A141
Sousa S. G. et al., 2008, A&A, 487, 373
Southworth J., 2011, MNRAS, 417, 2166

Southworth J., 2012a, in Orbital Couples: Pas de Deux in the Solar System and the Milky Way, Arenou F., Hestroffer D., eds., pp. 51–58
Southworth J., 2012b, MNRAS, 426, 1291
Southworth J. et al., 2012, MNRAS, 426, 1338
Southworth J. et al., 2013, MNRAS, 434, 1300
Sozzetti A., Torres G., Charbonneau D., Latham D. W., Holman M. J., Winn J. N., Laird J. B., O'Donovan F. T., 2007, ApJ, 664, 1190
Sozzetti A., Yong D., Carney B. W., Laird J. B., Latham D. W., Torres G., 2006, AJ, 131, 2274
Spiegel D. S., Burrows A., 2013, ApJ, 772, 76
Steffen M., Caffau E., Ludwig H.-G., 2013, Mem. S.A.It., 24, 37
Steffen M., Ludwig H.-G., Caffau E., 2009, Mem. S.A.It., 80, 731
Street R. A. et al., 2010, ApJ, 720, 337
Strömgren B., 1966, ARA&A, 4, 433
Struve O., 1930, ApJ, 72, 1
Struve O., 1952, The Observatory, 72, 199
Struve O., Elvey C. T., 1934, ApJ, 79, 409
Takeda Y., 1995, PASJ, 47, 337
Takeda Y., Kawanomoto S., 2005, PASJ, 57, 45
Takeda Y., Ohkubo M., Sadakane K., 2002, PASJ, 54, 451
Takeda Y., Ohkubo M., Sato B., Kambe E., Sadakane K., 2005a, PASJ, 57, 27
Takeda Y. et al., 2005b, PASJ, 57, 13
Tassoul J.-L., Tassoul M., 2004, A concise history of solar and stellar physics. Princeton University Press, Princeton
Thorén P., Feltzing S., 2000, A&A, 363, 692
Thorne A., 1988, Spectrophysics. Routledge, Chapman & Hall
Torres G., Andersen J., Giménez A., 2010, A&AR, 18, 67
Torres G., Fischer D. A., Sozzetti A., Buchhave L. A., Winn J. N., Holman M. J., Carter J. A., 2012, ApJ, 757, 161
Torres G., Winn J. N., Holman M. J., 2008, ApJ, 677, 1324
Triaud A. H. M. J., 2011, Ph.D. Thesis, Université de Genève
Triaud A. H. M. J. et al., 2013a, A&A, 551, A80
Triaud A. H. M. J. et al., 2010, A&A, 524, A25
Triaud A. H. M. J. et al., 2013b, A&A, 549, A18
Triaud A. H. M. J. et al., 2011, A&A, 531, A24
Tsantaki M., Sousa S. G., Adibekyan V. Z., Santos N. C., Mortier A., Israelian G., 2013, A&A, 555, A150
Valenti J. A., Fischer D. A., 2005, ApJS, 159, 141
Valenti J. A., Piskunov N., 1996, A&AS, 118, 595
van Leeuwen F., 2007, A&A, 474, 653
Wahlgren G. M., 2005, Memorie della Societa Astronomica Italiana Supplementi, 8, 108
Wahlgren G. M., 2010, in EAS Publications Series, Vol. 43, Non-LTE Line Formation for Trace Elements in Stellar Atmospheres, Monier R., Smalley B., Wahlgren G., Stee P., eds., pp. 91–114
Walker G. et al., 2003, PASP, 115, 1023
Wallace L., Hinkle K. H., Livingston W. C., Davis S. P., 2011, ApJS, 195, 6
West R. G. et al., 2013, preprint, arXiv:1310.5607
West R. G. et al., 2009, AJ, 137, 4834
Wilson D. M. et al., 2008, ApJL, 675, L113
Winn J. N., 2011, in Exoplanets, Seager S., ed., University of Arizona Press, pp. 55–77

Woolf V. M., Wallerstein G., 2005, MNRAS, 356, 963
Yi S., Demarque P., Kim Y.-C., Lee Y.-W., Ree C. H., Lejeune T., Barnes S., 2001, ApJS, 136, 417
Zhao G., Butler K., Gehren T., 1998, A&A, 333, 219